Excited-State Properties of Organic Inorganic Halide Perovskites from First-Principles

Yinan Chen

Hertford College

University of Oxford

Thesis submitted for the Degree of

Doctor of Philosophy in Condensed Matter Physics

January 2025

Abstract

In this thesis, we employ state-of-the-art first-principles calculations to understand optoelectronic properties and excited states in perovskite-based materials. We primarily focus on three groups of perovskites - mixed iodide/bromide perovskites, layered perovskites, and perovskite-intergrowth heterostructures.

For mixed halide $\mathrm{CsPb(Br}_x\mathrm{I}_{1-x})_3$ perovskites, we applied the virtual crystal approximation (VCA) within density functional theory (DFT), the GW approximation, and the Bethe-Salpeter equation (BSE) to calculate structural, vibrational, and optoelectronic properties for a series of mixed halide perovskites. We show that the VCA incorporated with GW+BSE framework can accurately reproduce experimental trends across the full halide mixing range. The study demonstrates that mixed iodide/bromide perovskites can be modelled as homovalent alloys, and local structural distortions do not play a significant role for the properties of these uniformly mixed systems.

Layered organic-inorganic halide perovskites exhibit remarkable structural and chemical diversity. In these materials, excitons are primarily believed to be strongly confined within the inorganic metal halide layers, and the interlayer coupling generally suppressed by the organic cations. We present a systematic approach to study the energy and spatial distribution of the lowest-energy excitons in layered organic-inorganic halide perovskites from first-principles many-body perturbation theory. We find that the quasiparticle band structures, absorption spectra, and exciton binding energies depend strongly on the distance between and the alignment of adjacent metal halide perovskite layers. Furthermore, we show that exciton delocalisation can be tuned by changing the interlayer distance and alignment, both parameters determined by the chemical composition and size of the organic cations. The calculations presented in Chapter 4 establish the general intuition needed to engineer excitonic properties in novel halide perovskite nanostructures.

Finally, we extend our exciton analysis approach to perovskite-intergrowth heterostructures by systematically constructing hypothetical molecular components ($i.e.$ **AMTP**, **ATP**, and **HMA**) in a series of lead halide perovskites-intergrowth heterostructures. We observe a change from Type I to Type II band alignment in these materials and see a clear correlation between the band alignment and the absence of inter/intralayer excitons. Several dark interlayer excitons can be found in Type II heterostructures below the absorption spectra onset. Such correlation can also be found when comparing the experimentally realised materials (**1-Na** and **1-Li**) as presented in Chapter 5.

By systematically investigating the band structures, the optical absorption spectra, exciton decompositions and localisation, charge-density and potential landscapes in these heterostructures, we uncover the structural and electrostatic origin of the band alignment change. We have shown that even subtle structural modifications, such as the repositioning of charged ions, can alter the electrostatic energy landscape between the layers, which in turn influences the band alignment and consequently, exciton localisation.

These insights highlight the power of structural and molecular engineering in tuning the optoelectronic and excited-state properties of perovskite-based materials. The research presented in the thesis provides a robust theoretical foundation for studying excitons and designing advanced functional materials with tunable properties, and devices across a wide range of applications, including solar cells and light-emitting diodes.

Contents

List of Figures

List of Tables

List of Abbreviations

1,5-DAN naphthalene-1,5-diamine

4AMP 4-aminomethyl piperidinium

AMHC *trans*-(4-aminomethyl)cyclohexanecarboxylic acid

AMTP 4-(ammoniomethyl)-tetrahydropyran

ATP 4-aminotetrahydropyran

BSE Bethe-Salpeter Equation

BZ Brillouin Zone

C12DA 1,12-dodecane diammonium

CBB Conduction Band Bottom

CBM Conduction Band Minimum

CYS Cysteamine

DFPT Density Functional Perturbation Theory

DFT Density Functional Theory

DJ Dion-Jacobson

ECF Exciton Correlation Function

EOA ethanolammonium

FA Formamidinium ($CH(NH_2)_2^+$)

FWHM Full Width at Half-Maximum

GGA Generalised Gradient Approximation

HMA (Hydroxymethyl)-ammonium

IR Infrared

LDA Local Density Approximation

LED Light Emitting Diode

LO Longitudinal Optical

MA Methylammonium ($CH_3NH_3^+$)

MBPT Many-Body Perturbation Theory

MLWFs Maximally Localised Wannier Functions

PBE Perdew-Burke-Ernzerhof

RPA Random Phase Approximation

RP Ruddlesden-Popper

SOC Spin-Orbit Coupling

TMDCs Transition Metal Dichalcogenides

UV-VIS Ultraviolet-Visible

VBM Valence Band Maximum

VBT Valence Band Top

VCA Virtual Crystal Approximation

List of publications

1. Yinan Chen, Silvia G. Motti, Robert D. J. Oliver, Adam D. Wright, Henry J. Snaith, Michael B. Johnston, Laura M. Herz, and Marina R. Filip, "Optoelectronic Properties of Mixed Iodide–Bromide Perovskites from First-Principles Computational Modeling and Experiment," *The Journal of Physical Chemistry Letters*, 2022, **13** (18), 4184-4192.
2. Yinan Chen and Marina R. Filip, "Tunable Interlayer Delocalisation of Excitons in Layered Organic–Inorganic Halide Perovskites," *The Journal of Physical Chemistry Letters*, 2023, **14** (47), 10634-10641.
3. Raisa-Ioana Biega, Yinan Chen, Marina R. Filip, and Linn Leppert, "Chemical Mapping of Excitons in Halide Double Perovskites," *Nano Letters*, 2023, **23** (17), 8155-8161.

The work presented in Chapters 3 and 4 has been reported in Publication 1 and 2. The work presented in Chapters 5 and 6 is currently being prepared for publication.

Some of the calculations presented in Chapters 5 and 6 were performed based on earlier refined experimental structures. Later experimental refinements introduced minor adjustments to the structures, and our updated calculations show these changes do not affect the principal conclusions. Results incorporating the revised structures are included in the manuscripts to be published.

Some figures in Chapter 3 and 4 are reproduced or adapted from Publications 1 and 2 under the *CC-BY 4.0* license.

1 | Introduction

1.1 Introduction to metal halide perovskites

The emergence of perovskite materials represents one of the most significant developments in materials science and semiconductor physics of the past decade due to their exceptional optoelectronic performance and unique combination of properties [13–17].

The advancement of perovskite materials research has followed a fascinating trajectory, marked by several ground-breaking discoveries. While the oxide perovskites have been initially studied extensively for their ferroelectric and magnetic properties since the early 20th century [18, 19], the discovery of halide perovskites opened up a transformative new era for the field [20, 21]. The first synthesis of organic-inorganic hybrid perovskites was reported by Weber in 1978 [20], but their potential remained largely unexplored until the early 2000s. In 2009, Kojima and colleagues demonstrated the first application of organic metal halide perovskites in solar cells, achieving a modest power conversion efficiency of 3.8% [21]. In 2012, Lee and colleagues made a breakthrough by developing solar cells based on meso-superstructured perovskites that achieved a remarkable 10.9% efficiency, demonstrating exceptional photovoltaic properties including high open-circuit voltages exceeding 1.1V [13]. These discoveries triggered a remarkable surge in research activity, leading to rapid improvements in both application and understanding of these materials. Within just a decade, perovskite solar cells achieved certified efficiencies exceeding 27%, closely matching the traditional silicon solar cells [22].

Initially discovered by Gustav Rose in 1839 in the Ural Mountains of Russia, and named after Russian mineralogist Lev Perovski, the term perovskite originally referred to calcium titanate ($CaTiO_3$). Today, this classification includes a vast family of structurally and compositionally diverse compounds that share similar characteristic crystal structure. They consist of anionic octahedra connected through their corners in various dimensions and charge-compensated by inorganic or organic cations.

The structural diversity of perovskite materials represents one of their most compelling characteristics, leading to their application across a broad spectrum of optoelectronic devices. In photovoltaic applications, the strong absorption coefficients of iodide perovskites (>10^4 cm^{-1}) [13], long carrier diffusion lengths (exceeding 1 μm) [23], and tunable bandgaps (1.2-3.0 eV) [17] make them ideal candidates for both single-junction and tandem solar cells [24, 25]. Halide perovskites also exhibit remarkable properties including high defect tolerance and efficient radiative recombination [26], which have enabled the development of light-emitting diodes with external quantum efficiencies exceeding 20% [27]. Furthermore, the compositionally tunable emission wavelength, and the quantum confinement effects in low-dimensional perovskites have positioned these materials as promising candidates for next-generation display technologies and lighting applications [28].

In this chapter, we will give an introductory overview of the perovskite materials investigated in detail throughout this thesis, focusing on their diverse structural configurations, unique properties and applications.

1.2 Three-dimensional halide perovskites

Three-dimensional halide perovskites typically have the chemical formula ABX_3, where B represents a divalent cation (such as Pb^{2+} or Sn^{2+}), and X denotes halide anions [29,30]. The crystal structure consists of corner-sharing BX_6 octahedra, forming cavities that accommodate the A-site cation, which can be either inorganic (such as Cs^+) or molecular cations like methylammonium ($CH_3NH_3^+$, MA^+) or formamidinium ($CH(NH_2)_2^+$, FA^+) [29] as shown in Figure 1.1.

The electronic properties of these materials are primarily determined by the B-site metal and X-site halogen around the band edges [31], while A-site cation states are typically located far from the band edges. The band gap can be changed by more than 1 eV through halogen substitution [32], and replacing Pb with Sn can reduce it by over 400 meV [33, 34]. The A-site cations indirectly influence these properties through steric effects on the BX_6 octahedra [35], enabling band gap adjustments up to 300 meV.

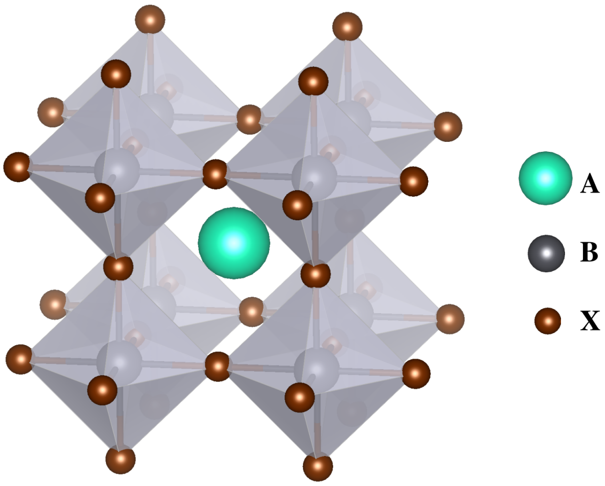

Figure 1.1: The crystal structure of cubic perovskite ABX_3. Blue spheres represent the A cations, grey spheres represent the B cations, and brown spheres represent the X anions that forms an octahedra

Recent developments have focused on mixed-composition perovskites, incorporating combinations of organic/inorganic cations [36, 37] (FA/MA/Cs), metals [38], and halogens [3]. This mixing strategy not only enables fine-tuning of optical properties but also improves thermal and photostability by suppressing phase transitions and halide segregation under illumination [3, 39]. However, these materials present rather complex behaviours upon mixing, such as the “band gap bowing” effect in mixed-metal systems [40, 41], where the band gap of the mixed composition deviates from a linear interpolation between the two ends, showing a downward parabolic behaviour. Understanding these phenomena has been challenging both experimentally and theoretically due to the structural complexity and disorder associated with chemical mixing.

The complex behaviour of mixed-halide perovskites necessitates a comprehensive theoretical-experimental approach for investigation. In Chapter 3, we will present a detailed study of halogen mixing in lead-halide perovskites, specifically focusing on iodide-bromide systems. We employ the virtual crystal approximation (VCA), which offers a computationally efficient method to model alloyed systems by replacing the randomly distributed atomic species with a weighted average "virtual atom". When combined with state-of-the-art first principles calculations, this approach provides reliable predictions of electronic and optical properties while avoiding the computational complexity of explicit disorder modelling. With VCA, we systematically investigate how halogen mixing influences key optoelectronic properties across different composition ratios.

1.3 Layered perovskites

Layered organic-inorganic halide perovskites represent a structurally and chemically heterogeneous family of functional semiconductors [42], which have drawn significant attention for various optoelectronic applications, including solar cells, light-emitting diodes, photodetectors, and lasers [43, 44]. These materials are common derivatives of the 3D perovskites which maintain the corner-sharing octahedral building blocks, consist of alternating layers of octahedral networks and organic molecular cations [45].

While these materials are formally extending in three-dimensional, their electronic and optical properties exhibit quasi-2D behaviour due to the alternating layered structure [44]. The inorganic layers act as semiconductor quantum wells, while the organic layers serve as potential barriers, leading to strongly bound excitons with binding energies often exceeding 300 meV [46]. Interlayer electronic coupling and charge transfer are typically suppressed [47,48], resulting in excitons localised within the inorganic layers [46].

The Dion-Jacobson/Ruddlesden-Popper series, with chemical formula $A_{n-1}A'_2B_nX_{3n+1}$, represents a prominent class of these materials, where A is typically an inorganic or small organic cation, A’ is usually a large bulky organic molecule (such as butylammonium or phenethylammonium), and n denotes the number of perovskite layers per unit cell [49]. The structural diversity of these materials stems from the incorporation of different organic cations A’, which enables precise control over the structural configuration - the organic spacers can modulate the thickness of the layer or the interlayer spacing, affect the alignment of adjacent inorganic layers, and even change the planarity of the metal-halide sheets by introducing tiltings and distortions [43, 50, 51].

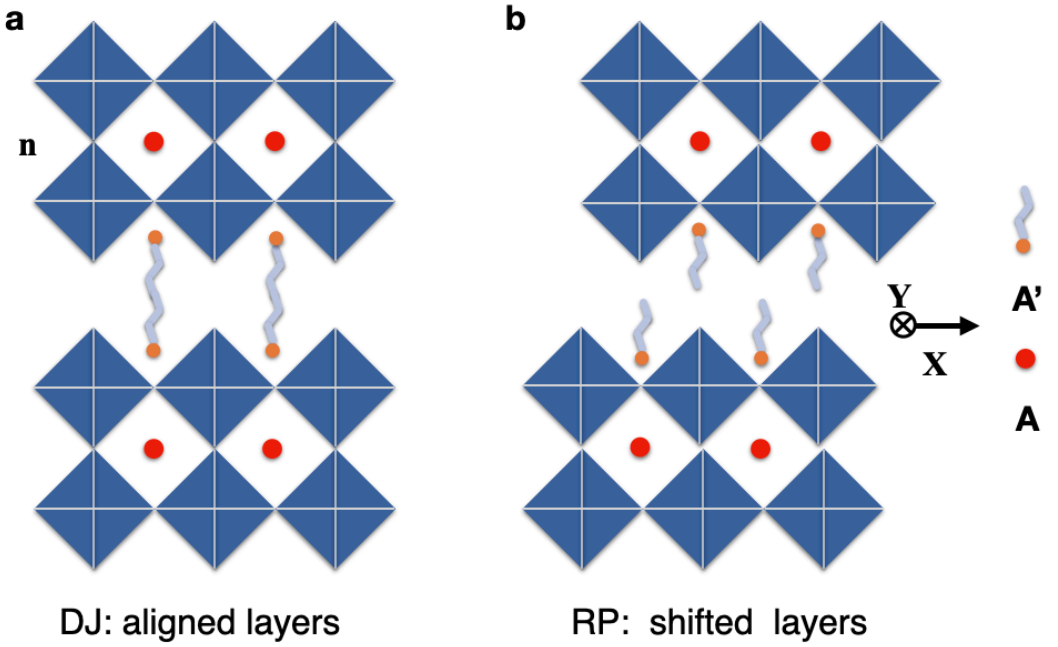

Figure 1.2: Schematic representation of Dion-Jacobson (a) and Ruddlesden-Popper (b) viewed along the inorganic layer.

This structural tunability translates directly into modifiable optoelectronic properties, as the quantum and dielectric confinement effects are highly sensitive to these architectural parameters [44, 52]. In other low-dimensional materials (e.g. transition metal dichalcogenides (TMDCs)), the phenomenon of exciton delocalisation across layers has been extensively studied [53–55]. In these systems, long-lived interlayer excitons can form and delocalise across different layers [53], with properties that can be tuned through layer twisting [54] and heterostructure engineering [55].

Recent experimental studies of layered perovskites, have revealed similar observations as those in TMDCs, including evidence of interlayer exciton transport [56], exciton delocalisation [57], and charge transfer excitons [58]. Strong electron-phonon and exciton-phonon coupling manifest in regularly spaced photoluminescence peaks [59], and the formation of self-trapped excitons contributes to broad photoluminescence spectra and white light emission [42].

While such exciton engineering is becoming possible in layered perovskites through advanced synthesis techniques and experimental characterisation, theoretical understanding through first-principles calculations remains limited due to the complexity of these organic-inorganic semiconductors. Early computational work by Molina-Sánchez [60] demonstrated that organic cations often contribute little to the band-edge electronic states, allowing them to replace these cations with Cs in model structures. Using this simplified approach, they obtained exciton binding energies for bromide-based monolayers as high as 600 meV. Filip et al. [46] built on these insights and carried out detailed GW+BSE calculations of Ruddlesden-Popper perovskites, systematically varying the size and presence of organic cations. Their results highlight the essential role of organic cations in dielectric screening: replacing them with Cs, or using smaller cations, significantly enhances quantum confinement effects and increases exciton binding energies, while the presence of larger organic molecules can counteract confinement and reduce binding energies by several hundreds of meV. These combined theoretical efforts provide crucial guidance for understanding and designing excitonic properties in layered perovskites. Despite these advances, a comprehensive understanding of interlayer exciton delocalisation in these systems remains unclear.

In Chapter 4, we will present a comprehensive theoretical investigation of exciton delocalisation in layered perovskites using state-of-the-art GW+BSE calculations. Our analysis reveals key structural features determining the distribution of photo-excited electron-hole pairs and quantifies how interlayer exciton delocalisation can be tuned through control of the distance and alignment of inorganic layers. This study provides fundamental insights into the microscopic mechanisms governing excited states properties in layered perovskites, with important implications for even more complex low dimensional materials.

1.4 Perovskite heterostructures

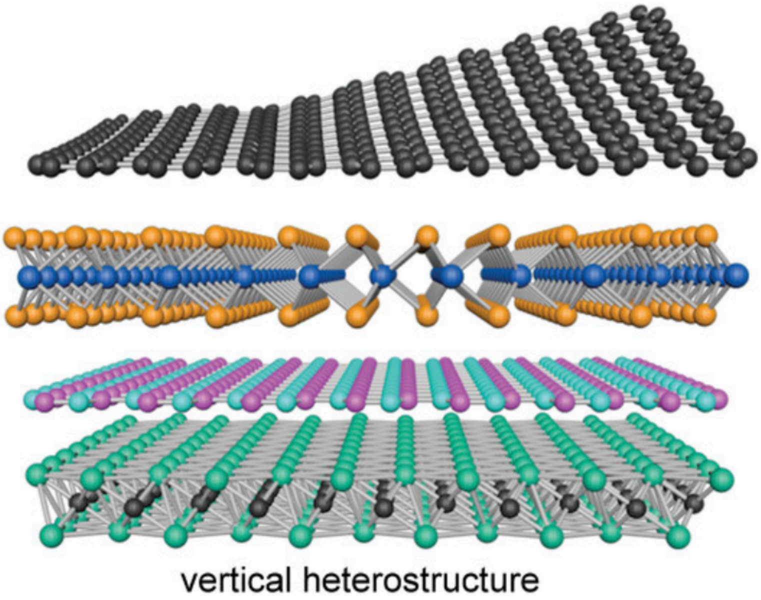

Figure 1.3: Schematic diagram of a heterostructure. Figure adapted from Ref. [1] with full-access rights.

The exploration of optoelectronic and excited state properties in layered systems has recently expanded beyond traditional layered perovskites to more complex van der Waals heterostructures. Within this field, the study of interlayer excitons has emerged as a particularly fascinating area of research [53]. Interlayer excitons represent electron and hole pairs that are spatially separated across different layers of a heterostructure, with a distinct optical and electronic properties compared to intralayer excitons (confined electron-hole pairs within the same layer) [53, 61].

The fundamental physics of interlayer excitons have been extensively studied in TMDCs. These interlayer excitons exhibit several remarkable properties, including

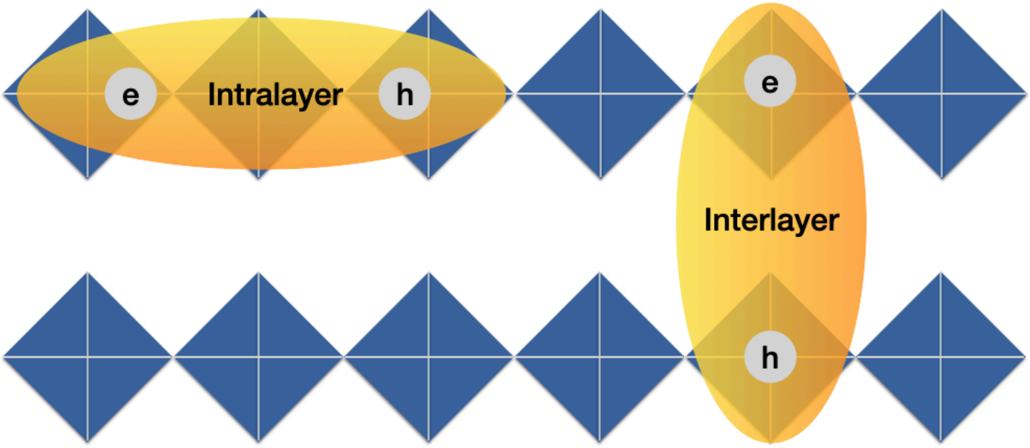

Figure 1.4: Schematic diagram of interlayer and intralayer exciton in layered materials.

significantly extended exciton lifetimes, reduced binding energies and susceptibility to electric field control [61–63]. The binding energy of interlayer excitons exhibits strong dependence on the dielectric environment of the heterostructure [61]. Furthermore, the spatial separation of electrons and holes across different layers leads to reduced wavefunction overlap, resulting in longer radiative lifetimes and modified optical selection rules compared to conventional intralayer excitons [61].

In TMDCs van der Waals heterostructures, the relative alignment of electronic bands between adjacent layers plays a crucial role in determining optoelectronic and excitonic properties. These systems typically exhibit either Type I or Type II band alignment, where Type I structures feature both conduction and valence band extrema in the same layer, naturally confining electrons and holes within that layer [64, 65]. In contrast, Type II heterostructures are characterised by a staggered band alignment, where the conduction band minimum and valence band maximum reside in different layers. This band offset naturally promotes the spatial separation of electrons and holes across the interface, facilitating the formation of interlayer excitons [64, 65]. Understanding and controlling this band alignment through material selection and interface engineering thus provides a powerful strategy for tailoring excitonic properties in these systems.

Recent developments in the field have revealed even more complex phenomena, such as moiré excitons in twisted bilayer systems. These structures create periodic potential landscapes that can localise excitons, leading to modified energy spectra and novel quantum optical effects [66, 67]. The ability to control these properties through twist angle engineering has opened new possibilities for manipulating excitonic behaviour [66, 67].

While TMDCs serve as model platforms for understanding spatially indirect excitations, recent advances in synthetic chemistry have enabled the development of novel perovskite-based heterostructures through solution-phase self-assembly approaches [12]. Unlike traditional van der Waals heterostructures that rely on mechanical stacking or layer-by-layer deposition, these perovskite-based heterostructures can be synthesised through solution-state self-assembly in a single step. This approach not only enables precise atomic-level control over interfaces but also provides significantly broader compositional and structural diversity, along with improved scalability for practical applications [12]. This approach has led to the creation of perovskite-intergrowth heterostructures, where different inorganic frameworks are connected through carefully designed organic linkers [12].

Recent GW+BSE calculations of these newly synthesised heterostructures including inorganic lead-bromide/chloride perovskites and non-perovskite layers, revealed that chemical engineering of such hetero-interfaces may lead to yet another route to not only control the energy but also the delocalisation of excitons in these superstructures [12]. However, several aspects remain to be fully understood, particularly the role of structural and compositional parameters in mediating interlayer interactions and their impact on excitonic properties.

The theoretical investigations in Chapters 5 and 6 will explore the possibilities for observing interlayer excitons in perovskite heterostructures using first-principles computations. Through systematic ab initio calculations and in-depth analysis of excitons, we will examine how molecular and structural engineering can be used to tune band alignment and control exciton localisation. These studies will help uncover phenomena unique to perovskite heterostructures, including the observation of multiple excitonic species, the influence of ion/charge migration on interlayer coupling, and the role of structural parameters in exciton localisation.

1.5 Summary and organisation of the thesis

This thesis investigates optoelectronic and excited states properties of perovskite based semiconductors including mix halide perovskites, low-dimensional perovskites and perovskites based heterostructures using state-of-the-art first principle computation techniques, with particular emphasis on understanding and tuning excited state prosperities in perovskite materials.

The remaining part of the thesis is organised as follows:

- Chapter 2 presents the theoretical framework and computational methods employed throughout this work, including density functional theory (DFT), many-body perturbation theory, and quantitative approaches developed for analysing excitons.
- Chapter 3 investigates the properties of mixed-halide perovskites, focusing on how halogen mixing influences key optoelectronic properties through a combination of the VCA and first-principles calculations.
- Chapter 4 presents a comprehensive study of exciton delocalisation in Dion-Jacobson layered perovskites, revealing how structural features determine the distribution of photo-excited electron-hole pairs.
- Chapter 5 explores the formation and properties of interlayer excitons in perovskite heterostructures, establishing relationships between structural parameters, band alignment and exciton behaviour.

- Chapter 6 investigates the mechanisms driving band alignment changes in perovskite heterostructures and develops strategic approaches for controlling electronic properties through molecular and structural engineering.

2 | Methods

In this chapter, we introduce the computational methods used throughout this thesis, including DFT and the GW + BSE framework.

The chapter is organised as follows: we first present the fundamental aspects of DFT, including the Hohenberg-Kohn theorems and Kohn-Sham equations. Then, we discuss many-body perturbation theory within the GW approximation for accurate electronic structure calculations, followed by the BSE method for treating optical excitations. Finally, we discuss additional computational techniques we've used or implemented in this thesis, including the VCA [68] for alloy systems and methods for analysing excited states properties, such as exciton decomposition analysis and exciton correlation analysis.

This chapter aims to provide an introductory overview and touches on the mathematical deviation which are most relevant to the computational studies presented in this thesis. A more comprehensive introduction of the implementation details for DFT and the GW+BSE framework, can be found in several reviews and textbooks [2, 69–76].

2.1 Density functional theory

2.1.1 Many-body Schrödinger equation and Born-Oppenheimer approximation

When we discuss a system with many electrons and many nuclei, we need to introduce a so-called many-body wavefunction, Ψ, which depends on the coordinates of all particles. The quantum-mechanical behaviour of a non-relativistic system of N electrons and M nuclei is governed by the many-body Schrödinger equation:

$$\hat{H}\Psi(\mathbf{r}_1, \dots, \mathbf{r}_N; \mathbf{R}_1, \dots, \mathbf{R}_M) = E\Psi(\mathbf{r}_1, \dots, \mathbf{r}_N; \mathbf{R}_1, \dots, \mathbf{R}_M), \tag{2.1}$$

where $\hat{H}$ is the Hamiltonian operator, Ψ is the total many-body wavefunction and E is the total energy. $\mathbf{r}_i$ are electronic coordinates, and $\mathbf{R}_I$ are nuclear coordinates. Under the Born-Oppenheimer approximation [2], the nuclear motion is decoupled from the electronic motion due to the large mass difference. As a result, we can treat the nuclei as stationary at fixed positions and focus on solving the electronic Schrödinger equation shown below:

$$\hat{H}_{\text{el}}\psi(\mathbf{r}_1, \dots, \mathbf{r}_N) = E_{\text{el}}\psi(\mathbf{r}_1, \dots, \mathbf{r}_N), \tag{2.2}$$

where $\hat{H}_{\text{el}}$ is the electronic Hamiltonian, and E_{el} is the electronic energy.

2.1.2 Hohenberg-Kohn theorems and Kohn-Sham equations

The many-body electronic Hamiltonian $\hat{H}_{\text{el}}$ appearing in the above expression is given as the follows, in atomic units [2]:

$$\hat{H}_{\text{el}}(\mathbf{r}_1, \mathbf{r}_2, \cdots, \mathbf{r}_N) = -\sum_i \frac{1}{2}\nabla_i^2 + \sum_i V_{\text{n}}(\mathbf{r}_i) + \frac{1}{2}\sum_{i \neq j} \frac{1}{|\mathbf{r}_i - \mathbf{r}_j|}. \tag{2.3}$$

Here, the first term $= -\sum_i \frac{1}{2}\nabla_i^2$ is the kinetic energy of the electrons, the last term $\frac{1}{2}\sum_{i\neq j}\frac{1}{|\mathbf{r}_i - \mathbf{r}_j|}$ represents the electron-electron repulsion, and $V_{\text{n}}(\mathbf{r}_i)$ represents the external Coulomb potential experienced by electron i due to the nuclei, given by

$$V_{\text{n}}(\mathbf{r}) = -\sum_a \frac{Z_a}{|\mathbf{r} - \mathbf{R}_a|}, \tag{2.4}$$

where Z_a is the atomic number of nucleus a located at position $\mathbf{R}_a$.

The electronic total energy, E_{el}, of the many-electron system, is a functional of the electronic wavefunction $\psi\left(\mathbf{r}_1, \ldots, \mathbf{r}_N\right)$.

$$E_{\text{el}} = \langle\psi|\hat{H}_{\text{el}}|\psi\rangle = \int d\mathbf{r}_1 \ldots d\mathbf{r}_N \psi^*\left(\mathbf{r}_1, \ldots, \mathbf{r}_N\right) \hat{H}_{\text{el}} \psi\left(\mathbf{r}_1, \ldots, \mathbf{r}_N\right). \tag{2.5}$$

When solving the many-body Schrödinger equation under the Born-Oppenheimer approximation, the most complicated part is the Coulomb interaction between the electrons. If we neglect this term, each electron moves independently in the external potential from the nuclei, the many-body problem separates into N identical one-electron problems:

$$\left[-\frac{1}{2}\nabla^2 + V_{\text{n}}(\mathbf{r})\right] \phi_i(\mathbf{r}) = \epsilon_i, \phi_i(\mathbf{r}), \tag{2.6}$$

known as the *independent electron approximation* [2].

Starting from the idea that each particle moves independently in an external average field, instead of treating the system as fully interacting, we can heuristically treat the complex many body interactions between particles by approximating the influence of all other particles on any given particle as an average effect. Under this *mean field approximation*, the many-body Schrödinger equation reduces to a set of single-particle equations [2]:

$$\left[-\frac{1}{2}\nabla^2 + V_{\text{eff}}(\mathbf{r})\right] \phi_i\left(\mathbf{r}\right) = \epsilon_i \phi_i\left(\mathbf{r}\right), \tag{2.7}$$

where $V_{\text{eff}}(\mathbf{r})$ is the effective potential experienced by an electron, including the external potential from the nuclei and the mean-field due to other electrons.

For a system of identical fermions the overall wavefunction must be antisymmetric under particle exchange [77]. Accordingly, the many-electron wavefunction is constructed as a *Slater determinant* of the single-particle spin-orbitals,

$$\psi(\mathbf{x}_1,\dots,\mathbf{x}_N)=\frac{1}{\sqrt{N!}}\begin{vmatrix}\phi_1(\mathbf{x}_1) & \phi_2(\mathbf{x}_1) & \cdots & \phi_N(\mathbf{x}_1)\\ \phi_1(\mathbf{x}_2) & \phi_2(\mathbf{x}_2) & \cdots & \phi_N(\mathbf{x}_2)\\ \vdots & \vdots & \ddots & \vdots\\ \phi_1(\mathbf{x}_N) & \phi_2(\mathbf{x}_N) & \cdots & \phi_N(\mathbf{x}_N)\end{vmatrix}, \tag{2.8}$$

where $\mathbf{x}_i=(\mathbf{r}_i,s_i)$ combines spatial and spin coordinates.

Each solution $\phi_i(\mathbf{r})$ in Eq. (2.7) is in fact a *spin-orbital* $\phi_i(\mathbf{r},s)\equiv\phi_i(\mathbf{x})$ that depends on both spatial coordinate $\mathbf{r}$ and spin variable s. For compactness we suppress the explicit spin label in the derivation of equations, but it is fully retained when we assemble the many-electron state to satisfy the required antisymmetry under the exchange of the coordinates and the Pauli exclusion principle [2].

While the mean-field approximation simplifies the many-body Schrödinger equation with 3N dimensions into a set of 3-dimensional single-particle equations, it relies on explicit assumptions about the form of the effective potential $V_{\text{eff}}(\mathbf{r})$. In practice, the Hartree potential $V_{\text{H}}(\mathbf{r})$ accounts for classical Coulomb interactions [78], but capturing the quantum mechanical exchange and correlation effects within $V_{\text{xc}}(\mathbf{r})$ requires further refinement. This is where DFT provides a robust framework.

The core concept of DFT is based on the Hohenberg-Kohn theorem [79], which states the total energy of many electrons in their ground state is a functional of the electron density. The electronic charge density is a function of a single position variable $\mathbf{r}$, defined as [2]:

$$n(\mathbf{r})=N\int \mathrm{d}\mathbf{r}_2\dots\,\mathrm{d}\mathbf{r}_N\psi^*\left(\mathbf{r},\mathbf{r}_2,\dots,\mathbf{r}_N\right)\psi\left(\mathbf{r},\mathbf{r}_2,\dots,\mathbf{r}_N\right). \tag{2.9}$$

Under the *independent electrons approximation*, the electron charge density can be obtained by adding up the probabilities of finding electrons in each occupied state i [2],

$$n(\mathbf{r}) = \sum_i |\phi_i(\mathbf{r})|^2 . \tag{2.10}$$

Furthermore, the Hohenberg-Kohn theorem implies that the exact ground-state density and energy can in principle be obtained by minimising the total-energy functional $E[n]$ with respect to the electron density [2],

$$\frac{\delta E[n]}{\delta n} = 0. \tag{2.11}$$

This is subject to the constraint that the single particle wavefunctions satisfy the orthonormality [2]:

$$\left\langle \phi_i \mid \phi_j \right\rangle = \delta_{ij}, \tag{2.12}$$

which guarantees that the density in Eq. 2.10 is correctly normalised to N electrons.

However, this theorem does not say anything about how to construct such a functional. To construct this functional, we can first combine Eqs. 2.3 and 2.5, and write the total energy as follows,

$$E = \langle\Psi| \sum_i V_n(\mathbf{r}_i) |\Psi\rangle + \langle\Psi| -\sum_i \frac{1}{2}\nabla_i^2 + \frac{1}{2}\sum_{i\neq j} \frac{1}{|\mathbf{r}_i - \mathbf{r}_j|} |\Psi\rangle. \tag{2.13}$$

The first term in the above can be written explicitly to be dependent on the charge density n as, $\langle\Psi| \sum_i V_n(\mathbf{r}_i) |\Psi\rangle = \int d\mathbf{r}\, n(\mathbf{r}) V_n(\mathbf{r})$, using the relation between the electron density and the wavefunction. However, the dependence on the charge density is implicit for the kinetic energy and electron-electron Coulomb energy terms. Kohn and Sham [80] introduced a set of non-interacting single-particle equations as in the *independent electron approximation* to reproduce the exact many-body Schrödinger equation while still accounting for the electron-electron interaction term. The electron-electron Coulomb interaction is split into two potentials: the Hartree term and the exchange-correlation term, both of which are functionals of the electron density, $n(\mathbf{r})$ [80]:

$$E[n] = \int d\mathbf{r}\, n(\mathbf{r}) V_n(\mathbf{r}) - \sum_i \int d\mathbf{r}\, \phi_i^*(\mathbf{r}) \frac{\nabla^2}{2} \phi_i(\mathbf{r}) + \frac{1}{2} \int d\mathbf{r}\, d\mathbf{r}' \frac{n(\mathbf{r}) n(\mathbf{r}')}{|\mathbf{r}-\mathbf{r}'|} + E_{xc}[n]. \tag{2.14}$$

Here, the first term represents the external potential energy, which describes the interaction between the electron density and the external potential $V_n(\mathbf{r})$. The second term corresponds to the kinetic energy of the electrons, calculated from the single-particle wavefunctions $\phi_i(\mathbf{r})$. The third term is the Hartree energy, which describes the classical electrostatic repulsion between a single electron and the charge density of all electrons [78, 80]. Finally, the term $E_{xc}[n]$ represents the exchange-correlation energy, accounting for all many-body effects beyond the Hartree term, $i.e.$, exchange and correlation.

Now that we have the functional E, to solve the constrained optimisation problem defined in Eqs. 2.11 and 2.12, we introduce the Lagrange functional [2]:

$$L = E - \sum_{ij} \lambda_{ij} \left[\langle \phi_i \mid \phi_j \rangle - \delta_{ij} \right], \tag{2.15}$$

where λ_{ij} are the Lagrange multipliers, and to search for the extrema of L,

$$\frac{\delta L}{\delta \phi_i^*} = 0 \longrightarrow \frac{\delta E}{\delta \phi_i^*} = \sum_j \lambda_{ij} \phi_j. \tag{2.16}$$

We obtain the following equation by using the chain rule of functional derivation and inserting Eq. 2.14,

$$\left[-\frac{\nabla^2}{2} + V_{\mathrm{n}}(\mathbf{r}) + \int d\mathbf{r}' \frac{n(\mathbf{r}')}{|\mathbf{r}-\mathbf{r}'|} + \frac{\delta E_{xc}}{\delta n} \right] \phi_i(\mathbf{r}) = \sum_j \lambda_{ij} \phi_j(\mathbf{r}). \tag{2.17}$$

Here the Hartree potential, $V_H(\mathbf{r})$, which satisfies Poisson's equation from classical electrostatics: $\nabla^2 V_H(\mathbf{r}) = -4\pi n(\mathbf{r})$ and the exchange and correlation potential, $V_{xc}(\mathbf{r})$, are introduced in the third and fourth terms in the brackets, respectively.

Since the Hamiltonian and the Lagrange multipliers are all Hermitian, $i.e.$ $\lambda^*_{ij} = \lambda_{ji}$ [2], then we can diagonalise the Lagrange multipliers martrix λ_{ij} to obtain the 'rotated' wavefunctions ϕ_i and corresponding eigenvalues ϵ_i. The Kohn–Sham equations are thus given by [80]:

$$\begin{aligned} \left[-\frac{1}{2}\nabla^2 + V_n(\mathbf{r}) + V_H(\mathbf{r}) + V_{xc}(\mathbf{r})\right]\phi_i(\mathbf{r}) &= \epsilon_i\phi_i(\mathbf{r}), \\ V_n(\mathbf{r}) &= -\sum_I \frac{Z_I}{|\mathbf{r}-\mathbf{R}_I|}, \\ \nabla^2 V_H(\mathbf{r}) &= -4\pi n(\mathbf{r}), \qquad (2.18) \\ V_{xc}(\mathbf{r}) &= \frac{\delta E_{xc}[n]}{\delta n}(\mathbf{r}), \\ n(\mathbf{r}) &= \sum_i |\phi_i(\mathbf{r})|^2, \end{aligned}$$

where $\phi_i(\mathbf{r})$ are the single particle eigenfunctions (also known as Kohn-Sham orbitals), ε_i are the corresponding single-particle eigenvalues (also known as Kohn-Sham eigenvalues). In practice, the exchange interaction is calculated within local or semi-local approximations to the non-local Fock exchange potential in Hartree-Fock theory, which arises due to the Pauli exclusion principle [2]. The sequence of equations is solved iteratively until the change in the total energy calculated at two consecutive steps is converged to a chosen threshold, as shown in Fig. 2.1.

2.1.3 Exchange-correlation functionals

The exact analytical form of $V_{\mathrm{xc}}[n(\mathbf{r})]$ is unknown, and numerical approximations are necessary in practical applications. The simplest method to obtain the exchange-correlation functional uses the so-called local density approximation (LDA) [81–83].

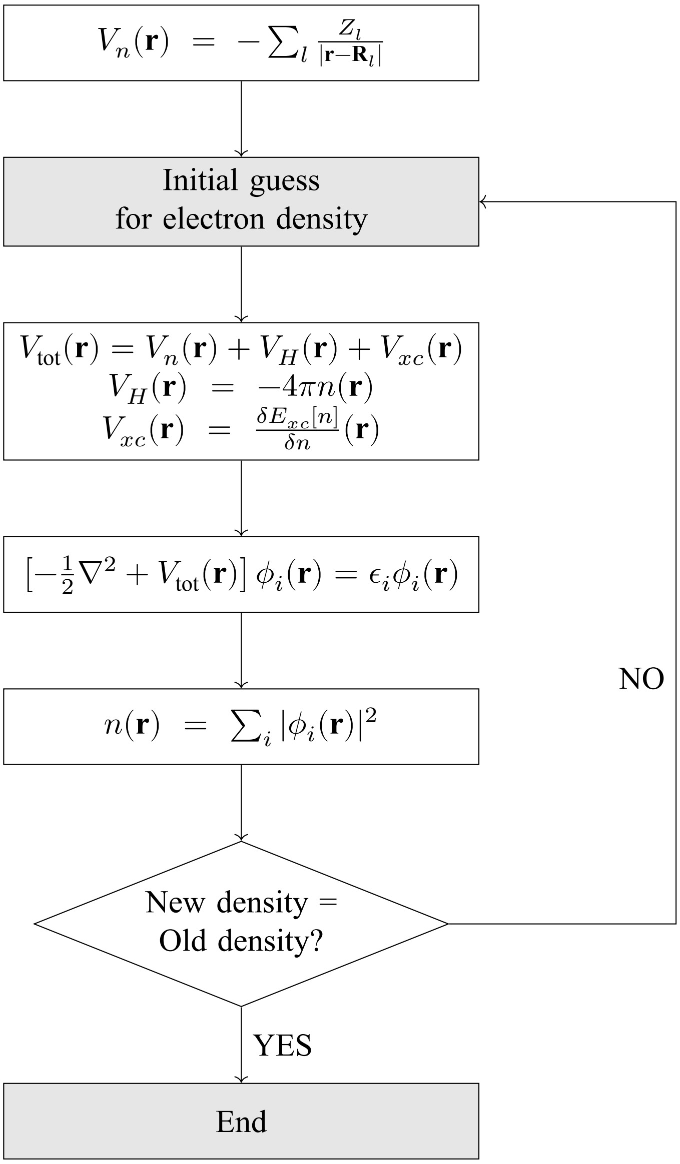

Figure 2.1: Schematic flowchart showing the procedure for finding self-consistent solutions to the Kohn-Sham equations. The equality in the decision box indicates that the difference between the current and previous electron densities is within a specified threshold. In practice, the total energies are often evaluated from charge density and converged within a threshold between two successive iterations. The flowchart is reproduced from Ref. [2].

The LDA assumes that the exchange and correlation energies depend only on the local electron density $n(\mathbf{r})$ [84]. This simple approximation has been successfully applied and provided comparable results with experimental measurements for systems with slowly varying densities. However, the LDA tends to overbind atoms, causing underestimation of the bond lengths and the cell volume and overestimation of the bulk modulus [85].

The generalised gradient approximation (GGA) improves the LDA approximation of the exchange correlation energy by incorporating the gradient of the electron density $\nabla n(\mathbf{r})$ into the exchange-correlation functional [86], in order to account for the non-homogeneity of the electron density distribution in a real system.

The Perdew-Burke-Ernzerhof (PBE) functional [86] is one of the most widely used GGA functionals, due to its balance between accuracy and computational efficiency. The PBE functional has been shown to provide improved accuracy over LDA for various properties, including ground state energies, equilibrium geometries, and the binding energies [86] of molecules and solids [85]; this is especially true for covalent bonds and weakly bonded system [87].

Due to these advantages, the PBE functional is widely applied in electronic structure calculations for solids, molecules, and surfaces. In addition to LDA and GGA, more advanced exchange-correlation functionals called *hybrid functionals* have been developed to further improve the accuracy of DFT. Hybrid functionals incorporate a portion of the non-local Fock exchange (exact exchange) from Hartree-Fock theory into the semi-local exchange-correlation functional. This partial inclusion of exact exchange typically corrects some of the self-interaction errors inherent in LDA/GGA and leads to better predictions of electronic and structural properties for a wide range of systems.

A prominent example is the PBE0 hybrid functional [88, 89], which is constructed by mixing a fixed fraction (typically 25%) of the Fock exchange with the PBE. The exchange-correlation energy in PBE0 can be written schematically as [88]:

$$E_{\text{xc}}^{\text{PBE0}} = \alpha E_x^{\text{HF}} + (1-\alpha)E_x^{\text{PBE}} + E_c^{\text{PBE}}, \tag{2.19}$$

where E_x^{HF} is the Hartree-Fock exchange energy, E_x^{PBE} and E_c^{PBE} are the PBE exchange and correlation energies, respectively, and α is a mixing parameter (0.25 in the original PBE0 formulation). By including exact exchange, PBE0 often provides more accurate band gaps, total energies, and defect formation energies than standard GGA functionals, albeit at a substantially higher computational cost [90]. Due to the high computational cost, we will primarily use PBE for structural relaxations and as a starting point for more accurate many-body calculations throughout this thesis, while employing PBE0 hybrid functionals for specific cases where higher accuracy is required for electronic properties.

2.1.4 Practical DFT calculations and convergence parameters

In this section we will try to bridge the theoretical details described so far and the practical calculations within DFT for crystalline solids in a plane-wave representation. The goal is to highlight the principal convergence parameters involved in practical calculations. All DFT calculations discussed throughout this thesis are performed using the Quantum Espresso code [91,92].

In plane-wave DFT implementations, the electronic wavefunctions are expressed as a linear combination of plane waves. The expansion of the wavefunction takes the form:

$$\phi_i(\mathbf{r}) = \sum_{\mathbf{G}} c_{i,\mathbf{G}} e^{i\mathbf{G}\cdot\mathbf{r}},$$

where $\mathbf{G}$ represents reciprocal lattice vectors, and $c_{i,\mathbf{G}}$ are the expansion coefficients. The maximum kinetic energy of the plane waves included in the basis is controlled by the *energy cutoff* parameter E_{cut} :

$$\frac{\hbar^2|\mathbf{G}|^2}{2m} \leq E_{\text{cut}}.$$

Only plane waves with kinetic energy less than E_{cut} are included in the calculation.

The choice of E_{cut} affects the accuracy of the computed properties. A higher energy cutoff includes more plane waves, resulting in a more accurate representation of the wavefunctions and charge density. However, this also increases computational cost. To ensure convergence, E_{cut} must be tested systematically. Convergence is achieved when increasing E_{cut} further does not significantly change the calculated total energy or other properties, such as forces or stress tensors.

The electronic structure of crystalline solids is periodic, allowing the wavefunctions to be represented in terms of Bloch states:

$$\psi_{n\mathbf{k}}(\mathbf{r}) = e^{i\mathbf{k}\cdot\mathbf{r}} u_{n\mathbf{k}}(\mathbf{r}),$$

where **k** is a wavevector in the first Brillouin zone, and $u_{n\mathbf{k}}(\mathbf{r})$ is a periodic function with the same periodicity as the lattice.

Since the the wavevector **k** in Brillouin zone is a continuous quantity, it must be sampled using a discrete grid in numerical calculations. The choice of **k**-point sampling is critical for ensuring accuracy in quantities such as total energy, forces, and electronic density of states. Typically, the Brillouin zone is sampled using a Monkhorst-Pack grid [93]:

$$\mathbf{k} = \frac{n_1}{N_1}\mathbf{b}_1 + \frac{n_2}{N_2}\mathbf{b}_2 + \frac{n_3}{N_3}\mathbf{b}_3,$$

where n_1, n_2, n_3 are integers, N_1, N_2, N_3 define the density of the grid, and $\mathbf{b}_1, \mathbf{b}_2, \mathbf{b}_3$ are the reciprocal lattice basis vectors.

A denser **k**-point grid improves the accuracy of the integration over the Brillouin zone but increases computational cost.

In practice, convergence testing involves performing calculations for a series of E_{cut} and **k**-point grids and monitoring the changes in total energy or other relevant quantities. For example, the total energy is considered converged if its change between two successive E_{cut} or **k**-point values is less than a predefined threshold (e.g., 1 meV/atom).

2.2 Virtual crystal approximation

The VCA [68] is an effective method used to model disordered or alloyed crystalline materials within the framework of periodic boundary conditions [94]. In VCA, the disordered system is approximated by a hypothetical “virtual” crystal in which the atoms at specific lattice sites are replaced by averaged pseudopotentials or atomic potentials that interpolate between those of the constituent elements. This approach allows us to simulate systems with fractional site occupancies without the need for large supercells, significantly reducing computational costs.

In this thesis, we will use the VCA in the context of mixed halide perovskites, such as $\text{CsPb}(\text{I}_{1-x}\text{Br}_x)_3$, VCA allows for modelling the continuous variation of properties with the halide mixing ratio x. The virtual halogen atom at the X-site is constructed by averaging the properties of iodine and bromine atoms according to their concentration. The VCA pseudopotential can be expressed as a sum of local V_{loc} and non local part V_{nl}, $V^{(vca)} = V_{loc}^{(vca)} + V_{nl}^{(vca)}$. The local part is constructed by compositionally averaging the potentials of the parent compounds,

$$V_{loc}^{(vca)} = xV_{loc}^{(1)} + (1-x)V_{loc}^{(2)}. \tag{2.20}$$

The non local part is given by

$$V_{nl}^{(vca)} = \sum_{ij} |\beta_i^{(1)}\rangle x D_{ij}^{(1)} \langle\beta_j^{(1)}| + \sum_{ij} |\beta_i^{(2)}\rangle (1-x) D_{ij}^{(2)} \langle\beta_j^{(2)}|, \tag{2.21}$$

where $\beta_i^{(n)}(r)$ are the projectors for state i of atom n, with corresponding coefficients $D_{ij}^{(n)}$ [68, 91]. VCA is employed by generating pseudopotentials for the virtual atom using the virtual_v2.x utility as implemented in Quantum Espresso.

2.3 Many-body perturbation theory

While DFT has been successful in understanding the ground-state properties of many-electron systems such as structural properties, it has well-known limitations in accurately predicting fundamental band gaps [83,95]. DFT calculations using local or semi-local exchange-correlation functionals such as LDA and GGA tend to significantly underestimate experimental band gaps. This is usually referred to as the “band gap problem” [83, 95].

This underestimation arises from fundamental issues in approximate functionals, particularly the self-interaction error and the lack of derivative discontinuity in the exchange-correlation potential [83, 95].

The fundamental gap, often measured in experiments, is the difference between the electron affinity and the ionisation energy [95, 96]:

$$E_{\text{gap}}^{qs} = (E_{N+1} - E_N) - (E_N - E_{N-1}), \tag{2.22}$$

where E_N is the total energy of the system in its ground state, E_{N+1} and E_{N-1} is the total energy of the system with one extra/missing electron.

While standard DFT could in principle calculate these total energies in the ground state, it fails to capture the correct physics of the electron addition/removal process, particularly the many-body screening effects that occur when a charge is added to or removed from the system [96].

Many-body perturbation theory (MBPT) provides a framework for treating these electron-electron interactions more accurately. Within this framework, the GW approximation has emerged as a powerful and widely used method for calculating quasiparticle energies [73, 75, 97]. In the GW approximation, electron addition and removal processes are described by so-called 'quasiparticles' [98]. Intuitively, a quasiparticle is pictured as an electron (or hole) surrounded by a 'cloud' of opposite charges corresponding to the response of the polarisable charge density to the addition or removal of an electron [98].

2.3.1 Quasiparticles and the GW approximation

We first consider the excitation of a single quasiparticle added to the many-body ground state described using the Green's function formalism. The probability of finding a particle at a position **r** at time t, after adding a particle at position **r**′ at time t', is described by the single-particle Green's function at zero temperature,

$$G(\mathbf{r},t;\mathbf{r}',t') = -i\langle\Psi_0^N|T[\psi(\mathbf{r},t),\psi^{\dagger}(\mathbf{r}',t')]|\Psi_0^N\rangle, \tag{2.23}$$

where $\psi(\mathbf{r},t)$ and $\psi^{\dagger}(\mathbf{r}',t')$ are the second-quantised operators for annihilating or creating a particle at time t and t', position **r** and **r**′, respectively; $|\Psi_0^N\rangle$ is the many-body ground state for N particles, and T indicates that the operators are time-ordered so that the earlier time is on the right.

If we assume time-translational invariance, the Green's function can be expressed in the

Lehman (or spectral) representation after a Fourier transform with respect to $t - t'$:

$$\begin{aligned} G(\mathbf{r},\mathbf{r}',\omega) = \sum_s & \frac{\langle \Psi_0^N | \psi(\mathbf{r}) | \Psi_s^{N+1} \rangle \langle \Psi_s^{N+1} | \psi^\dagger(\mathbf{r}') | \Psi_0^N \rangle}{\omega - (E_s^{N+1} - E_0^N) + i\eta} \\ & + \frac{\langle \Psi_0^N | \psi^\dagger(\mathbf{r}) | \Psi_s^{N-1} \rangle \langle \Psi_s^{N-1} | \psi(\mathbf{r}') | \Psi_0^N \rangle}{\omega + (E_s^{N-1} - E_0^N) - i\eta}, \end{aligned} \tag{2.24}$$

where $\eta = 0^+$, $|\Psi_s^{N\pm 1}\rangle$ represents the eigenstates of the many-body Hamiltonian with $N \pm 1$ electrons, and $E_s^{N\pm 1}$ is the total energy of the $(N \pm 1)$-body system in the s^{th} excited state.

Since the exact eigenstates of the interacting many-body Hamiltonian are unknown, we begin by considering the Green's function written in terms of Kohn-Sham states:

$$G_0(\mathbf{r},\mathbf{r}',\omega) = \sum_s \frac{\phi_s^{\text{KS}}(\mathbf{r}) \phi_s^{\text{KS}*}(\mathbf{r}')}{\omega - \varepsilon_s^{\text{KS}} \pm i\eta}, \tag{2.25}$$

where $\phi_s^{\text{KS}}(\mathbf{r})$ and $\varepsilon_s^{\text{KS}}$ are the Kohn-Sham orbitals and eigenvalues obtained from a DFT calculation, respectively. The sign of η depends on whether the state is above or below the Fermi energy.

The electron-electron interactions can be included as a perturbation on the Kohn-Sham Hamiltonian, leading to the Dyson equation for the interacting single-particle Green's function [75]:

$$G(\mathbf{r},\mathbf{r}',\omega) = G_0(\mathbf{r},\mathbf{r}',\omega) + \int G_0(\mathbf{r},\mathbf{r}_1,\omega)[\Sigma(\mathbf{r}_1,\mathbf{r}_2,\omega) - V_{xc}(\mathbf{r}_1)\delta(\mathbf{r}_1 - \mathbf{r}_2)] G(\mathbf{r}_2,\mathbf{r}',\omega) d\mathbf{r}_1 d\mathbf{r}_2. \tag{2.26}$$

Here, Σ is a non-local and energy-dependent operator known as the self-energy operator, which describes the many-body interactions beyond the mean-field level. The self-energy represents the difference between the energy of the quasiparticle and the energy of the Kohn-Sham particle [70, 75].

A practical approach to perform the perturbative expansion of Σ is to expand in terms of the screened Coulomb interaction W rather than the bare Coulomb interaction [73]. Since the screened Coulomb interaction is significantly weaker than the bare interaction, truncating at the first term in this expansion provides a good approximation for the electron self-energy in most systems. This approach is known as the GW approximation, first systematically developed by Hedin [73].

The GW approximation derives its name from expressing the self-energy Σ as a convolution of the Green's function G and the screened Coulomb interaction W [73],

$$\Sigma(\mathbf{r},\mathbf{r}',\omega) = \frac{i}{2\pi}\int G(\mathbf{r},\mathbf{r}',\omega-\omega')W(\mathbf{r},\mathbf{r}',\omega')e^{i\omega'\eta}d\omega', \tag{2.27}$$

where W is related to the bare Coulomb interaction v through the dielectric function ϵ:

$$W(\mathbf{r},\mathbf{r}',\omega) = \int \epsilon^{-1}(\mathbf{r},\mathbf{r}'',\omega)v(\mathbf{r}'',\mathbf{r}')d\mathbf{r}''. \tag{2.28}$$

The dielectric function and polarisability are related through the following definition:

$$\epsilon(\mathbf{r},\mathbf{r}',\omega) = \delta(\mathbf{r},\mathbf{r}') - \int v(\mathbf{r},\mathbf{r}'')\chi(\mathbf{r}'',\mathbf{r}',\omega)d\mathbf{r}'', \tag{2.29}$$

where the polarisability χ expressed as the convolution of two Green's functions [73],

$$\chi(\mathbf{r},\mathbf{r}',\omega) = -\frac{i}{2\pi}\int G(\mathbf{r},\mathbf{r}',\omega')G(\mathbf{r}',\mathbf{r},\omega'-\omega)d\omega'. \tag{2.30}$$

In principle, Hedin's equation [73] should be solved self consistently: In order to obtain Σ, we must know G, which in turn relies on knowing the self energy Σ.

Solving the above equations self-consistently within the GW approximation is computationally intensive. A practical implementation of the GW method was developed by

Hybertsen and Louie [70] which uses the Kohn-Sham orbitals to construct both the polarisability and the Green's function for performing GW calculations from *ab initio*. Within the random phase approximation (RPA) [99], the irreducible polarisability is a convolution of two mean-field Green's functions G_0 [70],

$$\chi^0(\mathbf{r},\mathbf{r}',\omega) = -\frac{i}{2\pi}\int G_0(\mathbf{r},\mathbf{r}',\omega')G_0(\mathbf{r}',\mathbf{r},\omega'-\omega)d\omega'. \tag{2.31}$$

Here, G_0 can be written in terms of the mean-field eigenstates as in Eq. 2.25. In the basis of Kohn-Sham orbitals, the irreducible polarisability function can be written as [100–102]:

$$\begin{aligned}\chi^0(\mathbf{r},\mathbf{r}',\omega) = 2\sum_v^{occ}\sum_c^{unocc} \phi_v^{\mathrm{KS}}(\mathbf{r})\phi_c^{\mathrm{KS}}(\mathbf{r})\phi_v^{\mathrm{KS}}(\mathbf{r}')\phi_c^{\mathrm{KS}}(\mathbf{r}')\\ \times\left(\frac{1}{\omega-(\varepsilon_c^{\mathrm{KS}}-\varepsilon_v^{\mathrm{KS}})+i\eta}-\frac{1}{\omega+(\varepsilon_c^{\mathrm{KS}}-\varepsilon_v^{\mathrm{KS}})-i\eta}\right),\end{aligned} \tag{2.32}$$

where v and c denote occupied valence and unoccupied conduction states, respectively.

In G_0W_0 approximation [70], the self energy operator $\Sigma(\mathbf{r},\mathbf{r}';\omega)$ is expressed as the convolution of a mean-field Green's function G_0 and the screened Coulomb interaction W_0,

$$\Sigma(\mathbf{r},\mathbf{r}',\omega) = \frac{i}{2\pi}\int G_0(\mathbf{r},\mathbf{r}',\omega-\omega')W_0(\mathbf{r},\mathbf{r}',\omega')e^{i\omega'\eta}d\omega'. \tag{2.33}$$

G_0 is written as in Eq.2.25 and $W_0(\mathbf{r},\mathbf{r}',\omega) = \int d\mathbf{r}''\epsilon^{-1}(\mathbf{r},\mathbf{r}'',\omega)v(\mathbf{r}'',\mathbf{r}')$ when the dielectric function is calculated using the irreducible polarisability χ_0 as $\epsilon(\mathbf{r},\mathbf{r}',\omega) = \delta(\mathbf{r},\mathbf{r}') - \int d\mathbf{r}''v(\mathbf{r},\mathbf{r}'')\chi_0(\mathbf{r}'',\mathbf{r}',\omega)$ under the RPA.

Within the ab initio GW approach, assuming the Kohn-Sham orbitals approximate the quasiparticle wavefunctions, the quasiparticle energy can be calculated in lowest order eigenvalue perturbation theory with equations [76]:

$$\varepsilon_{n\mathbf{k}}^{\mathrm{QP}} = \varepsilon_{n\mathbf{k}}^{\mathrm{KS}} + \langle n\mathbf{k}|\Sigma^{GW}(\varepsilon_{n\mathbf{k}}^{\mathrm{QP}}) - V_{xc}|n\mathbf{k}\rangle. \tag{2.34}$$

This approximation works well when the DFT eigenvectors are similar to the GW eigenvectors, which is often the case for moderately correlated systems. It is also possible to evaluate the GW quasiparticle energies by diagonalising $\langle n\mathbf{k}|\Sigma^{GW}|n'\mathbf{k}\rangle$ and repeating the calculation using the GW eigenvalues and eigenvectors.

Several approaches have been proposed so far for performing G_0W_0 calculations, primarily distinguished by how the frequency-dependent dielectric function is calculated or approximated ($i.e.$ using plasmon-pole models [70,103]), or in some approaches [70], neglected. While full-frequency calculations are computationally demanding, they provide accurate descriptions of spectral features including quasiparticle lifetimes and satellites [104, 105]. A more efficient alternative is to use plasmon-pole model approximations for the dielectric function, which are particularly popular for calculating quasiparticle band gaps and band structures. However, the choice of plasmon-pole model can significantly impact the results, with differences in computed band gaps of up to 1 eV depending on the system. In this thesis, we employ the Godby-Needs plasmon-pole model [103], which has been shown to yield good agreement with full-frequency calculations for a wide range of semiconductors and insulators [106].

2.3.2 Wannier interpolation of quasiparticle band structures

A practical challenge in *ab initio* GW calculations is that the quasiparticle energies $\varepsilon_{\mathbf{k}}^{\mathrm{QP}}$ are typically evaluated on a relatively coarse **k**-point mesh due to computational limit [107]. To achieve a more refined sampling of the band structure and accurate determination of band extrema, we employ Wannier interpolation based on maximally localised Wannier functions (MLWFs) [108, 109].

The procedure consists of two main steps. First, we construct MLWFs from the Kohn-

Sham wavefunctions obtained from DFT calculations. A set of N generalised Wannier functions $|w_n(\mathbf{R})\rangle$ labelled by index n and lattice vector **R** is obtained through the unitary transformation [110]:

$$|w_n(\mathbf{R})\rangle = \frac{V}{(2\pi)^3} \int_{\text{BZ}} d\mathbf{k} \sum_m U^{(\mathbf{k})}_{mn} e^{-i\mathbf{k}\cdot\mathbf{R}} |\psi^{\text{KS}}_{m\mathbf{k}}\rangle, \tag{2.35}$$

where $U^{(\mathbf{k})}_{mn}$ is optimised to minimise the real-space spread of the Wannier functions.

Second, we use these MLWFs as a basis to interpolate the quasiparticle energies. The GW calculations are performed on a coarse **k**-point grid, and the quasiparticle corrections to the Kohn-Sham eigenvalues are obtained. The short-range nature of the Wannier basis allows for efficient interpolation of these corrections to arbitrary **k**-points without requiring additional GW calculations. The interpolated Hamiltonian at any **k**-point can be constructed as:

$$H_{mn}(\mathbf{k}) = \sum_{\mathbf{R}} e^{i\mathbf{k}\cdot\mathbf{R}} H_{mn}(\mathbf{R}), \tag{2.36}$$

where $H_{mn}(\mathbf{R})$ are the real-space Hamiltonian matrix elements that include the GW corrections.

In this thesis, we employ the Wannier90 code [111, 112] to construct MLWFs and perform band structure interpolation. The specific computational details, including the choice of initial projections, energy windows for the Wannierisation procedure, and convergence criteria, are provided in Appendix A.1.2.

2.3.3 Bethe-Salpeter equation

After obtaining accurate quasiparticle energies from GW calculations, one might expect to accurately predict optical properties through simple inter-band transitions. However, this approach fails to capture important features in experimental optical spectra, as optical absorption fundamentally involves the interaction between correlated electrons and holes upon photo-excitation.

While the GW approximation successfully describes single-particle excitations, optical absorption inherently involves the interaction between excited electrons and holes, requiring a more sophisticated treatment. The BSE emerges naturally from many-body perturbation theory as the framework for describing two-particle excitations. A general discussion and derivation of this theoretical framework can be found in the literature [71, 72]. In the Tamm-Dancoff approximation, the BSE takes the form of an effective two-particle Hamiltonian eigenvalue problem [72]:

$$\left(\varepsilon^{\mathrm{QP}}_{c\mathbf{k}_e} - \varepsilon^{\mathrm{QP}}_{v\mathbf{k}_\mathrm{h}}\right) A^S_{c\mathbf{k}_\mathrm{e}v\mathbf{k}_\mathrm{h}} + \sum_{c'\mathbf{k'}_\mathrm{e}\nu'\mathbf{k'}_\mathrm{h}} \langle c\mathbf{k}_\mathrm{e}v\mathbf{k}_\mathrm{h}|\, K^{\mathrm{eh}}\, |c'\mathbf{k'}_\mathrm{e}v'\mathbf{k'}_\mathrm{h}\rangle\, A^S_{c'\mathbf{k'}_\mathrm{e}v'\mathbf{k'}_\mathrm{h}} = \Omega^S\left(\mathbf{k}_\mathrm{e} - \mathbf{k}_\mathrm{h}\right) A^S_{c\mathbf{k}_\mathrm{e}\nu\mathbf{k}_\mathrm{h}}, \tag{2.37}$$

where $\varepsilon^{e(h)}_{c(v)\mathbf{k}}$ are the quasiparticle energies of occupied (v) and unoccupied (c) single-particle states, $|c\mathbf{k}^e v\mathbf{k}^h\rangle$ is the direct product of occupied and unoccupied single-particle states, $A^S_{c\mathbf{k}^e v\mathbf{k}^h}$ are the coefficients of the exciton wavefunction in the single-particle basis corresponding to the state S with energy Ω^S and K_{eh} is the electron-hole kernel. We highlight here that in the expressions above we have assumed that excitons carry a finite momentum equal to $\mathbf{Q} = \mathbf{k}^e - \mathbf{k}^h$, for the sake of completeness. In most practical calculations of linear optical absorption spectra or exciton binding energies, it is sufficient to compute zero-momentum excitons [113], therefore in this thesis, we only solve BSE with $\mathbf{k}^e = \mathbf{k}^h$. It is however important to note that finite momentum excitons play a key role in the physics of exciton-phonon interactions which underpins important phenomena such as exciton dynamics, exciton diffusion and radiative recombination [114–117].

The electron-hole kernel K^{eh} comprises two distinct contributions: A repulsive, energy-independent exchange term arising from bare Coulomb interaction, and an attractive, energy-dependent direct term derived from the screened Coulomb interaction [72]. The former determines the singlet-triplet splitting in systems with weak spin-orbit coupling while the latter incorporates the dielectric screening effects [72, 113, 114].

In standard implementations, the frequency dependence of the direct term is typically neglected, which is justified when the exciton binding energy is much smaller than the plasma frequency [72]. However, this approximation breaks down for systems with very large binding energies (like carbon nanotubes [118]) or when polar ionic vibrations significantly contribute to the dielectric function [6, 119, 120].

The solution of Eq. 2.37 are the eigenvalues Ω^S (excited state energies) and $A^S_{cv\mathbf{k}}$ (exciton coefficients), the exciton wavefunction can be written in the basis of the free electron/hole wavefunction as

$$\Psi^S(\mathbf{r}_e, \mathbf{r}_h) = \sum_{cv\mathbf{k}} A^S_{cv\mathbf{k}} \phi^*_{v\mathbf{k}}(\mathbf{r}_h) \phi_{c\mathbf{k}}(\mathbf{r}_e), \tag{2.38}$$

and the exciton binding energy is the difference between the quasiparticle band gap and excited state energies, $E^S_B = E^{QP}_{gap} - \Omega^S$.

From these solutions, the optical absorption spectrum can be computed through the imaginary part of the dielectric function, which is computed as [72, 76]

$$\epsilon_2(\omega) = \frac{16\pi}{\omega^2} \sum_S |\mathbf{e} \cdot \langle 0|\mathbf{v}|S\rangle|^2 \delta(\omega - \Omega^S), \tag{2.39}$$

where $|0\rangle$ and $|S\rangle$ correspond to the ground and excited state S, respectively, **e** is the light polarisation vector and **v** is the velocity operator, approximated as the momentum operator $\mathbf{v} = i$□, as implemented in BerkeleyGW package [76].

The absorption coefficient $\alpha(\omega)$ is calculated as

$$\alpha(\omega) = \frac{2\omega}{c} \sqrt{\frac{1}{2} \left(-\varepsilon_1(\omega) + \sqrt{\varepsilon_1^2(\omega) + \varepsilon_2^2(\omega)} \right)}. \tag{2.40}$$

This formalism has been applied successfully in describing optical properties across a wide range of materials, from bulk semiconductors to low-dimensional systems, capturing essential features of experimental optical response. The MBPT calculations within the GW+BSE framework presented in this thesis were performed using the BerkeleyGW package [76].

2.4 Exciton correlation function

The exciton correlation function (ECF) is a tool used to analyse the spatial distribution and correlation of the electron and hole in an excitonic state. It provides insights into the extent of exciton delocalisation and helps distinguish between different types of excitons, such as Frenkel (localised) and Wannier-Mott (delocalised) excitons [121].

The ECF $\mathcal{F}(\mathbf{r})$ is defined as:

$$\mathcal{F}(\mathbf{r}) = \int |\Psi_s(\mathbf{r}_e = \mathbf{r}_h + \mathbf{r}, \mathbf{r}_h)|^2 d\mathbf{r}_h, \tag{2.41}$$

which represents the probability density of finding the electron at a displacement **r** from the hole.

By examining $\mathcal{F}(\mathbf{r})$, we can determine the average electron-hole separation as:

$$\langle r \rangle = \int |\mathbf{r}| \mathcal{F}(\mathbf{r}) d\mathbf{r}. \tag{2.42}$$

The spatial extent of the exciton can be inferred from the width of $\mathcal{F}(\mathbf{r})$.

Localised excitons (Frenkel) show a sharp peak in $\mathcal{F}(\mathbf{r})$ at small **r**, while delocalised excitons (Wannier-Mott) exhibit a broader $\mathcal{F}(\mathbf{r})$, indicating larger electron-hole separation. In layered perovskites, the ECF can reveal whether excitons are confined within a single layer (intralayer excitons) or delocalised across multiple layers (interlayer excitons). By analysing the distribution of $\mathcal{F}(\mathbf{r})$ along the directions parallel and perpendicular to the layers, we can quantify the degree of exciton localisation and understand the influence of structural parameters on excitonic properties.

As part of the study in this thesis, we have implemented a Python package that interfaces seamlessly with BerkeleyGW package to calculate and visualise the ECF. The implementation takes advantage of the plotxct utility in BerkeleyGW package, which generates exciton wavefunctions for specified hole positions from the BSE solutions. The code automates the generation of plotxct input files for a user-defined grid of hole positions, systematically sampling the spatial distribution of the hole. The density of this sampling grid is a key convergence parameter for the ECF, and a detailed convergence study of the hole grid density is presented in Appendix A.2.5.

The package then processes all the resulting single-hole exciton wavefunctions from the plotxct computation outputs (reformulating the wavefunctions with respect to the relative position between electrons and holes) to construct the converged ECF according to the formalism described above. The code outputs the 3D ECF in the a3Dr file (as used in PARATEC code) format for further visualisation and analysis. Additionally, we have implemented visualisation tools in the package for post-processing the a3Dr file, which generates 2D heat maps and 1D profiles of the ECF to assist the analysis of exciton spatial distribution. This automated workflow significantly streamlines the analysis of the excitonic correlations directly from BSE solution. This code has been successfully applied to calculate and visualise the ECF for various structures with different unit cells and symmetries as shown in Chapter 4,5 and 6.

2.5 Eigenvector analysis and decomposition

To analyse the nature of excitonic states, we perform an eigenvector decomposition, calculating the contributions from different bands and **k**-points.

The two-particle exciton state can be written as a superposition of electron states in the conduction band and hole states in the valence band in Dirac notation as:

$$|S\rangle = \sum_{\mathbf{k},c,v} A^S_{vc\mathbf{k}} \left|\psi_{\mathbf{k},c}\right\rangle \otimes \left|\tilde{\psi}_{\mathbf{k},v}\right\rangle , \tag{2.43}$$

where $A^S_{vc\mathbf{k}}$ is the expansion coefficients for the excitonic state S, $\left|\psi_{\mathbf{k},c}\right\rangle$ and $\left|\tilde{\psi}_{\mathbf{k},v}\right\rangle$ are the electron/hole state in the conduction/valence bands at momentum **k**.

The weight of a particular valence band v in exciton state S is:

$$W_S(v) = \sum_{c,\mathbf{k}} \left|A^S_{vc\mathbf{k}}\right|^2 . \tag{2.44}$$

Similarly, the weight for a conduction band c is:

$$W_S(c) = \sum_{v,\mathbf{k}} \left|A^S_{vc\mathbf{k}}\right|^2 . \tag{2.45}$$

For a given exciton state S and a given valence bands v_x, the contribution to the exciton states from transitions involving this valence band v_x at a particular **k**-point is given by the summation of the contributions from all conduction bands,

$$w_S(v_x, \mathbf{k}) = \sum_{c} \left|A^S_{(v_x)c\mathbf{k}}\right|^2 . \tag{2.46}$$

Similarly, the exciton weight for a specific conduction band c_x at **k** is:

$$w_S(c_x, \mathbf{k}) = \sum_{v} \left|A^S_{v(c_x)\mathbf{k}}\right|^2 . \tag{2.47}$$

To determine the atomic contribution for each exciton state, we combine these exciton weights with the projections of the electronic states onto atomic orbitals.

The Bloch states for electrons in band c, or holes in band v and wavevector **k** are expanded in terms of atomic orbital basis functions $|a, \nu\rangle$:

$$|\psi_{c\mathbf{k}}\rangle = \sum_{a,\nu} C_{a\nu}^{c\mathbf{k}} |a, \nu\rangle, \tag{2.48}$$

$$\left|\tilde{\psi_{v\mathbf{k}}}\right\rangle = \sum_{a',\nu'} C_{a'\nu'}^{v\mathbf{k}*} |a', \nu'\rangle, \tag{2.49}$$

where $C_{a\nu,n\mathbf{k}} = \langle a, \nu|\psi_{n\mathbf{k}}\rangle$ are the coefficients (n represents the band index, $n = v$ for holes and c for electrons). Here a labels the atom, and ν denotes the orbital character (e.g., s, p, d orbitals).

The percentage of a Bloch state $\psi_{n\mathbf{k}}$ from an atomic orbital $|a, \nu\rangle$ is given by the square modulus of the expansion coefficients

$$P_{n\mathbf{k}}(a, \nu) = |\langle a, \nu|\psi_{n\mathbf{k}}\rangle|^2 . \tag{2.50}$$

The pseudo-atomic orbital basis from the pseudopotentials form an almost orthonormal local basis. Overlaps between projectors on different sites are negligible: $\langle a, \nu|a', \nu'\rangle \simeq \delta_{a,a'}\delta_{\nu,\nu'}$, and for each band n and **k**-point, the projections satisfy: $\sum_{a,\nu} |C_{a\nu}^{n\mathbf{k}}|^2 \simeq 1$. In practice, the cross-site overlaps that break strict orthogonality are below a few percent; we therefore renormalise the weights throughout our calculation.

By combining the exciton weights with the above atomic orbital projections, we can compute the decomposition of the exciton wavefunction onto specific atomic orbitals. To do that, we compute the projection of the two-particle exciton state onto the basis $\langle a_e, \nu_e; a_h, \nu_h| = \langle a_e, \nu_e| \otimes \langle a_h, \nu_h|$, which corresponds to the projection of exciton state onto atomic orbitals basis for electron and holes, respectively.

First, we write the exciton state in terms of atomic orbital basis:

$$
\begin{aligned}
|S\rangle &= \sum_{\mathbf{k}} \sum_{v,c} A^S_{vc\mathbf{k}} \left(\sum_{a_e,\nu_e} C^{c\mathbf{k}}_{a_e\nu_e} |a_e, \nu_e\rangle \right) \otimes \left(\sum_{a_h,\nu_h} C^{v\mathbf{k}\,*}_{a_h\nu_h} |a_h, \nu_h\rangle \right) \\
&= \sum_{a_e,\nu_e} \sum_{a_h,\nu_h} \left(\sum_{\mathbf{k}} \sum_{v,c} A^S_{vc\mathbf{k}} C^{c\mathbf{k}}_{a_e\nu_e} C^{v\mathbf{k}\,*}_{a_h\nu_h} \right) |a_e, \nu_e\rangle \otimes |a_h, \nu_h\rangle \,.
\end{aligned}
$$

The projection onto atomic orbitals is as follows:

$$
\langle a_h, \nu_h; a_e, \nu_e \mid S\rangle = \left(\langle a_e, \nu_e| \otimes \langle a_h, \nu_h| \right) |S\rangle. \tag{2.51}
$$

Substitute the expanded form of $|S\rangle$ and with

$$
\begin{aligned}
&\langle a_h, \nu_h; a_e, \nu_e \mid S\rangle \\
&= \left(\langle a_e, \nu_e| \otimes \langle a_h, \nu_h| \right) \left(\sum_{a'_e,\nu'_e} \sum_{a'_h,\nu'_h} \left(\sum_{\mathbf{k},v,c} A^S_{vc\mathbf{k}} C^{c\mathbf{k}}_{a'_e\nu_e} C^{v\mathbf{k}\,*}_{a'_h\nu_h} \right) |a'_e, \nu'_e\rangle \otimes |a'_h, \nu'_h\rangle \right) \\
&= \sum_{a'_e,\nu'_e} \sum_{a'_h,\nu'_h} \left(\sum_{\mathbf{k},v,c} A^S_{vc\mathbf{k}} C^{c\mathbf{k}}_{a'_e\nu'_e} C^{v\mathbf{k}\,*}_{a'_h\nu'_h} \right) \left(\langle a_e, \nu_e \mid a'_e, \nu'_e\rangle \, \langle a_h, \nu_h \mid a'_h, \nu'_h\rangle \right).
\end{aligned}
$$

With the atomic orbital basis being orthonormal $\langle a, \nu | a', \nu'\rangle = \delta_{a,a'}\delta_{\nu,\nu'}$, the above can be further simplified:

$$
\begin{aligned}
\langle a_h, \nu_h; a_e, \nu_e \mid S\rangle &= \sum_{a'_e,\nu'_e} \sum_{a'_h,\nu'_h} \left(\sum_{\mathbf{k},v,c} A^S_{vc\mathbf{k}} C^{c\mathbf{k}}_{a'_e\nu'_e} C^{v\mathbf{k}\,*}_{a'_h\nu'_h} \right) \delta_{a_e,a_e'}\delta_{\nu_e,\nu_e'}\delta_{a_h,a'_h}\delta_{\nu_h,\nu_h'} \\
&= \sum_{\mathbf{k},v,c} A^S_{vc\mathbf{k}} C^{c\mathbf{k}}_{a_e\nu_e} C^{v\mathbf{k}\,*}_{a_h\nu_h}.
\end{aligned}
$$

We define the electron decomposition of the exciton states into atomic orbital $|a_e, \nu_e\rangle$ as the summation of the square modules of the projection over all possible hole orbitals,

$$
\begin{aligned}
D_e(a_e, \nu_e) &= \sum_{a_h, \nu_h} \left|\langle a_h, \nu_h; a_e, \nu_e \mid S\rangle\right|^2 && (2.52)\\
&= \sum_{a_h, \nu_h} \left| \sum_{\mathbf{k}, v, c} A^S_{vc\mathbf{k}} C^{c\mathbf{k}}_{a_e \nu_e} C^{v\mathbf{k}\,*}_{a_h \nu_h} \right|^2 && (2.53)\\
&= \sum_{a_h, \nu_h} \left(\sum_{\mathbf{k}, v, c} A^S_{vc\mathbf{k}} C^{c\mathbf{k}}_{a_e \nu_e} C^{v\mathbf{k}\,*}_{a_h \nu_h} \right) \left(\sum_{\mathbf{k}', v', c'} A^{S*}_{v'c'\mathbf{k}'} C^{c'\mathbf{k}'*}_{a_e \nu_e} C^{v'\mathbf{k}'}_{a_h \nu_h} \right) && (2.54)\\
&= \sum_{a_h, \nu_h} \sum_{\mathbf{k}, v, c} \sum_{\mathbf{k}', v', c'} A^S_{vc\mathbf{k}} A^{S*}_{v'c'\mathbf{k}'} C^{c\mathbf{k}}_{a_e \nu_e} C^{c'\mathbf{k}'*}_{a_e \nu_e} C^{v\mathbf{k}\,*}_{a_h \nu_h} C^{v'\mathbf{k}'}_{a_h \nu_h} && (2.55)\\
&= \sum_{\mathbf{k}, v, c} \sum_{\mathbf{k}', v', c'} A^S_{vc\mathbf{k}} A^{S*}_{v'c'\mathbf{k}'} C^{c\mathbf{k}}_{a_e \nu_e} C^{c'\mathbf{k}'*}_{a_e \nu_e} \left(\sum_{a_h, \nu_h} C^{v\mathbf{k}\,*}_{a_h \nu_h} C^{v'\mathbf{k}'}_{a_h \nu_h} \right). && (2.56)
\end{aligned}
$$

We note the term in the last parentheses is an inner product over the atomic orbital coefficients for the hole states, using the orthonormality of Bloch states:

$$
\left(\sum_{a_h, \nu_h} C^{v\mathbf{k}\,*}_{a_h \nu_h} C^{v'\mathbf{k}'}_{a_h \nu_h} \right) = \langle \psi_{v\mathbf{k}} | \psi_{v'\mathbf{k}'} \rangle = \delta_{v,v'} \delta_{\mathbf{k},\mathbf{k}'}. \qquad (2.57)
$$

Substituting back the delta functions and if we only consider only the diagonal terms (where $c' = c$),

$$
\begin{aligned}
D_e\left(a_e, \nu_e\right) &= \sum_{\mathbf{k}, v} \sum_{c, c'} A^S_{vc\mathbf{k}} A^{S*}_{vc'\mathbf{k}} C^{c\mathbf{k}}_{a_e \nu_e} C^{c'\mathbf{k}*}_{a_e \nu_e} && (2.58)\\
&\approx \sum_{\mathbf{k}, v} \sum_{c} \left|A^S_{vc\mathbf{k}}\right|^2 \left|C^{c\mathbf{k}}_{a_e \nu_e}\right|^2 && (2.59)\\
&= \sum_{\mathbf{k}, v} w_S(v, \mathbf{k}) P_{n\mathbf{k}}(a_e, \nu_e), && (2.60)
\end{aligned}
$$

where $w_S(v, \mathbf{k})$ and $P_{n\mathbf{k}}(a_e, \nu_e)$ are defined in 2.46 and 2.50 and can be obtained via solving the BSE and using DFT methods, respectively.

Similarly, for the hole component:

$$D_h\left(a_h, \nu_h\right) = \sum_{\mathbf{k},c} w_S(c, \mathbf{k}) P_{n\mathbf{k}}(a_h, \nu_h). \tag{2.61}$$

These integrals effectively weigh the contribution of each atomic orbital to the exciton wavefunction. Finally, to identify inter- or intra-layer exciton, we can sum these weights to map the exciton onto specific regions within the material.

A Python script was implemented to analyse the spatial and orbital character of excitonic states by decomposing the BSE eigenvectors onto atomic orbitals based on the above idea. The script takes the BSE eigenvectors from BerkeleyGW and the projected density of states from DFT calculations as input, calculates the contributions from different atomic orbitals to both the electron and hole components of the exciton wavefunction according to the formalism described above. The code allows for analysing exciton spatial distribution directly from BSE solutions (the eigenvectors) without additionally using the plotxct utility in BerkeleyGW, and has been applied to the exciton decomposition analysis in the layered perovskite-intergrowth heterostructures presented in Chapter 6.

3 | Optoelectronic properties of mixed halide perovskites from first principles

3.1 Introduction

In this chapter, we will focus on halide perovskites, a distinct class of materials that exhibit a versatile crystal structure for photovoltaic applications. Perovskites generally represent a group of crystal structures with chemical formula ABX_3, where A is a monovalent cation and B is a divalent cation, and X is an anion. The simplest cubic perovskite structure consists of small B cations located in the centre of the BX_6 octahedra, and larger A cations located at the centre of the corner-sharing octahedra framework. Since the first report of application in solar cells in 2009 [21], halide perovskites have demonstrated remarkably rapid advancements in device applications [24, 122, 123] and power conversion efficiencies, achieving over 27% [22] within over a decade of research.

Improving the stability of perovskite solar cells is key in the design of devices and materials. Hybrid halide perovskites, such as methylammonium lead triiodide ($MAPbI_3$) and formamidinium lead triiodide ($FAPbI_3$), are prone to degradation in the presence of moisture, light, and heat due to the decomposition of their volatile organic components [124, 125]. Developing solar cells with mixed cation and/or mixed halide perovskites is a promising route to improve stability [3, 38, 126, 127]. For example, McMeekin et al. [3] have demonstrated a mixed cation and mixed halide perovskite, $FA_{0.83}Cs_{0.17}Pb(Br_xI_{1-x})_3$, which exhibits both structural and thermal stability. They successfully fabricated all-perovskite solar cell devices using these chemically mixed perovskites, achieving an open-circuit voltage of 1.2 volts and a power conversion efficiency of 14.7%.

Chemically mixed perovskites, including those with mixed monovalent cations at the A-site [126], divalent cations at the B-site [38], and halogen anions at the X-site [127,128], have been extensively investigated. These mixed-ion perovskites exhibit tunable optical and transport properties, demonstrating improved stability and efficiency compared to perovskites with single cations or halides. The tunability of the band gap is primarily attributed to the compositional and structural flexibility of the inorganic B-X framework [129, 130], as the electronic states at the valence and conduction band edges in halide perovskites are primarily derived from the orbitals of B-site cations and X-site halogens. Prior studies on lead based mixed halide perovskite series $APbX_3$ (A = MA, FA) [128, 131–133] have shown that optical and transport properties, as well as device performance, can be tuned by varying the Br/I mixing ratio. Noh et al. [131] reported a band gap bowing parameter of 0.33 eV for $MAPbX_3$, while Suarez et al. [132] found almost no band gap bowing. Eperon et al. [133] demonstrated that band gap tunability can also be achieved by mixing Pb with Sn at the B-site, resulting in perovskites with excellent thermal and atmospheric stability for use in all-perovskite solar cells. While A-site cations do not directly contribute to the band edge states, as their electronic states are far from the band edges [130], they can indirectly influence the optical properties by causing structural deformation of the inorganic B-X framework. This can include changes in unit cell volume, octahedral distortion, and dimensional reduction [134]. The degree of octahedral tilting can be modified by using A-site cations of different sizes, with enhanced tilting leading to an increase in the band gap [130]. In addition to optical properties, A-site cation mixing can also lead to enhanced stability, suppressed halide segregation, and tunable carrier transport properties, which has been previously reported in FA/MA [135], FA/Cs [3, 136], and MA/Cs [137] mixing systems. These findings highlight the importance of exploring various combinations of mixed-ion perovskites to optimise their properties, both theoretically and experimentally.

Following this rapid experimental progress, theoretical investigations on these mixed systems, especially mixed halide perovskites are also emerging [138–143]. Ref. [138]

used DFT-LDA to screen for potential homovalent lead substitutes in halide perovskites and identified Mg as a promising candidate for partial Pb replacement. Ref. [139–141] employed DFT to calculate the structural, optical, and transport properties of $MAPbI_3$ and its compounds alloyed with chlorine and bromine. Ref. [142] performed DFT computations on the bulk tin mixed-halide $CsSnX_3$ perovskite, and Ref. [143] investigated different configurations of mixed cation mixed halide lead perovskites $APbX_3$ with DFT, and extracted the compositional free energy, electronic band gaps, based on which they established a theory to study halide segregation.

However, first-principles calculations rely on periodic boundary conditions and frozen core approximations, necessitating the use of large supercells containing tens or hundreds of atoms to simulate compositional and orientational disorder in materials by exchanging random atoms in the supercell structure. Modelling the supercell structure of mixed halide perovskites in first-principles calculations also requires careful treatment of symmetry [142, 143]. These factors contribute to the high computational cost of supercell methods, even at the DFT level, and will anticipate difficulties in applying more precise yet computationally demanding GW+BSE methods introduced in the last chapter. As a result, GW+BSE investigations on mixed systems are still lacking.

To advance the theoretical understanding of mixed perovskites, it is crucial to develop more efficient computational methods that can accurately capture the complex nature of these systems while minimising computational costs. This will enable researchers to apply advanced techniques like GW and BSE to mixed perovskites, providing deeper insights into their electronic and optical properties and guiding the design of high-performance perovskite-based devices.

VCA has proven to be a valuable tool for treating alloyed materials and modelling mixed-ion systems while reducing computational costs. VCA is an approximation that allows the study of a crystal with primitive periodicity, composed of “virtual” atoms that interpolate between the behaviour of two atoms with similar electronic configurations. Several studies have applied VCA methods to mixed halide perovskites, such as $CH_3NH_3PbX_3$ [144] and $CsPbX_3$ [145]. In Ref. [144], Jong et al. investigated the trends in structural, electronic, and optical properties of $MAPbX_3$ using DFT-LDA with VCA. They found that as the Br concentration increases, the lattice constant decreases, while the band gap and exciton binding energy (calculated using a hydrogenic model) increase quadratically. Yu et al. [145] applied VCA in DFT with hybrid HSE functionals to study the all-inorganic perovskite series $CsPbX_3$. Their results showed better agreement with experimental band gaps compared to DFT-PBE. Despite these advancements, there is a lack of complete ab initio studies on mixed halide perovskites using state-of-the-art GW+BSE methods. In this chapter, we will try to incorporate VCA into GW+BSE calculations, as a more accurate and efficient approach to understanding the electronic and optical properties of these materials.

In this chapter, we will demonstrate a theoretical scheme to apply VCA in conjunction with DFT and GW+BSE, to systematically investigate the structural, electronic, optical, vibrational and transport properties of mixed halide perovskites. This work was conducted in collaboration with experimentalists from the group of Prof. Laura Herz at the Department of Physics, University of Oxford. Experimental data presented in this chapter was measured by Dr. Silvia Motti.

It is important to note that while the experimental data is based on the mixed cation mixed halide perovskites $FA_{0.83}Cs_{0.17}PbX_3$, our theoretical work focuses on the cubic $CsPbX_3$. Although we have excluded the FA cation in our model, the comparison of results remains meaningful for two reasons:

1. Our primary focus is on the general trends in properties that change with the halide anion concentration.

2. The A-site cation does not directly contribute to the electronic properties of the perovskite.

By replacing the FA cation with Cs in our model, we have reduced the computational cost while maintaining a relatively accurate representation of the trends in electronic properties. However, it should be acknowledged that there may be discrepancies in the vibrational and transport properties due to the absence of the FA cation in our model. These discrepancies will be discussed in detail throughout this chapter.

3.2 Lattice parameters

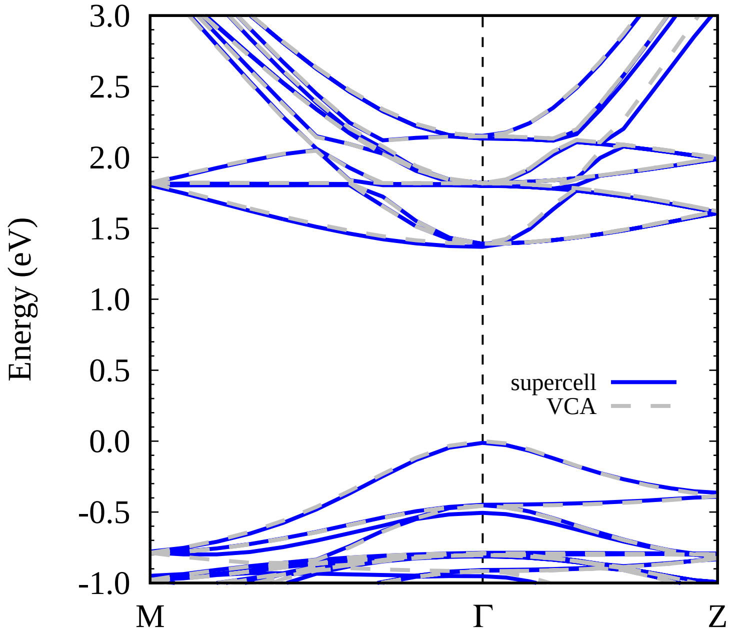

Figure 3.1: Partial electronic band structures of mixed halide perovskite $CsPb(I_{0.958}Br_{0.042})_3$ along M-Γ-Z. Blue solid line: A 2×2×2 supercell with a randomly substituted atom, Grey dashed line: A 2×2×2 supercell with virtual atoms $X = I_{0.958}Br_{0.042}$ using VCA.

To test the reliability of the VCA approach for mixed halide perovskites, we compared the results generated by VCA with those obtained using the corresponding supercell approach. We constructed a disordered $CsPb(I_{0.958}Br_{0.042})_3$ by creating a 2×2×2 supercell from a $CsPbI_3$ unit cell and substituting one I atom with one Br atom. We then compared the band structure calculated from the supercell with substitution to that of a supercell containing a virtual atom $X = I_{0.958}Br_{0.042}$ using a path M-Γ-Z as shown in FIG. 3.1. The alignment of the two band structures validates the reliability of VCA in providing accurate predictions of the electronic properties of mixed halide perovskites. This finding is crucial, as it demonstrates that VCA can be used as an efficient and reliable alternative to the more computationally expensive supercell approach when studying the electronic properties of these materials.

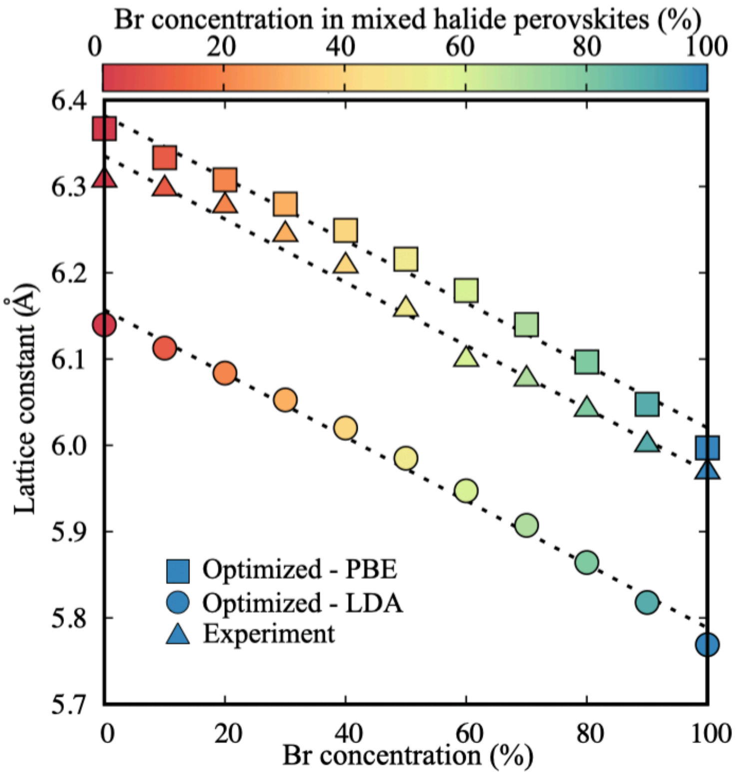

Figure 3.2: Comparison between optimised lattice parameters computed within DFT-PBE (squares), DFT/LDA (disks) and from measurements (triangles). The measured lattice parameters are for $FA_{0.83}Cs_{0.17}PbX_3$, extracted from Ref. [3].

The cubic structure of the mixed halide series $CsPbI_{31-x}Br_x$ was fully optimised at the DFT level for each concentration. The optimised lattice constants a were found to exhibit a linear relationship with Br concentration, as depicted in FIG. 3.2. As anticipated, DFT-LDA underestimates the lattice constants, whereas DFT-PBE overestimates them across all concentrations. It is important to note that we are optimising the lattice constants for Cs-based perovskites, which will result in a lattice contraction compared to the experimental perovskites $FA_{0.83}Cs_{0.17}PbX_3$ used for comparison. The superior agreement between PBE-optimised lattice constants and experimental values, compared to

LDA-optimised lattice constants, can be attributed to the cancellation of errors arising from PBE overestimation and A-site cation shrinking. The calculated lattice constants of 6.367 Å for $CsPbI_3$ and 5.997 Å for $CsPbBr_3$ were verified to be in good agreement with experimental findings. The obtained lattice parameters adhere to Vegard's law [146], which predicts a linear dependence of lattice constants on the mixing ratio.

3.3 Vibrational properties

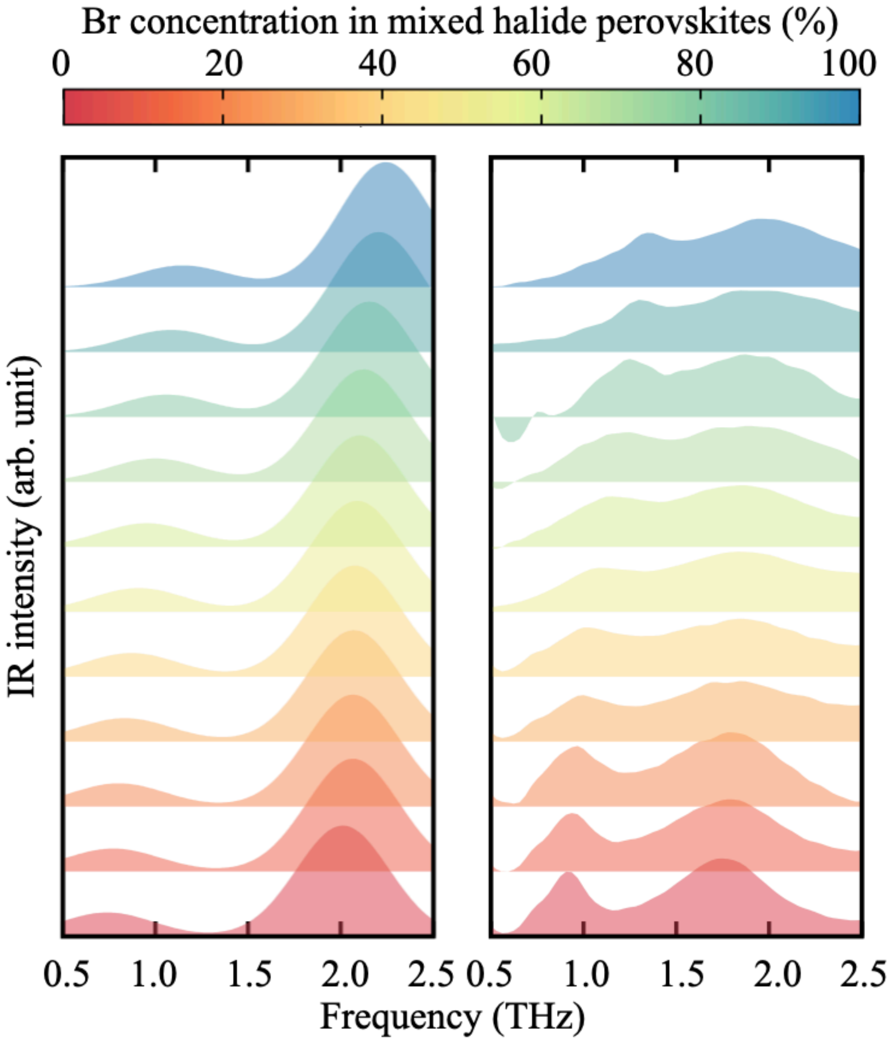

Figure 3.3: a: Infrared absorption spectra of $CsPbX_3$ from DFPT. b: Infrared absorption spectra of $FA_{0.83}Cs_{0.17}PbX_3$ from experiment. An offset of each concentration in y axis has been added between curves for clarity.

To understand vibrational properties of this mixed series, we employ density functional perturbation theory (DFPT) using the VCA. Both the LDA and PBE are applied to test the sensitivity of our results. We calculate the normal vibrational modes within the harmonic approximation at the Γ point. The Born effective charges and the dielectric permittivity tensors are also calculated. The IR spectrum is proportional to $\omega\epsilon_2(\omega)$ and defined as the following [147],

$$I(\omega) = \frac{e^2}{M_0} \sum_{\alpha\nu} \left|Z^*_{\alpha\nu}\right|^2 \delta\left(\omega - \omega_\nu\right), \tag{3.1}$$

where $Z_{\alpha\nu}$ is the dimensionless effective charge vectors for each vibrational mode ν, defined as [147],

$$Z^*_{\alpha\nu} = \sum_{\kappa\beta} \sqrt{\frac{M_0}{M_\kappa}} e_{\kappa\beta,\nu} \frac{\Omega}{e} \frac{\partial P_\alpha}{\partial u_{\kappa\beta}}, \tag{3.2}$$

where κ labels the atoms in the unit cell, α and β indicate Cartesian directions, Ω is the unit cell volume, and e is the electron charge, **P** is the macroscopic polarisation (dipole per unit cell), $u_{\kappa\beta}$ is an atomic displacement from equilibrium, M_κ are the nuclear masses, M_0 is the average mass over the unit cell, and $e_{\kappa\beta,\nu}$ are the vibrational eigenmodes with frequency ω_ν. To plot our IR spectra as shown in Figure 3.3, we replace the Dirac delta functions by Gaussians with a broadening of 0.1 THz. In all DFPT calculations we apply the acoustic sum rule to the interatomic force constants, and the atomic masses used for virtual atoms are linearly interpolated between Br and I as we change the mixing ratio.

15 zone centre phonon modes across the entire mixed halide series are calculated (in decreasing order of their energy): two groups of triply degenerate IR-active modes, one group of triply degenerate nonpolar modes, three acoustic modes, and three modes with imaginary phonon frequencies. The presence of the anharmonic soft modes indicates

the structural instabilities at low temperature associated with the structural distortion and PbX_6 octahedra tilting in the absence of temperature effects [148]. The calculated and measured THz spectra exhibit two primary IR-active peaks within the 0.5-2.5 THz frequency range. As illustrated in Figure 3.4, the calculated positions of these peaks show good agreement with experimental measurements, with discrepancies of less than $\pm$ 0.3 THz ($\sim \pm$ 1 meV) observed across the entire range of concentrations. Minor differences in the calculated positions and spectral weights of IR-active peaks can be attributed to several factors, including the absence of the FA cation in our atomistic models, the slight mismatch between computed and measured lattice parameters, and the omission of temperature effects. Importantly, both IR-active mode frequencies exhibit the same dependence trend on Br concentration as observed experimentally, supporting our assumption of uniformity.

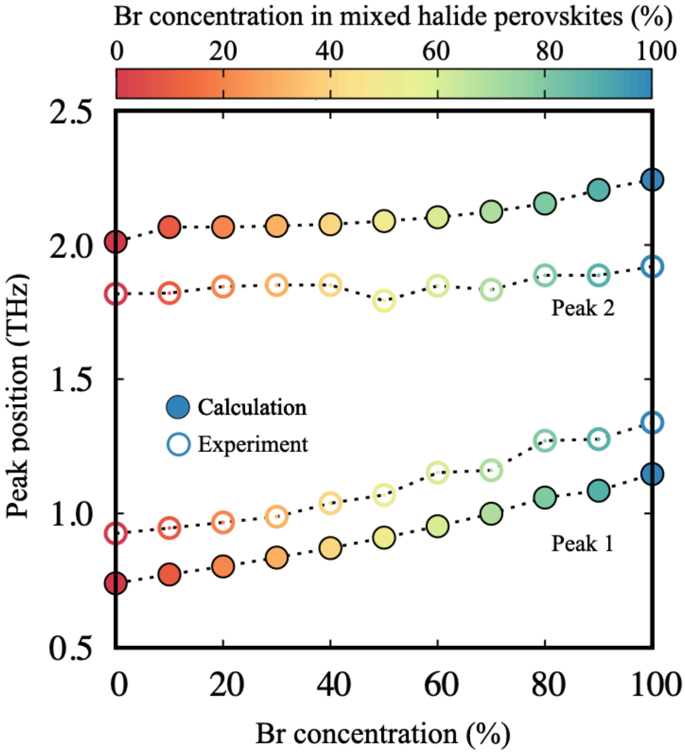

Figure 3.4: Extracted peak frequencies from DFPT with LDA and PBE, and from experimental THz spectra. The red curves are for the first peaks, the blue curves are for the second peak.

3.4 Electronic properties

In this section, we will focus on the electronic properties. We first calculated the band gaps for the $CsPb(Br_xI_{1-x})_3$ series at different levels of theory and compared it against the experimental values. Band gaps for $CsPbX_3$ at different theory levels from DFT with PBE and PBE0 functionals to our one-shot G_0W_0 calculations are compared with experimental values for $FA_{0.83}Cs_{0.17}PbX_3$ and plotted in FIG. 3.5. We found that when introducing spin orbit coupling effects in our calculations, the band gaps will be 1.2 eV lower than band gaps without spin orbit coupling due to a split of Pb 6p states. These results agree well with what has been found in other theoretical works [149], where SOC corrections are calculated as 1.25 eV for $CsPbI_3$ and 1.23 eV for $CsPbBr_3$. DFT-PBE yields a band gap of 0.18 eV for $CsPbI_3$ and 0.56 eV for $CsPbBr_3$ and underestimates the band gap about 1.4 eV for $CsPbI_3$ and 1.8 eV for $CsPbBr_3$. Furthermore, PBE0 functionals opens the a band gap by approximately 1 eV as compared to PBE results. This is due to the inclusion a fraction of of the Hartree-Fock exact exchange in PBE0.

In general, local and semi-local density-functional approximations (*e.g.*, LDA, PBE) tend to underestimate electronic band gaps primarily due to the self-interaction error [83]. To obtain more rigorous descriptions of the electronic band structure, many-body perturbation theory within the GW approximation are often used [150]. Figure 3.5 shows a comparison of quasiparticle band gaps for the $CsPb(Br_xI_{1-x})_3$ series calculated using the one-shot G_0W_0 approximation, incorporating spin-orbit coupling, as implemented in the BerkeleyGW code [76]. We use Kohn-Sham eigenvalues and eigenfunctions calculated within DFT-PBE, as implemented in the Quantum Espresso code [91], as a starting point for the one-shot G_0W_0 (hereafter referred to as G_0W_0@PBE, detailed computational setup along with convergence tests can be found in the Appendix A.1.2). The calculations are compared against experimental quasiparticle band gaps derived from optical absorption spectra fitted using the Elliott model [5] (as discussed

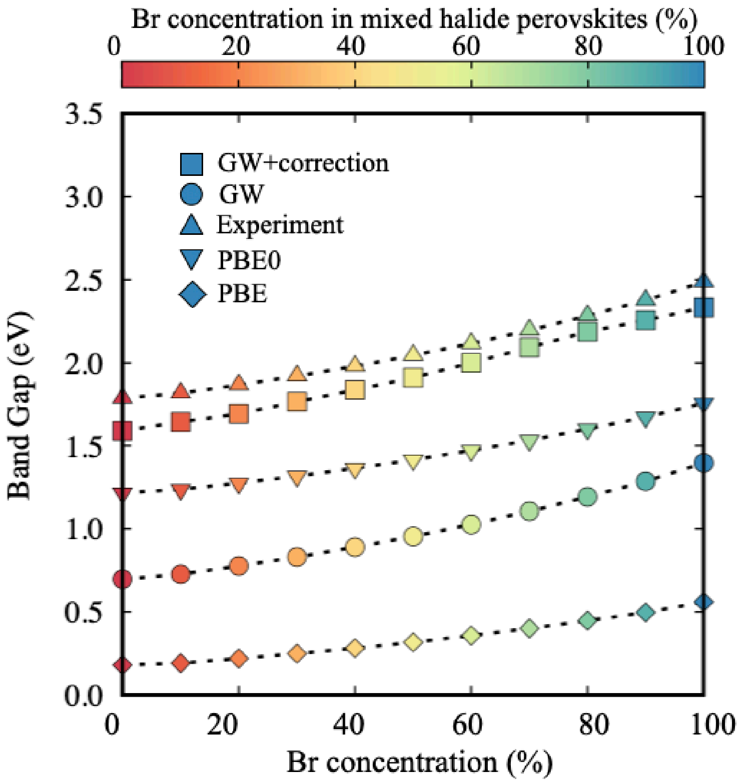

Figure 3.5: Band gaps extracted at different levels of theory and compared with experimental values. Dashed lines are guide to the eye.

in Ref. [151]). The calculated band gaps consistently underestimate the experimental values by $\sim$ 0.9 - 1 eV, while accurately capturing the trend with respect to the Br concentration. This significant quantitative discrepancy arises from two primary origins:

1. The G_0W_0 framework typically yields quasiparticle band gaps that are strongly dependent on the mean-field starting point [152–154]; this can be addressed by employing suitable hybrid functional starting points [152,154] or by implementing self-consistency in GW methods [149, 155, 156], both of which are computationally demanding techniques. Particularly, self-consistency has been shown to blue-shift quasiparticle band gaps by 0.4 and 0.6 eV for lead-iodide and lead-bromide perovskites, respectively [149].

2. Quasiparticle band gaps computed for the high-temperature cubic perovskite phase will systematically underestimate the experimental values due to the absence of thermal effects, which blue-shift the quasiparticle band gap of cubic $\mathrm{CsPbI_3}$ and $\mathrm{CsPbBr_3}$ by 0.7 and 0.5 eV, respectively [149].

The systematic underestimation of our computed quasiparticle band gaps is thus fully accounted for by these two contributions. With both thermal effect and self-consistency corrections taken into account in our G_0W_0 results, we apply a rigid shift of 1.1 eV across the entire series (a shift value based on Ref. [149], hereafter referred to as a “thermal correction”) to obtain corrected band gaps for $\mathrm{CsPbX_3}$ as, $E_{\text{gap}}^{\text{theory}} = E_{\text{gap}}^{\text{GW}} + \Delta_T + \Delta_{QSGW}$. The corrected band gaps yield error within 0.2 eV from experiment for all concentrations, as shown in FIG. 3.5. It should be noted while we compare our theoretical results for cubic $\mathrm{CsPbX_3}$ against experimental values for $\mathrm{FA_{0.83}Cs_{0.17}PbX_3}$, we obtain good agreement partially because the A-site cation typically does not significantly modify the band-edge electronic states [130]. However, we note that additional factors - such as additional structural distortions induced by the organic cation - may also lead to partial cancellation of errors.

We calculated the quasiparticle band structure of $\mathrm{CsPbX_3}$ including spin orbit coupling as shown in FIG. 3.6. In addition to the band gap blue-shift, we also observe that an increased concentration of Br leads to an increase in the valence band width by up to 0.5 eV and a subtle decrease in the curvature of the valence and conduction band edges, as illustrated in the quasiparticle band structure (Figure 3.6), indicating a change in charge-carrier effective masses.

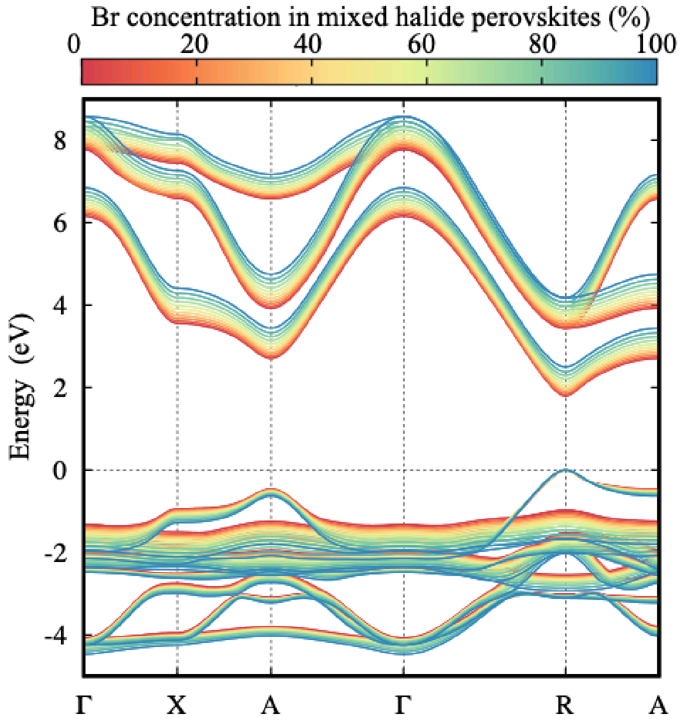

Figure 3.6: Quasiparticle band structures calculated from G_0W_0@PBE including thermal corrections, aligned to the top of the valence band.

3.5 Charge carrier effective mass

Electron and hole effective masses m_e^* and m_h^*, are calculated from Wannier interpolated quasiparticle band structures with a parabolic band model using the following formula,

$$m_{\mathrm{e,h}}^* = \left[\frac{1}{\hbar^2}\frac{\partial^2 E_{\mathrm{c,v}}(\mathbf{k})}{\partial k^2}\right]^{-1}, \tag{3.3}$$

where $E_{\mathrm{c,v}}(\mathbf{k})$ is the conduction band minimum and valence band maximum, respectively. The reduced effective masses are calculated as $\mu = m_e^* \cdot m_h^*/(m_e^* + m_h^*)$. Reduced effective masses calculated within standard $G0W0$@PBE are underestimated with respect to tabulated experimental values in the literature [4] by more than 50%, consistent with the quasiparticle band gap underestimation described above and in agreement with past calculations.

According to the $\mathbf{k} \cdot \mathbf{p}$ perturbation theory, the effective mass has a linear correlation with the band gap of semiconductors, for an isotropic two-band model semiconductor, with band gap E_g and matrix element $\mathbf{p}_{cv}$ between the valence and the conduction wavefunctions at the band edge, the electron and hole effective mass are give as the following [157],

$$\frac{m_e}{m^*} = 1 + \frac{2}{m_e}\frac{\left|\mathbf{p}_{cv}\right|^2}{E_g}, \tag{3.4}$$

where m_e is the electron rest mass, m^* is the charge-carrier effective mass for electron and hole, E_g is the band gap, $\mathbf{p}_{cv}$ is the transition matrix element between the valence band top and conduction band bottom [157]. We fitted our effective masses from Wannier+G_0W_0 with the quasiparticle band gaps for CsPbX$_3$ as shown in FIG. 3.7, the computed reduced effective masses follow very closely this simple model as $m_e/\mu = 17.43 \times 1/E_g + 2$, here m_e represents free electron mass.

A recent experimental study of the relationship with band gaps and charge carrier effective masses across several perovskites, also reveals a linear relationship between the inverse of effective mass m_e/μ and the inverse of band gaps E_g^{-1} [4]. The slope we extract from our linear fitting for the reduced effective mass μ is 17.43, in good agreement with the slope fitted for experimental band gaps and effective masses of 17.3, as reported in Ref. [4].

Such excellent fitting to the parametric linear model and good agreement with experi-

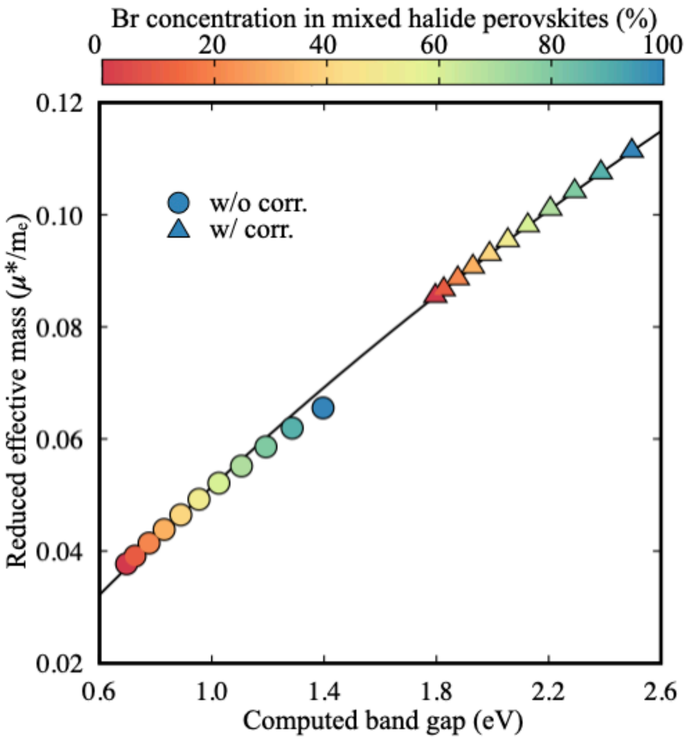

Figure 3.7: Computed reduced effective masses (μ^*) as a function of band gaps (E_g) with and without thermal corrections (triangles and disks respectively). The black line corresponds to the expression $\frac{m_e}{\mu^*} = 2 + \frac{17.43}{E_g}$ (where m_e is the electron rest mass), obtained by fitting uncorrected effective masses using $\mathbf{k} \cdot \mathbf{p}$ perturbation theory. Effective masses with thermal corrections are extrapolated using this expression.

ment fitted parameters validates the feasibility of applying the parametric model in our calculations for these systems. We can therefore use it to extrapolate effective masses with thermally corrected quasiparticle band gaps. By extrapolating the mass-gap dependency to the corrected band gaps obtained in the previous section, we can obtain corrected effective masses, with $\mu = 0.085m_e$ for CsPbI$_3$ and $\mu = 0.111m_e$ for CsPbBr$_3$. Figure 3.8 shows by taking into account thermal correction, computed reduced effective masses yield better agreement with measurements for CsPbBr$_3$ and CsPbI$_3$, as reported in Ref. [4].

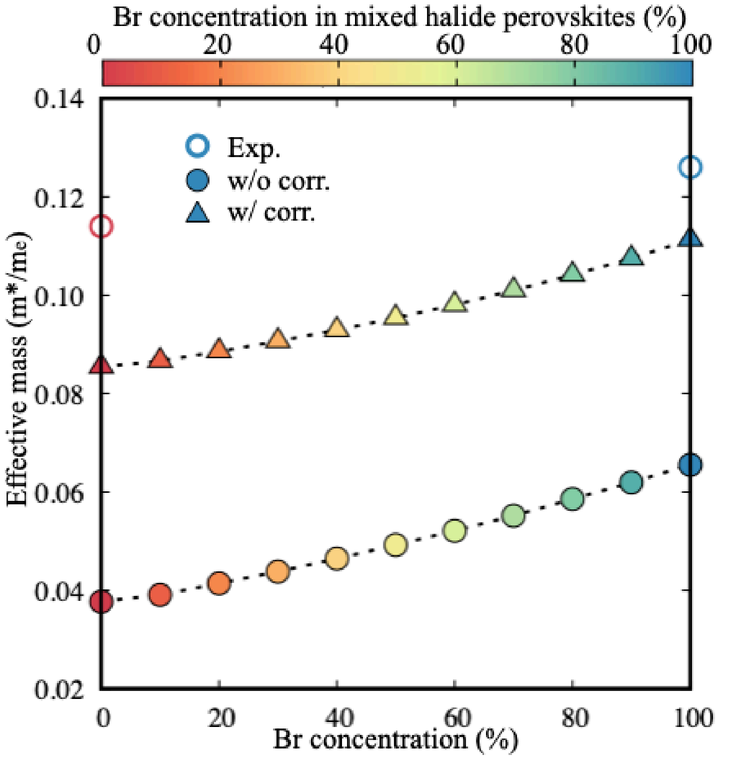

Figure 3.8: Reduced effective masses calculated from Wannier interpolated quasiparticle band structures (filled circles) and extrapolated effective masses with thermally corrected quasiparticle band gaps according to the $\mathbf{k} \cdot \mathbf{p}$ perturbation theory (filled triangles), compared with experimental values (empty circles) for CsPbI$_3$ and CsPbBr$_3$ reported in Ref. [4]. All data points are colour coded according to the concentration of Br, as shown in the colour bar, and the dotted lines are guides to the eye.

3.6 Dielectric constants

In Figure 3.9, we then present a comprehensive analysis of the electronic properties by comparing the high-frequency (ε_{∞}) and low-frequency (ε_0) dielectric constants obtained from theoretical calculations and experimental measurements. The high-frequency dielectric constants, computed using the random-phase approximation (RPA) [101,102], demonstrate a remarkable agreement with experimental values across the mixed-halide series, which is consistent with previous calculations of dielectric constants reported in the literature [6]. Regarding the low-frequency dielectric constants, it is noteworthy that the range of computed and measured values generally exhibit good agreement. However, some non-systematic discrepancies are observed in the experimental values. These discrepancies can be primarily attributed to experimental uncertainties arising from variations in substrate and film thickness, the accuracy of fits employed to extract the values from the complex dark conductivity spectra, and the overall signal-to-noise ratio of the acquired data.

3.7 Optical properties

In the next section, we will focus on the analysis of optical properties. FIG. 3.10 shows the computed (with correction) and measured absorption spectra.

When solving the BSE to obtain the optical absorption spectrum, it is a well-known problem that interaction matrix elements need to be constructed on a very fine **k**-point grid because excitons are correlated states with a wave function that has fine structures in k space. For example, even for bulk semiconductors such as GaAs, very fine uniform grids containing over a million k points are necessary to resolve the exciton energies and wave functions [72]. To obtain a reasonable value of binding energy while using reasonable computational resources, we employ a patched sampling scheme in our BSE calculation [158]. The patched sampling method is based on the fact that a weakly

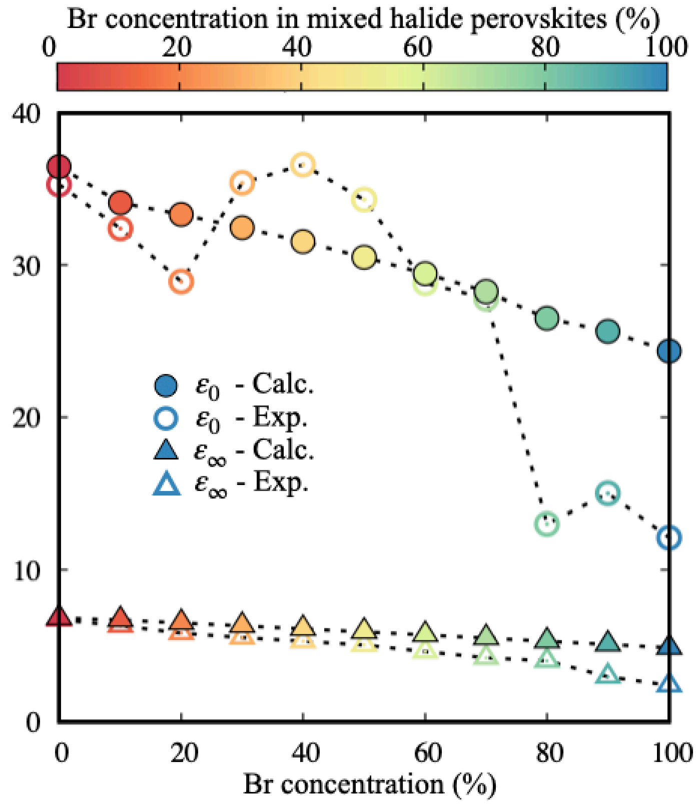

Figure 3.9: Comparison of low- and high-frequency dielectric constants calculated from DFPT for $CsPb(Br_xI_{1-x})_3$ and measured experimentally for $FA_{0.83}Cs_{0.17}PbX_3$. The dashed black line is a guide to the eye. All data points are colour coded according to the concentration of Br, as indicated by the colour bar.

bound exciton is highly localised in reciprocal space around the R point for cubic $CsPbI_3$, implying that we do not need to calculate electronic states throughout the Brillouin Zone. Convergence details of the patch size and density can be found in the Appendix A.1.3.

We observe absorption coefficients in close qualitative agreement, displaying very similar lineshapes across the entire I-Br series within a range of 2 eV from the onset. The spectra feature an excitonic resonance at the onset of absorption, followed by a flat plateau and a sharp rise associated with the second lowest direct optical transition [151]. Experimental optical absorption spectra at concentrations of 80% and above are most significantly influenced by disorder and scattering factors, which consequently lead to a deviation from the smooth dependence of the measured exciton binding energies on the mixing concentration as shown in Figure 3.12a.

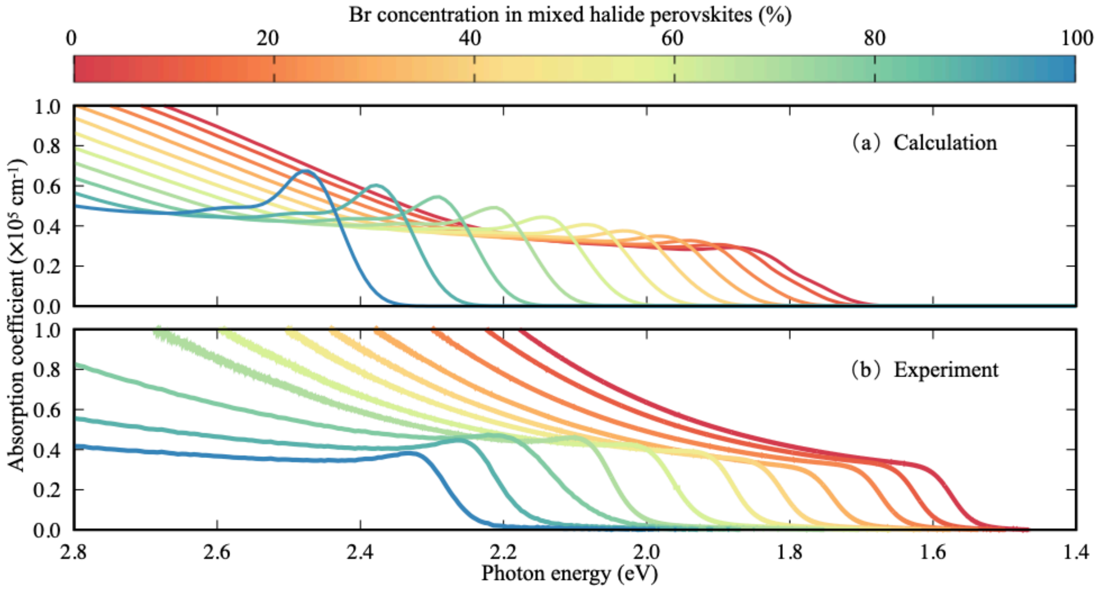

Figure 3.10: Calculated (a) and measured (b) optical absorption spectra for $FA_{0.83}Cs_{0.17}PbX_3$ and $CsPb(Br_xI_{1-x})_3$, respectively, across the entire I-Br series.

With calculated absorption spectra with and without electron hole interaction, we can extract the exciton binding energy from the first excitonic peak in the spectra and the quasiparticle band gap.

In Figure 3.11a, we first show a comparison between exciton binding energies calculated from GW+BSE as described above and binding energies using the hydrogenic model [7], $E_b = \mu^*/(m_e\varepsilon_\infty^2)$ Ry, where m_e is the electron rest mass, 1 Ry = 13.6057 eV is the Rydberg constant, and μ^* is the reduced effective mass from our quasiparticle band structure calculations. We find that *ab initio* exciton binding energies and hydrogenic model binding energies agree remarkably well, within a difference of at most 4 meV. This comparison indicates that the dielectric function can be approximated to be uniform throughout the crystal. We note that exciton binding energies calculated as described above are based on less converged RPA dielectric functions, as described in the previous section; According to the convergence test in Appendix A.1.2, the dielectric constant for $CsPbI_3$ is underestimated by approximately 25% in this setup, and this is bound to impact the accuracy of calculated exciton binding energy. To improve on this, we use the observation made in Figure 3.11a, and recalculate the exciton binding energy from BSE, by approximating the dielectric function as $\varepsilon(\mathbf{r}, \mathbf{r'}) \sim \varepsilon_\infty$ (uniform screening approximation), where ε_∞ is the fully converged RPA dielectric constant calculated using a $12 \times 12 \times 12$ grid (Details can be found in Appendix A.1.2). For completeness, we also compare these exciton binding energies against the Wannier-Mott model and again obtain an excellent agreement. We then calculate the exciton binding energies using the uniform screening approximation, using the best converged dielectric constant, to compare against the measured values.

As illustrated in Figure 3.12, there is a good agreement between measured and computed exciton binding energies within the G_0W_0+BSE framework (see Appendix A.1.3 for computational details and convergence). We note that experimental optical absorption spectra at concentrations of 80% and above exhibit the most significant contributions from disorder and scattering factors, which consequently lead to a deviation from the smooth dependence of the measured exciton binding energies on the mixing concentration.

Despite that, it is important to recognise that the quantitative agreement between computed and measured exciton binding energies arises from the cancellation of two distinct

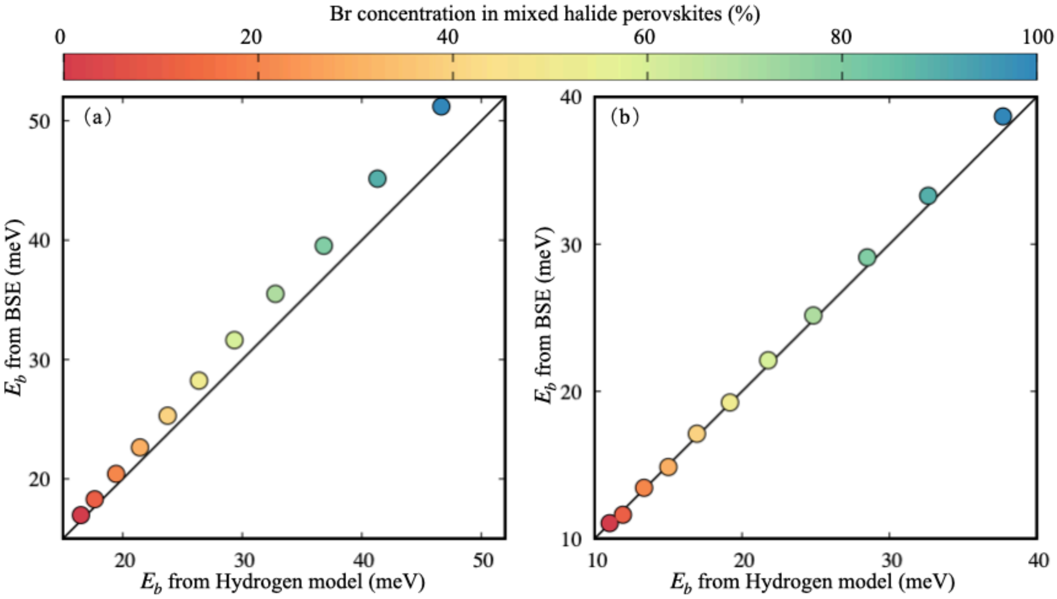

Figure 3.11: (a) Comparison of exciton binding energies obtained from a BSE calculation using the RPA dielectric constant and self-energy evaluated on a coarse $6\times\ 6\times6$ **k**-point grid, versus exciton binding energies from the hydrogenic (Wannier–Mott) model using the same ε_∞ extracted from the coarse-grid RPA calculations. (b) Comparison between BSE calculated exciton binding energies using a dielectric function approximated as $\varepsilon(\mathbf{r},\mathbf{r}') \sim \varepsilon_\infty$, with ε_∞ calculated from RPA with a $12\times12\times12$ **k**-point grid and hydrogenic model exciton binding energies with the same ε_∞. All data points are colour coded according to the concentration of Br, as shown in the colour bar and the continuous black lines are the lines of perfect agreement between first principles and hydrogenic model.

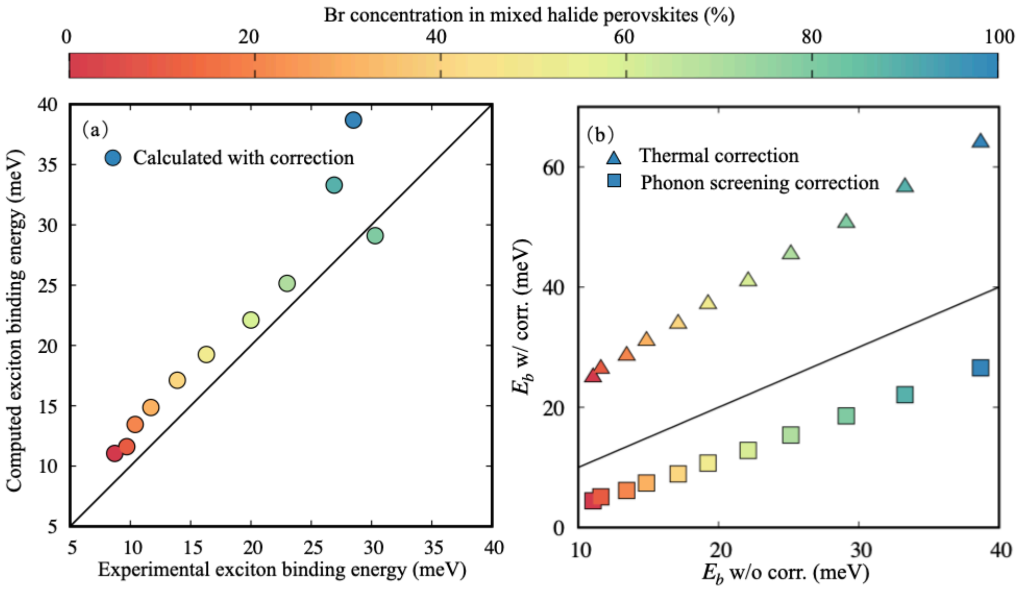

Figure 3.12: (a) Computed G_0W_0+BSE exciton binding energies plotted against measured exciton binding energies extracted from optical absorption spectra using the Elliot model [5], as described in the Appendix A.1.3; the continuous black line represents the line of perfect agreement between calculations and experiment. (b) Contributions to the calculated exciton binding energies from thermally corrected reduced effective masses (triangles) and phonon screening effects [6] (squares), as calculated using the hydrogenic model [7], which yields exciton binding energies in very close agreement with *ab initio* values. The continuous black line corresponds to the line of null correction.

effects that are not captured in our standard G_0W_0+BSE calculations. First, computed reduced effective masses (and consequently, binding energies) are underestimated by more than a factor of 2 in the absence of thermal corrections, as discussed earlier (the effect of thermal corrections on the exciton binding energy is depicted by the triangles in Figure 3.12b). Second, without the inclusion of phonon screening and polaronic interference effects [6, 159], the GW+BSE framework has been demonstrated to overestimate exciton binding energies for lead halide perovskites by up to a factor of 3 (phonon screening effects on the exciton binding energy are represented by the squares in the inset of Figure 3.12b). These contributions effectively cancel each other out, resulting in the close agreement with experiment shown in the main panel of Figure 3.12b.

Despite these systematic error cancellations, the dependence of exciton binding energy on Br concentration follows a consistent trend, irrespective of the level of theory employed in computations.

3.8 Charge carrier mobility calculation

Charge carrier mobility in polar semiconductors like halide perovskites is predominantly limited by the interaction between charge carriers and longitudinal optical (LO) phonons via the Fröhlich mechanism. The Fröhlich polaron model describes the formation of polarons—quasiparticles consisting of a charge carrier surrounded by a cloud of lattice polarisation—and provides a theoretical framework for calculating charge carrier mobility due to polaron scattering.

The strength of the electron-phonon interaction in the Fröhlich model is characterised by the Fröhlich coupling constant α, defined as:

$$\alpha = \frac{e^2}{\hbar}\left(\frac{1}{\varepsilon_\infty} - \frac{1}{\varepsilon_0}\right)\left(\frac{m^*}{2\hbar\omega_{\text{LO}}}\right)^{1/2}\frac{1}{(4\pi\epsilon_0)}, \tag{3.5}$$

where e is the elementary charge, $\hbar$ is the reduced Planck constant, ε_∞ and ε_0 are the high-frequency (electronic) and static (ionic) dielectric constants, respectively, m^* is the effective mass of the charge carrier (electron or hole), ω_{LO} is the LO phonon frequency, and ϵ_0 is the vacuum permittivity.

The charge carrier mobility μ at temperature T is calculated using the simplified expression derived from the Fröhlich polaron model, as derived in Ref. [8],

$$\mu = \frac{e\hbar}{m_e k_B T} \frac{0.052 \left(\frac{\hbar\omega_{\mathrm{LO}}}{k_B T}\right)^{3.3} + 0.34}{\alpha \left(\frac{m^*}{m_e}\right)}, \tag{3.6}$$

where m_e is the electron rest mass and k_B is the Boltzmann constant. This expression accounts for the temperature dependence and the polaronic effects on charge carrier mobility.

To compute the mobility, we determined the necessary parameters as follows:

Effective Mass (m^*) are calculated from the curvature of the quasiparticle bands obtained from Wannier-interpolated G_0W_0 calculations. The effective mass tensor is computed as $m^*_{ij} = \hbar^2 \left(\frac{\partial^2 E(\mathbf{k})}{\partial k_i \partial k_j}\right)^{-1}$.

The LO phonon frequency (ω_{LO}) is obtained from DFPT [160] calculations using VCA [68]. The highest energy LO phonon mode at the Γ point is considered, as it contributes most significantly to polaron scattering [8].

The high-frequency dielectric constant ε_∞ is calculated within the random-phase approximation (RPA) [99] using DFPT. The static dielectric constant ε_0 includes both electronic and ionic contributions and is obtained by summing over all phonon modes [8].

All calculations are performed for each composition x in the $\mathrm{CsPb(I_{1-x}Br_x)_3}$ series to account for the variation of these parameters with halide mixing.

The model derived in Ref. [8] assumes that charge transport is limited by scattering with

LO phonons (Fröhlich interaction), other scattering mechanisms (e.g., acoustic phonons, impurities, defects) are negligible, the band structure near the band edges is parabolic, and the effective masses are isotropic. The temperature dependence is captured through the Bose-Einstein distribution of phonons. While this model provides a good estimate of intrinsic charge carrier mobility, it is expected to overestimate mobility in real materials where additional scattering mechanisms are present [8].

The LO phonon modes and dielectric constants are extracted from DFPT-PBE calculations with VCA. The effective masses are extracted from Wannier interpolated G_0W_0 band structures with thermal correction. All parameters in the expression of charge-carrier mobility are calculated in this work, and reported in Table A.1.

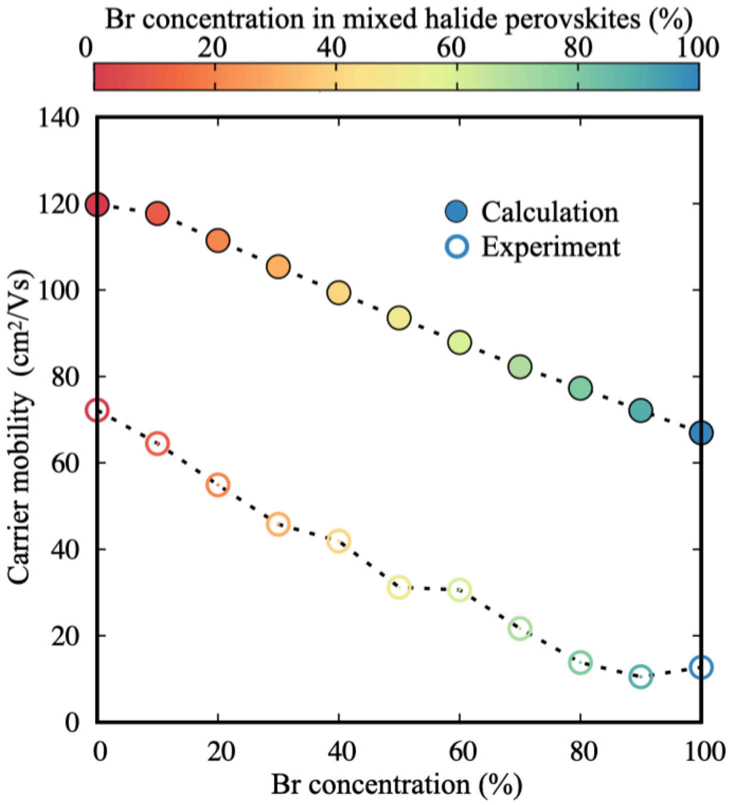

Figure 3.13: Electron-hole sum mobilities calculated using the model proposed by Ref. [8] (disks) and measured experimentally (empty disks). The dashed lines are guides to the eye. In all plots, the data point colours follow the concentration of Br, indicated by the colour bar.

Figure 3.13 presents a comparison between the computed and experimentally determined electron-hole sum mobilities across the I-Br mixed-halide series. The THz mobility measurements probe the material on a relatively short range (tens of nm), which is shorter than other methods [161]. Consequently, these measurements are more reflective of the intrinsic properties of the lattice and are less influenced by morphology and other artifacts, resulting in a smooth and clean experimental trend devoid of any bending or non-monotonic effects. The computed electron-hole sum mobilities consistently overestimate the experimental values by nearly a factor of two throughout the series, which can be attributed to the exclusion of scattering mechanisms beyond electron-phonon coupling with a single LO phonon (e.g., scattering with other phonons and/or defects) in our calculations [8]. Despite these discrepancies, the calculated charge-carrier mobilities exhibit the same trend and order of magnitude as those measured experimentally, further validating the assumption of a uniform distribution of halogen ions in these perovskites and corroborating that long-range electron-phonon interactions are the dominant factor governing charge-carrier transport in halide perovskites across this series, which is entirely consistent with previous studies of $MAPbI_3$ [8, 162].

3.9 Summary

In conclusion, we have presented a comprehensive theoretical study of the optoelectronic properties of mixed halide perovskites $CsPbX_3$ using state-of-the-art first principles techniques, including DFT, DFPT, and G_0W_0+BSE. The VCA has been successfully applied at different levels of theory, proving to be a reliable and promising approach for studying various properties of alloyed systems. By comparing our theoretical results with experimental measurements, we have demonstrated that the VCA can accurately reproduce the measured trends of both ground and excited state properties, such as lattice parameters, THz and UV-VIS optical absorption spectra, dielectric constants, quasiparticle band gaps, exciton binding energies, and charge-carrier mobilities.

Our results emphasise that the tunability achieved via chemical mixing for key quantities, such as band gaps or charge-carrier mobilities, is not due to spurious inhomogeneities in samples or disorder-induced effects, but is instead achieved by tuning the energetics of the halogen site and the unit cell volume via a uniform mixing of Br and I. Furthermore, our findings clearly delineate the ideal behaviour of mixed halide perovskites, providing a template against which phenomena such as degradation, halide segregation, structural disorder, or sample inhomogeneity may be easily identified by analysing trends in the properties discussed here.

The success of applying the VCA in conjunction with spin-orbit coupling and excitonic effects allows us to study more complex mixed-ion systems in future studies. Given the importance of homovalent alloyed perovskites in the continuous development of efficient photovoltaic devices, particularly in tandem cell architectures, the framework presented here can be used as a general and reliable approach to understand chemistry-property relationships in these complex systems.

4 | Tunable exciton delocalisation in layered perovskites

4.1 Introduction of layered perovskites

In the previous chapter, we demonstrate that the mixed halogen composition in hybrid halide perovskites have a direct influence on their electronic and optical properties. The investigations reveal that these properties follows a monotonic trend when linearly mixing Br and I. While the A-site cation is believed not to directly contribute to the states at the band edges, it indirectly influences the material's electronic properties by introducing structural steric effects such as tiltings and distortions in the inorganic octahedral network [130]; these yield a band gap tunability range of more than 300 meV, redshifting as the size of the cation increases [130, 133, 134].

Moreover, as the size of the A-site cation varies, the perovskites might undergo structural reconfiguration. In general, the formation of perovskite structure can often be estimated by the Goldschmidt tolerance factor, $t = (R_A + R_X) / \left[\sqrt{2}\,(R_B + R_X)\right]$, [163], in which R_A, R_B and R_X represent the effective radii of the A, B, and X site ions, respectively. For 3D perovskites, such as $MAPbI_3$, $FAPbI_3$, the tolerance factor typically ranges between 0.8 and 1 [164], where the cations are coordinated at the centre of the inorganic octahedra. When larger amine cations are incorporated into the structure, such as butylammonium (BA) and phenylethylammonium (PEA), typically resulting in $t > 1$, the inorganic octahedral network reorganises into 2D layers along different crystal planes, forming layered perovskites. The structural composition of layered perovskites is characterised by an alternating arrangement of inorganic layers, consisting of corner-sharing metal-halide octahedra, and large organic molecular cations [45], as shown in Figure 4.1.

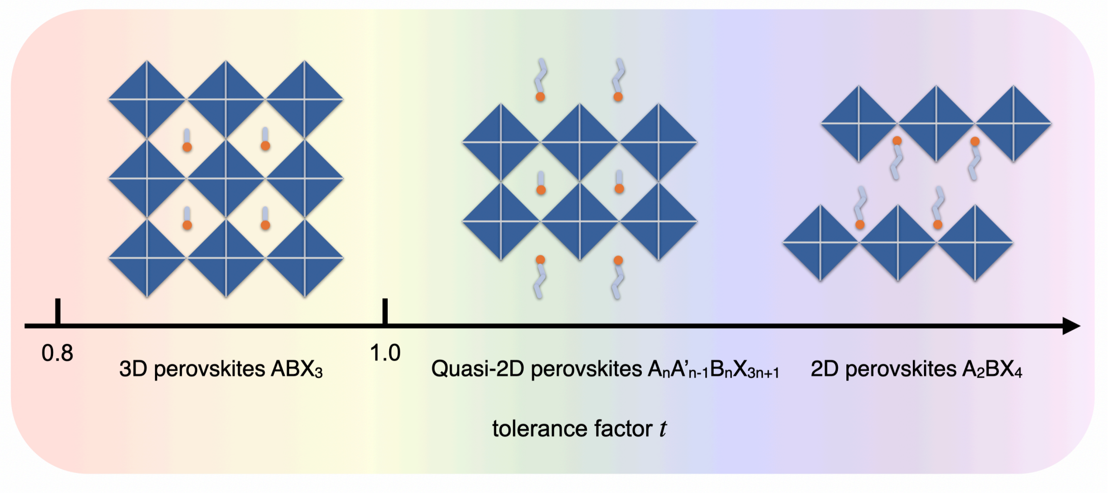

Figure 4.1: Schematic diagrams of perovskite structures: 3D, quasi-2D, and 2D configurations (left to right). The rainbow colour gradient illustrates the general trend in the band gap, transitioning from 3D to 2D perovskites, towards which band gap typically increases.

Layered organic-inorganic halide perovskites represent a structurally and chemically diverse class of functional semiconductors [42] exhibiting promising optoelectronic properties [43, 44, 49]. These materials have been demonstrated as promising stable alternatives to their 3D counterparts, with a wide range of applications in solar cells [43, 165–167], light-emitting diodes [42, 45, 168] photodetectors [169], photocatalysts [170], and lasers [171]. It is not only the increased chemical stability and extensive applications but also the more diverse and tunable optoelectronic properties that make this group of materials highly attractive for investigation.

As illustrated in Figure 4.2, the unique configuration of layered organic-inorganic halide perovskites gives rise to a diverse range of structural and chemical compositions. This versatility allows for the fine-tuning of various structural parameters, each of which can significantly influence the material's optoelectronic properties.

One key parameter that can be modulated is the interlayer distance D. This can be achieved by employing molecules with different alkylammonium chain lengths, effectively controlling the spacing between the inorganic layers. Filip et al. [46] demonstrated that interlayer organic cations in quasi-2D perovskites contribute significantly to the dielectric screening, countering quantum confinement effects on the quasiparticle band gap and the exciton binding energy. They proposed a simple electrostatics model inspired by parallel-plate capacitors to decouple the organic cation and inorganic layer contributions to the effective dielectric constants, showing that dielectric properties of layered perovskites are broadly tunable via the interlayer cation.

Additionally, the layer alignment can be adjusted and characterised by alignment coordinates (X, Y), which are defined in crystal coordinates and correspond to the in-plane projection of the vector connecting two closest Pb atoms from adjacent inorganic layers [172]. Marchenko et al. [172] introduced a quantitative layer shift factor for the classification and comparison of layered perovskite structures. They demonstrated correlations between the layer alignment and the band gap, revealing significant structure-property relationships. In this context, two specific alignments are of our particular interest: the Dion-Jacobson (DJ) alignment, denoted as (0,0), where adjacent layers are directly stacked on top of each other, and the Ruddlesden-Popper (RP) alignment, denoted as (0.5, 0.5), where adjacent layers are offset by half a unit cell in both in-plane directions. These alignments represent two extreme classifications in the spectrum of possible layer arrangements and often serve as reference points for understanding the structural and electronic properties of layered perovskites.

Another significant parameter is the number of layers n separated by large organic cations. This can be modified by different chemical composition of the layered perovskites [173]. Li et al. [173] presented a series of 2D Dion-Jacobson halide perovskites, and found that the band gap decreases when increasing the number of layers n separated by the organic spacers.

In the rightmost panel of Figure 4.2, we schematically depict how octahedral tilting can be modulated as a tunable structural parameter. Octahedral tilting is reflected in bond angle changes within the inorganic framework. Prasanna et al. [174] identified two competing mechanisms through which the A-site cation influences the band gap of 3D metal halide perovskites. They found that using a smaller A-site cation can distort the perovskite lattice either by tilting the MX_6 octahedra or by contracting the lattice isotropically. They report these effects have opposite impacts on the band gap: octahedral tilting tends to increase the band gap, while lattice contraction tends to decrease it. This understanding provides a strategy to systematically tune the band gap and band positions of metal halide perovskites through the control of the cation composition. Filip et al. [130] demonstrated a strong correlation between the optical band gap and the largest metal-halide-metal bond angle in metal-halide perovskites. Their work showed that this simple structural descriptor could be used to predict and tune the optical gap from the mid-infrared to the visible range. They proposed that precise band gap engineering could be achieved by controlling these bond angles through the steric size of the molecular cation. Krach et al. [175] investigated the effect of octahedral tilting distortions on various properties of all-inorganic $Cs_{n+1}Pb_nX_{3n+1}$ RP perovskites. They found that, unlike in 3D perovskites, polar structures may arise from a combination of octahedral tilts in these layered systems. Moreover, they demonstrated that Rashba/Dresselhaus splitting in these materials is determined by the direction and Pb-I orbital contribution of the polar distortion mode. Their work provides design rules for tuning structural distortions and band-structure properties in all-inorganic RP perovskites through the interplay of the amplitude, direction, and chemical character of the antiferrodistortive distortion modes contributing to each octahedral tilt pattern.

These structural parameters - layer distance, alignment, layer thickness, and octahedral tilting - provide a rich toolset for tuning the properties of layered perovskites. By carefully controlling these parameters, researchers can potentially engineer materials with desired optoelectronic characteristics for specific applications. This structural versatility, combined with the diverse range of possible chemical compositions, underpins the immense potential of layered organic-inorganic halide perovskites as functional materials for optoelectronic devices, as evidenced by the promising solar cell performances achieved with these materials [173].

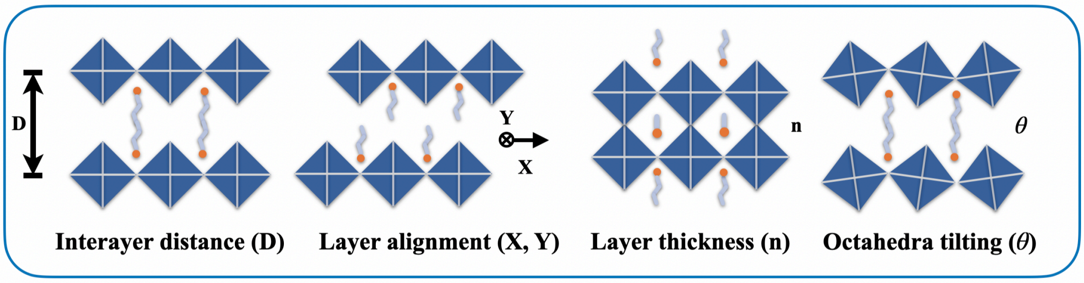

Figure 4.2: A schematic diagram of different tunable structural features in layered perovskites, including (from left to right) interlayer distance D, layer alignment represented by alignment coordinates (X,Y), layer thickness n and octahedral tilting represented by bond angles.

4.2 Excitons in layered perovskites

Despite being formally classified as bulk 3D materials, the alternating inorganic and organic layers in layered perovskites are thought to induce quasi-2D behaviour in their electronic and optical properties, potentially resulting in unique phenomena not observed in their 3D counterparts [44, 52].

As previously discussed in Chapter 1, the interlayer charge transfer excitons has been the centre of the low-dimensional materials, especially for TMDCs, both for bulk structures and for multi-layer heterostructures [176–178]. In TMDCs, interlayer electronic coupling and charge transfer are significant due to the relatively small interlayer distances and the absence of large organic spacers between the layers. This allows for efficient interlayer interactions and the formation of interlayer excitons. In contrast, it has been generally accepted that interlayer electronic coupling and charge transfer are suppressed in layered hybrid halide perovskites [47, 48, 179]. The layered structure of large organic spacers in perovskites introduces strong dielectric and quantum confinement effects and suppresses the electronic coupling between the layers [180]. Photo-excited electron-hole pairs (excitons) are strongly bound and localised within the inorganic layer due to these confinement effects in some layered perovskites [46, 60]. However, recent experimental findings have challenged this conventional understanding. Several studies have reported evidence suggesting the possibility of interlayer exciton transport [56], interlayer exciton delocalisation [57], and the existence of charge transfer excitons [58] in bulk layered perovskite systems. These phenomena have attracted significant attention for their potential applications in various applications in solar cell, light emitting diodes, photo detectors and photocatalysts [56–58, 181, 182].

The emergence of these new findings necessitates a comprehensive re-evaluation of our understanding of how the localisation of excitons in layered organic-inorganic halide perovskites can be tuned through the exploration of the diverse chemical and structural heterogeneity of this family of materials.

The correlation of photo-excited electron-hole pairs localised in spatially separated layers is partly facilitated by the coupling of single-particle wave functions from neighbouring layers [55]. It is also associated with a type-II energy band alignment in heterostructures [53, 183], and/or with spin-valley locking resulting from broken inversion symmetry [177]. Similar phenomena have been extensively studied in low-dimensional van der Waals systems, particularly those based on TMDCs, where long-lived excitons delocalised across different layers have been observed [53, 184, 185].

However, the mechanism of interlayer electronic coupling in layered perovskites remains unclear, given that organic molecules can separate metal-halide layers by considerable distances, sometimes exceeding a nanometre [186]. In this chapter, we present a detailed first-principles study of the spatial delocalisation of excitons in bulk layered perovskites. We employ state-of-the-art methodological frameworks, including the GW approximation [70] and the BSE [71, 72], which have been successfully applied to understand the photophysics of heterogeneous systems, including TMDCs [176, 187] and metal halide perovskites [6, 130, 149, 156, 188, 189].

Our study focuses on lead-iodide layered perovskites with planar inorganic layers that are one octahedron thick, where quantum confinement effects are most pronounced [190]. We propose key structural features of layered perovskites that serve as primary descriptors for the distribution of photo-excited electron-hole pairs across these materials. Furthermore, we quantify the tunability of interlayer exciton delocalisation through the control of the distance and alignment of the inorganic layers via modulating organic molecular spacers.

By visualising the two-particle exciton wave function computed as a solution of the BSE, we reveal the spatial delocalisation of excitons in these complex materials systems. We also estimate the average electron-hole separation corresponding to particular excited states, providing a quantitative assessment of the real-space extent of the exciton wave function.

Through this comprehensive analysis, we also aim to rationalise the physical mechanism for interlayer exciton delocalisation based on the orbital decomposition of band edge states. Our findings not only contribute to the fundamental understanding of these materials but also provide crucial insights for tuning the properties of perovskite materials for specific applications in optoelectronic devices.

4.3 Band gap trend

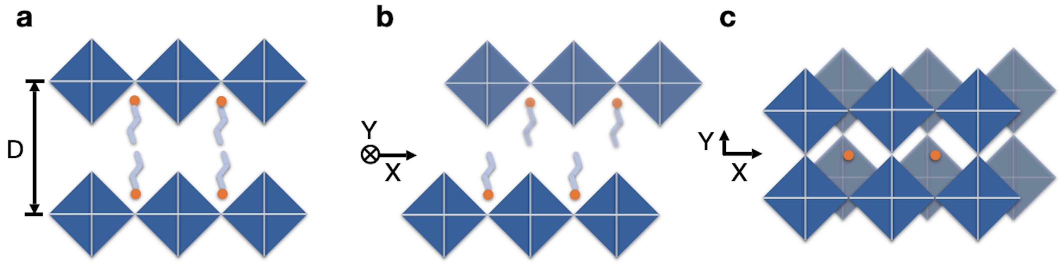

Figure 4.3: Schematic representation of Dion-Jacobson (a) and Ruddlesden-Popper (b) viewed along the inorganic layer, and an intermediate phase (c) along the direction perpendicular to the inorganic layer. The interlayer distance D and the alignment coordinates (X, Y) are represented on the figures a-c. Alignment coordinates X and Y are defined in crystal coordinates and correspond to the in-plane projection of the vector connecting two closest Pb atoms from adjacent inorganic layers.

In this section, we present our findings on how the structural parameters of layered perovskites influence their electronic properties, specifically on the fundamental band gaps. Our investigation centres on two key structural features: the interlayer distance (D) and the alignment between adjacent layers, characterised by coordinates (X, Y), as illustrated in Figures 4.3.

To systematically study these effects, we artificially constructed a series of model layered perovskite structures with undistorted PbI_6 octahedra. In these models the organic cations are replaced by Cs to reduce computational complexity while maintaining the essential structural characteristics. We manually constrained these structures to specific interlayer distances and layer alignments without structural relaxation (details of model construction are provided in Appendix A.2.1). Such simplified model systems have been successfully employed and proven previously [46, 60, 190, 191] to capture the primary trends in the photophysics of layered perovskites at a significantly reduced computational cost.

We then employed DFT [79, 91] and the GW approximation [70, 76, 192] to compute their electronic structure (computational details and convergence tests can be found in Appendix A.2.2).

Figure 4.4 presents the computed band gaps within DFT using the generalised gradient approximation and including spin-orbit coupling (DFT-PBE+SOC) for various layer alignments. The map spans from the DJ phase [9, 44] with alignment (0,0) to the RP phase [49, 193, 194] with alignment (0.5, 0.5). We observe a consistent blue shift in the band gap as the alignment transitions from DJ towards RP, aligning with previous DFT studies in the literature [172].

To further explore the impact of interlayer distance, we compute G_0W_0 quasiparticle band gaps for a subset of structures with varying interlayer distances (Figure 4.5b). The results reveal a strong dependence of quasiparticle band gaps on both interlayer distance and alignment, with values of 0.3 and 1.0 eV for RP and DJ perovskites, respectively. This trend is also observed in standard DFT-PBE calculations as seen in Figure 4.5a,

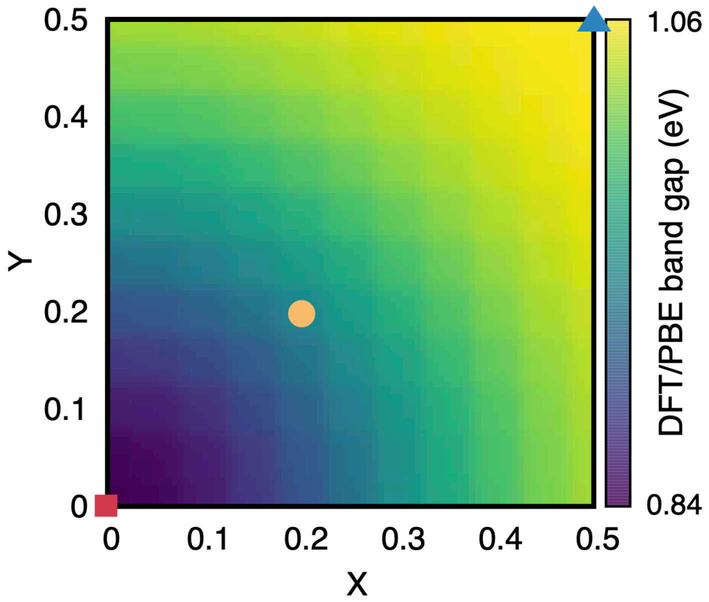

Figure 4.4: DFT-PBE band gaps for model layered perovskites with an interlayer distance of 11 Å, as a function of the alignment coordinates X and Y.

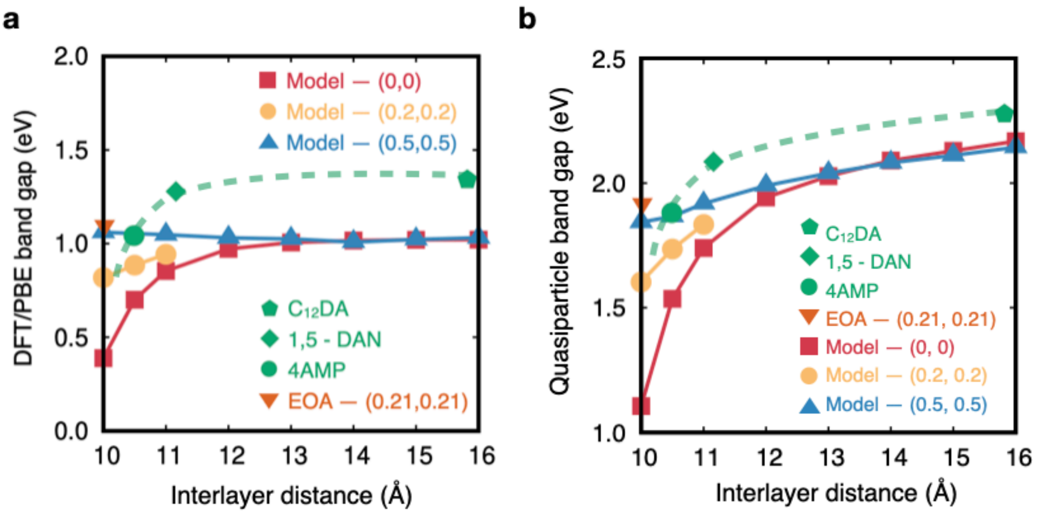

Figure 4.5: (a) DFT and (b) quasiparticle band gaps of layered perovskites as a function of interlayer distance for different layer alignments. Green data points with different shapes correspond to experimental structures in the DJ alignment, and the orange triangle corresponds to an experimental structure with intermediate $(0.21, 0.21)$ alignment. Green dashed lines are guides to the eye for the experimental DJ structures.

indicating that these variations are primarily driven by changes in the crystal structure geometry.

Notably, at large interlayer distances, DJ and RP perovskites exhibit nearly identical band gaps, consistent with the expectation that the system approaches the monolayer limit as the amount of vacuum between layers increases. An intermediate layer alignment of $(0.2, 0.2)$ yields a similar quasiparticle band gap trend, as indicated in the yellow line.

To validate these trends, we compute quasiparticle band gaps for four experimentally realised layered perovskite structures (as shown in Figure 4.6): (4AMP)PbI_4 (4AMP = 4-aminomethyl piperidinium) [9], (C_{12}DA)PbI_4 (C12DA = 1,12-dodecane diammonium) [10], (1,5-DAN)PbI_4 (1,5-DAN = naphthalene-1,5-diamine) [10], and (EOA)PbI_4 (EOA = ethanolammonium) [11]. These structures sample DJ alignments with interlayer distances of 10.5, 11.2, and 15.8 Å, and an intermediate alignment $(0.21, 0.21)$ with an interlayer distance of 10.0 Å, respectively. The experimental and model structures demonstrate consistent trends, with quasiparticle band gaps of experimental structures slightly larger than those of the models.

We attribute the agreement with band gaps computed for the models to a cancellation of errors originating from the absence of both octahedral tilting and organic cations in the model structures. Octahedra tilting is expected to red-shift quasiparticle band gaps by more than 0.5 eV [35,46], while the absence of organic cations has been shown to blue-shift quasiparticle band gaps by more than 0.3 eV due to an underestimation of dielectric screening [46,195]. Despite these subtleties, the excellent agreement between band gap trends computed for model and experimental structures confirms that our calculations on model layered perovskites capture the principal physical trends. This validation supports the use of these models for further systematic exploration of excited state properties in layered perovskites.

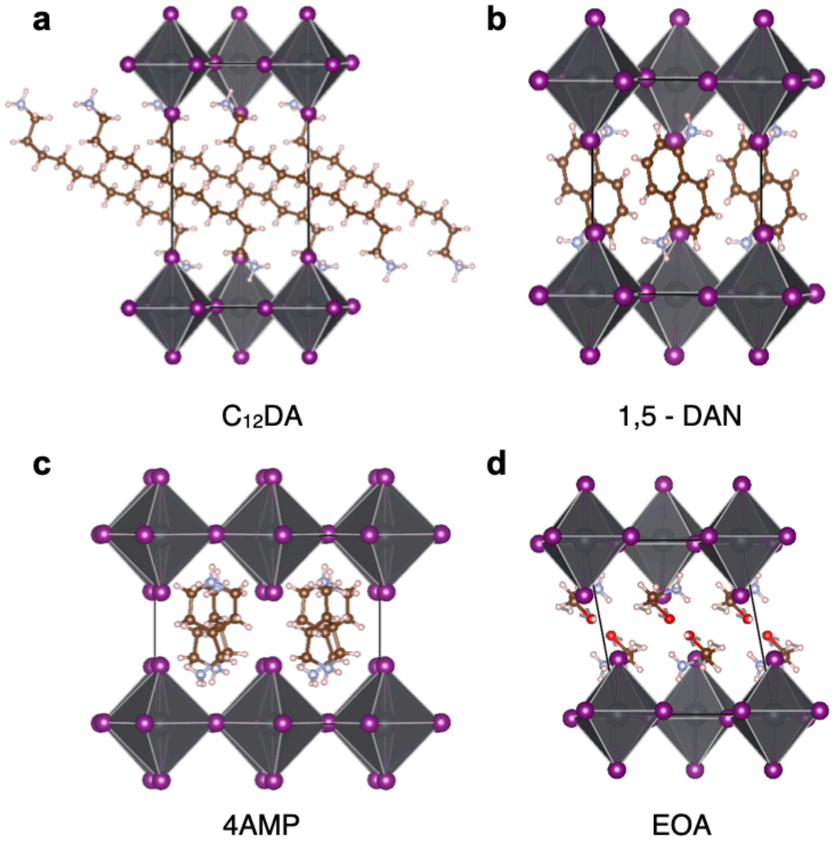

Figure 4.6: Crystal structures of experimentally realised layered perovskites with different interlayer disntances and alignments. (a) (4AMP)PbI_4 where 4AMP = 4-aminomethyl piperidinium, (b) (C_{12}DA)PbI_4 where C_{12}DA = 1,12-dodecane diammonium, (c) (1,5-DAN)PbI_4 where 1,5-DAN = naphthalene-1,5-diamine, and (d) (EOA)PbI_4 where EOA = ethanolammonium. Atoms are colour coded as follows: Pb - grey, I - purple, C - brown, N - light blue, O - red, H - pink.

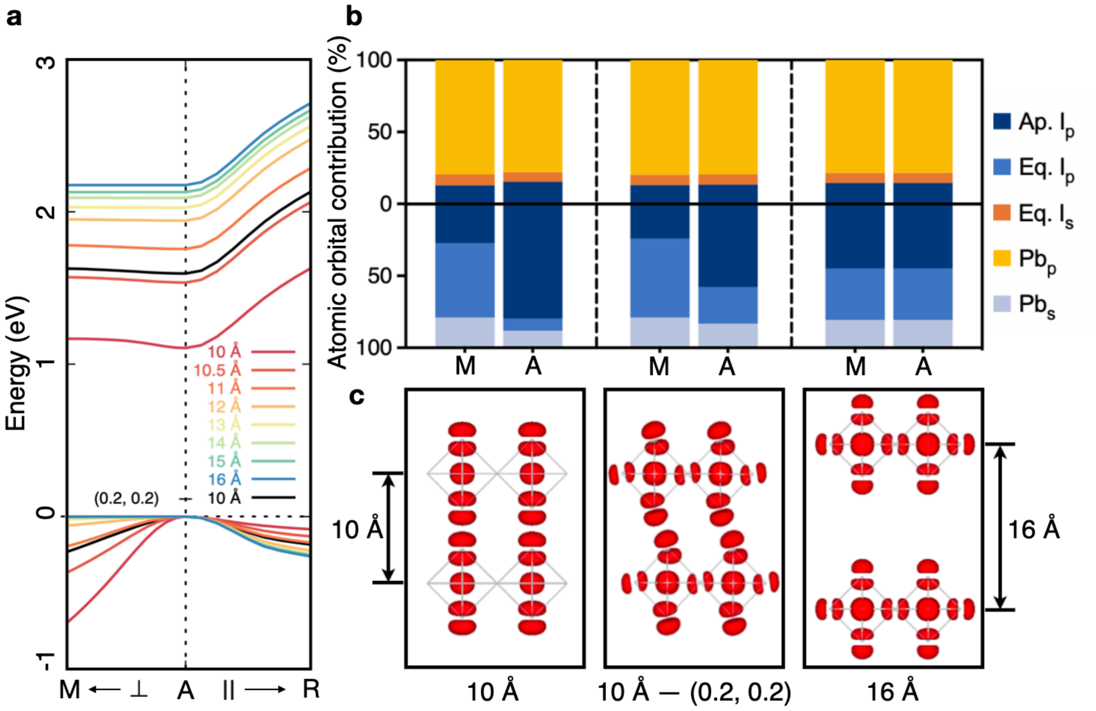

Figure 4.7: (a) Quasiparticle band structures calculated from G_0W_0@PBE+SOC for DJ model perovskites with interlayer distances from 10 Å to 16 Å and for one intermediate model with alignment (0.2, 0.2) and an interlayer distance of 10 Å. (b) Atomic orbital contribution for the VBT (bottom half) and CBB (top half) of DJ model perovskites with interlayer distances of 10 Å and 16 Å (left and right, respectively), and one intermediate model with alignment (0.2, 0.2) and an interlayer distance of 10 Å (middle). (c) Squared modulus of the electron wave function corresponding to the VBT at high symmetry point A for DJ layered perovskites with interlayer distances of 10 Å and 16 Å (left and right, respectively) and an intermediate model with alignment (0.2, 0.2) and an interlayer distance of 10 Å (middle).

To elucidate the band gap trends observed in Figure 4.5, we conducted an in-depth analysis of the quasiparticle band structures for model perovskites. Our focus was on structures with DJ alignment and varying interlayer distances, as well as one with intermediate alignment (0.2, 0.2) and an interlayer distance of 10 Å (Figure 4.7a). Extended band structures for representative models are shown below in Figure 4.8.

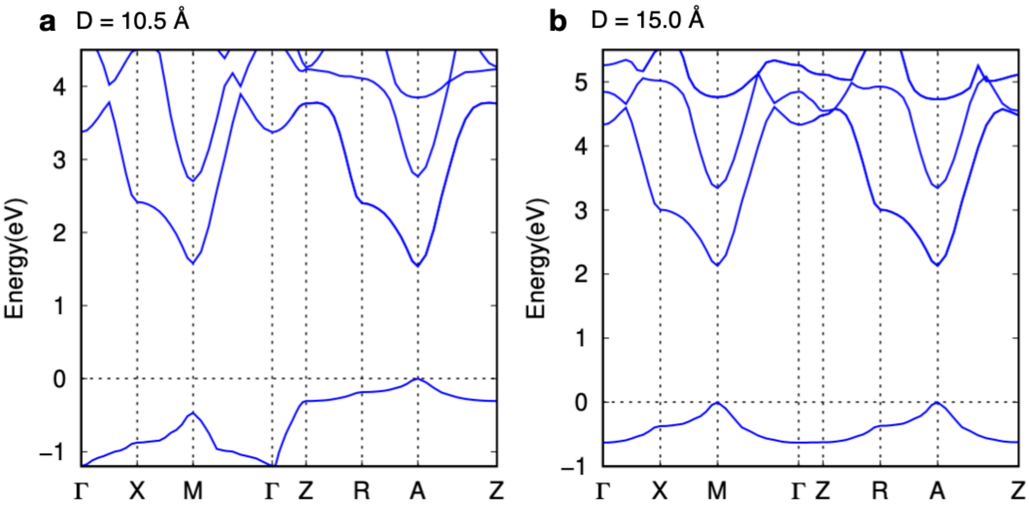

Figure 4.8: Quasiparticle band structures of model DJ structures with interlayer distances of 10.5 Å (a) and 15.0 Å (b).

Our analysis reveals several key observations. Firstly, we note a red-shift in the quasiparticle band gap as the interlayer distance decreases, consistent with our earlier findings. Additionally, we observe an increase in the dispersion of the valence band edge along the high-symmetry direction A [(0.5, 0.5, 0.5)] - M [(0.5, 0.5, 0)], which corresponds to the direction perpendicular to the inorganic layer in real space. Interestingly, the direction A - R [(0, 0.5, 0.5)], parallel to the inorganic layer in real space, displays the opposite trend. The conduction band edge exhibits a similar, albeit more gradual, change in band curvature along the A - M direction, while remaining unaffected along the A - R direction, regardless of interlayer distance or alignment.

To understand these trends, we analyse the orbital contributions at the conduction and valence band edges (Figures 4.7 b and c). The electronic wave function corresponding to the valence band top (VBT) undergoes renormalisation as the distance between inorganic layers decreases. At large interlayer distances and in RP models, the VBT is degenerate at the A and M points, with a predominant I-p character and nearly equal contributions from apical (out-of-plane) and equatorial (in-plane) I-p orbitals. As the interlayer distance decreases and the alignment approaches DJ, we observe a splitting of the A/M degeneracy. The VBT at the A-point becomes dominated by contributions from apical I-p orbitals. This leads to increased overlap of adjacent out-of-plane I-p orbitals along the direction perpendicular to the inorganic layer, resulting in more dispersive electronic bands along the corresponding reciprocal space path.

These trends are consistent with previous reports of band structures in similar layered perovskites [172]. They suggest that by carefully tuning the interlayer distance and alignment, it is possible to induce interlayer electronic coupling in otherwise quantum-confined layered perovskites.

To further validate our findings, we compute quasiparticle band structures for selected experimental structures, as shown in Figure 4.9. These results closely mirror the trends observed in our model systems. For instance, the (4AMP)PbI_4 structure, which has the smallest interlayer distance (10.5 Å) among the DJ-aligned perovskites studied, exhibits the most dispersive bands along the interlayer direction (Y_2 to Γ). In contrast, the (C_{12}DA)PbI_4 structure, with the largest interlayer distance of 15.8 Å, shows nearly flat bands along this same direction. The (EOA)PbI_4 structure, which has an intermediate alignment of (0.21, 0.21) and an interlayer distance of 10.0 Å, and the (1,5-DAN)PbI_4 structure with an interlayer distance of 11.2 Å, both display intermediate levels of band dispersion along the perpendicular direction. These results from experimental structures corroborate our conclusion that interlayer distance and alignment are indeed the primary geometric parameters facilitating interlayer electronic coupling in layered perovskites, with octahedral distortions and tilting playing a secondary role. These observations also align with the charge carrier effective masses calculated, as shown in Table 4.1.

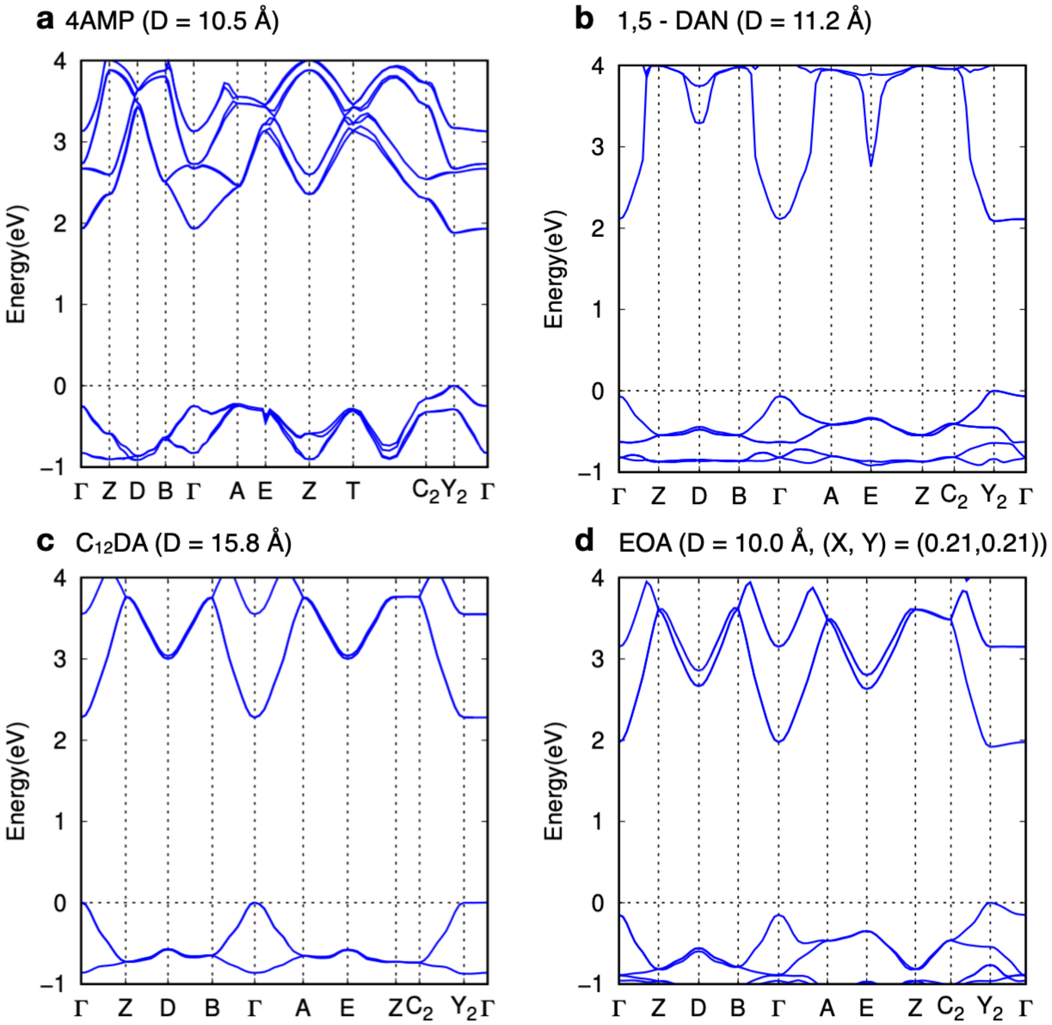

Figure 4.9: Quasiparticle band structures for experimental structures (a) (4AMP)PbI_4 [9], (b) (1,5 - DAN)PbI_4 [10], (c) (C_{12}DA)PbI_4 [10] and (d) (EOA)PbI_4 [11], featuring different interlayer distances and different layer alignment.

System	D(Å)	**Valence (m_h)**		**Conduction (m_e)**	
		$\perp$	$\|\|$	$\perp$	$\|\|$
DJ - Models	10	0.10	0.41	0.33	0.13
	10.5	0.21	0.38	1.14	0.13
	11	0.42	0.33	2.54	0.13
	12	1.38	0.28	8.12	0.13
	13	4.03	0.27	24.69	0.13
	14	14.48	0.26	50.33	0.13
	15	44.45	0.26	155.78	0.13
	16	45.66	0.26	8950.98	0.13
4AMP	10.5	0.32	0.43	1.43	0.19
1,5 - DAN	11.2	1.31	0.36	2.64	0.20
C$_{12}$DA	15.8	16.51	0.26	81.42	0.20
EOA (intermediate)	10.0	0.59	0.29	1.73	0.16

Table 4.1: Calculated G_0W_0 electron and hole effective masses, along directions perpendicular ($\perp$) and parallel ($||$) to the perovskite planes, in unit of electron rest mass m_0, as a function of interlayer distances D, for DJ models and experimental structures.

4.4 Optical properties

The linear optical absorption spectra computed within the GW+BSE framework for model layered perovskites, as shown in Figures 4.10(a,b), 4.11 and 4.12, reveal several intriguing features. Across all examined structures, we observe the emergence of a sharp peak at the onset of absorption, indicative of a bound exciton. This distinctive peak is followed by a flat plateau and a subsequent sharp rise associated with the second lowest direct optical transition.

Notably, for structures with a small interlayer distances and nearly-DJ layer alignment, we observe a red-shift in the absorption onset. Furthermore, these structures exhibit enhanced absorption of light polarised perpendicularly to the inorganic layers, while simultaneously showing suppressed absorption of light polarised along the inorganic layers, as show in Figure 4.10, 4.11 and 4.12. This observation aligns well with the renormalisation of the valence band top (VBT) orbitals that occurs when the inorganic layers are brought into close proximity.

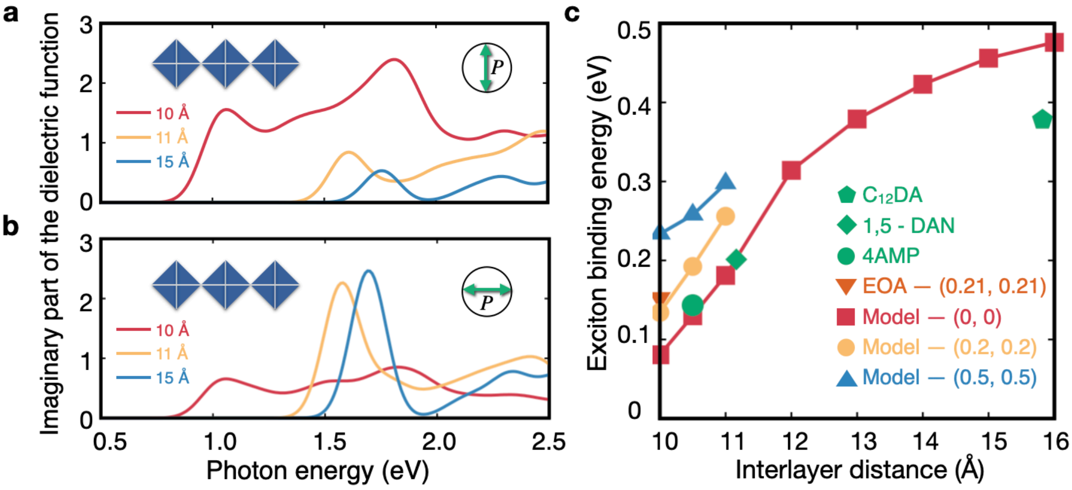

Figure 4.10: (a,b) Calculated imaginary part of the dielectric function for light polarisation perpendicular to the inorganic layer (a) and parallel to the inorganic layer (b) for layered perovskites with interlayer distances of 10 Å (red), 11 Å (yellow) and 15 Å (blue); (c) Exciton binding energies computed from G_0W_0+BSE as a function of interlayer distance and layer alignment. The legend follows the same convention as in Figure 4.5.

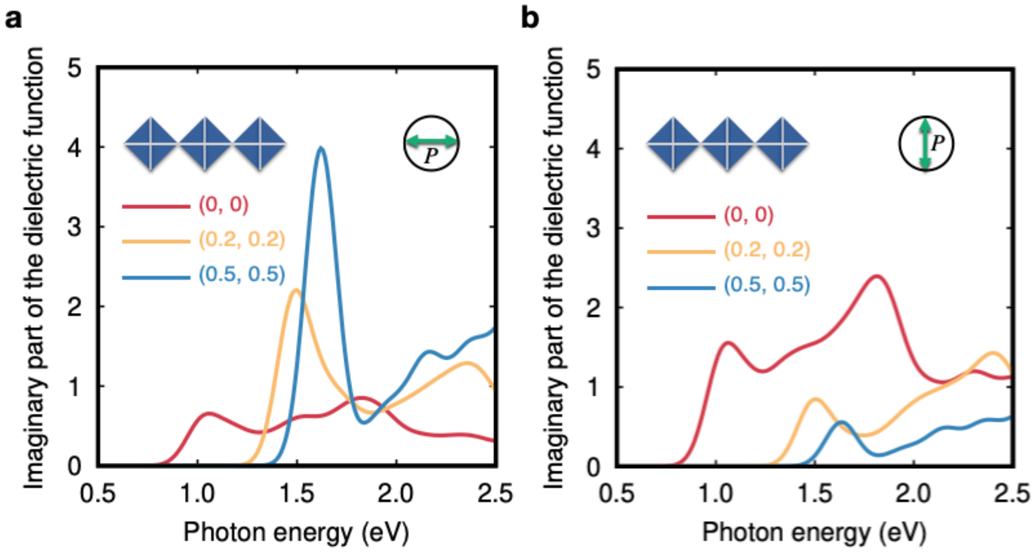

Figure 4.11: Calculated imaginary part of the dielectric function with light polarisation parallel to the inorganic layer (a) and perpendicular to the inorganic layer (b) for model structures with different layer alignment at a fixed interlayer distances of 10 Å.

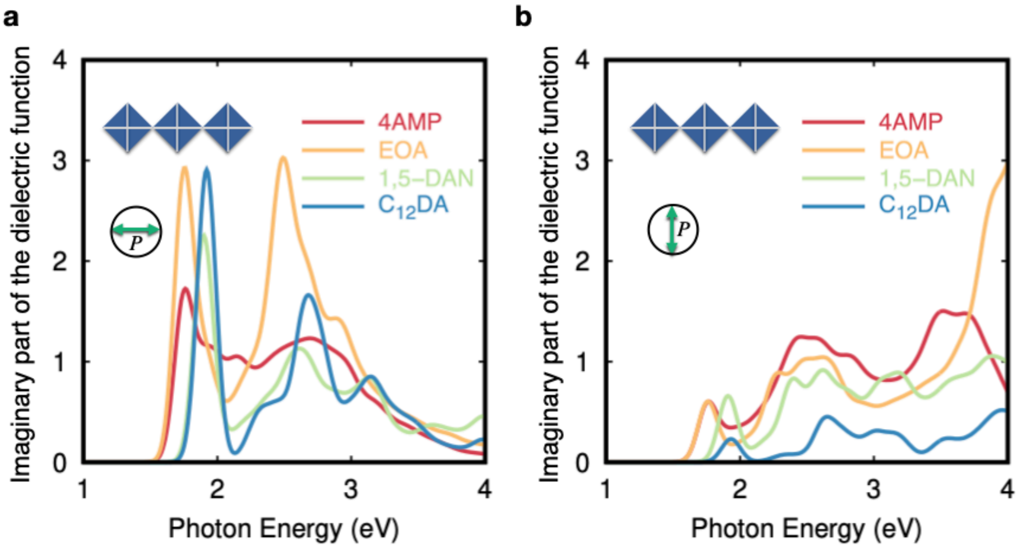

Figure 4.12: Calculated imaginary part of the dielectric function with light polarisation parallel to the inorganic layer (a) and perpendicular to the inorganic layer (b) for four representative experimental structures as described in the main text.

As the interlayer distance decreases, we note that the signature excitonic peak shifts closer to the 'continuum' part of the spectrum. This shift suggests a potential decrease in exciton binding energy as the inorganic layers come into closer proximity. To verify this hypothesis, we conducted explicit calculations, the results of which are presented in Figure 4.10(c).

Our calculations confirm that the exciton binding energy indeed decreases with decreasing interlayer distance. Interestingly, the range of exciton binding energies spanned for interlayer distances between 10 Å and 16 Å is most pronounced for DJ alignments. Moreover, the exciton binding energies computed for experimental crystal structures closely align with our calculations for model systems, as shown in Figure 4.10(c).

These findings consistently support our earlier assumption that the interlayer distance and alignment are the primary parameters driving these trends in layered perovskites. The observed changes in optical properties and exciton binding energies provide valuable insights into the electronic structure and excitonic behaviour of these materials, highlighting the potential for tuning their excited states properties through careful control of structural parameters.

4.5 Tunable exciton delocalisation

Building upon our previous findings on the influence of interlayer distance and alignment on electronic structure and optical properties, we now turn our attention to the spatial characteristics of excitons in layered perovskites. The exciton binding energy, which we found to be tunable through structural parameters, is generally correlated with the average real-space separation between photo-excited electrons and holes in isotropic materials. The exciton binding energy increases as the average electron-hole separation decreases, indicating that layered perovskites with reduced interlayer distances may exhibit more delocalised excitons.

With this hypothesis, we analyse the two-particle exciton wave function, $\Psi\left(r_e, r_h\right)$, corresponding to the lowest (non-degenerate) bound state. Visualisation of the probability of localisation for a photo-excited electron with a fixed hole position (shown in Figures 4.13) reveals striking differences between structures with different interlayer distances. For larger interlayer distances (16 Å), photo-excited electrons are strongly confined within a single inorganic layer, consistent with previous studies. In contrast, structures with smaller interlayer distances (10.5 Å) show a non-trivial probability of electron localisation extending across the first and second nearest neighboring layers.

To quantitatively assess exciton delocalisation, we employ the ECF, introduced in Ref. [121], and defined as follows,

$$\mathcal{F}(r) = \frac{\int_\Omega \left|\Psi\left(r_e = r + r_h, r_h\right)\right|^2 dr_h}{\int_\Omega \int_{\Omega_{\mathrm{uc}}} \left|\Psi\left(r_e, r_h\right)\right|^2 dr_e dr_h}, \tag{4.1}$$

where $r = r_e - r_h$ and Ω_{uc} and Ω are the volumes of the perovskite unit cell and a supercell large enough to contain the full extent of the exciton, respectively. The ECF

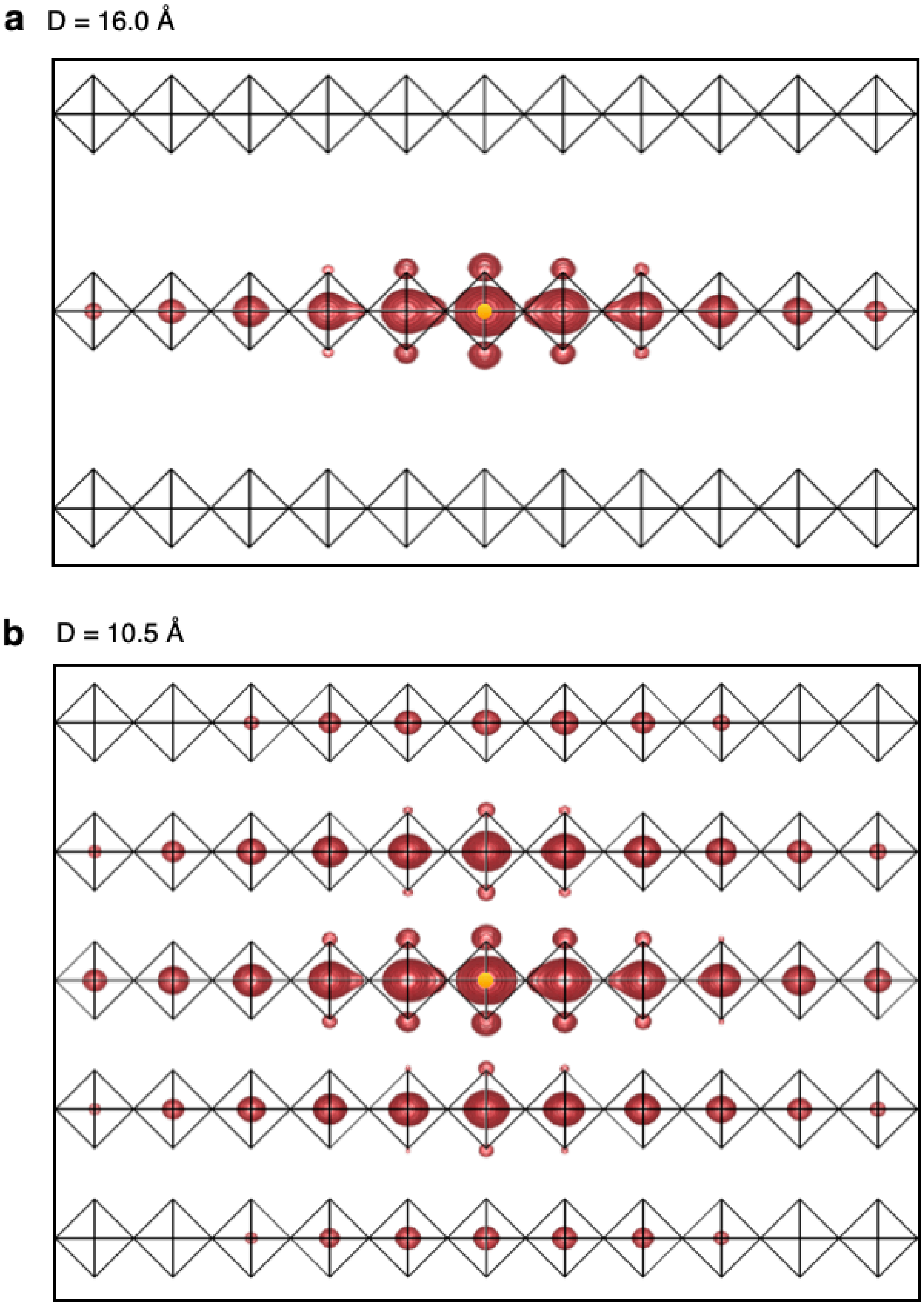

Figure 4.13: Isosurfaces representing the out-of-plane and in-plane spatial distribution of the lowest energy exciton for a model DJ with an interlayer distance of 16 Å (a) and 10.5 Å (b); the hole position is fixed at the center Pb atom of the central layer, marked by the yellow points.

represents the probability that the electron and hole in a specific state are separated by a vector r [121, 196]. This approach offers a more robust analysis, which is independent of the arbitrary choice of hole positions, in contrast with the qualitative pictures shown in Figure 4.13a and b. By doing that, we are able to focus on the quantitative trend on how the extent of exciton varies with structural parameters.

In our analysis, we focused primarily on the lowest energy excitonic state, which is the first in a group of four lowest energy excited states. These states arise from the spin-degenerate valence band top and conduction band bottom, as also discussed in Ref. [46]. It is important to note that this lowest energy state is optically inactive. We chose to analyse this state specifically because it is non-degenerate, making it less computationally demanding to study in detail.

To ensure the robustness of our conclusions, we examined whether our choice of focusing on the lowest energy state might have biased our results. To this end, we compared the ECF profiles for all four lowest energy states in two DJ model structures with different interlayer distances. As shown in Figure 4.14, the ECF displays remarkably similar profiles across all four states for both structures along both in plane and interlayer directions.

Furthermore, we quantified the average electron-hole separation for these four states in both the in-plane and interlayer directions. The results, presented in Table 4.2, demonstrate that the variation in average separation is minimal. Specifically, the in-plane separation varies within a range of 2.2 Å, while the interlayer separation varies within 1.6 Å across the four states.

As shown in Figures 4.15, 4.16 and 4.17, the in-plane ECF shows a wider extent for smaller interlayer distances and alignment coordinates, indicating greater in-plane delocalisation. While the out-of-plane $\mathrm{ECF}_{\perp}$ of all structures exhibit a narrow peak centred around 3.1 Å, (indicating that bound electron-hole pairs in these states have the highest

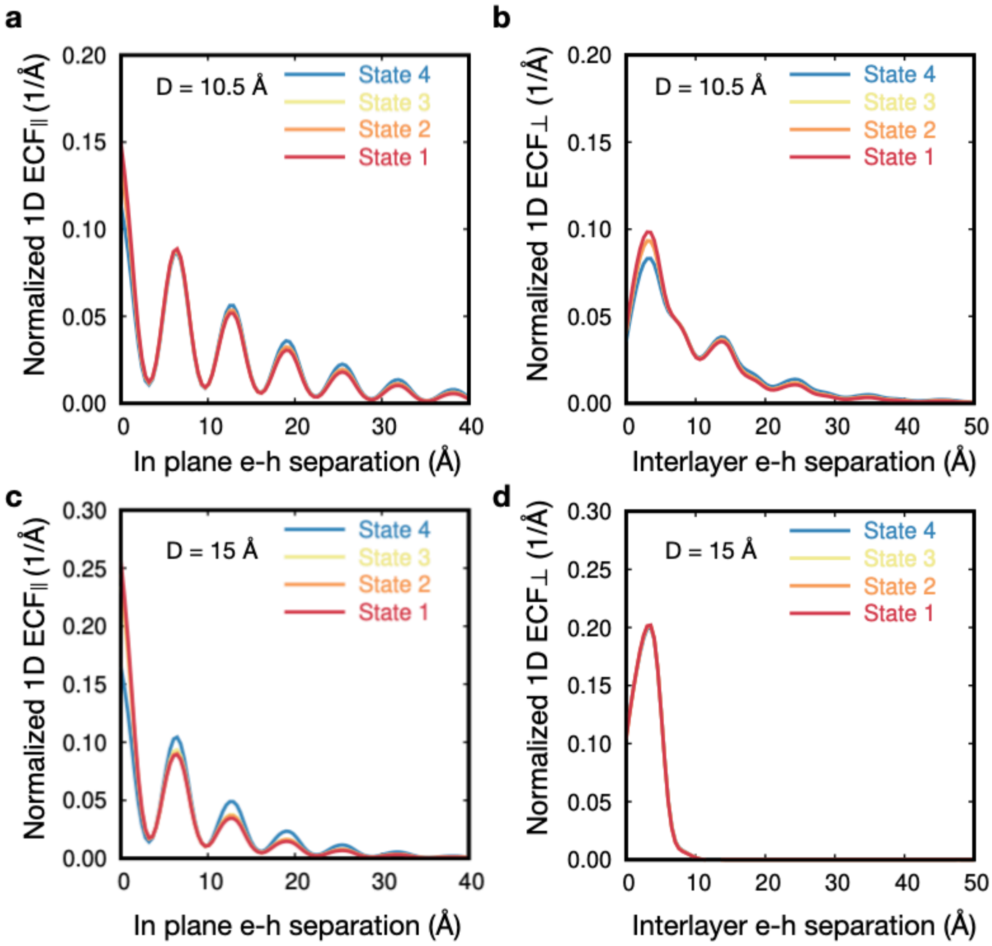

Figure 4.14: Comparison of the normalised 1D ECF for different excited states of 2 representative DJ model structures. (a) shows the ECF along the in-plane direction for D = 10.5 Å, while (b) represents the ECF along the out-of-plane direction. (c) and (d) show the ECF along in-plane and out-of-plane direction, respectively, for D = 15 Å.

D	States	Interlayer e-h sep.	In-plane e-h sep.	E_b (meV)
10.5 Å	1	9.3 Å	10.6 Å	130
	2	9.8 Å	11.0 Å	124
	3	9.8 Å	11.0 Å	124
	4	10.9 Å	12.0 Å	112
15 Å	1	3.1 Å	6.5 Å	456
	2	3.1 Å	6.8 Å	435
	3	3.1 Å	6.8 Å	435
	4	3.1 Å	8.7 Å	371

Table 4.2: Calculated average electron-hole separation along the in-plane and interlayer directions for the first 4 excited states of two model DJ structures with interlayer distances of 10.5 Å and 15 Å, together with their exciton binding energies.

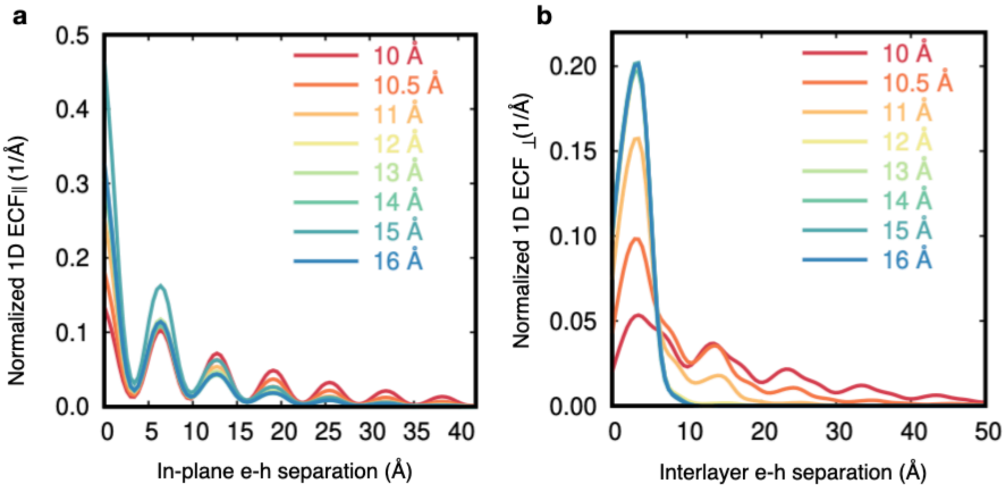

Figure 4.15: Normalised 1D ECF versus electron-hole relative position in-plane (a) and across layers (b), for DJ model structures with interlayer distances from 10 to 16 Å.

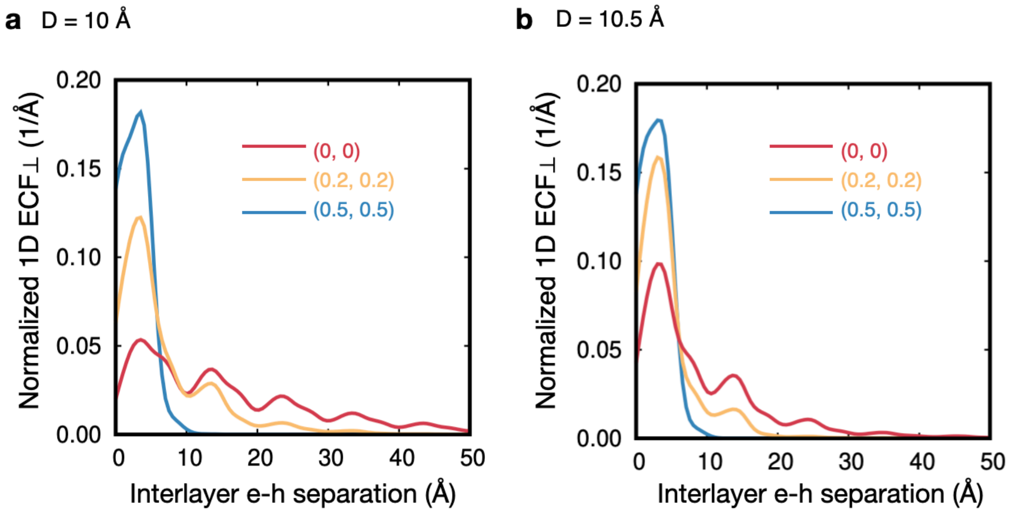

Figure 4.16: Normalised 1D ECF along the out-of-plane direction, for DJ model structures with different layer alignment and interlayer distances of 10 Å (a) and 10.5 Å (b).

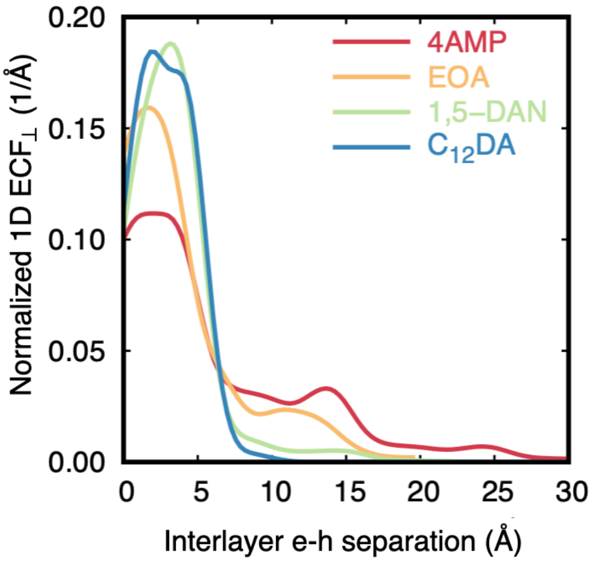

Figure 4.17: Normalised 1D ECF along the out-of-plane direction for 4 representative experimental structures as described in the main text.

probability to be 3.1 Å apart, approximately the width of a Pb-I bond length, or half the width of one inorganic layer), the probability density distribution changes markedly with interlayer distance and alignment. For structures with large interlayer distances or RP alignment, this peak reaches a maximum probability density of nearly 20% per Å. However, for DJ-aligned structures with 10 Å interlayer distance, the maximum probability density of this peak drops to 5% per Å or less. Additionally, for these DJ-aligned structures, we observe multiple equally spaced peaks at larger electron-hole distances, indicating a substantial interlayer delocalisation of the exciton wave function across several neighbouring layers.

We quantify the average in-plane and interlayer electron-hole separation for various model and experimental structures (Figure 4.18bd) as discussed in Chapter 2. For DJ-aligned perovskites, this separation decreases from over 16 Å out-of-plane and 14 Å in-plane (delocalised exciton) to approximately 3 Å out-of-plane and in-plane (localised exciton) as the interlayer distance increases from 10 Å to 12 Å. Intermediate-aligned perovskites show a similar but more gradual trend. Beyond 12 Å, the average separation remains roughly constant. Notably, RP-aligned structures consistently show intralayer confinement regardless of interlayer distance. The observed trends in exciton delocalisation align well with our earlier findings on band structure and optical properties. Together, these results paint a comprehensive picture of how structural parameters influence the excitonic behaviour, particularly exciton delocalisation of layered perovskites via altering the interlayer electronic coupling.

4.6 Summary

In conclusion, the study in this chapter of layered organic-inorganic lead-iodide perovskites using state-of-the-art *GW*+BSE calculations reveals the profound impact of interlayer distance and alignment on the optoelectronic and excited state properties of these materials . We demonstrate that electronic and optical coupling between adja-

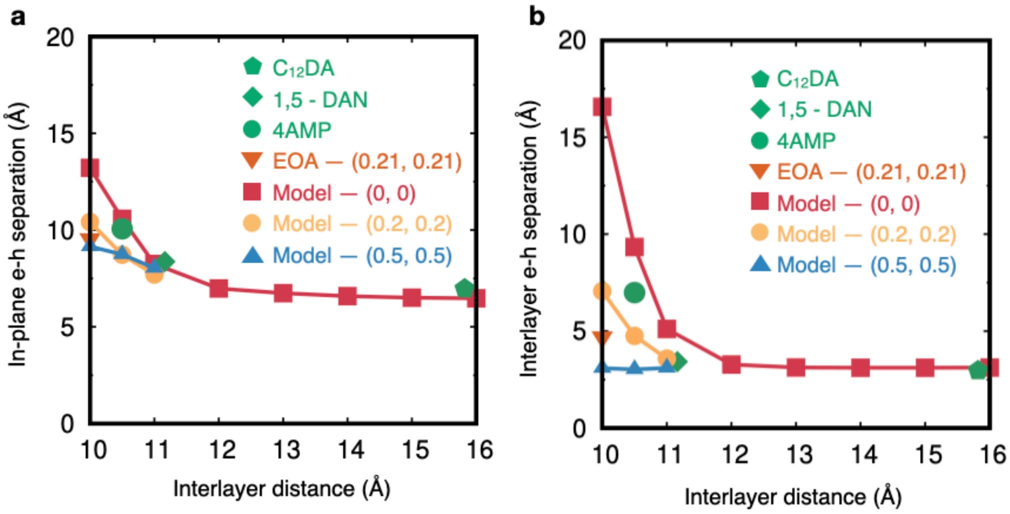

Figure 4.18: Average in plane (a) and interlayer (b) electron-hole separation as a function of the interlayer distance for different structure types: RP models (blue triangles), intermediate models (yellow disks), DJ models (red squares) and experimental structures as described in Figure 4.3 (green and orange data points).

cent inorganic layers can be achieved by carefully tuning these structural parameters, primarily through the interaction of apical iodine orbitals from neighbouring layers.

A key finding of our work is the possibility to overcome exciton confinement within a single lead-iodide layer, achieving interlayer delocalisation of bound electron-hole pairs in bulk layered perovskites. The results consistently show that interlayer distance and alignment are the primary drivers of exciton delocalisation in layered perovskites. The ability to tune exciton spatial characteristics through structural modifications offers exciting prospects for optimising these materials for LED and photovoltaic device applications, which could benefit from enhanced charge transfer excitons [197] and stronger photo-emission [198].

Importantly, the trends observed in our model systems are corroborated by calculations on experimentally realised layered perovskites, validating the broader applicability of our findings. While conventional methods of controlling interlayer distance in layered materials often involve applied pressure [199, 200], this approach has its limitations. In heterogeneous and soft layered perovskites, strain-induced structural changes in both the inorganic and organic layers may be more difficult to control and could have secondary effects on the electronic structure [200]. In contrast to conventional layered materials, tuning interlayer separation and alignment in layered perovskites can also be realised intrinsically, through a judicious choice of the organic spacers. [201]. This feature provides a more controllable and potentially less disruptive method for manipulating interlayer coupling.

The insights gained from this study extend beyond bulk materials to isolated nanostructures and self-assembled heterostructures, suggesting broader implications for the design of perovskite-based functional materials. The study in this chapter not only advances our fundamental understanding of exciton physics in layered perovskites but also provides essential groundwork for exploring more complex systems. In the next chapter, we will apply the same methods to study excitons in layered perovskite-intergrowth heterostructures, which offer additional degrees of freedom for manipulating exciton properties, potentially enabling even finer control over optical and electronic characteristics. We hope this study could serve as a solid foundation for future research exploring the intricate role of phonons in exciton localisation within these complex systems, using for example similar first-principles approaches to those recently reported in Ref. [202].

5 | Interlayer excitons in perovskite-intergrowth heterostructures

The previous chapter explores exciton delocalisation in layered organic-inorganic halide perovskites, demonstrating how exciton properties are primarily influenced by the spacing and alignment of neighbouring layers, which can be tuned through cation spacers. This investigation establishes a fundamental understanding of the relationship between structural and optoelectronic, excitonic characteristics. Building on these insights, the current chapter extends the exploration of exciton properties ($e.g$ the binding energy, exciton delocalisation) in semiconductors by examining a novel class of materials: perovskite-intergrowth heterostructures, as first introduced in Ref. [12].

Through a systematic analysis of electronic band structures, absorption properties, and exciton characteristics, we show that interlayer excitons are likely to be observed in this complex group of heterostructures via structural or molecular engineering. This finding opens up new possibilities for tailoring excitonic properties in perovskite-based materials and deepens the understanding of the fundamental principles governing exciton properties in layered systems.

In particular, this study demonstrates the change from intralayer to interlayer excitons with structural modifications for a set of such perovskite-intergrowth heterostructures, providing insights into how subtle changes in molecular composition can lead to significant alterations in electronic structure and excitonic properties. By investigating the mechanism behind these changes, we establish design principles for engineering perovskite-intergrowth heterostructures with desired optoelectronic and/or excitonic characteristics.

5.1 Introduction

As shown in previous chapter, layered organic-inorganic halide perovskites are known for their structural flexibility [42–44, 49]. In these materials, the alkylammonium cation plays a crucial role by creating an organic layer that effectively separates the perovskite sheets [203, 204]. By carefully designing the structure of the organic cation, one can systematically synthesise a wide range of halide perovskites with predictable properties. This ability to fine-tune the structure opens up possibilities for creating an extensive class of these materials, each with potentially unique characteristics.

Recently, Shi et al. [205] have employed a sequential film deposition strategy to generate isostructural intergrowths of organic-inorganic perovskites on planar surfaces. Aubrey et al [12] have applied this strategy and demonstrated that incorporating a secondary functional group into an alkylammonium ion can template the intergrowth of a distinct, dimensionally reduced structure between the perovskite sheets. The bifunctional ligand binds to the perovskite layer on the ammonium end and templates intergrowth structure on the other end, resulting recurrent co-crystallisation of an extended non-perovskite metal-ligand bond network within a layered perovskite structure, forming perovskite-intergrowth heterostructures, as illustrated in Figure 5.1. The soft perovskite lattice is able to withstand significant structural distortions with ease, enabling a variety of non-perovskite structures, which may not exist otherwise, to be stabilised within the heterostructures.

In particular, single crystals of $(\mathrm{Pb_2Cl_2})(\mathbf{CYS})_2\mathrm{PbCl_4}(\mathbf{CYS} = +\ \mathrm{NH_3(CH_2)_2S^-})$ heterostructures, featuring a lead chloride intergrowth and a smaller zwitterion cysteamine $+\ \mathrm{NH_3(CH_2)_2S^-}$ molecule, and $(\mathrm{PbBr_2})_2(\mathbf{AMTP})_2\mathrm{PbBr_4}(\mathbf{AMTP}+ =$ 4-(ammoniomethyl)-tetrahydropyran) with lead bromide intergrowth, were first introduced in Ref. [12] as two representative lead based intergrowth-perovskite heterostructures that have been synthesised. While both structures exhibit similar features

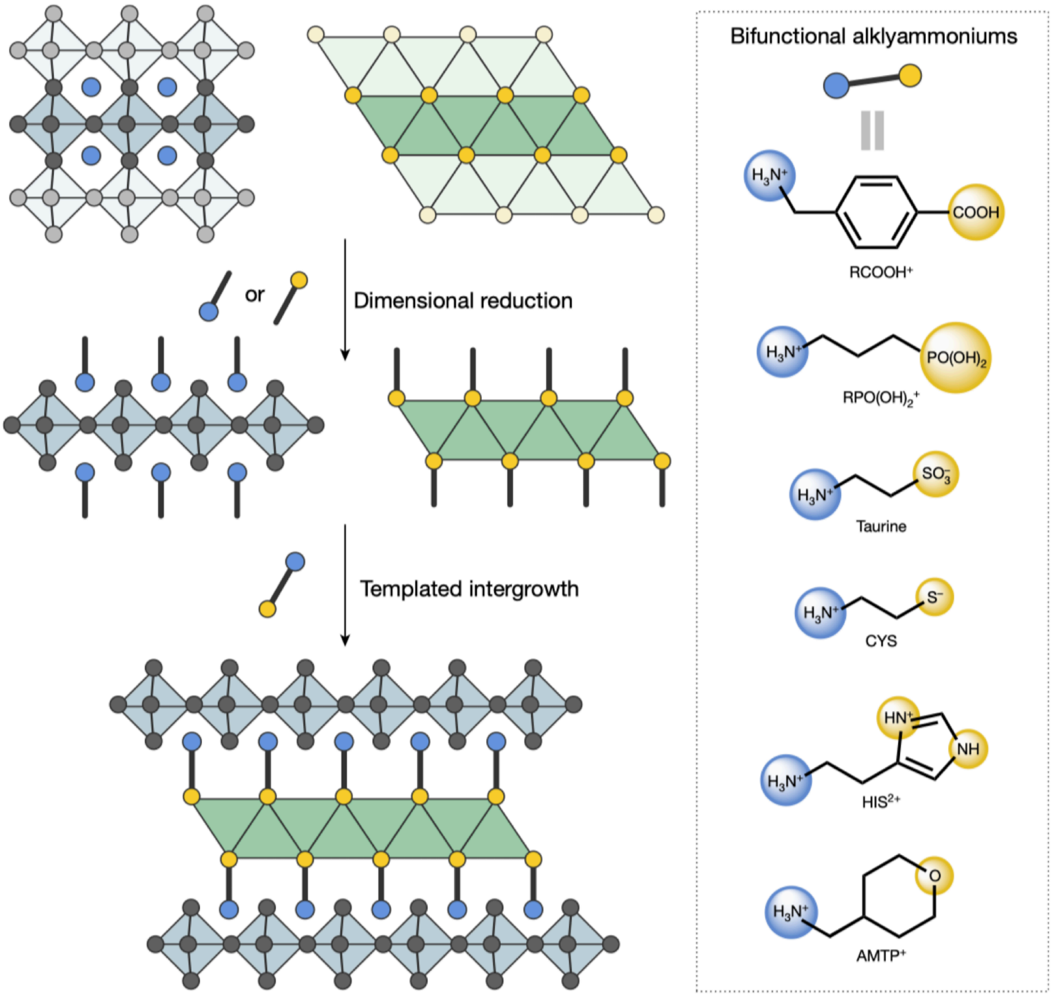

Figure 5.1: Schematic illustration of the reaction design strategy for synthesising templated perovskite intergrowths. The perovskite lattices are depicted in light blue, while a hypothetical, lattice-matched structure is shown in green. Blue and yellow circles represent the templating groups for the perovskite and intergrowth structures, respectively (see inset). This approach enables the targeted synthesis of complex heterostructures of desired electronic properties. Figure adapted from Ref. [12] with permission, granted through the RightsLink permission system.

in their PbX_4^- perovskite sublattice and intergrowth sublattice (both isostructural to 3D PbX_2 (X = Br, Cl) sliced along the (001) plane) [206], they differ significantly in their structural connectivity and electronic properties.

In $(PbBr_2)_2$(**AMTP**)$_2$$PbBr_4$, the positively charged **AMTP+** compensates for the negatively charged perovskite slab PbX_4^-, while the charge-neutral intergrowth is templated by the tetrahydropyran tails of the molecule. The perovskite and intergrowth layers are distinctly separated by the organic **AMTP+** layer, resulting in a band structure and optical properties excitonic features similar to typical 2D lead-halide perovskites [12, 207], with excitons localised within the perovskite layers [12].

In contrast, (Pb_2Cl_2)(**CYS**)$_2$$PbCl_4$ features a smaller, charge-neutral **CYS** molecule to directly template the intergrowth, connecting it to the perovskite layers via a shared bridging chloride ion, as shown in Figure 5.2 b. This configuration affects the band structure due to state mixing around the valence band top and conduction band bottom, altering optical absorption features and the charge distribution compared to typical Pb-Cl layered perovskites. Consequently, the structure exhibits a broadened absorption onset and more complex excitonic characteristic, with excitonic states extending across both perovskite and intergrowth layers. This demonstrates a more nuanced interaction between structural configuration and optical properties in these rather complex materials [12].

5.2 The hypothetical structures construction

The complexity and diversity of these perovskite-intergrowth heterostructures open up even more possibilities for fine-tuning their properties through structural modifications than typical layered hybrid halide perovskites. Inspired by the previous chapter, we then turn to explore approaches for modifying the interlayer spacing and introducing adjustable metal-ligand interactions between the intergrowth and perovskite

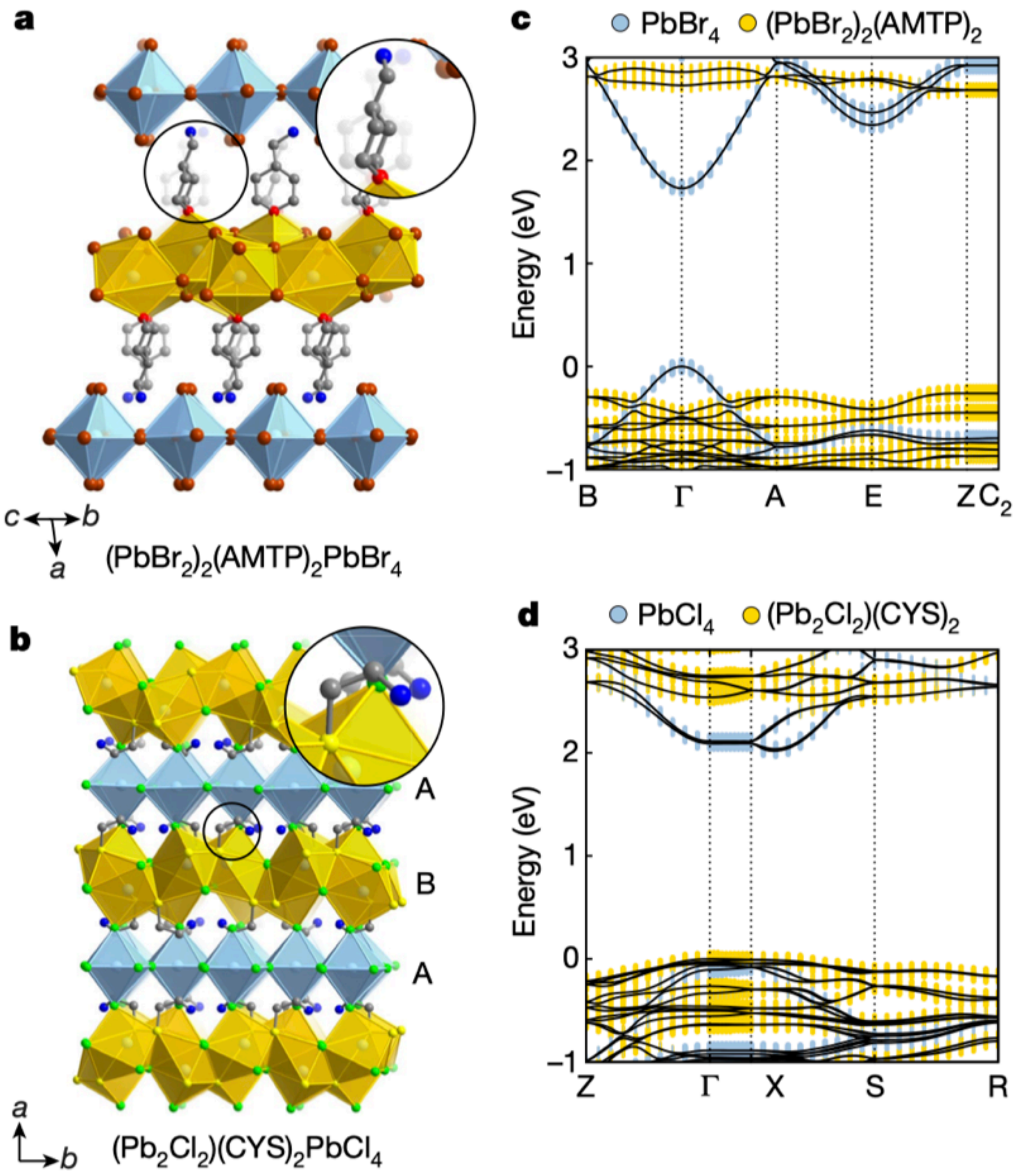

Figure 5.2: Comparison of structural and electronic properties of perovskite-PbX_2 (X = Cl, Br) heterostructures. **a,** Single-crystal X-ray diffraction structure of $(PbBr_2)_2$(**AMTP**)$_2$$PbBr_4$. **b,** Single-crystal X-ray diffraction structure of (Pb_2Cl_2)(**CYS**)$_2$$PbCl_4$. Insets in **a** and **b** show coordination of **AMTP**$^+$ and **CYS** to the intergrowths, respectively. Atom colours: Pb (light blue), Cl (lime-green), Br (orange), S (yellow), C (grey), O (red), and N (blue). Perovskite sublattices are shaded in light-blue, and PbX_2-like sublattices in yellow. Hydrogen atoms are omitted for clarity. **c,** DFT-PBE calculated band structure of $(PbBr_2)_2$(**AMTP**)$_2$$PbBr_4$. **d,** DFT-PBE calculated band structure of (Pb_2Cl_2)(**CYS**)$_2$$PbCl_4$. Figure adapted from Ref. [12] with permission, granted through the RightsLink permission system.

sublattices [208]. Our focus is centred on a specific class of heterostructures, with layers separated by expansive organic molecules, derived from the parent compound $(PbBr_2)_2$(**AMTP**)$_2$$PbBr_4$. Unlike in (Pb_2Cl_2)(**CYS**)$_2$$PbCl_4$, where the connectivity between layers hinders structural modifications to the interlayer spacing, the separated layers in $(PbBr_2)_2$(**AMTP**)$_2$$PbBr_4$ allows such tunability via engineering the molecules. We apply various hypothetical strategies to alter the size and composition of organic components, investigating their impact on the overall electronic and excitonic properties, specifically focusing on their correlation with electronic band structures and exciton localisation. By systematically exploring these structural modifications, we seek to uncover new avenues for tuning the optoelectronic and excitonic properties of these advanced materials.

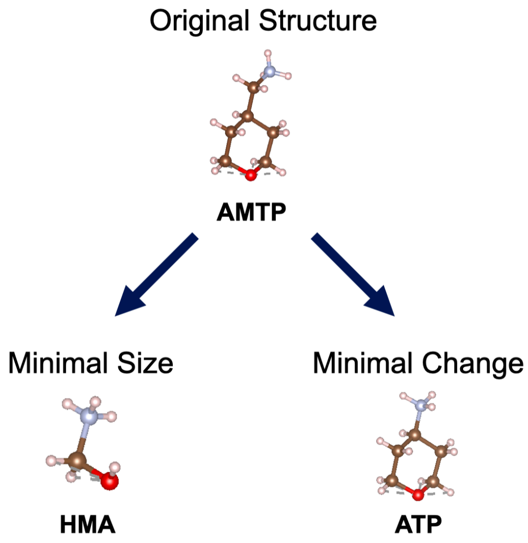

Figure 5.3: Schematic diagram demonstrating the design principles of hypothetical perovskite-intergrowth heterostructures. **Left:** A minimal structure using **HMA** (1-hexanemethylammonium) as the organic cation, preserving the fundamental functional groups; **Right:** A structure with minimal change using **ATP** (4-aminothiophenol) as the organic cation, with only one CH_2 group taken from the original **AMTP**. The perovskite and intergrowth layers are schematically represented in blue and yellow, respectively.

We employ a systematic approach to design hypothetical structures by modifying the **AMTP** molecule to a reduced structural motif, as illustrated in Figure 5.3. These modifications aim to slightly change the molecular structure and adjust the interlayer distance without altering the rest of the framework. Specifically, we replace the **AMTP** molecule with two other cations: a smaller $HOCH_2NH_3^+$ ((Hydroxymethyl)-ammonium) molecule, created by preserving the minimal functional groups; and a larger 4-(amino)tetrahydropyran configuration, created by removing one CH_2 group from the side chain of the tetrahydropyran ring (hereafter referred to as **HMA** and **ATP**, respectively).

These modifications are carefully designed to maintain the overall spatial configuration and bonding environment of the original molecule as a starting point for structure optimisation. The bond lengths in the initial structures are as follows: 1.51 Å for C-C and C-N bonds, 1.44 Å for C-O bonds, 0.91 Å for N-H bonds, and 0.99 Å for C-H bonds, using experimental measurements from the original **AMTP** molecule [12] to ensure a close approximation to reasonable molecular dimensions.

Following the construction of **HMA** and **ATP**, we quantify the change in interlayer separation as follows. We first measure the size of the modified molecules relative to the original **AMTP**. Subsequently, an adjustment was made to the unit cell lattice parameters to reflect this change. This adjustment preserved the relative offset in the in-plane directions and the internal tilting and distortions of the inorganic octahedra, while accommodating the modified molecule along the z-direction. This approach allows us to maintain the essential structural characteristics of the original heterostructure while introducing controlled modifications.

We then conducted a variable cell relaxation with DFT-PBE methods to further optimise the structure for all three structures studied. This relaxation process allows for a further refinement of the hypothetical structures, ensuring that they represent energetically favourable configurations.

It is crucial to emphasise that the hypothetical structures discussed above have not been synthesised experimentally, and their existence and stability require further analysis.

These theoretical models serve as valuable examples for demonstrating how tuning structural parameters can impact optoelectronic and excited-state properties, which will be explored in depth in this chapter. By investigating these hypothetical structures, we try to gain insights into the structure-property relationships in perovskite-intergrowth heterostructures, potentially guiding future experimental efforts in materials design and synthesis.

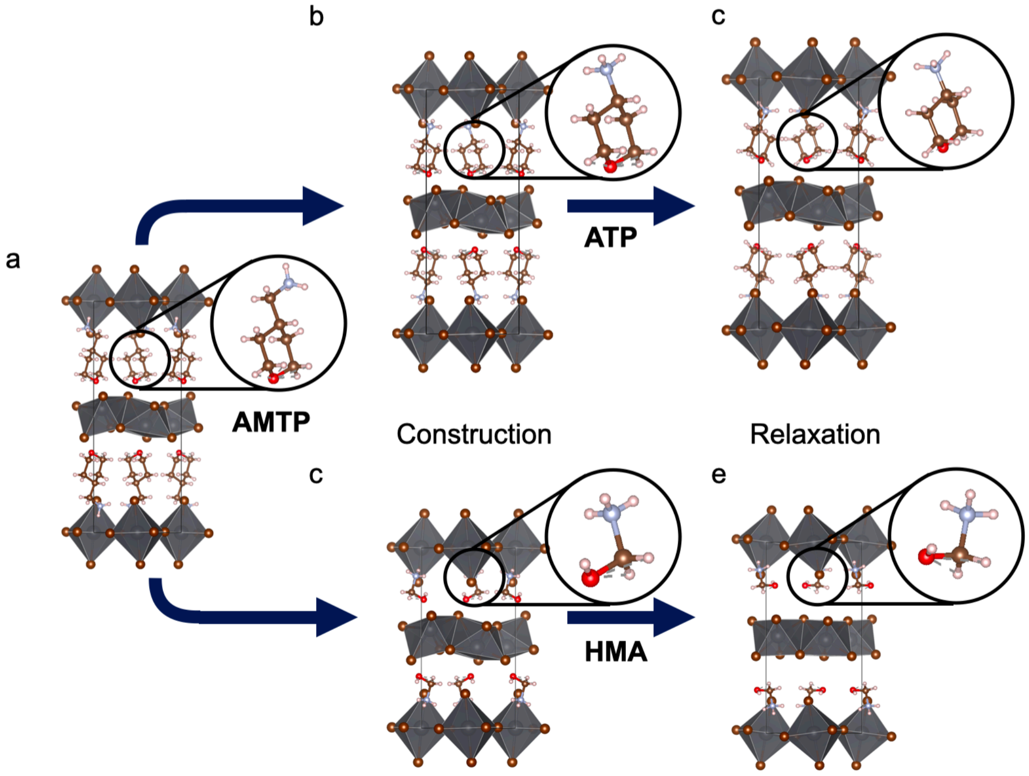

Figure 5.4: Schematic visualisation of the structures in perovskite-intergrowth heterostructures, showing the transition from initial hypothetical structures to their DFT-PBE optimised state. On the left, the original $(PbBr_2)_2$(**AMTP**)$_2$$PbBr_4$ heterostructure is displayed for reference. The middle panels (b and c) represent the initial constructed structures for **HMA** (top) and **ATP** (bottom), respectively. The right panels (d and e) represent the corresponding relaxed structures after the optimisation process.

Figure 5.4 presents a side-by-side comparison of the original **AMTP** heterostructure, the initial hypothetical structures for **HMA** and **ATP**, and their corresponding relaxed structures. Two significant changes are observed in the relaxation process of the **HMA** structure. Firstly, there is a notable increase in the interlayer spacing, as evidenced by the expansion of lattice parameters. The projected interlayer distance for the **HMA** structure increases from the initially assumed 15.82 Å to 17.70 Å, resulting in a substantial increase in the separation between the organic molecules and the neighbouring intergrowth layers. However, it is important to note that the interlayer distance in the relaxed **HMA** structures still remain smaller than the 21.83 Å observed in the relaxed **AMTP** structure. Secondly, a significant reorganisation occurs in the intergrowth layer, involving considerable atomic rearrangements, as clearly depicted in Figure 5.4 (panels b-e).

In contrast, the **ATP** structures exhibit markedly different behaviour during relaxation. The changes observed in the **HMA** structures are not replicated in the **ATP** case. The lattice parameter in the perpendicular direction undergoes a rather minor change from 21.83 Å to 21.25 Å, a difference of less than 3%. This small change can be attributed to the structural similarity between **ATP** and **AMTP**. A similar phenomenon has been observed when comparing PMA and PEA based perovskites structures, where slight modifications in the organic components result in negligible changes in lattice parameters [207].

5.3 Optoelectronic properties of hypothetical structures

After determining the optimised structural configurations, we conducted a comprehensive analysis of the optoelectronic properties of **AMTP**-based materials in comparison to the hypothetical **HMA** and **ATP** structures.

Figure 5.5 presents the computed projected band structures for the **AMTP**, **ATP**, and **HMA** structures. All three structures exhibit direct band gaps at the Γ point, with band gaps of 1.72 eV for **AMTP**, 1.43 eV for **ATP**, and 0.93 eV for **HMA**. In all three cases, the bands originating from the perovskite sublattice (light blue) and the intergrowth layer (orange) are not hybridised, as indicated by the similar band shapes and dispersions across the different systems.

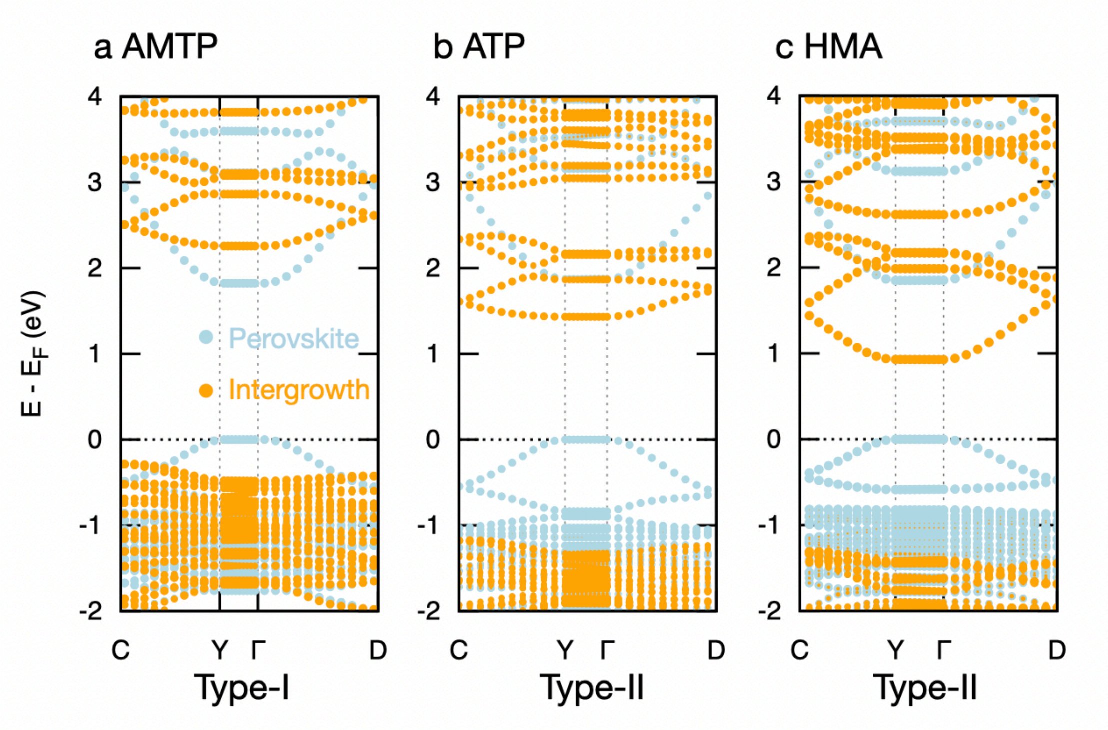

Figure 5.5: Projected band structures of perovskite-intergrowth heterostructures. colour encoded to identify orbital contributions from different sublattices of the heterostructures: the perovskite layer PbX_4^{2-} is shown in light blue, the combined intergrowth layer (PbX_2 and O) is shown in orange. Panel (a)(b)(c) corresponds to the **AMTP** structure, **ATP** and **HMA** structure, respectively.

A significant difference lies in the band alignment between the perovskite and intergrowth layers. In the **AMTP** structure (panel a), both the conduction band minimum and the valence band maximum consist of bands primarily from the perovskite sublattice, exhibiting characteristics typical of type-I heterostructures (see Figure 5.6). In contrast, both **ATP** (panel b) and **HMA** (panel c) structures demonstrate properties more closely aligned with type-II heterostructures (see Figure 5.6). In both modified structures, the conduction band minimum originates from the atomic orbitals of intergrowth layer, while the valence band maximum consists of bands from the perovskite layer.

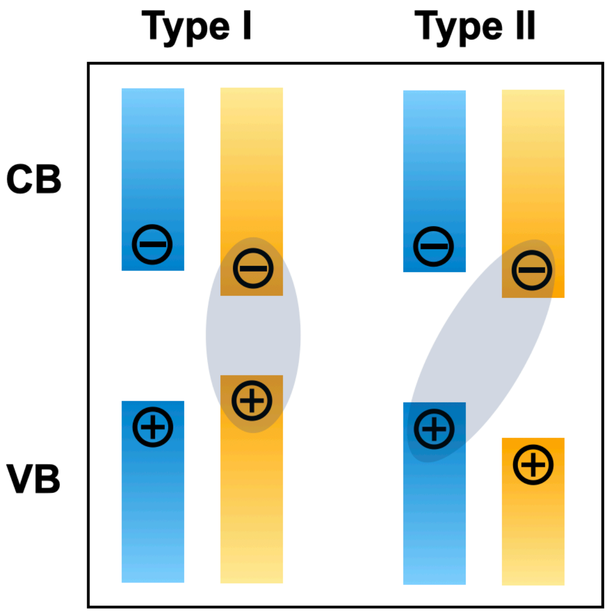

Figure 5.6: Schematic diagram showing the band alignment in Type I and II heterostructures. Charge carriers are indicated by circles, different colour represents valence and conduction bands from different parts in heterostructures.

In addition, the calculations reveal that the bandgaps for **HMA** are approximately 1 eV smaller than those of the **AMTP** structure (see Figure 5.5). This significant difference in bandgap is consistently observed using both the DFT-PBE methods and G_0W_0 method (1.91 eV for **HMA** and 2.83 eV for **AMTP** at G_0W_0 level), lending robustness to the findings.

The band gap reduction in **HMA** structures usually indicate differences in their optical absorption spectra compared to the **AMTP** configuration. A smaller bandgap typically results in a red-shift of the absorption spectrum. Moreover, the shift from a type-I to a type-II heterostructure suggests potential changes in charge carrier dynamics, exciton properties, and overall photophysical properties, which leads us to the next part of the analysis.

The investigation then further extend to the absorption spectra for these heterostructures, as shown in Figure 5.7.

In this study, we select **AMTP** as a representative of Type I heterostructures, and **HMA** as the representative for Type II. In both cases, we observe a characteristic excitonic spectral profile. The onset of absorption is marked by a sharp peak, indicating a bound exciton. This excitonic peak is followed by a flat plateau region, which then changes into a steep rise corresponding to the onset of the continuum states.

Despite the substantial 1 eV difference in bandgap energies, the absorption spectra across these heterostructures exhibit surprisingly similar onsets, with differences less than 0.1 eV for both with and without electron hole correlation. Moreover, the overall line shape and progression of the absorption spectra are notably consistent across both structures.

This unexpected similarity in absorption spectra, despite significant bandgap differences, suggests a complex interplay between electronic structure and optical properties in these materials. It indicates that the optical properties of these heterostructures is governed by mechanisms that go beyond simple bandgap considerations.

To understand this, we further calculate the oscillator strengths, which revealed the existence of several dark states both with and without e-h correlations, situated below the absorption onset for **HMA** structures, as shown in Figure 5.7 d and f. These dark states indicate the occurrence of complex transitions not captured in the absorption spectra. Such states could arise from various phenomena, including symmetry-forbidden transitions, charge transfer states, or localised excitations that do not contribute significantly to the overall optical absorption [209]. The presence of these dark states highlights the complexity of the electronic structure in these materials and underscores the importance of considering factors beyond simple bandgap calculations when predicting optical properties [209, 210].

This part of the analysis is crucial for understanding the underlying relationship between electronic transitions and the optical absorption of these heterostructures. To further clarify the correlation between band alignment and optical absorption and to provide insights into the nature of the dark states, a systematic and in-depth exploration of excitons is necessary.

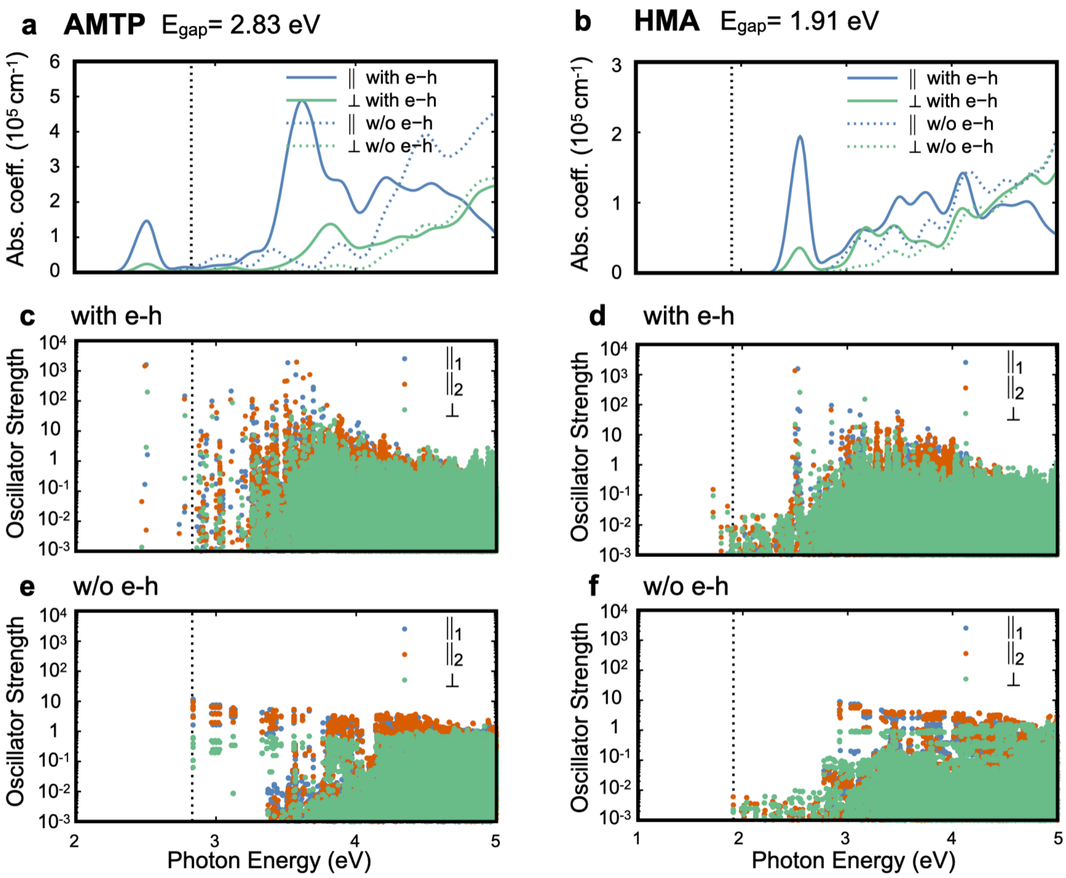

Figure 5.7: The absorption coefficient (a,b) and oscillator strength with (c,d) and without (e,f) e-h correlation of perovskite-intergrowth heterostructures with **AMTP** (left), **HMA**(right), calculated within the G_0W_0+BSE framework.

5.4 Exciton analysis of hypothetical structures

Similar to the analysis presented in the previous chapter, we employ the ECF to investigate the spatial correlation between electrons and holes for the excited states of these materials. The holes are sampled on a uniform grid (2 × 2 × 16) consists of total 64 sampling points within the primitive cell at the centre of a 10 × 10 × 4 supercell, with the densest sampling corresponding to the direction perpendicular to the plane

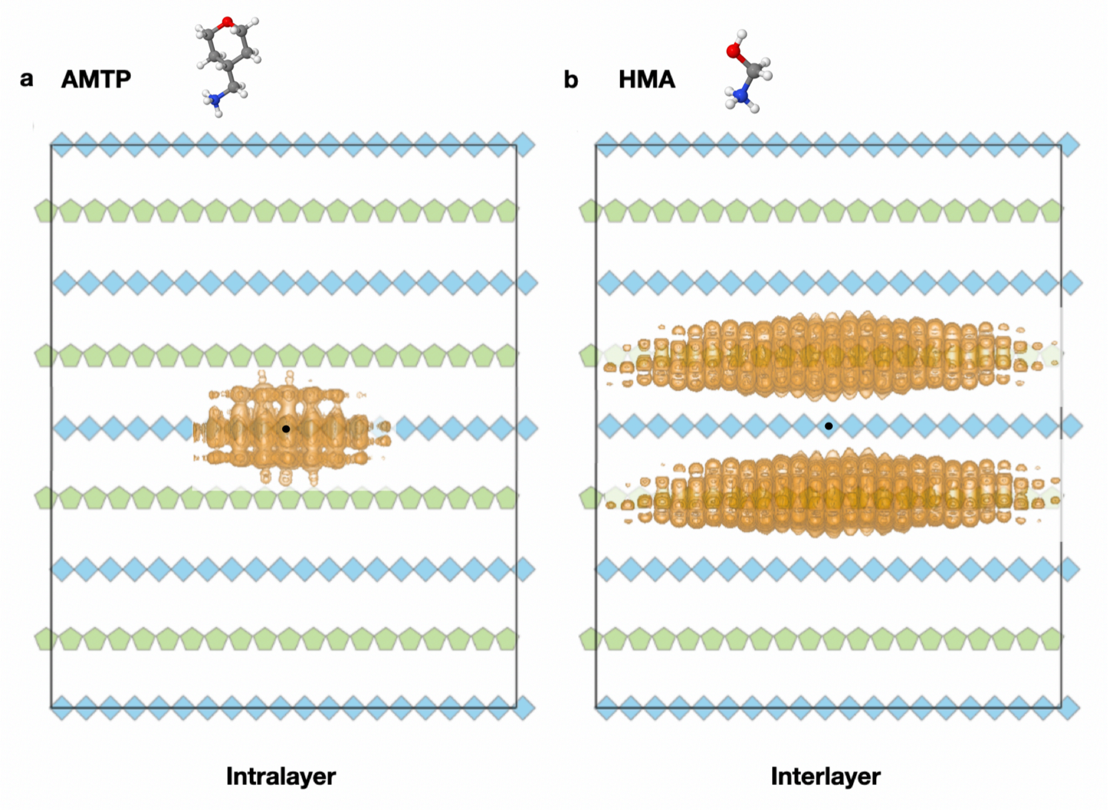

Figure 5.8: Visualisation of ECF in lithium and sodium-based heterostructures. **a,b.** Isosurfaces representing the ECF for the lowest energy excitons in **a. AMTP** and **b. HMA**. The background structures are provided as a visual guide and do not indicate the actual localisation of the exciton wavefunction. The origin is shown by the black dot at the centre of the supercell.

The ECF represents the probability density to find the electron-hole pair that are separated by $\mathbf{r} = \mathbf{r}_e - \mathbf{r}_h$ in an exciton. Figure 5.8 shows the isosurfaces (with the origin at the supercell centre) that map the out-of-plane spatial distribution of the lowest-energy exciton within the **HMA** hypothetical heterostructures, alongside the original **AMTP** heterostructures. The analysis of Figure 5.8 reveals distinct exciton characteristics between the two structures. In the **HMA** structures, the lowest-energy excitons exhibit an inter-layer delocalisation, indicating a separation of electron-hole pairs across different layers. This is evidenced by the ECF isosurfaces showing a layered configuration with the highest probability points situated at least one layer apart. Such interlayer excitons are also previously seen in TMDCs heterostructures [176–178].

In contrast, the **AMTP** heterostructures display intra-layer excitonic delocalisation. Here, electrons and holes are predominantly localised within the same layer, as shown by the ECF's highest probability points being centred at the origin. The difference in exciton spatial distribution between **HMA** and **AMTP** structures underscores the profound impact of molecular engineering on the exciton localisation and charge transfer characteristics of these perovskite-intergrowth heterostructures.

5.5 Summary of the AMTP group heterostructures

With the above analysis of the hypothetical structures alongside the original **AMTP** heterostructures, we can conclude so far that the **AMTP** heterostructure exhibits a type-I band alignment, while the two hypothetical variants - **HMA** and **ATP** - display type-II band alignments. Notably, the **HMA** structures have a bandgap approximately 1 eV narrower than that of **AMTP**. Despite this significant difference in bandgap, the **AMTP** and **HMA** structures demonstrate a similar absorption onset around 2.5 eV. This similarity is attributed to the presence of dark excitons below the absorption onsets, which are not visible in the absorption spectra.

Analysis of the ECF for these lowest-lying dark states reveals their nature as interlayer excitons in the **HMA** structure, with electrons and holes excited in separate layers. In contrast, the lowest-lying exciton in the type-I **AMTP** heterostructure is identified as an intralayer exciton, with electrons and holes excited within the same layer.

These observations suggest a potential correlation between band alignment and the manifestation of interlayer excitons in heterostructures. However, before we can propose any potential correlation, it is crucial to determine whether these phenomena are observed beyond hypothetical structures. To this end, we will adopt a methodical approach using experimentally realised structures as detailed in the next section.

5.6 1-Na and 1-Li heterostructures

We now shift the focus to experimentally realised perovskite-intergrowth heterostructures, as shown in Figure 5.9. These materials were synthesised by the collaborators, Dr. Arundhati Deshmukh in Prof. Hemamala Karunadasa's group at Stanford University. The synthesis details and experimental results, along with the computational findings presented in this chapter, are part of a manuscript currently in preparation.

The structures under investigation are layered heterostructures comprising alternating perovskite $[PbCl_4]^{2-}$ layers and non-perovskite $[PbCl_2L_2]^2$ intergrowth layers, where L represents a bifunctional ligand, as shown in Figure 5.9. These heterostructures incorporate sodium and lithium atoms respectively in the intergrowth layers, marking the first incorporation of smaller alkali metal ions in lead halide perovskites. These heterostructures provide a unique platform to explore rational structural design, tunable electronic properties, and exciton properties in real systems.

Figure 5.9 shows the structures of the two layered heterostructures. The intergrowth layer can be described as corner-sharing 8-coordinate polyhedra. These polyhedra are derived from regular $PbX_6{}^{2}-$ octahedra by bifurcating the apical (out-of-plane) Pb-X bonds into two bonds with the bidentate carboxylate group. The general formula for this structure can be written as $M_2(PbCl_2)L_2(PbCl_2)$, where the first half $M_2(Pb_2Cl_2)L_2$ represents the intergrowth layer and the second half $(PbCl_4)$ represents a 2D perovskite, with L being the zwitterionic ligand. Here M represents Na, Li and L represents trans-(4-aminomethyl)cyclohexanecarboxylic acid (AMHC). For simplicity, we will refer to these two heterostructures as **1-Na** and **1-Li** hereafter.

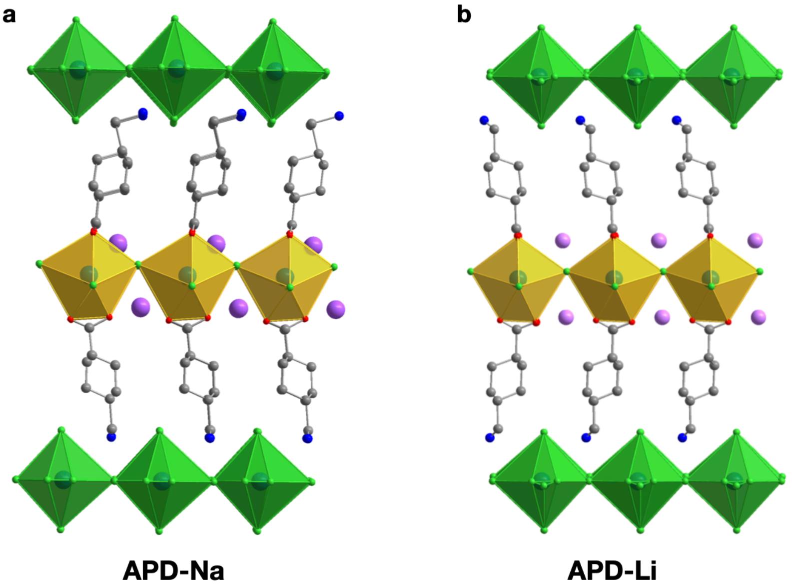

Figure 5.9: Structural representations of perovskite and perovskite-derived heterostructures. Single crystal structure of the layered heterostructures $M_2(PbCl_2)L_2(PbCl_4)$ where M = Na (a), Li (b) and L = trans-(4-aminomethyl)cyclohexanecarboxylic acid (AMHC). Atoms are colour coded as follows: Li/Na - pink, C - grey, N - blue, O - red, Cl - green, Pb - teal. Hydrogen atoms are omitted for clarity.

Na or Li atoms occupy the cavity between the corner-sharing polyhedra in the intergrowth layers. The carboxylate groups at the top and bottom of each layer are oriented orthogonally to each other, and the Cl-Pb-Cl bonds parallel to the O-C-O bonds are pushed out of plane. This arrangement introduces significant in-plane and out-of-plane distortions in the intergrowth layer, which are known to influence electronic and optical properties in layered lead-halide hybrids. Previous studies have shown that out-of-plane distortions can improve the photoluminescence quantum yields in such structures [45,211].

Of particular interest is the low symmetry exhibited by these structures. They crystallise in the monoclinic $C2$ space group, belonging to the C_2 point group. The absence of bulk inversion symmetry in such space groups is associated with unique band structures and potential chiro-optical properties, adding another layer of complexity to their electronic properties [175,212].

By employing first-principles calculations on these materials, we try to ascertain whether similar optical and excitonic properties observed in the hypothetical structures are present in experimentally synthesised materials, which will provide a solid starting point for further exploration.

5.6.1 Optoelectronic properties

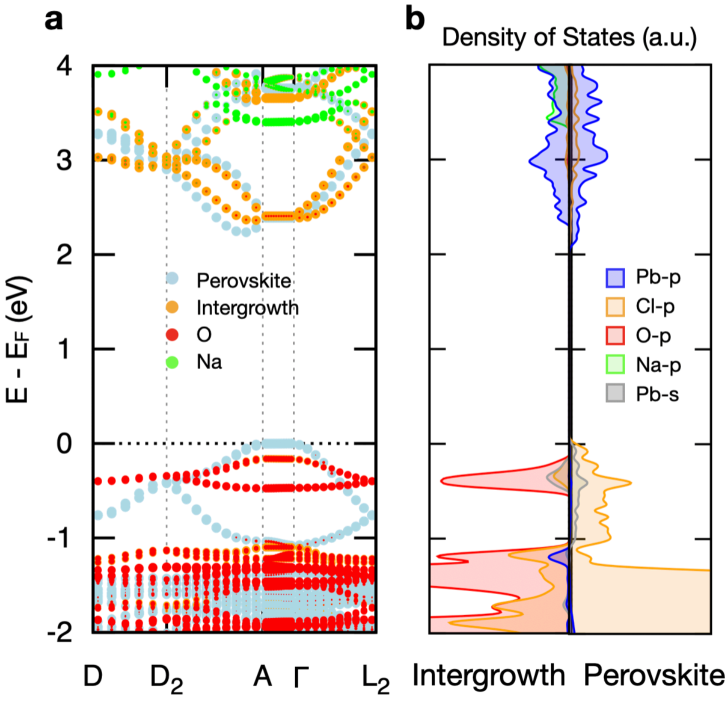

Figure 5.10: Band structure (a) and projected DOS (b) of the Na intergrowth. colour scheme for the band structures: red O; green Na; orange intergrowth Pb+Cl; blue perovskite Pb+Cl. colour scheme for pDOS: red O; green Na; orange Cl p; blue Pb p; grey Pb s.

In the analysis of the **1-Na** and **1-Li** heterostructures, we employ DFT with generalised-gradient approximation using PBE functional to calculate the electronic band structures. Unrelaxed experimental structures were used for all calculations on both heterostructures. The calculations of optimised structures will be discussed in detail in Chapter 6.

Both **1-Na** and **1-Li** heterostructures exhibit indirect bandgaps, as shown in Figures 5.10 and 5.11. In the conduction bands of both structures, we observe the presence of band splitting along the in-plane branch, due to the Rashba-Dresselhaus effect [212]. This phenomenon arises from the interplay of spin-orbit coupling (due to the presence of heavy atoms) and bulk inversion asymmetry, characteristic of polar point groups such as C_2 [175,212].

The calculations reveal different band alignments for the two structures, despite their structural similarities. **1-Na** displays a Type-I band alignment, with both the valence band maximum (VBM) and conduction band minimum (CBM) localised on the perovskite layer. The VBM primarily comprises Pb s (28.5% at Γ) and Cl p orbitals (70.0% at Γ) from the perovskites, with some O p state contributions just below (0.2 eV) at Γ, while the CBM mainly consists of Pb p orbitals (78.2 %) and Cl s orbitals (19.6%) from the perovskites. The calculated band gap is 2.39 eV at DFT-PBE level and 3.64 eV at G_0W_0 level.

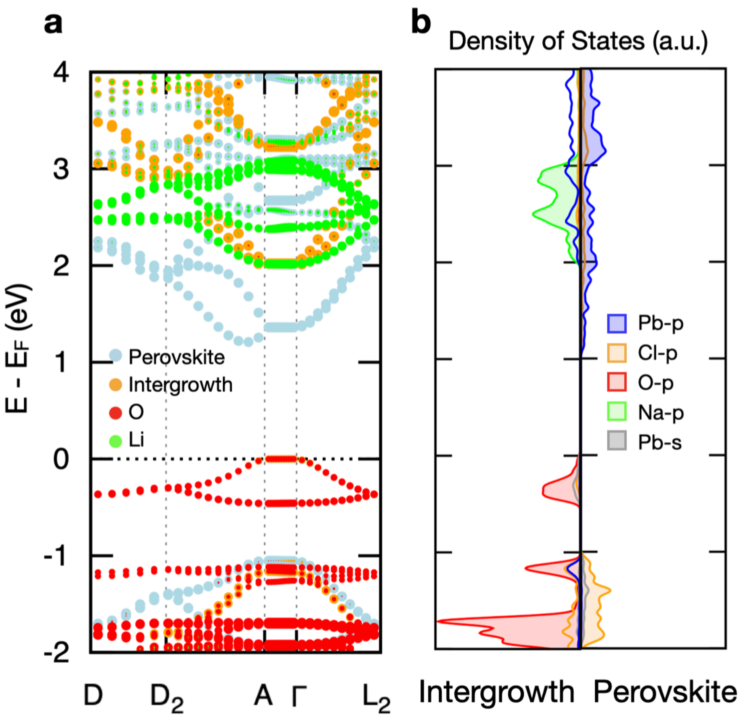

Figure 5.11: Band structure (a) and projected DOS (b) of the Li intergrowth. colour scheme for the band structures: red O; green Li; orange intergrowth Pb+Cl; blue perovskite Pb+Cl. colour scheme for pDOS: red O; green Li; orange Cl p; blue Pb p; grey Pb s.

In contrast, **1-Li** exhibits a different band alignment. The VBM is entirely contributed by the atomic orbitals from the intergrowth layer, predominantly composed of O p orbitals with minor contributions from Cl p and Pb s orbitals (28.4%). The CBM, however, mainly comprises Pb p orbitals from the perovskite layer. This spatial separation of VBM and CBM across different layers is a defining characteristic of Type-II heterostructures. The calculated band gap is 1.36 eV at DFT-PBE level and 2.60 eV at G_0W_0 level, approximately 1 eV lower than **1-Na**.

Notably, Na and Li orbitals do not directly contribute to the CBM. Instead, they are positioned much higher in the conduction bands. This suggests that the differences in band structures between **1-Na** and **1-Li** likely result from indirect effects related to the presence of these alkali metal atoms, rather than their direct electronic contributions.

Figure 5.7 shows the calculated absorption spectra, compared with experimental measurements. Both spectra show similarly high energy absorption onsets (approximately 3.0 eV for calculated values and 3.8 eV for measured values). The quasiparticle band gaps computed within the G_0W_0 + BSE framework are expected to be underestimated with respect to experiment by approximately $0.5 \sim 1$ eV. This is due to the sensitivity of single-shot G_0W_0 calculations to the mean-field starting point, which was pointed out for halide perovskites and other semiconductors in several prior studies [6,46,154].

The experimental onsets are consistent with the excitonic absorption onset of reported 2D Pb-Cl perovskites [213]. However, in contrast to typical 2D perovskites, there is an additional excitonic peak in both the heterostructures, a phenomenon observed in both calculated and measured absorption spectra. Previously reported Pb-Pb layered heterostructures exhibited only one excitonic peak below the band gap onset [12]. We attribute the second excitonic peak to be a result of the unique band structure where the perovskite layer and the intergrowth layer have bands at relatively close energies. This will be discussed in detail in the excitonic decomposition analysis in Chapter 6.

Similar to the observations in the hypothetical structures discussed earlier, in **1-Li**, we observe several optically dark lower energy transitions, as indicated by oscillator strength calculations shown in 5.12 e and f. These dark states explain why both **1-Na** and **1-Li** structures show similar absorption onsets for both spectra with and without e-h

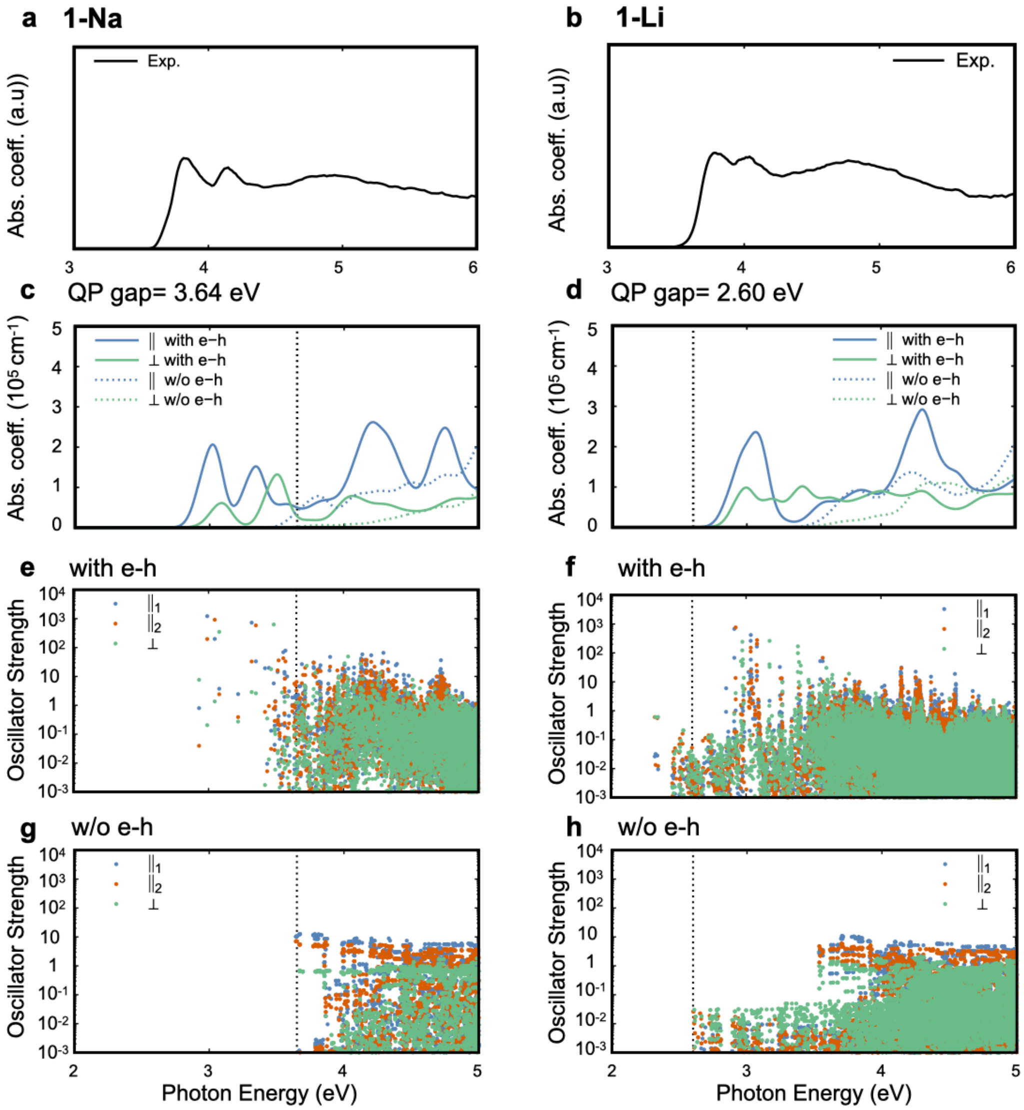

Figure 5.12: The absorption spectra measured experimentally (a,b) in arbitrary units, calculated with G_0W_0 + BSE framework(c,d) and oscillator strength with(e,f) and without (g,h) e-h correlation of perovskite-intergrowth heterostructures with **1-Na** (left), **1-Li** (right)

correlation around 3 eV, despite their differences in band alignment and bandgap. These findings highlights the underlying correlation between band alignment and optical properties we found in the hypothetical structures does indeed exist in these experimentally-realised perovskite-intergrowth heterostructures. The observation of type-II band alignment and optically dark states in **1-Li**, in particular, consistent with the prior observations. The distinct band alignments and optical properties of **1-Na** and **1-Li**, despite their structural similarities, underscore the potential for overcoming exciton confinement via structural engineering, which we will discuss further in detail.

5.6.2 ECF analysis

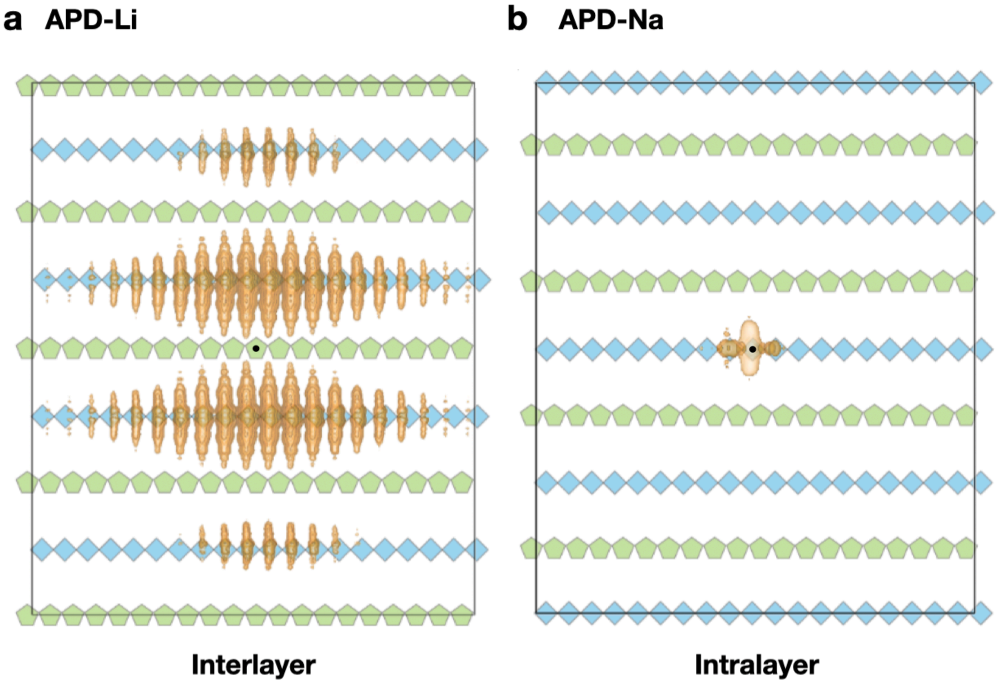

Figure 5.13: Visualisation of ECF in lithium and sodium-based heterostructures. **a,b.** Isosurfaces representing the ECF for the lowest energy excitons in **a. 1-Li** and **b. 1-Na**. The background structures are provided as a visual guide and do not indicate the exact localisation of the exciton wavefunction. The origin is shown by the black dot at the centre of the supercell.

In analogy to this study for the hypothetical structures, we seek the potential observation of interlayer excitons in the experimentally realised **1-Na** and **1-Li** heterostructures, given the Type-II band alignment in **1-Li**. To probe this, we calculate the ECF once again. Figure 5.13 presents the ECF for the lowest energy excitons in **1-Li** and **1-Na**, showing the probability distribution of the photo-excited electron. The analysis reveals striking differences between the two structures:

1-Li exhibits significant out-of-plane delocalisation of the ECF, extending across at least three unit cells in the direction perpendicular to the inorganic sheets. This interlayer exciton is also observed in the hypothetical **HMA** structures, consistent with Type II band alignment.

As a comparison, **1-Na** shows ECF localisation within a single layer, with notably lower in-plane delocalisation. This intra-layer excitonic properties is similar to what we observed in the **AMTP** hypothetical structures, where electrons and holes are predominantly localised within the same layer. The reduced delocalisation in **1-Na** could be attributed to the higher binding energy of the intralayer excitons, a common feature in Type-I heterostructures.

We note that the lowest energy interlayer exciton in **1-Li** has negligible oscillator strength, with the bright exciton lying higher in energy, as shown in Figure 5.12. This observation aligns with the general understanding that interlayer excitons typically have relatively lower oscillator strengths (10^{-2}) due to spatial separation. Although these dark states are not optically forbidden by symmetry (oscillator strengths being strictly 0), they often requiring pump-probe, photoluminescence or ultrafast techniques for detection. [53]. Recently, a similar phenomenon was observed in symmetric trilayer stacks of TMDCs where the electrons or holes tunnel across the middle layer, forming quadrupolar excitons [214, 215]. This parallel underscores the broader relevance of the findings to the general field of layered heterostructures beyond perovskites.

5.7 Summary

In conclusion, this chapter presents a comprehensive comparison between **AMTP**, **ATP**, and **HMA** structures, providing insights into the optoelectronic and excited-state properties of perovskite-intergrowth heterostructures. We observe that subtle molecular modifications in these structures do not necessarily lead to dramatic changes in their overall geometry. However, these minor alterations can have profound effects on their electronic properties. In particular, we demonstrate a significant shift in band alignment from Type I in **AMTP** structures to Type II in **HMA** structures. This change in electronic structure occurs without substantial changes to the absorption spectra, a phenomenon attributed to the presence of optically dark states below the absorption onset. The analysis of exciton properties reveals a change from intra-layer excitons in **AMTP** structures to inter-layer excitons in **HMA** structures, as evidenced by characteristic of the exciton correlation function.

Furthermore, we compare these hypothetical structures with experimentally realised materials, namely **1-Na** and **1-Li**. These structures exhibits characteristics consistent with the hypothetical models. The distinct excitonic features of **1-Na** and **1-Li**, despite their structural similarities, underscore the complex correlation between band alignment, structural configurations, and optical properties in perovskite-intergrowth heterostructures. These results demonstrate the power of molecular engineering in tuning exciton properties. The ability to manipulate exciton localisation through subtle structural modifications opens up exciting possibilities for tailoring these materials for specific optoelectronic applications.

The observations made in this chapter naturally lead to two critical questions that inspires further investigation: Is there a direct correlation between band alignment and exciton localisation, and can we develop a simple method to identify interlayer excitons? Additionally, what factors could potentially drive changes in band alignment, and how can we leverage these to tune the electronic properties of these materials?

These questions form the foundation for the next chapter, where we will further explore the relationship between structural modifications, electronic properties, and excitonic properties in perovskite-intergrowth heterostructures. Given the structural similarities between Li and Na compounds and the significant differences observed between **HMA** and **ATP** structures, the origin of band alignment emerges as a particularly intriguing question. Understanding the underlying mechanisms that drive these electronic structure changes could provide valuable insights into the fundamental principles governing the properties of these heterostructures. By addressing these questions, we aim to not only provide a more comprehensive understanding of these complex systems but also pave the way for rational design strategies in the development of novel functional materials.

Finally, the insights gained from this study highlight the potential of structural and molecular engineering in controlling exciton localisation. This approach offers a promising avenue for overcoming the limitations of exciton confinement in layered materials, potentially leading to enhanced charge separation and improved performance in various optoelectronic applications. As we move forward, exploring the precise mechanisms behind these phenomena and developing predictive models for exciton properties will be crucial in realising the full potential of these versatile heterostructures.

6 | Origin of interlayer excitons in perovskite-intergrowth heterostructures

6.1 Introduction

2D van der Waals heterostructures have emerged as a fascinating frontier in materials science, attracting significant research interest due to their unique ability to host exotic physical phenomena [216–220]. As we have shown in the previous chapter, heterostructures can be classified into Type I and Type II by different alignment behaviours of the bands. Of particular interest are Type II heterostructures, which have shown the ability to host interlayer excitons - quasiparticles with constituent electrons and holes spatially separated across different layers. This behaviour was initially observed in hetero-bilayers of TMDCs [53, 61, 62, 62]. The discovery of interlayer excitons in TMDCs has led to a surge of experimental studies aimed at visualising and characterising these charge transfer states [54, 221–223]

In the previous chapter, first-principles calculation for both hypothetical and experimentally realised structures reveals the emergence of interlayer excitons in perovskite-intergrowth heterostructures and that such interlayer delocalisation of excitons seems indeed to be closely related to Type II alignment. However, such a correlation is still an observation that requires additional elaboration at an atomic level. These findings are intriguing yet raise fundamental questions about the underlying physics of these correlations and the mechanism driving them.

As discussed in Chapter 2-4, first-principles calculations serve as a reliable tool to understand the nature of the excitons. In the last chapter, we have successfully employed ECF to visualise and quantify the real space separation of the correlated electrons and holes. For the first half of this chapter, we introduce an additional quantitative way to understand the electronic origin of the interlayer exciton by decomposing excitons building upon the knowledge of atomic orbital projection. By combining the electronic information from DFT and solution from BSE, we establish a quantitative way to describe the exciton origin from atomic orbitals, correlating the spatial localisation of the excitons with band alignment of heterostructures. For the second half of the chapter, we investigate possible factors influencing band alignment changes and explore strategies to manipulate the electronic properties of these materials.

6.2 Eigenvector analysis

To first gain insights of the excitonic characteristics, we conduct a quantitative analysis of the exciton eigenvectors calculated from the BSE. Our primary goal is to decompose these eigenvectors into their constituent band-to-band transitions, thereby uncovering the electronic origin of excitons in our material system.

The electron-hole excitation states are obtained via solving the BSE for each exciton state. As elaborated in Chapter 2, $A^S_{cv\mathbf{k}}$ are the coefficients of the exciton wavefunction written in the basis of the single particle states, $\left|\psi_{\mathbf{k},c}\right\rangle$ and $\left|\tilde{\psi}_{\mathbf{k},v}\right\rangle$, where S denotes the index of the exciton, **k** denotes the wave vector corresponding to the single particle states, c and v correspond to the conduction and valence band, respectively. These eigenvectors are complex-valued, encoding the contributions from different electron-hole pair configurations to each exciton state. The two-particle exciton state can be written as a superposition of electron states in the conduction band and hole states in the valence band as:

$$|S\rangle = \sum_{\mathbf{k},c,v} A^S_{vc\mathbf{k}} \left|\psi_{\mathbf{k},c}\right\rangle \otimes \left|\tilde{\psi}_{\mathbf{k},v}\right\rangle . \tag{6.1}$$

For a given exciton state S, the contribution from a specific conduction-to-valence band transition at a given **k**-point is determined by the weight $w(c, v, \mathbf{k}) = |A_{vc\mathbf{k}}|^2$.

To investigate the overall composition of each exciton state, we begin by calculating the squared magnitude of the exciton wavefunctions, $|A_{vc\mathbf{k}}|^2$, sum these contributions over all conduction bands and integrate them across the entire Brillouin zone to obtain the total contribution from a specific valence band v_x. This procedure is expressed as:

$$W_S(v_x) = \sum_{c,\mathbf{k}} \left|A^S_{(v_x)c\mathbf{k}}\right|^2 . \tag{6.2}$$

Similarly, we have the following for holes:

$$W_S(c_x) = \sum_{v,\mathbf{k}} \left|A^S_{v(c_x)\mathbf{k}}\right|^2 . \tag{6.3}$$

This summation gives the total contribution of a given valence/conduction band to the exciton state, providing a comprehensive picture of the band-to-band transitions involved.

The results are visualised in the scatter plot shown in Figure 6.1 and 6.2. The x-axis represents the energy of the exciton, while the y-axis indicates the contributing bands. The size of each scatter point is proportional to the magnitude of the contribution from a given band, summed over the BZ. Contributions from conduction bands are depicted in blue, positioned in the upper half of the plot, while contributions from valence bands are depicted in red, in the lower half of the plot. Although we have included 32 bands (16 valence and 16 conduction) in building the BSE kernel matrix elements (see Appendix A.3.3 for details), we limited the visualisation to 8 bands for **1-Na** and 12 bands for **1-Li**, as contributions from higher-lying bands are negligible and have been omitted for clarity.

As shown in Figure 6.1b, the eight lowest-energy excitons for **1-Na** can be roughly classified into two groups. The first four excitons primarily originate from transitions

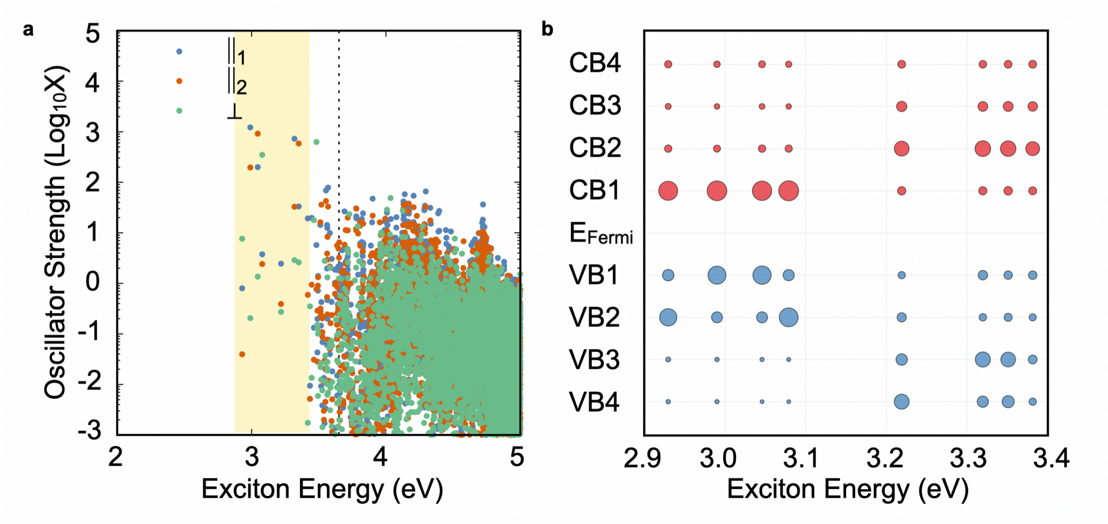

Figure 6.1: (a) Oscillator strength with e-h correlation of perovskite-intergrowth heterostructures **1-Na** (b) Scatter plot of the exciton eigenvector decomposition obtained from the BSE calculation for **1-Na**. The size of each point is proportional to the magnitude of the contribution from a specific band-to-band transition, integrated over the Brillouin zone. Blue points in the upper half correspond to contributions from conduction bands, and red points in the lower half correspond to contributions from valence bands. All studied excitons are marked under a yellow area in the Oscillator Strength plot (a).

between 2 top-most valence bands (VB-1 and VB-2) and the lowest conduction band (CB-1). In contrast, the next four excitons predominantly involve transitions from next 2 valence states (VB-3 and VB-4) to the second lowest energy conduction bands (CB-2).

In the case of **1-Li**, however, all eight excitons involve transitions between the top-most valence bands (VB-1 and VB-2) and the lowest conduction band (CB-1) though they are separated over a energy range of approximately 0.15 eV, as shown in Figure 6.2b. Inspired by the previous chapter, we also extended the exciton analysis to include the bright exciton under parallel-polarised light in Figure 6.2c. We observe a clear difference where the exciton arises from transitions involving the top two valence bands (VB-1 and VB-2) and higher-lying conduction bands (CB-5 and CB-6). This distinction suggests a fundamental difference in the character of these excitons.

While this decomposition effectively identifies contributions to each exciton from band-to-band transitions, it remains insufficient to predict the spatial localisation of the excitons, as the band projections onto atomic orbital can vary significantly across the Bril-

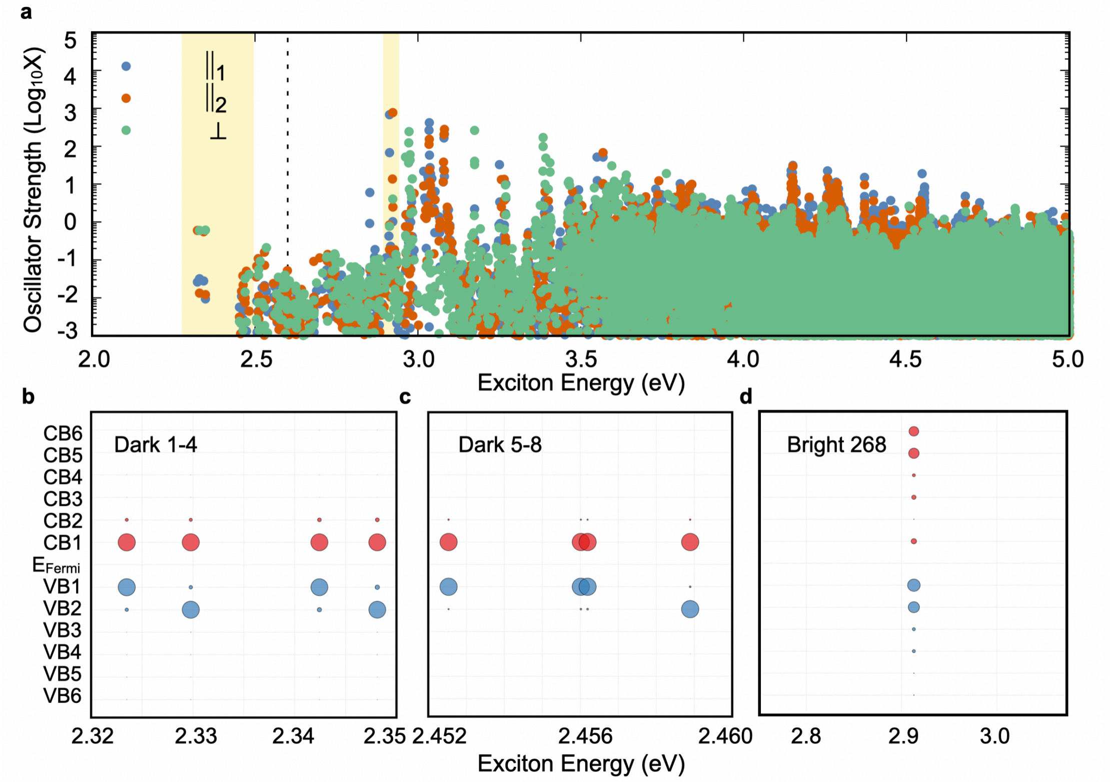

Figure 6.2: (a) Oscillator strength with e-h correlation of perovskite-intergrowth heterostructures **1-Li**. (b-d) Scatter plot of the exciton eigenvector decomposition obtained from the BSE calculation for **1-Li**. The size of each point is proportional to the magnitude of the contribution from a specific band-to-band transition, integrated over the Brillouin zone. Blue points in the upper half correspond to contributions from conduction bands, and red points in the lower half correspond to contributions from valence bands. All studied excitons are marked under a yellow area in the Oscillator Strength plot (a).

louin zone. In order to distinguish between interlayer and intralayer excitons, we need a more detailed analysis of these excited states at the atomic level.

In the next section, we will show a more comprehensive analysis of the band projections of the band contributions onto atomic orbitals. This additional step will allow us to trace the orbital contributions to specific layers and thereby distinguish between interlayer or intralayer excitons.

6.3 Exciton decomposition

With the aim to determine the spatial localisation of the excitons and identify interlayer and intralayer excitons, we extend our analysis beyond the visualisation presented earlier by combining the exciton eigenvectors with the atomic orbital projections of single-particle states. This approach allows us to decompose the exciton wavefunctions onto specific atomic orbitals, thereby providing atomic-level resolution of the excitonic characteristics.

Similar to the previous chapter, we start by analysing the eigenvector $|A_{vck}|^2$. Now, instead of integrating the weights all over the BZ, we focus on the k-resolved contribution. For a given exciton state S and a given valence band v_x, the weight of the exciton involving this particular valence band v_x at a particular **k**-point is given by the summation of the contributions from all conduction bands,

$$w_S(v_x, \mathbf{k}) = \sum_c \left| A^S_{(v_x)c\mathbf{k}} \right|^2 . \tag{6.4}$$

Similarly, the exciton weight for a specific conduction band c_x at **k** is:

$$w_S(c_x, \mathbf{k}) = \sum_v \left| A^S_{v(c_x)\mathbf{k}} \right|^2 . \tag{6.5}$$

The projection of a Bloch state $\psi_{n\mathbf{k}}$ onto an atomic orbital $|a, \nu\rangle$ is given by:

$$P_{n\mathbf{k}}(a, \nu) = |\langle a, \nu | \psi_{n\mathbf{k}} \rangle|^2 . \tag{6.6}$$

Here a labels the atom, and ν denotes the orbital character (e.g., s, p, d orbitals). These projections satisfy the orthogonality relations: $\langle a, \nu | a', \nu' \rangle = \delta_{a,a'} \delta_{\nu,\nu'}$, and for each band n and **k**-point, they sum to unity: $\sum_{a,\nu} P_{n\mathbf{k}}(a, \nu) = 1$.

By combining the exciton weights with the above atomic orbital projections, we can compute the decomposition of the exciton wavefunction onto specific atomic orbitals. For the electron, the decomposition is expressed as:

$$D_e\left(a_e, \nu_e\right) = \sum_{\mathbf{k},v} w_S(v, \mathbf{k}) P_{n\mathbf{k}}(a_e, \nu_e). \tag{6.7}$$

Similarly, for the hole:

$$D_h\left(a_h, \nu_h\right) = \sum_{\mathbf{k},c} w_S(c, \mathbf{k}) P_{n\mathbf{k}}(a_h, \nu_h). \tag{6.8}$$

These summations effectively weigh the contribution of each atomic orbital to the exciton wavefunction. Finally, to identify inter- or intra-layer excitons, we can sum these weights to map the exciton onto specific regions within the heterostructure.

Similar to the previous chapter, we focused our analysis on three key exciton states: the first (dark) exciton and the bright exciton under parallel-polarised light in **1-Li**, and the first (bright) exciton in **1-Na**. The contributions of electrons and holes from different regions within the heterostructure were calculated using Equations (6) and (7). The results are summarised in Table 6.1 and visualised in Figure 6.3. In the figure, the contributions from the perovskite layers are plotted in the upper half, while the combined contributions from the non-perovskite components (intergrowth layer, oxygen, Li/Na, and molecules) are plotted in the lower half. Electron contributions are depicted in blue, and hole contributions are depicted in red.

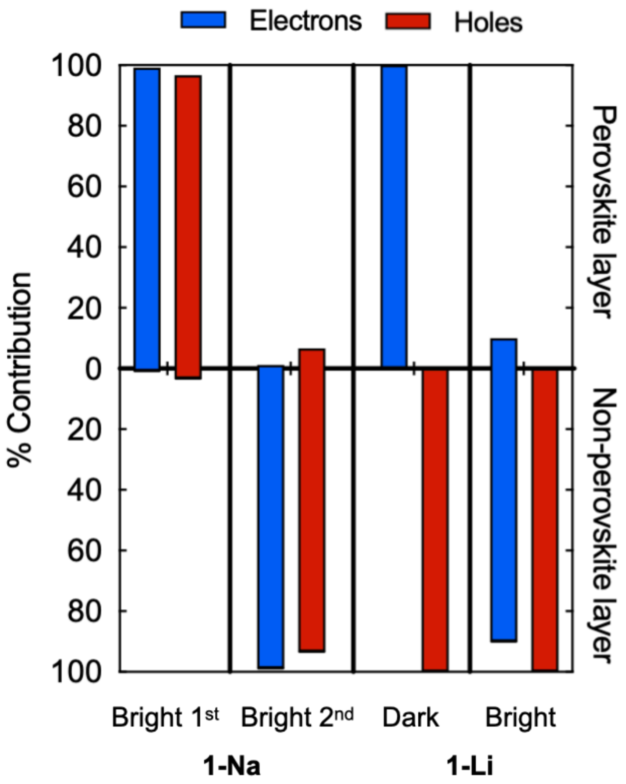

Figure 6.3: Visualisation of the electron and hole contributions for selected exciton states in **1-Na** (bright excitons corresponds first peak and second peak of absorption spectra) and in **1-Li** (first dark and bright excitons). The perovskite contributions are shown in the upper half, while the combined non-perovskite contributions (intergrowth layer, oxygen, Li/Na, and molecules) are shown in the lower half. Electron contributions are plotted in blue, and hole contributions are plotted in red.

For the first (dark) exciton in **1-Li**, the electron is almost exclusively localised within the perovskite layer. The hole, however, is predominantly distributed across the non-perovskite layer (with 38.56% on the Pb and Cl, 41.04% on the O atoms and 20.37% on the molecular cations), with negligible contributions from the perovskite layer and Li atoms. This significant spatial separation between the electron and hole indicates an *interlayer exciton*, a result consistent with Type II band alignment.

In contrast, the bright exciton in **1-Li**, with higher energy, exhibits a different distribu-

Table 6.1: Electron and hole contributions from different regions of the heterostructure for selected exciton states, expressed as percentages.

Exciton state	**Electron contributions**				
	Perovskite	Intergrowth	O	Li/Na	Molecule
1-Li Dark	100.00	0.00	0.00	0.00	0.00
1-Li Bright	10.05	74.43	3.54	10.72	1.26
1-Na Bright 1st	99.22	0.52	0.02	0.15	0.10
1-Na Bright 2nd	1.22	90.37	5.79	2.39	0.22
	Hole contributions				
	Perovskite	Intergrowth	O	Li/Na	Molecule
1-Li Dark	0.03	38.56	41.04	0.00	20.37
1-Li Bright	0.08	34.47	42.76	0.00	22.69
1-Na Bright 1st	96.67	1.47	1.86	0.00	0.00
1-Na Bright 2nd	6.77	44.99	48.23	0.00	0.01

tion. The electron is mainly localised within the non-perovskite layer, with substantial contributions from Pb and Cl (74.43%), Li atoms (10.72%) and O (3.54%), while the Pb and Cl of the perovskite layer contributes only 10.05%. The hole is distributed similarly to the dark exciton, with the majority of the weight on oxygen atoms (42.76%), the intergrowth layer (34.47%), and molecular entities (22.69%). The perovskite layer again contributes minimally. This exciton displays characteristics of an *intralayer exciton* within the non-perovskite layer, consistent with our observations.

For the first exciton in **1-Na**, corresponding to the first peak in the absorption spectra, the electron is almost exclusively localised within the perovskite layer (99.22%), with negligible contributions from other components. The hole shows a similar distribution, predominantly localised in the perovskite layer (96.67%), with minimal contributions from the non-perovskite layer $PbCl_2$ (1.47%) and O atoms (1.86%). The localisation of both electron and hole within the perovskite layer clearly indicates an intralayer exciton confined in the perovskite layer.

The exciton that corresponds to the second peak in the absorption spectra of **1-Na**, shows a different real space localisation. The electron is primarily localised within the non-perovskite layer, with dominant contributions from $PbCl_2$ (90.37%), and minor contributions from O atoms (5.79%) and Na atoms (2.39%). The perovskite layer only accounts for 1.22% of the real space localisation for the electron component. The hole is mostly distributed between O atoms (48.23%) and $PbCl_2$ in the intergrowth layer (44.99%), with the perovskite layer contributing 6.77%. This is consistent with an intralayer exciton within the intergrowth layer.

6.3.1 Correlation between band alignment and excitons

The exciton decompositions points to a correlation between band alignment and exciton localisation. In both structures, the band alignment appears to play a pivotal role in facilitating the formation of inter- or intralayer excitons. Specifically, in layered heterostructures, Type II band alignment tends to promote the formation of interlayer excitons whereas Type I band alignment usually corresponds to intralayer excitons. This correlation arises because, in Type II heterostructures, the valence band maximum and conduction band minimum reside in different layers. Upon optical excitation, electrons and holes in the lower lying excitons are naturally separated into these distinct layers, leading to interlayer exciton formation. In contrast, Type I heterostructures have both VBM and CBM located within the same layer, facilitating electron-hole overlap and intralayer exciton formation.

The spatial localisation of excitons has profound implications for exciton characteristic and, consequently, for the optoelectronic properties of these materials. Interlayer excitons, as observed in the dark exciton of **1-Li**, are expected to exhibit longer lifetimes and reduced radiative recombination rates due to the physical separation of electrons and holes [61]. This makes them attractive for applications requiring long-lived excitonic states, such as exciton-based information processing or long-range energy transport [53].

In contrast, intralayer excitons, as seen in the bright exciton of **1-Na**, are associated with a stronger confinement within this layer, and with higher oscillator strengths, leading to enhanced optical absorption and emission [224]. These properties are desirable for applications in light-emitting diodes and lasers [224, 225].

The atomic orbital decomposition analysis presented above provides a comprehensive understanding of the excitonic states in perovskite-intergrowth heterostructures. Our findings reveal that the nature of lowest lying excitons - whether interlayer or intralayer - is strongly influenced by the band alignment. Identifying the nature of band alignment thus provides an indicator for predicting excitonic behaviour in layered heterostructures.

Upon establishing this correlation between band alignment and exciton localisation, an intriguing question naturally arises: what underpins the difference in band alignment between materials with seemingly similar structures? Take the above case as an example, **1-Na** and **1-Li** share remarkable structural similarities, yet they exhibit different band alignments and excitonic behaviours. As shown in the previous chapter, while **AMTP** and **4ATP** have similar structures (the **4ATP** structure was hypothetically constructed based on the minimal variation of **AMTP**), they differ in their electronic properties: **AMTP** exhibits a Type I band alignment, whereas **4ATP** shows a Type II alignment. On the other hand, **HMA**, which has a somewhat different configuration from the former two, also shows a Type II band alignment. This observation suggests that subtle variations in composition or structural parameters can lead to significant changes in electronic properties.

This discrepancy raises fundamental questions about the origin of band alignment differences in these heterostructures. Understanding why materials like **1-Na** and **1-Li**, despite their structural similarities, exhibit different band alignments is essential for the rational design of heterostructures with desired excitonic properties. It indicates that factors beyond simple structural features - such as specific atomic compositions, local distortions, charge distribution or electrostatic effects - may play a critical role in determining the band alignment.

In the following section, we will demonstrate a detailed analysis of the structural and electronic differences between **1-Na** and **1-Li** to uncover the possible reasons behind their distinct band alignments and identify specific elements that influences excitonic properties, ultimately guiding the rational design of heterostructures with desired opto-electronic and exciton characteristics.

6.4 Origin of band alignment change

6.4.1 Atomic composition

The first factor we consider is the atomic composition. To determine whether the atomic composition - the presence of Li or Na in this case - is responsible for the different band alignments observed in **1-Li** and **1-Na**, we conducted a substitutional study. In this approach, we replaced the Li atoms in **1-Li** with Na atoms, and conversely, replaced the Na atoms in **1-Na** with Li atoms, while keeping all other structural configurations unchanged (*i.e.* lattice parameters and atomic positions).

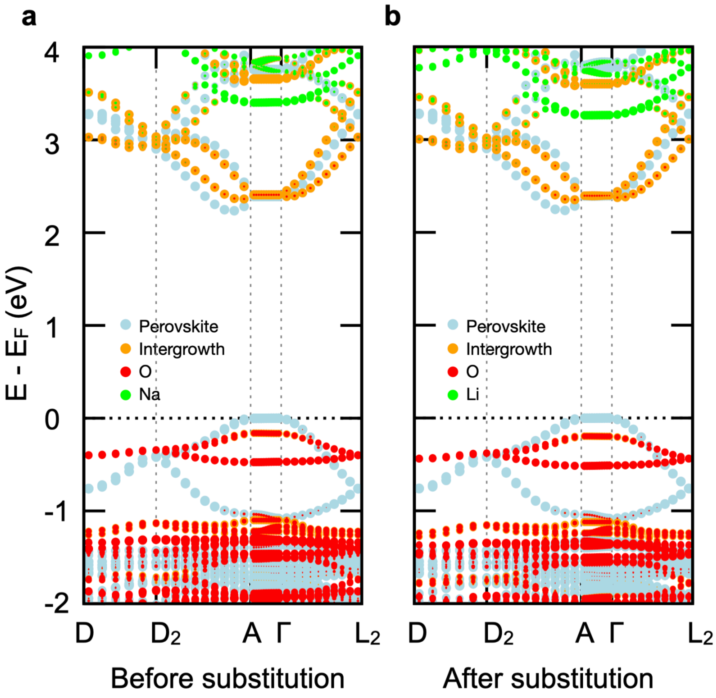

Figure 6.4: Comparison of the band structures for **1-Na** structure (a) and the modified **1-Na** structure where Na has been replaced with Li (b). The alkali metal contributions (Li/Na) are highlighted in green, O in red, the Pb and Cl of intergrowth layer in orange, and the perovskite bands in light blue.

Our calculations revealed that the band structures of both "substituted" systems remains unchanged compared to their original counterparts as shown in Figures 6.4 and 6.5. The overall band dispersions, band gaps, and projected band characters showed negligible differences after substituting Li with Na and vice versa without changing the structure.

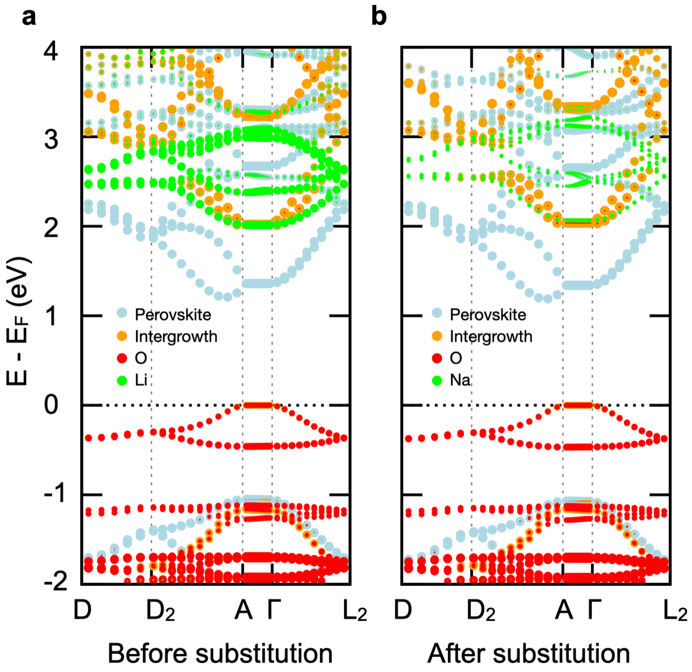

Figure 6.5: Comparison of the band structures for **1-Li** structure (a) and the modified **1-Li** structure where Li has been replaced with Na (b). The alkali metal contributions (Li/Na) are highlighted in green, O in red, the Pb and Cl of intergrowth layer in orange, and the perovskite bands in light blue.

The results suggest that the atomic composition of the alkali metal alone does not account for the differences in band alignment between **1-Li** and **1-Na**, we then proceed to explore other potential factors that might impact the band alignment. Specifically, we turn to the electronic characteristics of the individual layers and their interactions within the heterostructures.

6.4.2 Contribution of perovskites and intergrowth layers to the band structure

To investigate the role of interlayer interactions and the intrinsic properties of the perovskite and intergrowth layers, we isolate the perovskite and intergrowth layers from the heterostructure and analyse their individual electronic properties. The goal is to understand how each contributes to the overall band structure and how their interactions might influence the band alignment.

Figures 6.8a and b show the side views of the isolated intergrowth and perovskite structures for **1-Na**, respectively. Similarly, Figures 6.9a and b display the side views of the isolated intergrowth and perovskite structures for **1-Li**. To maintain the bond connectivity and relative chemical environment, Li/Na and O atoms (with a connecting C) were kept in the intergrowth part, while the remaining part of the molecule was allocated to the perovskite layer.

We introduced H atoms at the positions where covalent bonds were cleaved during the separation. All other structural parameters were kept unchanged to minimise any artificial effects arising from structural modifications. This preserves the molecular structures and ensures that the isolated layers remain representative of their original states.

Figure 6.6c shows the band structure for the original **1-Na**, while Figures 6.6d and 6.6e present the band structures for the isolated intergrowth and isolated perovskite layers, respectively. Similarly, Figures 6.7c–e display the corresponding band structures for original **1-Li** and corresponding sub-structures.

We noticed that the valence band dispersion of the isolated intergrowth layers is slightly larger than that of the original structures, which is attributed to the absence of the organic molecules. However, the band gaps of the isolated substructures remain relatively unchanged from those of the original structures.

Other than the slight difference for the intergrowth, the general shapes of the bands and the projected band characters remains consistent before and after isolation. This consistency in band shapes and dispersions indicates that the electronic states of the perovskite and intergrowth layers are relatively independent - the interaction between the layers is negligible and the bands remain their intrinsic characteristics upon isolation.

We also observe the similarity between the isolated perovskite layers of **1-Na** and **1-Li** as shown in Figure 6.6e and 6.7e. This is expected as there are no significant differences in the structure or composition of the perovskite sublattice between the two materials.

This suggests that any differences in the overall band alignment are unlikely to originate from the perovskite layers themselves.

In contrast, the isolated intergrowth layers exhibited notable differences between **1-Na** in Figure 6.6d and **1-Li** in Figure 6.7d. Specifically, we observed a substantial difference in the bandwidth of the valence band top and in the projections of the conduction bands, particularly in the alkali states depicted in green. The valence band top of the intergrowth layer in **1-Li** is notably wider than that in **1-Na**, and the conduction band projections indicate a stronger contribution from Li in **1-Li** compared to Na in **1-Na**. These discrepancies are likely associated with subtle structural distortions and rearrangements of atoms and/or charges within the intergrowth layers. Such variations in the electronic properties of the intergrowth layers could play a critical role in influencing the band alignment in the full heterostructures.

By isolating the layers and showing that their electronic structures are well separated and largely unaffected after isolation, we provide evidence that the differences in band alignment are not due to intrinsic electronic property of the perovskites sublattice, the strong electronic coupling or hybridisation between the perovskite and intergrowth layers. Instead, the primary factors driving the band alignment differences may lie in the subtle differences in the intergrowth parts (i.e. alkali metals, molecules and inorganic sublattices). This sets the stage for a more detailed investigation on how these elements within the intergrowth layers affect the overall electronic behaviour of the heterostructures.

6.4.3 Impact of structural optimisation

Following the isolation, which suggested that the structure of the intergrowth layer might influence the band alignment, we perform variable-cell structural relaxations using DFT-PBE in order to further investigate the structural origin of the band alignment change. Both lattice parameters and atomic positions were optimised to achieve the lowest pos-

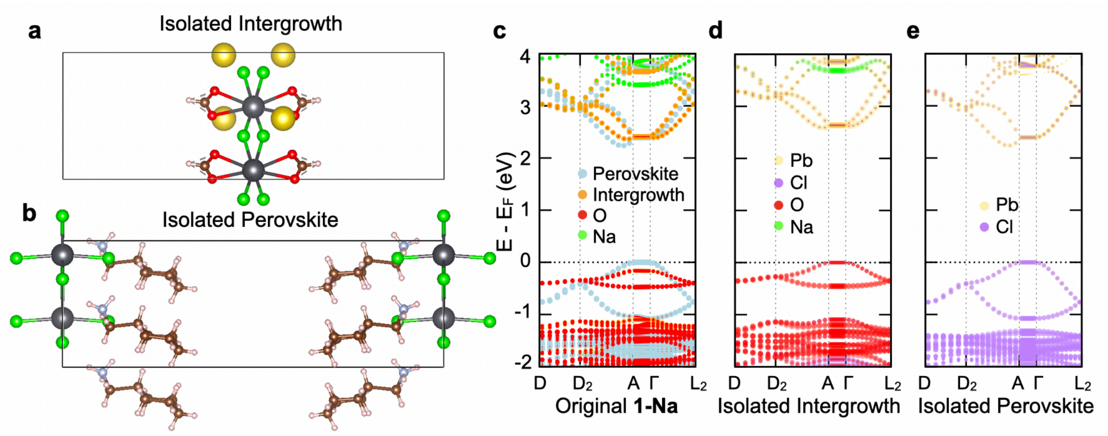

Figure 6.6: The band structure of the isolated sublattices (intergrowth and perovskite layers) compared to the original **1-Na** heterostructure. Bands are colour-coded based on composition: alkali metal (Na) in green, O in red, Pb in yellow and Cl in purple; the combined $PbCl_2$ of intergrowth layer in orange, and combined perovskite bands in light blue.

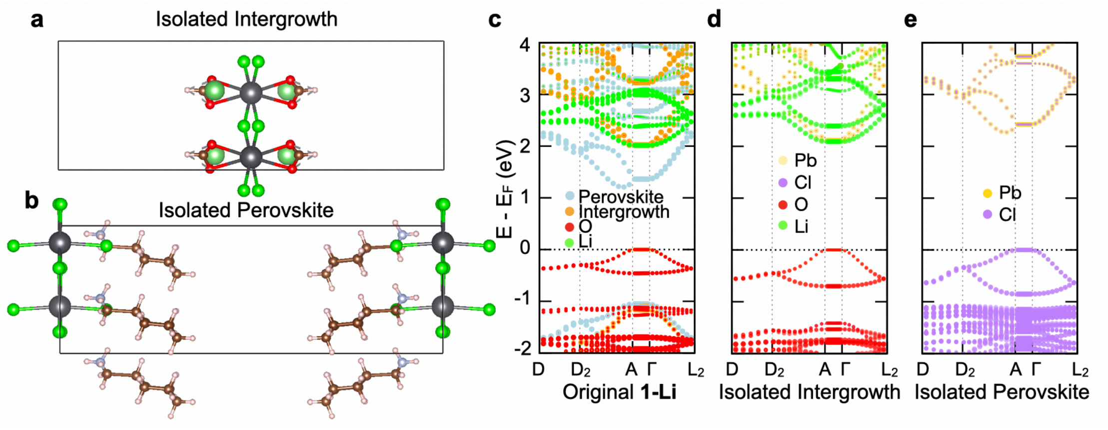

Figure 6.7: The band structure of the isolated sublattices (intergrowth and perovskite layers) compared to the original **1-Li** heterostructure. Bands are colour-coded based on composition: alkali metal (Li) in green, O in red, Pb in yellow and Cl in purple; the combined $PbCl_2$ of intergrowth layer in orange, and combined perovskite bands in light blue.

sible total energy configuration for each structure.

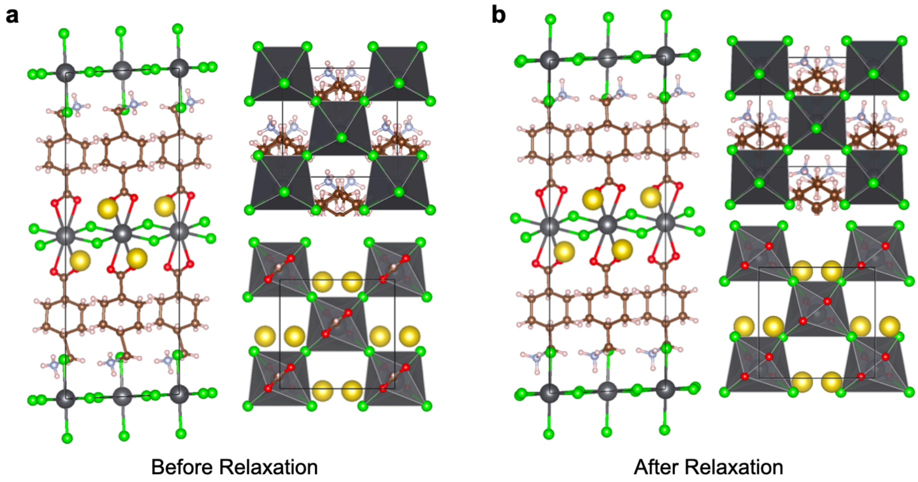

Figure 6.8: Structural changes in **1-Na** before (a) and after relaxation(b). For each panel, the side view of the full structure are shown in the left, and top views of the intergrowth and perovskite layers are shown in the right. colour coding of the atoms: grey spheres represent Pb, small green spheres represent Cl, red spheres represent O, and yellow spheres represent Na.

The relaxed structures and their corresponding band structures are presented in Figures 6.8, 6.9, 6.10 and 6.11. As shown in Figures 6.8 and 6.9, for both structures, we observe the structural changes in the perovskite layers upon relaxation, reflected in bond angles and shape of the octahedra. To quantify the structural changes, we calculated the in-plane (D_{in}) and out-of-plane (D_{out}) structural distortion parameters as shown in Table 6.2 (calculation details can be found in Appendix A.3.5). Both structures showed significant changes in their distortion parameters of the perovskite parts upon relaxation. These substantial changes in distortion parameters indicate considerable reorganisation of the octahedral networks in both structures. As a result, the band dispersion and width of the perovskite states changed significantly after relaxation in both **1-Na** and **1-Li**, as shown in Figures 6.10 and 6.11.

We also observe a different behaviour in the relaxation of the alkali metal atoms between **1-Na** and **1-Li**. Before the structure relaxation, the Li atom is well-centred within the cavity of the individual intergrowth layers, while for **1-Na**, Na is significantly off-centre, closer to the bridging Cl atoms, as shown in Figure 6.8 and 6.9.

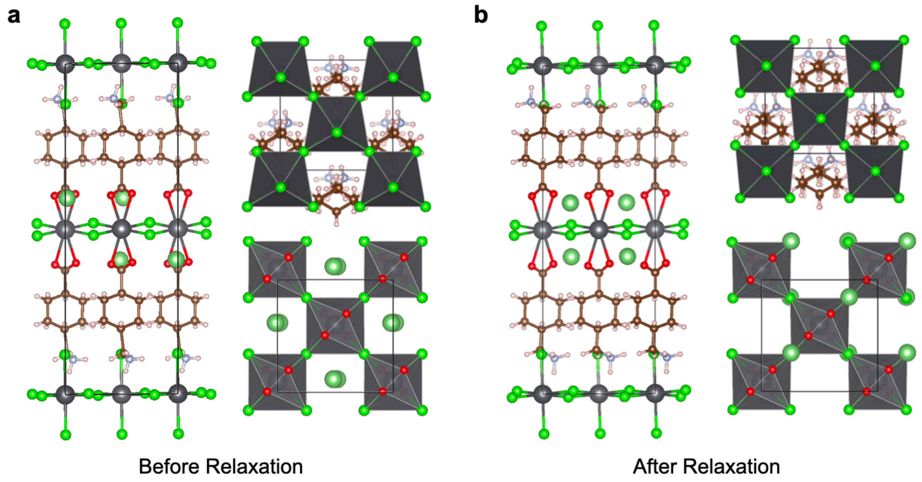

Figure 6.9: Structural changes in **1-Li** before (a) and after relaxation(b). For each panel, the side view of the full structure are shown in the left, and top views of the intergrowth and perovskite layers are shown in the right. colour coding of the atoms: grey spheres represent Pb, small green spheres represent Cl, red spheres represent O, and yellow spheres represent Li.

Heterostructure	Layer	Experimental			Relaxed		
		D_{in}	D_{out}	D_{tilt}	D_{in}	D_{out}	D_{tilt}
1-Na	Perovskite	21.3	0	21.3	4.1	1.0	4.3
	Non-perovskite	11.4	8.5	14.2	19.7	9.5	21.8
1-Li	Perovskite	22.8	0.06	22.8	10.3	3.1	10.7
	Non-perovskite	0.9	6.1	6.2	2.6	5.2	5.8

Table 6.2: Comparison of structural distortion parameters (°) for the perovskite and non-perovskite layers of the layered heterostructure before (Experimental) and after (Relaxed) structural optimisation.

In **1-Na**, the structural relaxation did not lead to significant changes to the intergrowth layer or the position of the Na atom within the intergrowth cavity. The Na atom remains relatively stationary, from (0.628, 0.980, 0.578) to (0.626, 0.967, 0.577) in crystal coordinates, and the overall intergrowth structure preserved its original configuration. As a result, the bands associated with the intergrowth layer did not exhibit substantial shifts in **1-Na** as shown in Figure 6.10.

In contrast, **1-Li** exhibited substantial structural rearrangements near the intergrowth cavity upon relaxation. The Li atom shifted from its initial position at the centre between two bridging Cl atoms (0.484, 0.117, 0.595) to a new position directly above one of the bridging Cl atoms (0.254, 0.347, 0.582).

For **1-Li**, the valence band maximum of the intergrowth layer (depicted in orange and red) moved to a significant lower energy relative to the perovskite VBM (depicted in blue). In addition, the valence bands widths of the intergrowth layer also increases drastically. These changes are attributed to the altered electronic environment caused by the new position of the Li atoms and the resulting changes in orbital interactions within the intergrowth layer.

For conduction bands in both **1-Na** and **1-Li**, there was red-shift of the conduction band minimum due to the relaxation of the perovskite layer towards optimised configurations. The splitting between the lowest 2 conduction branches was reduced in both structures after relaxation. This reduction in splitting can be directly associated with a decrease in the distortions within the perovskite lattice, which are known to induce splitting via the Rashba effect. This effect was particularly pronounced in **1-Na**, where the splitting nearly vanished, resulting in a transition to a direct band gap semiconductor. Additionally, after the relaxation, the CBM no longer exhibited hybridisation between the perovskite and intergrowth states.

Despite the changes in band dispersion and width caused by structural reconfiguration

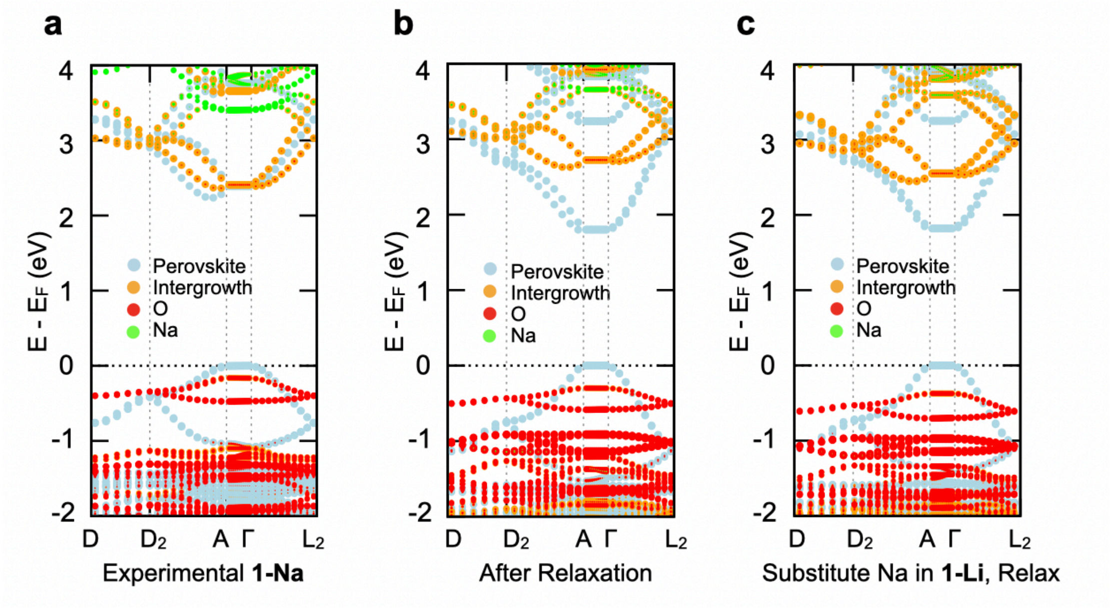

Figure 6.10: (a) Band structure of the original **1-Na** (a) before structural relaxation and (b) after relaxation; (c) Band structure for the **1-Li** structure where Li is substituted with Na, followed by structural optimisation.

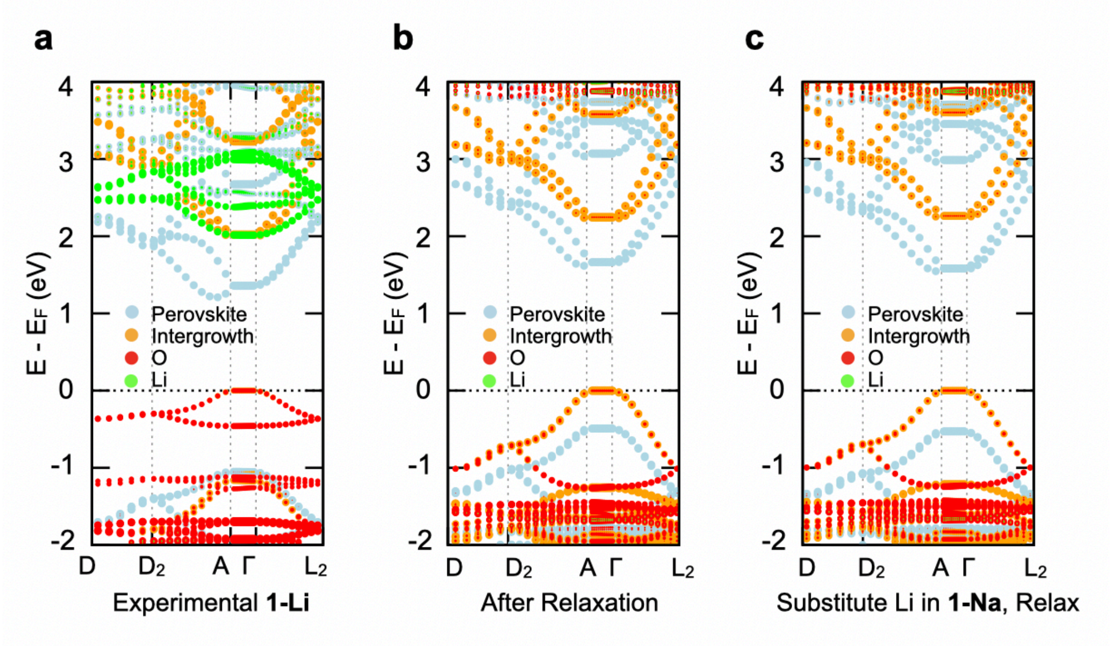

Figure 6.11: (a) Band structure of the original **1-Li** (a) before structural relaxation and (b) after relaxation; (c) Band structure for the **1-Na** structure where Na is substituted with Li, followed by structural optimisation.

and relaxation, the Type II and Type I band alignments were preserved for **1-Li** and **1-Na**, respectively, as illustrated in Figure 6.10b and 6.11b.

To further probe the effect of the alkali metal cations, we perform structural relaxations starting from the hypothetical structures where the Li and Na atoms were swapped: We replaced the Na atoms in **1-Na** with Li atoms, while keeping all other structural configurations consistent with **1-Na** ($i.e.$ lattice parameters and atomic positions). Subsequent structural relaxation yielded a structure and band alignment remarkably similar to that of relaxed **1-Li**. Similarly, substituting Na into the **1-Li** structure and performing structural relaxation resulted in a structure and band alignment nearly identical to the relaxed **1-Na**. These tests indicate that the presence of Li or Na determines the final relaxed structure and thus band alignment, irrespective of the starting configurations.

The different site positions of two alkali metals in the intergrowth cavity can be attributed to their ionic sizes and electrostatic interactions. Li has a smaller ionic radius and higher charge density compared to Na, allowing it to move more readily within the intergrowth cavity and interact strongly with surrounding atoms. This mobility leads to structural distortions and significant modifications in the electronic structure. Na, being larger in size, remains in its initial position, resulting in relatively smaller structural changes around the intergrowth cavity.

The structural relaxation study reveals that the charged alkali metals play a critical role in determining the structural and electronic properties of the heterostructures. Combined with the observations from “swapping experiments” above and hypothetical structures in the previous chapter - where altering the shape and size of the molecule effectively leads to charge redistribution, these findings suggest that the rearrangement of charge distribution caused by the relocation of charged atoms or functional groups may be the key factor to influence the relative positions of intergrowth and perovskites bands. While the reconfiguration of the structures in intergrowth and perovskites sublattices might just have a secondary effect via tuning the band width and dispersion intrinsically.

In the next section, we will explore the charge redistribution and electrostatic potential variations associated with cation movement. By analysing the charge density differences and potential landscapes, we aim to further understand the mechanisms underpinning the band alignment changes observed in these heterostructures.

6.4.4 Electrostatic potential landscape

To systematically investigate the mechanism underlying the band alignment transition, we analyse the electrostatic potential variations induced by the movement of Li cations. Specifically, we perform a series of calculations where the Li atom was incrementally moved along the direction perpendicular to the layers (the z-axis) in steps of approximately 0.223 Bohr (0.25% of the perovskite-intergrowth interlayer distance). At each step, all other atomic positions were kept fixed to isolate the impact of Li's position alone.

For each Li site position, we compute the planar-averaged electrostatic potential (V_{bare} + V_H) along the z-direction, as well as the band offset between the intergrowth layer and the perovskite layer (the energy difference between the first band from the perovskite component and first band from the intergrowth component). The potential difference was calculated as the difference between the potential at the centre of the intergrowth layer (orange dot) and that at the centre of the perovskite layer (blue dot). The results of these calculations are summarised in Table 6.3 and visualised in Figure 6.12.

As shown in Figure 6.12a, the movement of Li atoms leads to systematic changes in the electrostatic potential profile across the heterostructure. As Li moves towards the perovskite layer (in the positive z-direction), we observe an increase in the potential difference between the intergrowth and perovskite regions. This change in potential difference exhibits a strong correlation with the band offset between the two layers, as indicated by the linear relationship shown in Figure 6.12b.

To understand the origin of these potential variations, we analyse the charge density

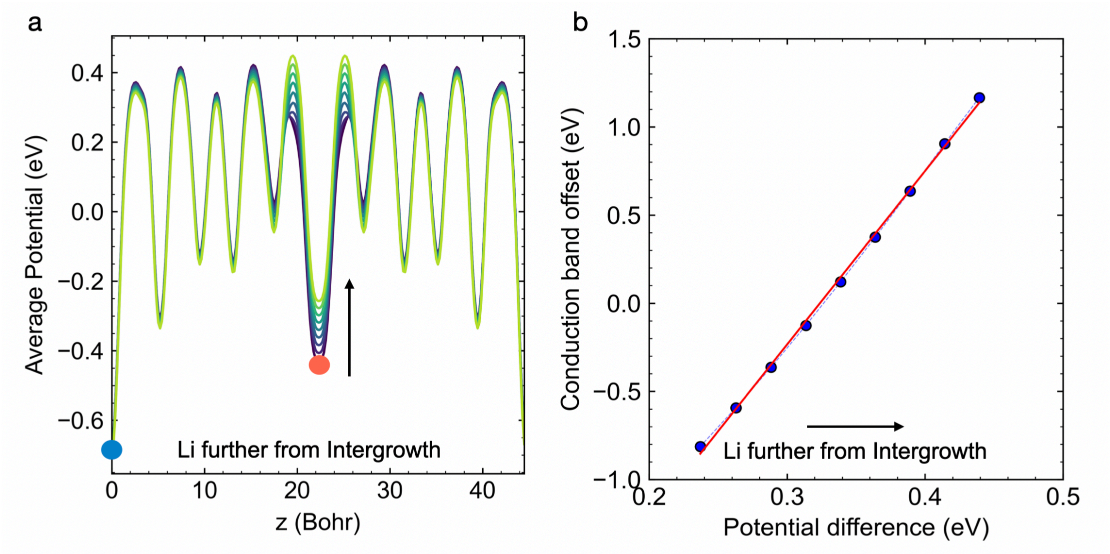

Figure 6.12: (a) Planar-averaged electrostatic potential along the z-direction for different Li positions in **1-Li**. The potential profiles correspond to different positions of the Li atom, with the direction of movement indicated by the arrow. (b) Correlation between the potential difference and the band offset, showing a linear relationship. The data points correspond to different positions of the Li atom.

Table 6.3: Relationship between Li position, band offset, and potential difference across the heterostructure in **1-Li**. Positive positions correspond to movement towards the perovskite layer.

Li position (Bohr)	Band offset (eV)	Potential difference (eV)
-0.669	-0.811	0.237
-0.446	-0.592	0.263
-0.223	-0.363	0.288
0.000	-0.125	0.314
0.223	0.121	0.339
0.446	0.375	0.364
0.669	0.637	0.389
0.892	0.905	0.414
1.116	1.167	0.439

redistribution associated with Li movement. Figure 6.13 shows the charge density difference ($\Delta\rho$) with respect to the configuration where the Li are placed closest to the intergrowth layer, along the z-direction for different Li positions.

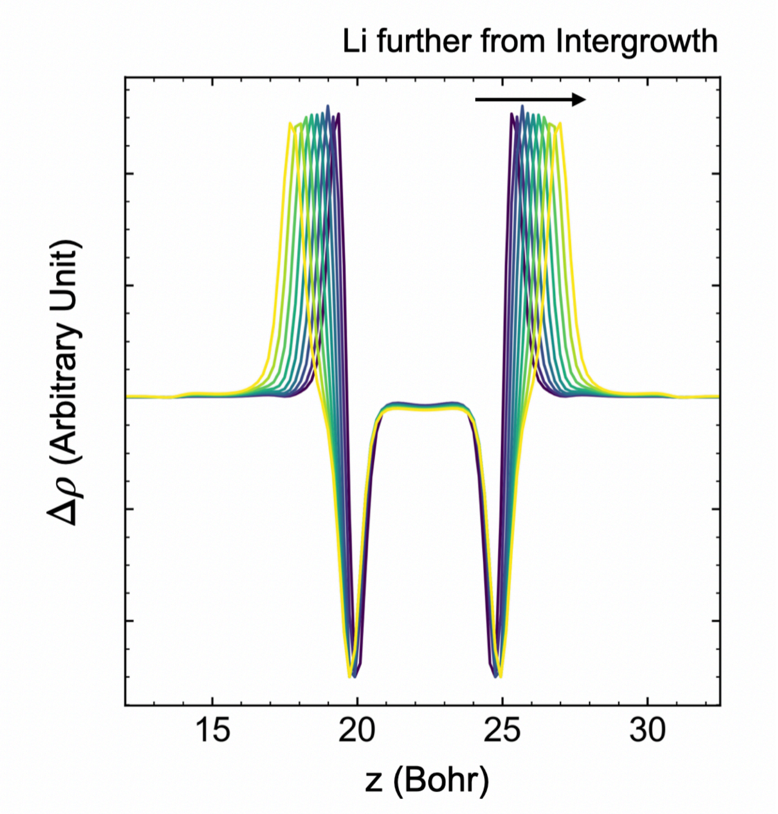

Figure 6.13: Planar-averaged charge density difference ($\Delta\rho$) along the z-direction for different Li positions in **1-Li**, with a reference to the configuration where Li are closest to the intergrowth. The profiles illustrate how the movement of Li ions induces charge redistribution across the heterostructure.

The charge density analysis reveals that the movement of Li ions induces charge redistribution within the intergrowth layer. This redistribution directly affects the electrostatic potential landscape across the heterostructure, which in turn influences the relative alignment of electronic energy levels between the intergrowth and perovskite layers. The linear relationship between the potential difference and band offset suggests that the electrostatic effects arising from charge redistribution play a important role in determining the band alignment in these systems.

These findings provide a mechanism for understanding how structural modifications, particularly the position of charged species between layers, can be used to tune the electronic properties of similar heterostructures via changing the electrostatic potential landscape.

6.5 Summary

In this chapter, we explored the origins of inter/intra layer excitons in perovskite-intergrowth heterostructures.

We decompose the exciton wavefunctions into their constituent atomic orbitals contributions, from first-principles calculations and eigenvector analysis. This quantitative approach allowed us to uncover the electronic contributions and spatial localisations of excitons, and identify inter/intralayer excitons in heterostructures like **1-Na** and **1-Li**.

Our analysis revealed a clear correlation between band alignment and exciton localisation. Specifically, Type II band alignment could be associated with the formation of interlayer excitons due to the spatial separation of the valence band maximum and conduction band minimum across different layers, while Type I band alignment tends to correlate with intralayer excitons formation, where electrons and holes reside within the same layer. This correlation not only provides a deeper understanding of excitonic behaviour but also offers a predictive indicator for designing heterostructures with desired excitonic/charge transfer character.

In order to investigate the origin of band alignment differences between structurally similar materials like **1-Na** and **1-Li**, we conducted substitutional study, layer isolation, and structural relaxation analysis.

By performing linear interpolations of the alkali metal positions, we demonstrate that the band alignment can be effectively tuned by changing the electrostatic potential landscape induced by the charged cations. The correlation between the cation position, electrostatic potential, and band offset underscores the importance of dipolar effects and charge redistribution in determining the electronic structure of these heterostructures.

In conclusion, this chapter provides a comprehensive understanding of the intricate relationship between band alignment, exciton localisation, and structural factors in perovskite-intergrowth heterostructures. We established that band alignment is a key determinant of exciton behaviour and that it can be manipulated through molecular and structural engineering, particularly by adjusting the positions of charged species within the intergrowth layers. These insights pave the way for the rational design of novel materials with tailored optoelectronic properties, offering promising avenues for advanced applications in photovoltaic, light-emitting devices, and exciton-based information processing.

7 | Conclusions

7.1 Summary

The studies presented in this thesis focus on investigating the optoelectronic and excited-state properties and their tunability of perovskite-based materials using first-principles calculations, specifically on three groups of systems: mixed halide perovskites, layered perovskites, and perovskite-intergrowth heterostructures.

In Chapter 3, the study of mixed halide perovskites, we demonstrate that the VCA can provide a computationally efficient yet sufficiently accurate framework for modelling the mixed-halide $CsPb(Br_xI_{1-x})_3$ series. By combining VCA with GW+BSE calculations, we successfully reproduced experimental trends in structural parameters, vibrational properties, and optoelectronic characteristics across the entire mixing range. Our calculations revealed that the tunability of properties primarily arises from uniform mixing rather than disorder effects. The work presented provides a reliable theoretical framework for studying mixed ion perovskites and laying the groundwork for understanding how structural modifications influence optoelectronic properties in perovskite materials.

This insight into property tunability naturally led us to investigate lower-dimensional systems, specifically Dion-Jacobson/Ruddlesden-Popper layered perovskites, where additional structural degrees of freedom offer even greater potential for property tunability. By developing and applying the ECF analysis, we revealed that exciton delocalisation can be systematically tuned through interlayer spacing and alignment. Notably, we demonstrate that reducing interlayer spacing below a certain threshold (around 12 Å) in Dion-Jacobson phases enables significant interlayer exciton delocalisation, with average e-h separation exceeding over the interlayer distance, while Ruddlesden-Popper alignment tends to confine excitons within a single layer. The ability to tune exciton delocalisation through structural parameters represents a significant advancement in our understanding of these materials and indicates structural origins to overcome the confinement of excitons in low-dimenensional perovskites.

The success of the ECF approach in analysing layered perovskites motivated a further exploration to more complex perovskite-intergrowth heterostructures. We establish a clear correlation between band alignment and exciton localisation through detailed analysis of both hypothetical and experimentally realised structures via a systematic investigation from first-principles results. Further investigation even reveals that band alignment, and consequently interlayer exciton character, can be controlled through the positioning of charged ions via modification of the electrostatic potential landscape.

7.2 Outlook

Throughout this thesis, we have progressively built the understanding of how structural and compositional modifications influence excitonic properties, moving from simple mixing in 3D systems to complex heterostructures. This systematic approach has revealed fundamental principles for controlling excited-state properties in perovskite materials, providing valuable guidance for the design of next-generation optoelectronic devices. Moving forward, several promising directions might emerge from this work:

The VCA framework has proven its effectiveness for capturing the ground state and even some excited state properties such as binding energies and optical spectra for mixed halide perovskites, its application could be extended to more complex and uniformly mixed-ion materials, particularly those involving multiple mixing sites or organic cations. An intriguing question could arise regarding the application of the exciton analysis methods presented here to these alloyed systems with VCA: how much can we understand the excitons (*e.g.*, the distribution or delocalisation) in complex materials with the "virtual atom" presented?

Additionally, the understanding of band alignment control through electrostatic effects in perovskite-intergrowth heterostructures opens new possibilities for designing materials with tunable excitonic properties. However, as we have discussed in the thesis, the optically dark interlayer excitons predicted by our calculations have yet to be experimentally observed. Developing theoretical frameworks to possibly guide experimental detection and characterisation of these states still remains an important challenge for future work.

Finally, while our work has extensively focused on mapping the real-space distribution of exciton wavefunctions, incorporating temperature effects and electron-phonon coupling into this analysis could be an interesting next step to explore. Understanding how thermal effects influence exciton transport and localisation will be essential for predicting material behaviour under realistic conditions.

These open questions present exciting challenges for the development of computational frameworks and new analytical tools for excited states. Addressing them through first-principles analysis not only deepens our understanding of these fascinating materials but will also guide the discovery of novel materials with tailored properties for a various applications. We hope that the research presented in this thesis will serve as a foundation for future investigations in this rapidly evolving field.

A | Appendix

A.1 Computational setup for Chapter 3

A.1.1 DFT calculations

First principles calculations are performed based on DFT using plane-wave pseudopotentials methods as implemented in the Quantum Espresso package (version 6.5). We employ fully-relativistic PBE norm-conserving pseudopotentials from the Pseudo Dojo repository, with the following valence electron configurations: Cs $5s^25p^66s^1$, Pb $5d^{10}6s^26p^2$, I $5s^25p^5$, Br $4s^24p^5$ and Cl $4s^24p^5$. The pseudopotentials of virtual halogen atoms are constructed using the virtual_v2.x utility in the Quantum Espresso package.

All calculations use a kinetic energy cutoff of 60 Ry and sample the Brillouin zone using a Γ centered $6\times6\times6$ Monkhorst-Pack mesh. The atomic positions and lattice parameters are fully optimised until the energy converges to less than 10^{-7} eV and the absolute value of force on the atom is less than 0.01 eV/Å. While structural optimisations are performed using a $6\times6\times6$ **k**-point grid without spin-orbit interactions, all other calculations reported throughout this work fully account for spin-orbit coupling.

We employ VCA by generating pseudopotentials for the virtual halide atom. This is achieved by linearly interpolating between the pseudopotentials of iodine and bromine. The plane-wave basis set and the Monkhorst-Pack **k**-point sampling remained the same as for the pure compounds. Structural optimisation was performed for each composition by relaxing both atomic positions and lattice parameters to account for the effects of halide mixing on the crystal structure. The calculated lattice constants shows linear dependence on the mixing ratio, consistent with Vegard's law.

We employ DFPT as implemented in the Quantum Espresso code to calculate vibrational properties of mixed halide systems. Normal vibrational modes are calculated within the harmonic approximation at the Brillouin zone center, using a dense grid of 12×12×12 for the ground state charge density. This setup achieves converged dielectric permittivity for $CsPbI_3$ and $CsPbBr_3$, as demonstrated in Figure A.1a. The IR absorption spectra are calculated using a Gaussian broadening corresponding to a full width at half-maximum (FWHM) of 0.6 THz to match experimental line shapes.

For all mixed species, atomic masses of virtual atoms are calculated by linearly interpolating between Br and I as the mixing ratio changes. The acoustic sum rule is applied to the interatomic force constants in all DFPT calculations.

A.1.2 Quasiparticle calculations

We calculate quasiparticle eigenvalues within the GW approximation as implemented in the BerkeleyGW package. One-shot G_0W_0 calculations are performed with a DFT-PBE starting point including spin orbit coupling. The frequency-dependent dielectric function is modelled via the Godby-Needs plasmon-pole model.

Convergence tests show that the quasiparticle band gap is converged within 50 meV for a grid density of 6×6×6, while the high frequency dielectric constant requires a denser sampling of 12×12×12 (Figure A.1a,b). Given that the quasiparticle band gap shows less sensitivity to the **k**-grid density, we employ a 6×6×6 grid for these calculations. In all cases we use a polarisability cutoff of 15 Ry and sum over 1000 bands, achieving converged quasiparticle corrections within less than 0.1 eV for both $CsPbI_3$ and $CsPbBr_3$ (Figure A.1c,d).

Both DFT and quasiparticle band structures are interpolated using maximally localised Wannier functions as implemented in the Wannier90 code. The initial guess for unitary transformations is constructed using p orbitals on Pb and halogen atoms, yielding 24 wannierised bands in total. The Wannier interpolated and DFT computed band structures show agreement within 1 meV in an energy window up to 2 eV above and below

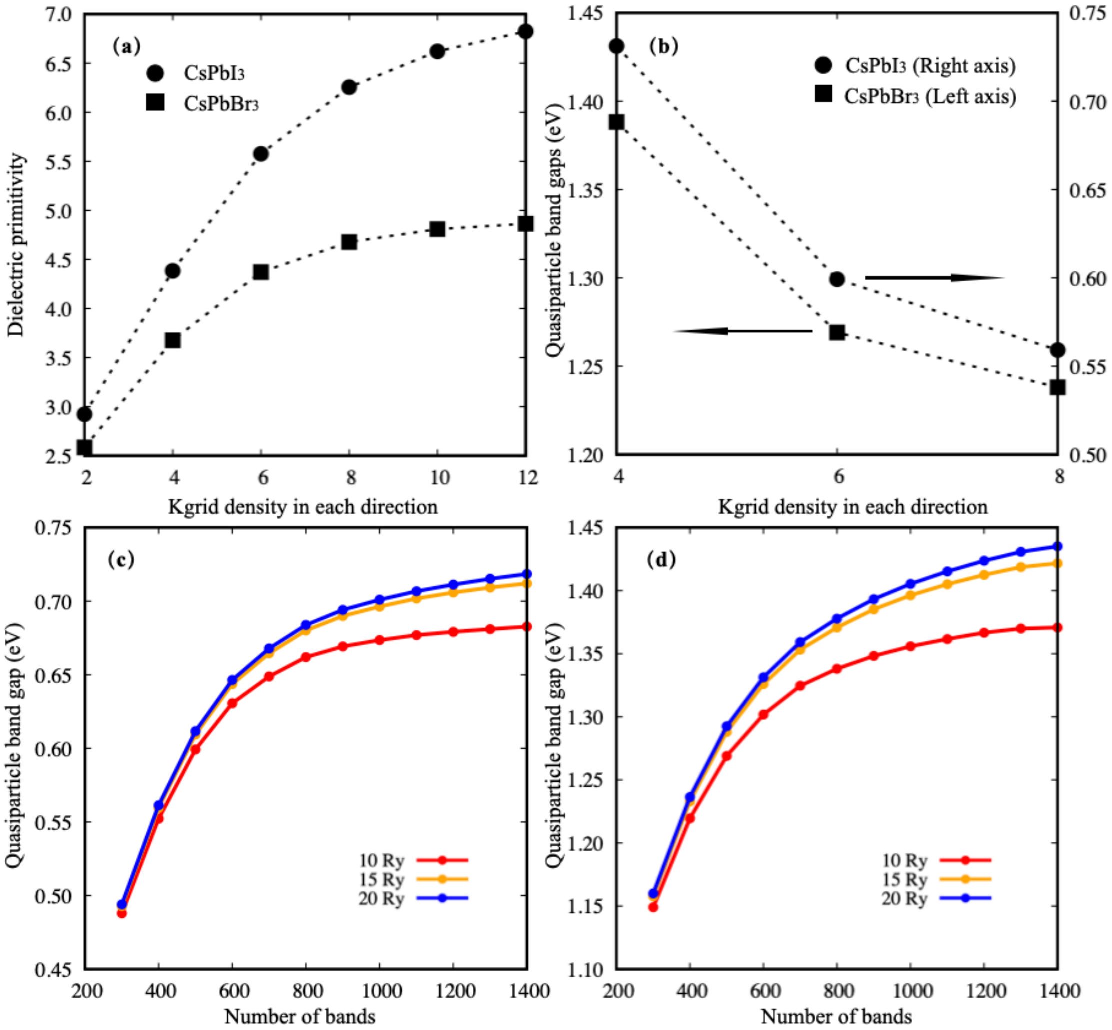

Figure A.1: (a) Convergence of high frequency dielectric constants ε_∞ for CsPbBr$_3$ (squares) and CsPbI$_3$ (disks) with respect to **k**-point grid density. (b) Convergence of quasiparticle band gaps with respect to **k**-point grid density for CsPbBr$_3$ (squares) and CsPbI$_3$ (disks). Convergence of quasiparticle band gaps with respect to the number of bands and polarisability cutoff for CsPbI$_3$ (c) and CsPbBr$_3$ (d), respectively.

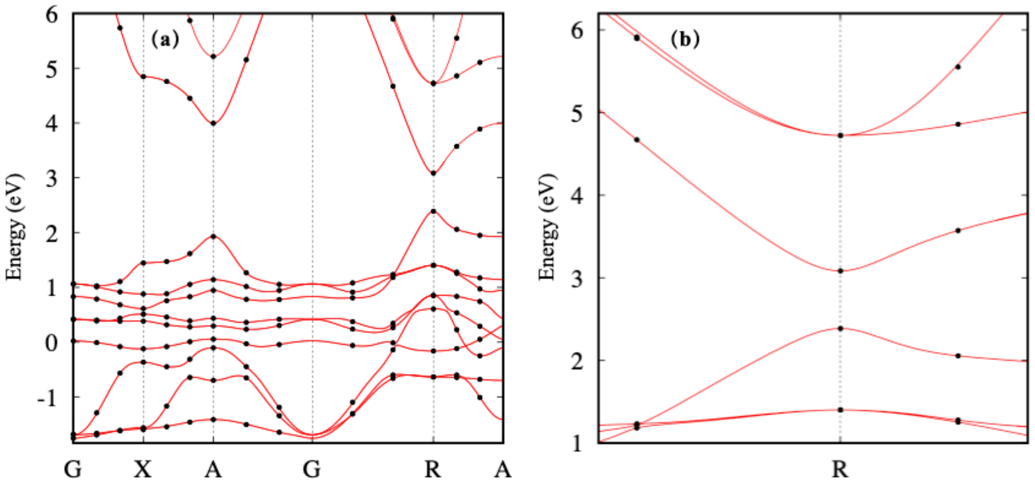

Figure A.2: Wannier interpolated band structure (red lines) overlayed with discrete quasiparticle eigenvalues (black dots) calculated for $CsPbI_3$. The left panel shows a full path band structure as indicated in the text above, the right panel shows a zoom-in figure at R, to better visualise the interpolation near the band edges.

the valence band top. The quasiparticle band structures are interpolated along path Γ (0, 0, 0) - X (0.5, 0, 0) - M (0.5, 0.5, 0) - Γ - R (0.5, 0.5, 0.5) - X using the Bloch to Wannier rotation matrices from the quasiparticle eigenvalues on a 6×6×6 grid. Tests against discrete quasiparticle energies confirm the same level of accuracy as in the DFT case (Figure A.2).

A.1.3 Optical excitation calculations

The optical absorption spectra including electron-hole interactions are calculated by solving the BSE within the Tamm-Dancoff approximation as implemented in BerkeleyGW [72]. The electron-hole kernel is constructed using 10 valence bands and 10 conduction bands on a coarse grid of 6×6×6 **k**-points, followed by interpolation to a fine grid of 40×40×40 **k**-points. The absorption spectrum calculations utilise 2 valence bands and 2 conduction bands (including spin degeneracy) in the fine grid. The absorption coefficient $\alpha(\omega)$ is calculated as $\alpha(\omega) = \frac{2\omega}{c}\sqrt{\frac{1}{2}\left(-\varepsilon_1(\omega) + \sqrt{\varepsilon_1^2(\omega) + \varepsilon_2^2(\omega)}\right)}$, with the exciton binding energy E_b obtained by subtracting the optical band gap from the quasiparticle band gap.

The patched sampling scheme is employed to converge the exciton binding energy with respect to the fine **k**-point mesh density. Extensive convergence tests for $CsPbI_3$ and $CsPbBr_3$ (Figure A.3) demonstrate that exciton binding energies are converged within 1 meV using patch radii of $0.07\times2\pi/a$ for $CsPbI_3$ and $0.25\times2\pi/a$ for $CsPbBr_3$, with densities equivalent to uniform (Γ-centered) $120\times120\times120$ and $70\times70\times70$ grids respectively. For the mixed-halide compounds in the series $CsPb(Br_xI_{1-x})_3$, both the patch size and sampling grid density are linearly interpolated.

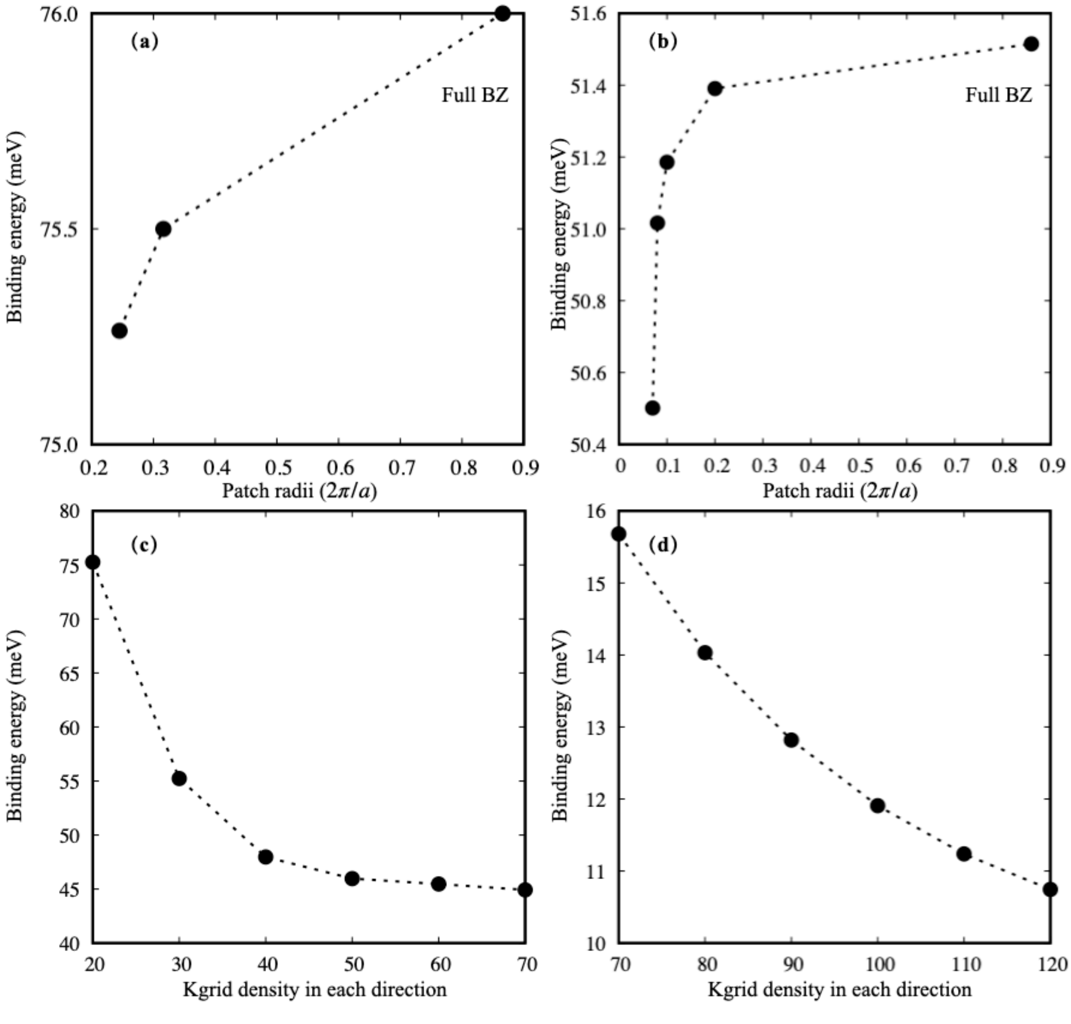

Figure A.3: Convergence of exciton binding energies with respect to patch size for (a) $CsPbI_3$ and (b) $CsPbBr_3$ (both tested using a $20 \times 20 \times 20$ **k**-point grid centered at Γ). The largest patch size corresponds to the full Brillouin zones in each case. Convergence of exciton binding energies with respect to grid densities for (c) $CsPbI_3$ and (d) $CsPbBr_3$ (calculated with converged patch radii of 0.07 $\times2\pi/a$ and 0.25 $\times2\pi/a$, respectively.

Table A.1: Parameters used to calculate the mobility μ_m: high-frequency (ε_∞) and static (ε_0) dielectric constants, the phonon energy of the principal LO mode ($\hbar\omega_{\mathrm{LO}}$), the corrected hole and electron effective masses (m_e^*/m_e, m_h^*/m_e) , the calculated Fröhlich coupling constant for hole and electron (α_h, α_e), the average electron and hole mobilities (μ_m^h, μ_m^e) and electron-hole sum mobility ($\mu_m^{\mathrm{sum}} = \mu_m^h + \mu_m^e$).

Br (%)	ε_∞	ε_0	$\hbar\omega_{\mathrm{LO}}$ (meV)	m_h^*/m_e	m_e^*/m_e	α_h	α_e	μ_m^h	μ_m^e	μ_m^{sum}
0	6.82	36.47	14.25	0.178	0.164	1.554	1.491	56.2	63.6	119.8
10	6.68	34.10	14.58	0.181	0.166	1.562	1.499	55.2	62.5	117.7
20	6.50	33.33	14.80	0.185	0.170	1.615	1.550	52.3	59.1	111.4
30	6.30	32.45	15.04	0.189	0.174	1.671	1.604	49.5	55.9	105.4
40	6.11	31.54	15.32	0.194	0.179	1.731	1.663	46.7	52.7	99.4
50	5.91	30.51	15.63	0.199	0.183	1.795	1.724	44.0	49.6	93.5
60	5.71	29.43	15.98	0.204	0.189	1.863	1.790	41.3	46.5	87.8
70	5.50	28.26	16.37	0.210	0.194	1.937	1.862	38.7	43.6	82.2
80	5.29	26.52	16.83	0.217	0.200	2.004	1.927	36.4	40.9	77.3
90	5.08	25.66	17.36	0.224	0.207	2.089	2.009	34.0	38.2	72.1
100	4.86	24.36	17.92	0.232	0.214	2.182	2.099	31.5	35.4	66.9

A.2 Computational setup for Chapter 4

A.2.1 Model construction

Model layered perovskites are constructed following the approach of Ref. [46], where the organic cation is replaced by monovalent Cs to obtain $\mathrm{Cs_2PbI_4}$. The unit cell contains a sheet of corner-shared undistorted and untilted $\mathrm{PbI_6}$ octahedra, with Pb-I bond length fixed at 3.184 Å, obtained from structural optimisation of cubic $\mathrm{CsPbI_3}$ using DFT-PBE. The interlayer distance, defined as the distance between inorganic layers measured from the Pb-containing planes, is varied from 10 Å to 16 Å in 1 Å steps, with an additional point at 10.5 Å to match experimental Dion-Jacobson structures. Model structures are obtained by relaxing Cs atoms while keeping $\mathrm{PbI_6}$ layers and lattice parameters fixed.

A.2.2 Ground state calculations

All DFT calculations are performed using Quantum Espresso (version 6.7) with the PBE exchange-correlation functional. We employ fully relativistic, norm-conserving pseudopotentials from the Pseudo Dojo repository, with spin-orbit coupling included in all electronic structure and optical property calculations. The plane wave basis set uses a kinetic energy cutoff of 50 Ry, and the Brillouin zone is sampled using a Γ-centered 6 × 6 × 4 Monkhorst-Pack mesh, with reduced sampling along the direction perpendicular to the perovskite planes.

A.2.3 Quasiparticle calculations

Quasiparticle band structures are calculated within the single-shot G_0W_0 approximation using the BerkeleyGW code [76]. The non-local, frequency-dependent dielectric function is calculated within the random phase approximation using the Godby-Needs plasmon-pole model [103]. All calculation parameters, chosen based on convergence tests shown in Figure A.4, are listed in Table A.2. This setup achieves quasiparticle band gaps converged within 0.1-0.2 eV. We note that the calculated quasiparticle band structures are expected to underestimate experimental values by approximately 0.5 eV due to the sensitivity of single-shot G_0W_0 calculations to the mean-field starting point, as reported for halide perovskites and other semiconductors in recent studies [6,46,153,154].

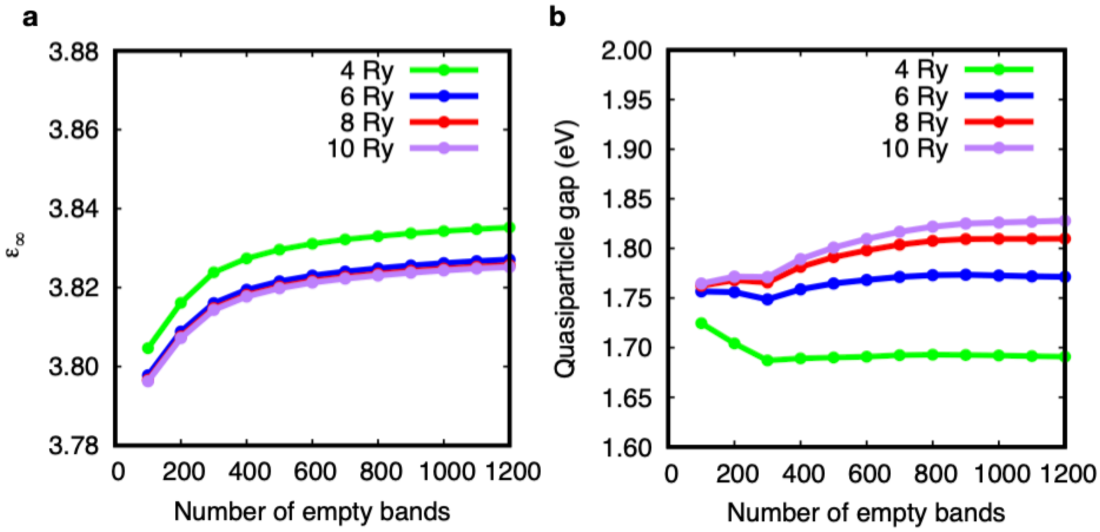

Figure A.4: Convergence of (a) high frequency limit of the dielectric constants ε_∞ and (b) quasiparticle band gaps for a model DJ structure with an interlayer distance of 11 Å with respect to energy cutoff for the dielectric matrix and number of empty bands.

Structure	**DJ**	**RP/Intermediate**	**Exp.**
Formula unit	1	2	2
GW empty bands	400	800	800
GW plane wave cutoff	6 Ry	6 Ry	6 Ry
GW **k**-point grid*	$6 \times 6 \times 4$	$6 \times 6 \times 2$	$4 \times 4 \times 4$
e-h kernel: **k**-point grid	$6 \times 6 \times 4$	$6 \times 6 \times 2$	$4 \times 4 \times 4$
e-h kernel: val. / cond.	8 / 8	8 / 8	16 / 16
absorption **k**-point grid	$30 \times 30 \times 10$	$30 \times 30 \times 5$	$20 \times 20 \times 10$
absorption val. / cond.	2 / 2	4 / 4	8 / 8

Table A.2: Computational setup for GW and BSE calculations.
*The same **k**-point grid was used for the calculation of the dielectric function and quasiparticle corrections. The dielectric function was computed on a half-shifted grid, while the quasiparticle energies were calculated on a Γ-centered grid.

A.2.4 Optical excitation calculations

The two-particle excitation energies are computed by solving the BSE within the Tamm-Dancoff approximation [72]. The exciton binding energy is calculated as the difference between the quasiparticle band gap and the energy of the first excited state. Exchange interaction is found to change the energy of the lowest excited state in (4 AMP)PbI$_4$ by less than 30 meV.

The imaginary part of the dielectric function is calculated using excitation energies and two-particle wave functions, with the velocity operator approximated as $\mathbf{v} = i\Box$. Calculation parameters are chosen based on convergence tests shown in Figure A.5 and Table A.3, yielding exciton binding energies converged within 50 meV.

A.2.5 Exciton wave function analysis

To characterise exciton localisation across inorganic layers, we compute the out-of-plane integrated ECF by integrating along the in-plane directions:

$$\mathcal{F}_\perp(z) = \int_\Omega \mathcal{F}(r) dxdy. \tag{A.1}$$

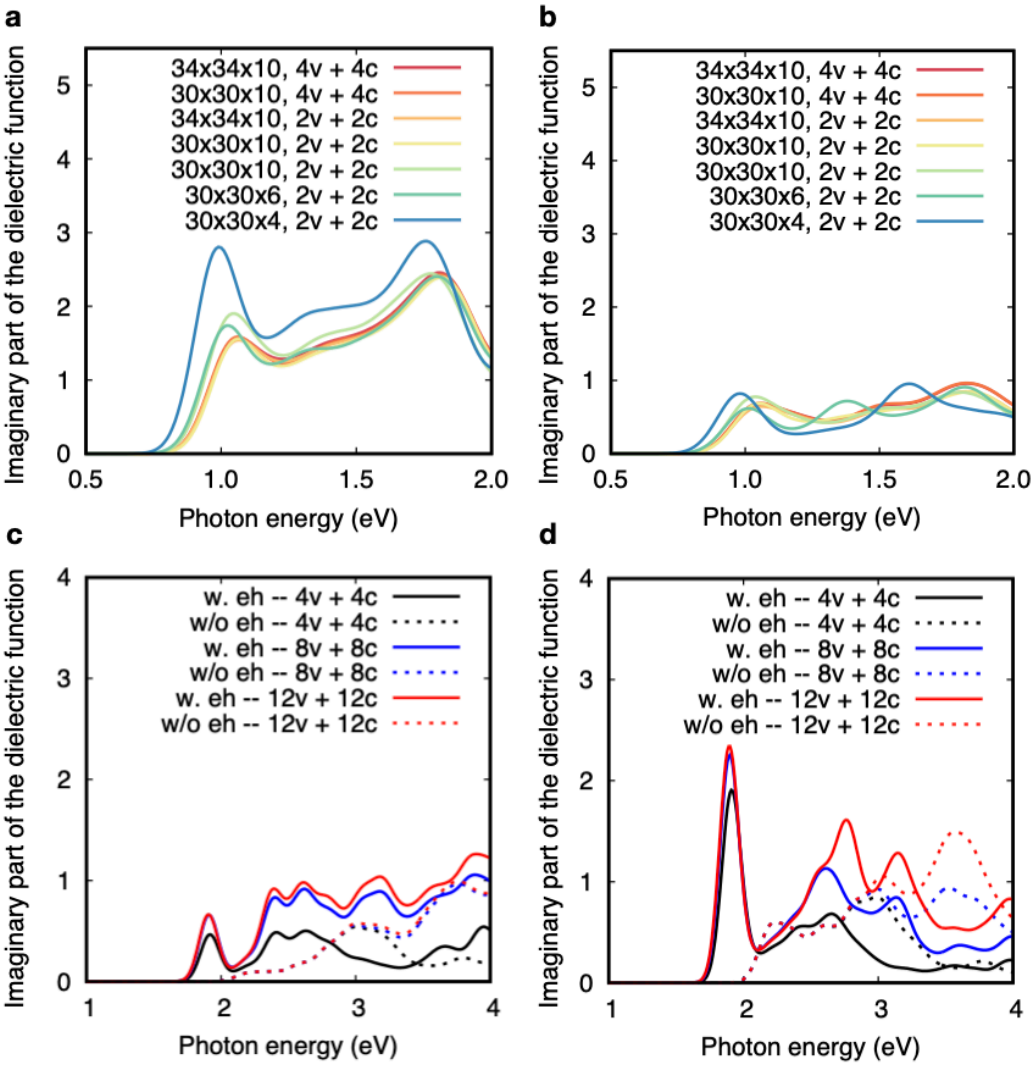

Figure A.5: Calculated imaginary part of the dielectric function with light polarisation perpendicular to the inorganic layer (Left) and parallel to the inorganic layer (Right) for model layered perovskites with an interlayer distance of 10 Å (a,b) using various fine grid density and numbers of bands, and for 1,5 - DAN (c, d) using a 20 × 20 × 10 fine grid and different numbers of bands.

System	Fine grid density	Val. / Cond.	E_b (meV)
DJ Model, 10 Å	30 × 30 × 4	2 / 2	273
	30 × 30 × 6	2 / 2	248
	30 × 30 × 10	2 / 2	230
	30 × 30 × 20	2 / 2	220
	34 × 34 × 10	2 / 2	229
	30 × 30 × 10	4 / 4	231
	34 × 34 × 10	4 / 4	230
1,5 - DAN	20 × 20 × 10	4 / 4	184
	20 × 20 × 10	8 / 8	201
	20 × 20 × 10	12 / 12	205

Table A.3: Calculated exciton binding energy for a model layered perovskite structure with interlayer distance of 10 Å and 1,5 - DAN using different Γ centered **k**-point grid densities and numbers of bands.

The ECF is computed by discrete summation over r_h sampled on a uniform grid in the primitive unit cell. Based on convergence tests (Figure A.6), holes are sampled along one line perpendicular to the perovskite layers with approximately 0.3 Å grid spacing, maintaining accuracy within 0.3 Å for the calculated interlayer electron-hole separation in the smallest interlayer distance model (Table A.4). The real space exciton wave function is computed in a 14 × 14 × 10 supercell to ensure wave function decay to less than 0.1% of the maximum value at the boundary.

Hole sampling density	Interlayer e-h sep.	In-plane e-h sep.
1 × 1 × 15	17.3 Å	21.4 Å
1 × 1 × 31	17.3 Å	21.4 Å
5 × 5 × 15	17.0 Å	21.7 Å

Table A.4: Calculated interlayer and in-plane average electron-hole separation for a model DJ structure with an interlayer distance of 10 Å using different hole sampling densities.

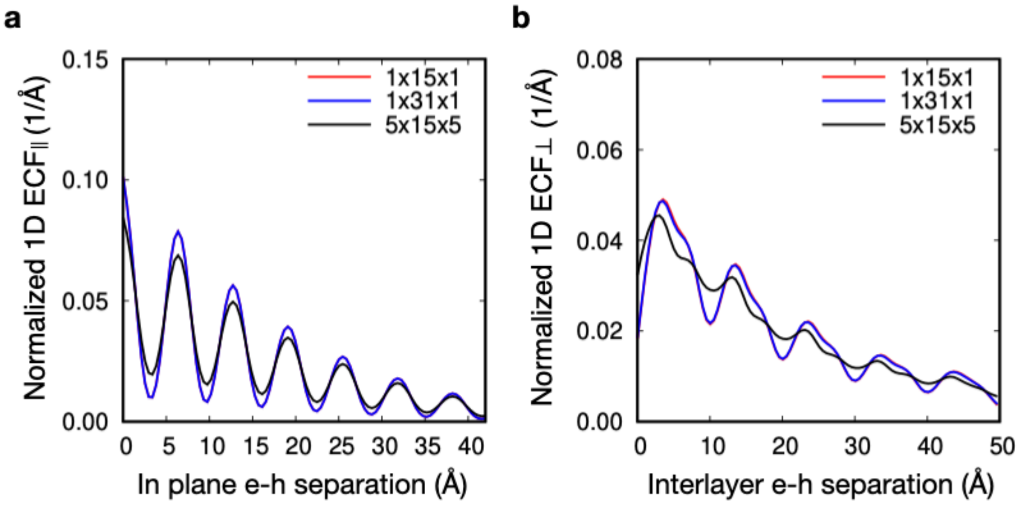

Figure A.6: Normalised 1D ECF for a model DJ structure with an interlayer distance of 10 Å, along the in-plane (a) and out-of-plane (b) direction, calculated with different hole sampling grids.

A.3 Computational setup for Chapter 5 and 6

A.3.1 Ground state calculations

All DFT calculations are performed using Quantum Espresso (version 6.7) with the PBE exchange-correlation functional. We employ fully relativistic, norm-conserving pseudopotentials from the Pseudo Dojo repository, with spin-orbit coupling included in all electronic structure and optical property calculations. The plane wave basis set uses a kinetic energy cutoff of 70 Ry, and the Brillouin zone is sampled using a Γ-centered $6 \times 6 \times 4$ Monkhorst-Pack mesh, with reduced sampling along the direction perpendicular to the perovskite planes.

A.3.2 Quasiparticle calculations

Quasiparticle band gaps are calculated within the single-shot G_0W_0 approximation using the BerkeleyGW code [76]. The non-local, frequency-dependent dielectric function is calculated within the random phase approximation using the Godby-Needs plasmon-pole model [103].

Convergence tests show that the quasiparticle band gap is converged within 50 meV for a grid density of 6×6×1. In all cases of perovskite-intergrowth we use a polarisability cutoff of 6 Ry and sum over 400 empty bands and occupied bands, achieving converged quasiparticle corrections within less than 0.1 eV for both **AMTP** and **1-Na**.(Figure A.1c,d).

Table A.5: Convergence of the quasiparticle band gap on the **k**-point grid density for **AMTP** calculated with a dielectric cutoff of 6 Ry and 400 empty bands.

k-point grid	**Quasiparticle Band Gap (eV)**
$4 \times 4 \times 1$	2.837
$4 \times 4 \times 2$	2.857
$6 \times 6 \times 1$	2.836
$8 \times 8 \times 1$	2.837

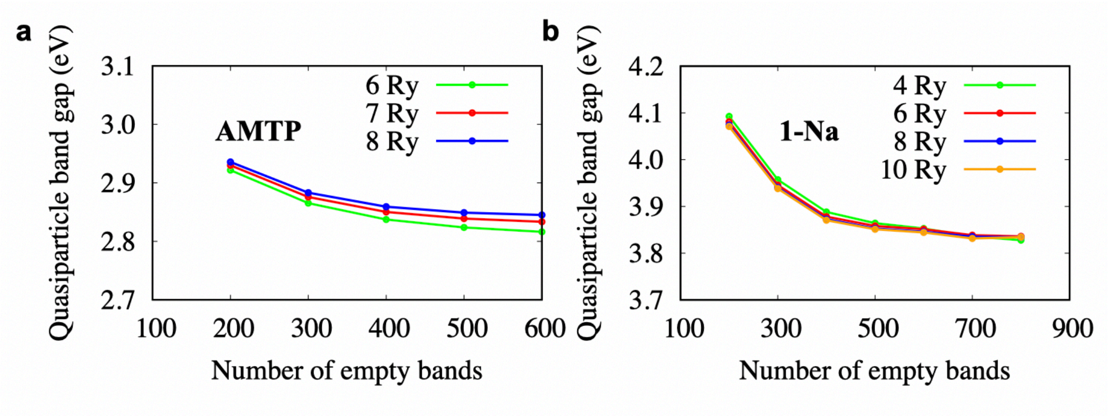

Figure A.7: Convergence of quasiparticle band gaps for (a) **AMTP** and (b) **1-Na** with a 4 × 4 × 1 and 6 × 6 × 1 **k**-point grid, respectively.

A.3.3 Optical excitation calculations

The two-particle excitation energies are computed by solving the BSE within the Tamm-Dancoff approximation [72]. The exciton binding energy is calculated as the difference between the quasiparticle band gap and the energy of the first excited state. Exchange interaction is found to change the energy of the lowest excited state in (4 AMP)PbI_4 by less than 30 meV.

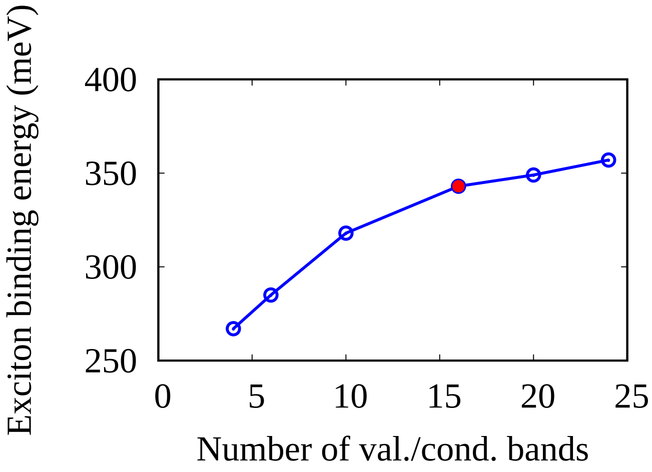

Figure A.8: Convergence of the exciton binding energy with respect to the number of valence and conduction bands used in the fine grid interpolation.

The imaginary part of the dielectric function is calculated using excitation energies and two-particle wave functions, with the velocity operator approximated as $\mathbf{v} = i$□. Calculation parameters are chosen based on convergence tests shown in Figure A.8 and Table A.6, yielding exciton binding energies converged within 50 meV.

Table A.6: Convergence of the exciton binding energy on the fine **k**-point grid density for **AMTP** calculated with 16 conduction and 16 valence bands.

k-point grid	E_b**(meV)**
$16 \times 16 \times 1$	351
$24 \times 24 \times 1$	363
$12 \times 12 \times 4$	366

A.3.4 Exciton correlation function calculation

The ECF is computed by discrete summation over r_h sampled on a uniform grid in the primitive unit cell. Holes are sampled along one line perpendicular to the perovskite layers with approximately 0.3 Å grid spacing. The real space exciton wave function is computed in a $8 \times 8 \times 4$ supercell to ensure wave function decay to less than 0.1% of the maximum value at the boundary.

A.3.5 Analysis of octahedral distortions

The octahedral distortion parameters for in-plane (D_{in}) and out-of-plane (D_{out}) directions were quantified following the methodology developed in Ref. [45], with modifications to account for Cl atoms replacing Br in the structures. The analysis uses atomic positions of Pb and in-plane Cl atoms expressed as Cartesian vectors obtained from crystallographic information files (CIF). A reference plane is defined through three non-colinear Pb atoms, allowing calculation of the Pb-Cl-Pb bond angle and its subsequent decomposition into components parallel and perpendicular to this reference plane. This approach remains valid for analysing the intergrowth layers in the reported structures, which contain four in-plane corner-sharing Pb-Cl bonds. The distortion parameters are computed using a modified version of the MATLAB code reported in Ref. [45].

Bibliography

[1] Ruijie Zhang, Menghan Li, Lin Li, Zhongming Wei, Fei Jiao, Dechao Geng, and Wenping Hu. The more, the better–recent advances in construction of 2D multi-heterostructures. *Advanced Functional Materials*, 31(26):2102049, 2021.

[2] Feliciano Giustino. *Materials modelling using density functional theory: properties and predictions*. Oxford University Press, 2014.

[3] David P. McMeekin, Golnaz Sadoughi, Waqaas Rehman, Giles E. Eperon, Michael Saliba, Maximilian T. Hörantner, Amir Haghighirad, Nobuya Sakai, Lars Korte, Bernd Rech, Michael B. Johnston, Laura M. Herz, and Henry J. Snaith. A mixed-cation lead mixed-halide perovskite absorber for tandem solar cells. *Science*, 351(6269):151–155, 2016.

[4] Michal Baranowski, Paulina Plochocka, Rui Su, Laurent Legrand, Thierry Barisien, Frederick Bernardot, Qihura Xiong, Christophe Testelin, and Maria Chamarro. Exciton binding energy and effective mass of $CsPbCl_3$: a magneto-optical study. *Photonics Res.*, 8(10):A50–A55, 2020.

[5] R. J. Elliott. Intensity of Optical Absorption by Excitons. *Phys. Rev.*, 108(6):1384–1389, 1957.

[6] M. R. Filip, J. B Haber, and J. B. Neaton. Phonon screening of excitons in semiconductors: Halide perovskites and beyond. *Phys. Rev. Lett.*, 127:067401, 2021.

[7] Gregory H. Wannier. The structure of electronic excitation levels in insulating crystals. *Phys. Rev.*, 52(3):191–197, 1937.

[8] Samuel Poncé, Martin Schlipf, and Feliciano Giustino. Origin of low carrier mobilities in halide perovskites. *ACS Energy Letters*, 4(2):456–463, 2019.

[9] Lingling Mao, Weijun Ke, Laurent Pedesseau, Yilei Wu, Claudine Katan, Jacky Even, Michael R. Wasielewski, Constantinos C. Stoumpos, and Mercouri G. Kanatzidis. Hybrid Dion–Jacobson 2D lead iodide perovskites. *Journal of the American Chemical Society*, 140(10):3775–3783, 2018.

[10] Andreas Lemmerer and David G. Billing. Lead halide inorganic–organic hybrids incorporating diammonium cations. *CrystEngComm*, 14(6):1954–1966, 2012.

[11] Andreas Lemmerer and David G. Billing. Effect of heteroatoms in the inorganic–organic layered perovskite-type hybrids $[(ZCnH_{2n}NH_3)_2PbI_4]$, n = 2, 3, 4, 5, 6; Z = OH, Br and I; and $[(H_3NC_2H_4S_2C_2H_4NH_3)PbI_4]$. *CrystEngComm*, 12(4):1290–1301, 2010.

[12] Michael L Aubrey, Abraham Saldivar Valdes, Marina R Filip, Bridget A Connor, Kurt P Lindquist, Jeffrey B Neaton, and Hemamala I Karunadasa. Directed assembly of layered perovskite heterostructures as single crystals. *Nature*, 597(7876):355–359, 2021.

[13] Michael M Lee, Joël Teuscher, Tsutomu Miyasaka, Takurou N Murakami, and Henry J Snaith. Efficient hybrid solar cells based on meso-superstructured organometal halide perovskites. *Science*, 338(6107):643–647, 2012.

[14] Jonas Diekmann, Pietro Caprioglio, Moritz H Futscher, Vincent M Le Corre, Sebastian Reichert, Frank Jaiser, Malavika Arvind, Lorena Perdigón Toro, Emilio Gutierrez-Partida, Francisco Pena-Camargo, et al. Pathways toward 30% efficient single-junction perovskite solar cells and the role of mobile ions. *Solar RRL*, 5(8):2100219, 2021.

[15] Haiming Zhu, Kiyoshi Miyata, Yongping Fu, Jue Wang, Prakriti P Joshi, Daniel Niesner, Kristopher W Williams, Song Jin, and X-Y Zhu. Screening in crystalline liquids protects energetic carriers in hybrid perovskites. *Science*, 353(6306):1409–1413, 2016.

[16] Yinsheng Guo, Omer Yaffe, Trevor D Hull, Jonathan S Owen, David R Reichman, and Louis E Brus. Dynamic emission stokes shift and liquid-like dielectric solvation of band edge carriers in lead-halide perovskites. *Nature Communications*, 10(1):1175, 2019.

[17] Nobuaki Kitazawa, Y Watanabe, and Y Nakamura. Optical properties of $CH_3NH_3PbX_3$ (X= halogen) and their mixed-halide crystals. *Journal of materials science*, 37:3585–3587, 2002.

[18] Nicola A Spaldin and Rammamoorthy Ramesh. Advances in magnetoelectric multiferroics. *Nature materials*, 18(3):203–212, 2019.

[19] James M Rondinelli and Sinisa Coh. Large isosymmetric reorientation of oxygen octahedra rotation axes in epitaxially strained perovskites. *Physical Review Letters*, 106(23):235502, 2011.

[20] Dieter Weber. $CH_3NH_3PbX_3$, ein Pb (ii)-system mit kubischer perowskitstruktur/$CH_3NH_3PbX_3$, a Pb (ii)-system with cubic perovskite structure. *Zeitschrift für Naturforschung B*, 33(12):1443–1445, 1978.

[21] Akihiro Kojima, Kenjiro Teshima, Yasuo Shirai, and Tsutomu Miyasaka. Organometal halide perovskites as visible-light sensitizers for photovoltaic cells. *J. Am. Chem. Soc.*, 131(17):6050–6051, 2009.

[22] Best research-cell efficiency chart. https://www.nrel.gov/pv/cell-efficiency.html. [Online; accessed Jan-2025].

[23] Ayan A Zhumekenov, Makhsud I Saidaminov, Md Azimul Haque, Erkki Alarousu, Smritakshi Phukan Sarmah, Banavoth Murali, Ibrahim Dursun, Xiao-He Miao, Ahmed L Abdelhady, Tom Wu, et al. Formamidinium lead halide perovskite crystals with unprecedented long carrier dynamics and diffusion length. *ACS Energy Letters*, 1(1):32–37, 2016.

[24] Samuel D Stranks, Giles E Eperon, Giulia Grancini, Christopher Menelaou, Marcelo JP Alcocer, Tomas Leijtens, Laura M Herz, Annamaria Petrozza, and Henry J Snaith. Electron-hole diffusion lengths exceeding 1 micrometer in an organometal trihalide perovskite absorber. *Science*, 342(6156):341–344, 2013.

[25] Kevin A. Bush, Axel F. Palmstrom, Zhengshan J. Yu, Mathieu Boccard, Rongrong Cheacharoen, Jonathan P. Mailoa, David P. McMeekin, Robert L. Z. Hoye, Colin D. Bailie, Tomas Leijtens, Ian Marius Peters, Maxmillian C. Minichetti, Nicholas Rolston, Rohit Prasanna, Sarah Sofia, Duncan Harwood, Wen Ma, Farhad Moghadam, Henry J. Snaith, Tonio Buonassisi, Zachary C. Holman, Stacey F. Bent, and Michael D. McGehee. 23.6%-efficient monolithic perovskite/silicon tandem solar cells with improved stability. *Nat. Energy*, 2(4):1–7, 2017.

[26] Weibin Chu, Qijing Zheng, Oleg V Prezhdo, Jin Zhao, and Wissam A Saidi. Low-frequency lattice phonons in halide perovskites explain high defect tolerance toward electron-hole recombination. *Science advances*, 6(7):eaaw7453, 2020.

[27] Baodan Zhao, Sai Bai, Vincent Kim, Robin Lamboll, Ravichandran Shivanna, Florian Auras, Johannes M Richter, Le Yang, Linjie Dai, Mejd Alsari, et al. High-efficiency perovskite–polymer bulk heterostructure light-emitting diodes. *Nature Photonics*, 12(12):783–789, 2018.

[28] Gabriel Lozano. The role of metal halide perovskites in next-generation lighting devices. *The Journal of Physical Chemistry Letters,*, 9(14):3987–3997, 2018.

[29] Mats Johnsson and Peter Lemmens. Crystallography and chemistry of perovskites. *arXiv preprint cond-mat/0506606*, 2007.

[30] Martin A Green, Anita Ho-Baillie, and Henry J Snaith. The emergence of perovskite solar cells. *Nature Photonics*, 8(7):506–514, 2014.

[31] Marina R. Filip, George Volonakis, and Feliciano Giustino. In Wanda Andreoni and Sidney Yip, editors, *Handbook of Materials Modeling: Applications: Current and Emerging Materials*, chapter Hybrid Halide Perovskites: Fundamental Theory and Materials Design, pages 1–30. Springer International Publishing, Cham, 2018.

[32] L. Protesescu, S. Yakunin, M. I. Bodnarchuk, F. Krieg, R. Caputo, C. H. Hendon, R. X. Yang, A. Walsh, and M. V. Kovalenko. Nanocrystals of cesium lead halide perovskites ($CsPbX_3$, X = Cl, Br, and I): Novel optoelectronic materials showing bright emission with wide color gamut. *Nano Lett.*, 15:3692–3696, 2015.

[33] N. K. Noel, S. D. Straks, A. Abate, C. Wehrenfennig, S. Guarnera, A.-A. Haghighirad, A. Sadhanala, G. E. Eperon, S. K. Pathak, M. B. Johnston, A. Petrozza, L. M. Herz, and H. J. Snaith. Lead-free organic–inorganic tin halide perovskites for photovoltaic applications. *Energy Environ. Sci.*, 7(9):3061–3068, 2014.

[34] P. Umari, E. Mosconi, and F. De Angelis. Relativistic *GW* calculations on $CH_3NH_3PbI_3$ and $CH_3NH_3SnI_3$ perovskites for solar cell applications. *Sci. Rep.*, 4(4467), 2014.

[35] Marina R Filip, Giles E Eperon, Henry J Snaith, and Feliciano Giustino. Steric engineering of metal-halide perovskites with tunable optical band gaps. *Nat. Commun.*, 5(1):1–9, 2014.

[36] Michael Saliba, Taisuke Matsui, Konrad Domanski, Ji-Youn Seo, Amita Ummadisingu, Shaik M. Zakeeruddin, Juan-Pablo Correa-Baena, Wolfgang R. Tress, Antonio Abate, Anders Hagfeldt, and Michael Grätzel. Incorporation of rubidium cations into perovskite solar cells improves photovoltaic performance. *Science*, 354(6309):206–209, 2016.

[37] Michael Saliba, Taisuke Matsui, Ji-Youn Seo, Konrad Domanski, Juan-Pablo

Correa-Baena, Mohammad Khaja Nazeeruddin, Shaik M. Zakeeruddin, Wolfgang Tress, Antonio Abate, Anders Hagfeldt, and Michael Grätzel. Cesium-containing triple cation perovskite solar cells: Improved stability, reproducibility and high efficiency. *Energy Environ. Sci.*, 9(6):1989–1997, 2016.

[38] Giles E Eperon, Tomas Leijtens, Kevin A Bush, Rohit Prasanna, Thomas Green, Jacob Tse-Wei Wang, David P McMeekin, George Volonakis, Rebecca L Milot, Richard May, et al. Perovskite-perovskite tandem photovoltaics with optimized band gaps. *Science*, 354(6314):861–865, 2016.

[39] A. J. Knight and L. M. Herz. Preventing phase segregation in mixed-halide perovskites: A perspective. *Energy Environ. Sci.*, 13(7):2024–2046, 2020.

[40] S. Larach, R. E. Shrader, and C. F. Stocker. Anomalous variation of band gap with composition in zinc sulfo- and seleno-tellurides. *Phys. Rev.*, 108(3), 1957.

[41] Kimberley J Savill, Aleksander M Ulatowski, and Laura M Herz. Optoelectronic properties of tin–lead halide perovskites. *ACS Energy Lett.*, 6(7):2413–2426, 2021.

[42] Matthew D Smith and Hemamala I Karunadasa. White-light emission from layered halide perovskites. *Accounts of chemical research*, 51(3):619–627, 2018.

[43] Jean-Christophe Blancon, Jacky Even, Costas C. Stoumpos, Mercouri G. Kanatzidis, and Aditya D. Mohite. Semiconductor physics of organic–inorganic 2D halide perovskites. *Nature Nanotechnology*, 15(12):969–985, 2020.

[44] Lingling Mao, Constantinos C. Stoumpos, and Mercouri G. Kanatzidis. Two-dimensional hybrid halide perovskites: Principles and promises. *Journal of the American Chemical Society*, 141(3):1171–1190, 2019.

[45] Matthew D. Smith, Adam Jaffe, Emma R. Dohner, Aaron M. Lindenberg, and Hemamala I. Karunadasa. Structural origins of broadband emission from layered

Pb-Br hybrid perovskites. *Chemical Science*, 8(6):4497–4504, 2017.

[46] Marina R Filip, Diana Y Qiu, Mauro Del Ben, and Jeffrey B Neaton. Screening of excitons by organic cations in quasi-two-dimensional organic–inorganic lead-halide perovskites. *Nano letters*, 22(12):4870–4878, 2022.

[47] X. Hong, T. Ishihara, and A. V. Nurmikko. Dielectric confinement effect on excitons in PbI_4^- based layered semiconductors. *Physical Review B*, 45(12):6961–6964, 1992.

[48] D. B. Mitzi, S. Wang, C. A. Feild, C. A. Chess, and A. M. Guloy. Conducting layered organic-inorganic halides containing $\langle 110 \rangle$-oriented perovskite sheets. *Science*, 267(5203):1473–1476, 1995.

[49] Constantinos C. Stoumpos, Duyen H. Cao, Daniel J. Clark, Joshua Young, James M. Rondinelli, Joon I. Jang, Joseph T. Hupp, and Mercouri G. Kanatzidis. Ruddlesden–Popper hybrid lead iodide perovskite 2D homologous semiconductors. *Chemistry of Materials*, 28(8):2852–2867, 2016.

[50] Matthew D Smith, Ethan J Crace, Adam Jaffe, and Hemamala I Karunadasa. The diversity of layered halide perovskites. *Annual Review of Materials Research*, 48(1):111–136, 2018.

[51] Ian C Smith, Matthew D Smith, Adam Jaffe, Yu Lin, and Hemamala I Karunadasa. Between the sheets: postsynthetic transformations in hybrid perovskites. *Chemistry of Materials*, 29(5):1868–1884, 2017.

[52] Shuyan Shao, Xiaodan Cui, and Zhen Li. Recent Progress in Understanding the Structural, Optoelectronic, and Photophysical Properties of Lead Based Dion–Jacobson Perovskites as Well as Their Application in Solar Cells. *ACS Materials Letters*, pages 891–917, 2022.

[53] Ying Jiang, Shula Chen, Weihao Zheng, Biyuan Zheng, and Anlian Pan. Inter-

layer exciton formation, relaxation, and transport in TMD van der Waals heterostructures. *Light: Science & Applications*, 10(1):72, 2021.

[54] Mit H Naik, Emma C Regan, Zuocheng Zhang, Yang-Hao Chan, Zhenglu Li, Danqing Wang, Yoseob Yoon, Chin Shen Ong, Wenyu Zhao, Sihan Zhao, et al. Intralayer charge-transfer moiré excitons in van der Waals superlattices. *Nature*, 609(7925):52–57, 2022.

[55] Junyi Liu, Zi Li, Xu Zhang, and Gang Lu. Unraveling energy and charge transfer in type-II van der Waals heterostructures. *npj Computational Materials*, 7(1):1–9, 2021.

[56] Alvaro J Magdaleno, Michael Seitz, Michel Frising, Ana Herranz de la Cruz, Antonio I Fernández-Domínguez, and Ferry Prins. Efficient interlayer exciton transport in two-dimensional metal-halide perovskites. *Materials Horizons*, 8(2):639–644, 2021.

[57] David Giovanni, Sankaran Ramesh, Marcello Righetto, Jia Wei Melvin Lim, Qiannan Zhang, Yue Wang, Senyun Ye, Qiang Xu, Nripan Mathews, and Tze Chien Sum. The Physics of Interlayer Exciton Delocalization in Ruddlesden-Popper Lead Halide Perovskites. *Nano Letters*, 21(1):405–413, 2021.

[58] George C Fish, Aaron T Terpstra, Algirdas Dučinskas, Masaud Almalki, Loï C Carbone, Lukas Pfeifer, Michael Grätzel, Jacques-E Moser, and Jovana V Milić. The impact of spacer size on charge transfer excitons in dion–jacobson and ruddlesden–popper layered hybrid perovskites. *The Journal of Physical Chemistry Letters*, 14(27):6248–6254, 2023.

[59] Daniel B. Straus, Sebastian Hurtado Parra, Natasha Iotov, Julian Gebhardt, Andrew M. Rappe, Joseph E. Subotnik, James M. Kikkawa, and Cherie R. Kagan. Direct Observation of Electron–Phonon Coupling and Slow Vibrational Relax-

ation in Organic–Inorganic Hybrid Perovskites. *Journal of the American Chemical Society*, 138(42):13798–13801, 2016.

[60] Alejandro Molina-Sánchez. Excitonic states in semiconducting two-dimensional perovskites. *ACS Applied Energy Materials*, 1(11):6361–6367, 2018.

[61] Pasqual Rivera, John R Schaibley, Aaron M Jones, Jason S Ross, Sanfeng Wu, Grant Aivazian, Philip Klement, Kyle Seyler, Genevieve Clark, Nirmal J Ghimire, et al. Observation of long-lived interlayer excitons in monolayer $MoSe_2$–WSe_2 heterostructures. *Nature communications*, 6(1):6242, 2015.

[62] Xiaoping Hong, Jonghwan Kim, Su-Fei Shi, Yu Zhang, Chenhao Jin, Yinghui Sun, Sefaattin Tongay, Junqiao Wu, Yanfeng Zhang, and Feng Wang. Ultrafast charge transfer in atomically thin MoS_2/WS_2 heterostructures. *Nature nanotechnology*, 9(9):682–686, 2014.

[63] Frank Ceballos, Matthew Z Bellus, Hsin-Ying Chiu, and Hui Zhao. Ultrafast charge separation and indirect exciton formation in a MoS_2–$MoSe_2$ van der Waals heterostructure. *ACS nano*, 8(12):12717–12724, 2014.

[64] Simone Latini, Kirsten T Winther, Thomas Olsen, and Kristian S Thygesen. Interlayer excitons and band alignment in MoS_2/hBN/WSe_2 van der Waals heterostructures. *Nano letters*, 17(2):938–945, 2017.

[65] L Meckbach, U Huttner, LC Bannow, T Stroucken, and SW Koch. Interlayer excitons in transition-metal dichalcogenide heterostructures with type-ii band alignment. *Journal of Physics: Condensed Matter*, 30(37):374002, 2018.

[66] Chenhao Jin, Emma C Regan, Aiming Yan, M Iqbal Bakti Utama, Danqing Wang, Sihan Zhao, Ying Qin, Sijie Yang, Zhiren Zheng, Shenyang Shi, et al. Observation of moiré excitons in WSe_2/WS_2 heterostructure superlattices. *Nature*, 567(7746):76–80, 2019.

[67] Kha Tran, Galan Moody, Fengcheng Wu, Xiaobo Lu, Junho Choi, Kyounghwan Kim, Amritesh Rai, Daniel A Sanchez, Jiamin Quan, Akshay Singh, et al. Evidence for moiré excitons in van der Waals heterostructures. *Nature*, 567(7746):71–75, 2019.

[68] L Bellaiche and David Vanderbilt. Virtual crystal approximation revisited: Application to dielectric and piezoelectric properties of perovskites. *Physical Review B*, 61(12):7877, 2000.

[69] Feliciano Giustino, Marvin L Cohen, and Steven G Louie. *GW* method with the self-consistent sternheimer equation. *Physical Review B-Condensed Matter and Materials Physics*, 81(11):115105, 2010.

[70] Mark S Hybertsen and Steven G Louie. Electron correlation in semiconductors and insulators: Band gaps and quasiparticle energies. *Phys. Rev. B*, 34(8):5390, 1986.

[71] Michael Rohlfing and Steven G Louie. Electron-hole excitations in semiconductors and insulators. *Physical Review Letters*, 81(11):2312, 1998.

[72] Michael Rohlfing and Steven G Louie. Electron-hole excitations and optical spectra from first principles. *Phys. Rev. B*, 62(8):4927, 2000.

[73] Lars Hedin. New method for calculating the one-particle Green's function with application to the electron-gas problem. *Physical Review*, 139(3A):A796, 1965.

[74] John C Inkson. *Many-body Theory of Solids: an Introduction*. Springer Science & Business Media, 2012.

[75] Ferdi Aryasetiawan and Olle Gunnarsson. The GW method. *Reports on progress in Physics*, 61(3):237, 1998.

[76] Jack Deslippe, Georgy Samsonidze, David A Strubbe, Manish Jain, Marvin L Cohen, and Steven G Louie. Berkeleygw: A massively parallel computer package

for the calculation of the quasiparticle and optical properties of materials and nanostructures. *Comput. Phys. Commun.*, 183(6):1269–1289, 2012.

[77] Paul Adrien Maurice Dirac. On the theory of quantum mechanics. *Proceedings of the Royal Society of London. Series A, Containing Papers of a Mathematical and Physical Character*, 112(762):661–677, 1926.

[78] John David Jackson. *Classical Electrodynamics*. Wiley, New York, NY, 3rd ed. edition, 1999.

[79] Pierre Hohenberg and Walter Kohn. Inhomogeneous electron gas. *Physical Review*, 136(3B):B864, 1964.

[80] Walter Kohn and Lu Jeu Sham. Self-consistent equations including exchange and correlation effects. *Physical Review*, 140(4A):A1133, 1965.

[81] Robert G Parr and W Yang. Density functional theory of atoms and molecules, 1989.

[82] David M Ceperley and Berni J Alder. Ground state of the electron gas by a stochastic method. *Physical Review Letters*, 45(7):566, 1980.

[83] John P Perdew and Alex Zunger. Self-interaction correction to density-functional approximations for many-electron systems. *Physical Review B*, 23(10):5048, 1981.

[84] PG Jambrina and J Aldegunde. Computational tools for the study of biomolecules. In *Computer Aided Chemical Engineering*, volume 39, pages 583–648. Elsevier, 2016.

[85] Andrea Dal Corso, Alfredo Pasquarello, Alfonso Baldereschi, and Roberto Car. Generalized-gradient approximations to density-functional theory: A comparative study for atoms and solids. *Physical Review B*, 53(3):1180, 1996.

[86] John P Perdew, Kieron Burke, and Matthias Ernzerhof. Generalized gradient approximation made simple. *Physical Review Letters*, 77(18):3865, 1996.

[87] VP Gupta. *Principles and applications of quantum chemistry*. Academic Press, 2015.

[88] Carlo Adamo and Vincenzo Barone. Toward reliable density functional methods without adjustable parameters: The PBE0 model. *The Journal of chemical physics*, 110(13):6158–6170, 1999.

[89] Matthias Ernzerhof and Gustavo E Scuseria. Assessment of the perdew–burke–ernzerhof exchange-correlation functional. *The Journal of Chemical Physics*, 110(11):5029–5036, 1999.

[90] C Adamo, Maurizio Cossi, and Vincenzo Barone. An accurate density functional method for the study of magnetic properties: the PBE0 model. *Journal of Molecular Structure: THEOCHEM*, 493(1-3):145–157, 1999.

[91] Paolo Giannozzi, Oliviero Andreussi, Thomas Brumme, Oana Bunau, M Buongiorno Nardelli, Matteo Calandra, Roberto Car, Carlo Cavazzoni, Davide Ceresoli, Matteo Cococcioni, et al. Advanced capabilities for materials modelling with quantum espresso. *J. Phys. Condens. Matter*, 29(46):465901, 2017.

[92] Paolo Giannozzi, Stefano Baroni, Nicola Bonini, Matteo Calandra, Roberto Car, Carlo Cavazzoni, Davide Ceresoli, Guido L Chiarotti, Matteo Cococcioni, Ismaila Dabo, et al. Quantum espresso: a modular and open-source software project for quantum simulations of materials. *Journal of physics: Condensed matter*, 21(39):395502, 2009.

[93] Hendrik J Monkhorst and James D Pack. Special points for brillouin-zone integrations. *Physical Review B*, 13(12):5188, 1976.

[94] Björn Winkler, Chris Pickard, and Victor Milman. Applicability of a quan-

tum mechanicalvirtual crystal approximation'to study al/si-disorder. *Chemical Physics Letters*, 362(3-4):266–270, 2002.

[95] Lu J Sham and Michael Schlüter. Density-functional theory of the energy gap. *Physical Review Letters*, 51(20):1888, 1983.

[96] Stephan Kümmel and Leeor Kronik. Orbital-dependent density functionals: Theory and applications. *Reviews of Modern Physics*, 80(1):3–60, 2008.

[97] Giovanni Onida, Lucia Reining, and Angel Rubio. Electronic excitations: Density-functional versus many-body Green's-function approaches. *Rev. Mod. Phys.*, 74(2):601–659, 2002.

[98] Dorothea Golze, Marc Dvorak, and Patrick Rinke. The GW compendium: A practical guide to theoretical photoemission spectroscopy. *Frontiers in chemistry*, 7:377, 2019.

[99] H Ehrenreich and Morrel H Cohen. Self-consistent field approach to the many-electron problem. *Physical Review*, 115(4):786, 1959.

[100] MeiYue Shao, Lin Lin, Chao Yang, Fang Liu, Felipe H Da Jornada, Jack Deslippe, and Steven G Louie. Low rank approximation in G_0W_0 calculations. *Science China Mathematics*, 59:1593–1612, 2016.

[101] Stephen L Adler. Quantum theory of the dielectric constant in real solids. *Physical Review*, 126(2):413, 1962.

[102] Nathan Wiser. Dielectric constant with local field effects included. *Physical Review*, 129(1):62, 1963.

[103] Rex W Godby and RJ Needs. Metal-insulator transition in kohn-sham theory and quasiparticle theory. *Phys. Rev. Lett.*, 62(10):1169, 1989.

[104] Johannes Lischner, GK Pálsson, Derek Vigil-Fowler, S Nemsak, J Avila, MC Asensio, CS Fadley, and Steven G Louie. Satellite band structure in sili-

con caused by electron-plasmon coupling. *Physical Review B*, 91(20):205113, 2015.

[105] Fabio Caruso, Henry Lambert, and Feliciano Giustino. Band structures of plasmonic polarons. *Physical Review Letters*, 114(14):146404, 2015.

[106] Paul Larson, Marc Dvorak, and Zhigang Wu. Role of the plasmon-pole model in the *GW* approximation. *Physical Review B-Condensed Matter and Materials Physics*, 88(12):125205, 2013.

[107] Weiwei Gao, Weiyi Xia, Xiang Gao, and Peihong Zhang. Speeding up *GW* calculations to meet the challenge of large scale quasiparticle predictions. *Scientific reports*, 6(1):36849, 2016.

[108] Nicola Marzari and David Vanderbilt. Maximally localized generalized wannier functions for composite energy bands. *Physical Review B*, 56(20):12847, 1997.

[109] Ivo Souza, Nicola Marzari, and David Vanderbilt. Maximally localized wannier functions for entangled energy bands. *Physical Review B*, 65(3):035109, 2001.

[110] DR Hamann and David Vanderbilt. Maximally localized wannier functions for *GW* quasiparticles. *Physical Review B-Condensed Matter and Materials Physics*, 79(4):045109, 2009.

[111] Arash A Mostofi, Jonathan R Yates, Giovanni Pizzi, Young-Su Lee, Ivo Souza, David Vanderbilt, and Nicola Marzari. An updated version of wannier90: A tool for obtaining maximally-localised wannier functions. *Computer Physics Communications*, 185(8):2309–2310, 2014.

[112] Giovanni Pizzi, Valerio Vitale, Ryotaro Arita, Stefan Blügel, Frank Freimuth, Guillaume Géranton, Marco Gibertini, Dominik Gresch, Charles Johnson, Takashi Koretsune, et al. Wannier90 as a community code: new features and applications. *Journal of Physics: Condensed Matter*, 32(16):165902, 2020.

[113] Marvin L Cohen and Steven G Louie. *Fundamentals of condensed matter physics*. Cambridge University Press, 2016.

[114] Sivan Refaely-Abramson, Felipe H da Jornada, Steven G Louie, and Jeffrey B Neaton. Origins of singlet fission in solid pentacene from an ab initio Green's function approach. *Physical Review Letters*, 119(26):267401, 2017.

[115] Gabriel Antonius and Steven G Louie. Theory of exciton-phonon coupling. *Physical Review B*, 105(8):085111, 2022.

[116] Jonah B Haber, Diana Y Qiu, Felipe H da Jornada, and Jeffrey B Neaton. Maximally localized exciton wannier functions for solids. *Physical Review B*, 108(12):125118, 2023.

[117] Diana Y Qiu, Galit Cohen, Dana Novichkova, and Sivan Refaely-Abramson. Signatures of dimensionality and symmetry in exciton band structure: Consequences for exciton dynamics and transport. *Nano letters*, 21(18):7644–7650, 2021.

[118] Catalin D Spataru and François Léonard. Tunable band gaps and excitons in doped semiconducting carbon nanotubes made possible by acoustic plasmons. *Physical Review Letters*, 104(17):177402, 2010.

[119] Antonios M Alvertis, Jonah B Haber, Zhenglu Li, Christopher JN Coveney, Steven G Louie, Marina R Filip, and Jeffrey B Neaton. Phonon screening and dissociation of excitons at finite temperatures from first principles. *Proceedings of the National Academy of Sciences*, 121(30):e2403434121, 2024.

[120] Christopher JN Coveney, Jonah B Haber, Antonios M Alvertis, Jeffrey B Neaton, and Marina R Filip. Rearrangement collision theory of phonon-driven exciton dissociation. *Physical Review B*, 110(5):054307, 2024.

[121] Sahar Sharifzadeh, Pierre Darancet, Leeor Kronik, and Jeffrey B Neaton. Low-energy charge-transfer excitons in organic solids from first-principles: The case

of pentacene. *The Journal of Physical Chemistry Letters*, 4(13):2197–2201, 2013.

[122] Mingzhen Liu, Michael B Johnston, and Henry J Snaith. Efficient planar heterojunction perovskite solar cells by vapour deposition. *Nature*, 501(7467):395–398, 2013.

[123] Julian Burschka, Norman Pellet, Soo-Jin Moon, Robin Humphry-Baker, Peng Gao, Mohammad K Nazeeruddin, and Michael Grätzel. Sequential deposition as a route to high-performance perovskite-sensitized solar cells. *Nature*, 499(7458):316–319, 2013.

[124] Qidong Tai, Peng You, Hongqian Sang, Zhike Liu, Chenglong Hu, Helen LW Chan, and Feng Yan. Efficient and stable perovskite solar cells prepared in ambient air irrespective of the humidity. *Nature communications*, 7(1):1–8, 2016.

[125] Jarvist M Frost, Keith T Butler, Federico Brivio, Christopher H Hendon, Mark Van Schilfgaarde, and Aron Walsh. Atomistic origins of high-performance in hybrid halide perovskite solar cells. *Nano letters*, 14(5):2584–2590, 2014.

[126] Waqaas Rehman, David P McMeekin, Jay B Patel, Rebecca L Milot, Michael B Johnston, Henry J Snaith, and Laura M Herz. Photovoltaic mixed-cation lead mixed-halide perovskites: Links between crystallinity, photo-stability and electronic properties. *Energy Environ. Sci.*, 10(1):361–369, 2017.

[127] Jeremy Hieulle, Xiaoming Wang, Collin Stecker, Dae-Yong Son, Longbin Qiu, Robin Ohmann, Luis K Ono, Aitor Mugarza, Yanfa Yan, and Yabing Qi. Unraveling the impact of halide mixing on perovskite stability. *J. Am. Chem. Soc.*, 141(8):3515–3523, 2019.

[128] Waqaas Rehman, Rebecca L Milot, Giles E Eperon, Christian Wehrenfennig, Jessica L Boland, Henry J Snaith, Michael B Johnston, and Laura M Herz. Charge-carrier dynamics and mobilities in formamidinium lead mixed-halide perovskites. *Advanced Materials*, 27(48):7938–7944, 2015.

[129] Wan-Jian Yin, Tingting Shi, and Yanfa Yan. Unusual defect physics in $CH_3NH_3PbI_3$ perovskite solar cell absorber. *Applied Physics Letters*, 104(6):063903, 2014.

[130] Marina R. Filip and Feliciano Giustino. GW quasiparticle band gap of the hybrid organic-inorganic perovskite $CH_3NH_3PbI_3$: Effect of spin-orbit interaction, semicore electrons, and self-consistency. *Phys. Rev. B*, 90(24):1–10, 2014.

[131] Jun Hong Noh, Sang Hyuk Im, Jin Hyuck Heo, Tarak N Mandal, and Sang Il Seok. Chemical management for colorful, efficient, and stable inorganic–organic hybrid nanostructured solar cells. *Nano Lett.*, 13(4):1764–1769, 2013.

[132] Belen Suarez, Victoria Gonzalez-Pedro, Teresa S Ripolles, Rafael S Sanchez, Luis Otero, and Ivan Mora-Sero. Recombination study of combined halides (Cl, Br, I) perovskite solar cells. *J. Phys. Chem. Lett.*, 5(10):1628–1635, 2014.

[133] Giles E Eperon, Samuel D Stranks, Christopher Menelaou, Michael B Johnston, Laura M Herz, and Henry J Snaith. Formamidinium lead trihalide: a broadly tunable perovskite for efficient planar heterojunction solar cells. *Energy Environ. Sci.*, 7(3):982–988, 2014.

[134] Norman Pellet, Peng Gao, Giuliano Gregori, Tae-Youl Yang, Mohammad K Nazeeruddin, Joachim Maier, and Michael Grätzel. Mixed-organic-cation perovskite photovoltaics for enhanced solar-light harvesting. *Angew. Chem.*, 126(12):3215–3221, 2014.

[135] Andreas Binek, Fabian C Hanusch, Pablo Docampo, and Thomas Bein. Stabilization of the trigonal high-temperature phase of formamidinium lead iodide. *The Journal of Physical Chemistry Letters,*, 6(7):1249–1253, 2015.

[136] Yun Hee Park, Inyoung Jeong, Seunghwan Bae, Hae Jung Son, Phillip Lee, Jinwoo Lee, Chul-Ho Lee, and Min Jae Ko. Inorganic rubidium cation as an en-

hancer for photovoltaic performance and moisture stability of HC (NH_2) 2 PbI_3 perovskite solar cells. *Advanced Functional Materials*, 27(16):1605988, 2017.

[137] Jue Gong, Peijun Guo, Savannah E Benjamin, P Gregory Van Patten, Richard D Schaller, and Tao Xu. Cation engineering on lead iodide perovskites for stable and high-performance photovoltaic applications. *Journal of Energy Chemistry*, 27(4):1017–1039, 2018.

[138] Marina R Filip and Feliciano Giustino. Computational screening of homovalent lead substitution in organic-inorganic halide perovskites. *J. Phys. Chem. C*, 120(1):166–173, 2016.

[139] Mohaddeseh Saffari, Mohammad Ali Mohebpour, H Rahimpour Soleimani, and Meysam Bagheri Tagani. DFT analysis and fdtd simulation of $CH_3NH_3PbI_{3-x}Cl_x$ mixed halide perovskite solar cells: Role of halide mixing and light trapping technique. *J. Phys. D: Appl. Phys*, 50(41):415501, 2017.

[140] Silvia Colella, Edoardo Mosconi, Paolo Fedeli, Andrea Listorti, Francesco Gazza, Fabio Orlandi, Patrizia Ferro, Tullo Besagni, Aurora Rizzo, Gianluca Calestani, et al. $MAPbI_{3-x}Cl_x$ mixed halide perovskite for hybrid solar cells: the role of chloride as dopant on the transport and structural properties. *Chem. Mater.*, 25(22):4613–4618, 2013.

[141] Jongseob Kim, Sung-Hoon Lee, Choong-Heui Chung, and Ki-Ha Hong. Systematic analysis of the unique band gap modulation of mixed halide perovskites. *Phys. Chem. Chem. Phys.*, 18(6):4423–4428, 2016.

[142] I. Ornelas-Cruz, A. Trejo, R. Oviedo-Roa, F. Salazar, E. Carvajal, A. Miranda, and M. Cruz-Irisson. DFT-Based Study of the Bulk Tin Mixed-Halide $CsSnI_{3-x}Br_x$ Perovskite. *Comput. Mater. Sci.*, 178:109619, 2020.

[143] Zehua Chen, Geert Brocks, Shuxia Tao, and Peter A Bobbert. Unified theory for light-induced halide segregation in mixed halide perovskites. *Nature Communi-*

cations, 12(1):1–10, 2021.

[144] Un-Gi Jong, Chol-Jun Yu, Jin-Song Ri, Nam-Hyok Kim, and Guk-Chol Ri. Influence of halide composition on the structural, electronic, and optical properties of mixed $CH_3 NH_3 Pb (I_{1-x} Br_x)_3$ perovskites calculated using the virtual crystal approximation method. *Phys. Rev. B*, 94(12):125139, 2016.

[145] Chol-Jun Yu, Un-Hyok Ko, Suk-Gyong Hwang, Yun-Sim Kim, Un-Gi Jong, Yun-Hyok Kye, and Chol-Hyok Ri. First-principles study on material properties and stability of inorganic halide perovskite solid solutions $CsPb(I_{1-x}Br_x)_3$. *Physical Review Materials*, 4(4):045402, 2020.

[146] Lars Vegard. Die konstitution der mischkristalle und die raumfüllung der atome. *Zeitschrift für Physik*, 5(1):17–26, 1921.

[147] Miguel A. Pérez-Osorio, Rebecca L. Milot, Marina R. Filip, Jay B. Patel, Laura M. Herz, Michael B. Johnston, and Feliciano Giustino. Vibrational Properties of the Organic-Inorganic Halide Perovskite $CH_3NH_3PbI_3$ from Theory and Experiment: Factor Group Analysis, First-Principles Calculations, and Low-Temperature Infrared Spectra. *Journal of Physical Chemistry C*, 119(46):25703–25718, 2015.

[148] Ruo Xi Yang, Jonathan M Skelton, E Lora da Silva, Jarvist M Frost, and Aron Walsh. Spontaneous Octahedral Tilting in the Cubic Inorganic Cesium Halide Perovskites $CsSnX_3$ and $CsPbX_3$ (X = F, Cl, Br, I). *J. Phys. Chem. Lett.*, 8(19):4720–4726, 2017.

[149] Julia Wiktor, Ursula Rothlisberger, and Alfredo Pasquarello. Predictive determination of band gaps of inorganic halide perovskites. *J. Phys. Chem. Lett.*, 8(22):5507–5512, 2017.

[150] Maxim Shishkin, Martijn Marsman, and Georg Kresse. Accurate quasiparticle spectra from self-consistent *GW* calculations with vertex corrections. *Physical*

Review Letters, 99(24):246403, 2007.

[151] Christopher L. Davies, Marina R. Filip, Jay B. Patel, Timothy W. Crothers, Carla Verdi, Adam D. Wright, Rebecca L. Milot, Feliciano Giustino, Michael B. Johnston, and Laura M. Herz. Bimolecular recombination in methylammonium lead triiodide perovskite is an inverse absorption process. *Nat. Commun.*, 9(1):293, 2018.

[152] Guy Ohad, Dahvyd Wing, Stephen E Gant, Ayala V Cohen, Jonah B Haber, Francisca Sagredo, Marina R Filip, Jeffrey B Neaton, and Leeor Kronik. Band gaps of halide perovskites from a Wannier-localized optimally tuned screened range-separated hybrid functional. *Physical Review materials*, 6(10):104606, 2022.

[153] Linn Leppert, Tonatiuh Rangel, and Jeffrey B. Neaton. Towards predictive band gaps for halide perovskites: Lessons from one-shot and eigenvalue self-consistent GW. *Phys. Rev. Mater.*, 3(10):103803, 2019.

[154] Stephen E Gant, Jonah B Haber, Marina R Filip, Francisca Sagredo, Dahvyd Wing, Guy Ohad, Leeor Kronik, and Jeffrey B Neaton. Optimally tuned starting point for single-shot gw calculations of solids. *Physical Review Materials*, 6(5):053802, 2022.

[155] Marina R Filip and Feliciano Giustino. GW calculations on hybrid organic-inorganic perovskites: Evidence of strong electronic polarization. *Physical Review B*, 90(24):245145, 2014.

[156] Federico Brivio, Keith T. Butler, Aron Walsh, and Mark van Schilfgaarde. Relativistic quasiparticle self-consistent electronic structure of hybrid halide perovskite photovoltaic absorbers. *Phys. Rev. B*, 89(15):155204, 2014.

[157] Giuseppe Grosso and Giuseppe Pastori Parravicini. In Giuseppe Grosso and Giuseppe Pastori Parravicini, editors, *Solid State Physics (Second Edition)*, chap-

ter 2 - Geometrical Description of Crystals: Direct and Reciprocal Lattices, pages 67–105. Academic Press, Amsterdam, 2014.

[158] F. H. da Jornada, Diana Y Qiu, and Steven G Louie. Nonuniform sampling schemes of the brillouin zone for many-electron perturbation-theory calculations in reduced dimensionality. *Phys. Rev. B*, 95(3):035109, 2017.

[159] S. D. Mahanti and C. M. Varma. Effective Electron and Hole Interactions in a Polarizable Field;. *Phys. Rev. Lett.*, 25(16):1115–1119, 1970.

[160] Stefano Baroni, Stefano De Gironcoli, Andrea Dal Corso, and Paolo Giannozzi. Phonons and related crystal properties from density-functional perturbation theory. *Reviews of modern Physics*, 73(2):515, 2001.

[161] Laura M. Herz. Charge-Carrier Mobilities in Metal Halide Perovskites: Fundamental Mechanisms and Limits. *ACS Energy Lett.*, 2(7):1539–1548, 2017.

[162] Adam D. Wright, Carla Verdi, Rebecca L. Milot, Giles E. Eperon, Miguel A. Pérez-Osorio, Henry J. Snaith, Feliciano Giustino, Michael B. Johnston, and Laura M. Herz. Electron–phonon coupling in hybrid lead halide perovskites. *Nat. Commun.*, 7(1):11755, 2016.

[163] W Travis, ENK Glover, H Bronstein, DO Scanlon, and RG Palgrave. On the application of the tolerance factor to inorganic and hybrid halide perovskites: a revised system. *Chemical science*, 7(7):4548–4556, 2016.

[164] Qingquan He, Michael Worku, Liangjin Xu, Chenkun Zhou, Sandrine Lteif, Joseph B Schlenoff, and Biwu Ma. Surface passivation of perovskite thin films by phosphonium halides for efficient and stable solar cells. *Journal of Materials Chemistry A*, 8(4):2039–2046, 2020.

[165] Ian C. Smith, Eric T. Hoke, Diego Solis-Ibarra, Michael D. McGehee, and Hemamala I. Karunadasa. A Layered Hybrid Perovskite Solar-Cell Absorber

with Enhanced Moisture Stability. *Angewandte Chemie International Edition*, 53(42):11232–11235, 2014.

[166] Hsinhan Tsai, Wanyi Nie, Jean-Christophe Blancon, Constantinos C. Stoumpos, Reza Asadpour, Boris Harutyunyan, Amanda J. Neukirch, Rafael Verduzco, Jared J. Crochet, Sergei Tretiak, Laurent Pedesseau, Jacky Even, Muhammad A. Alam, Gautam Gupta, Jun Lou, Pulickel M. Ajayan, Michael J. Bedzyk, Mercouri G. Kanatzidis, and Aditya D. Mohite. High-efficiency two-dimensional Ruddlesden–Popper perovskite solar cells. *Nature*, 536(7616):312–316, 2016.

[167] Rebecca L. Milot, Rebecca J. Sutton, Giles E. Eperon, Amir Abbas Haghighirad, Josue Martinez Hardigree, Laura Miranda, Henry J. Snaith, Michael B. Johnston, and Laura M. Herz. Charge-carrier dynamics in 2D hybrid metal–halide perovskites. *Nano letters*, 16(11):7001–7007, 2016.

[168] Daniele Cortecchia, Jun Yin, Annalisa Bruno, Shu-Zee Alencious Lo, Gagik G. Gurzadyan, Subodh Mhaisalkar, Jean-Luc Brédas, and Cesare Soci. Polaron self-localization in white-light emitting hybrid perovskites. *Journal of Materials Chemistry C*, 5(11):2771–2780, 2017.

[169] Lina Li, Zhihua Sun, Peng Wang, Weida Hu, Sasa Wang, Chengmin Ji, Maochun Hong, and Junhua Luo. Tailored Engineering of an Unusual $(C_4H_9NH_3)_2(CH_3NH_3)_2Pb_3Br_{10}$ two-dimensional multilayered perovskite ferroelectric for a high-performance photodetector. *Angewandte Chemie*, 129(40):12318–12322, 2017.

[170] Shan Chen, Huajie Yin, Porun Liu, Yun Wang, and Huijun Zhao. Stabilization and Performance Enhancement Strategies for Halide Perovskite Photocatalysts. *Advanced Materials*, 35(6):2203836, 2023.

[171] Chuanjiang Qin, Atula SD Sandanayaka, Chenyang Zhao, Toshinori Matsushima, Dezhong Zhang, Takashi Fujihara, and Chihaya Adachi. Stable room-

temperature continuous-wave lasing in quasi-2D perovskite films. *Nature*, 585(7823):53–57, 2020.

[172] Ekaterina I. Marchenko, Vadim V. Korolev, Artem Mitrofanov, Sergey A. Fateev, Eugene A. Goodilin, and Alexey B. Tarasov. Layer Shift Factor in Layered Hybrid Perovskites: Univocal Quantitative Descriptor of Composition–Structure–Property Relationships. *Chemistry of Materials*, 33(4):1213–1217, 2021.

[173] Xiaotong Li, Weijun Ke, Boubacar Traoré, Peijun Guo, Ido Hadar, Mikaël Kepenekian, Jacky Even, Claudine Katan, Constantinos C Stoumpos, Richard D Schaller, et al. Two-dimensional Dion-Jacobson hybrid lead iodide perovskites with aromatic diammonium cations. *Journal of the American Chemical Society*, 141(32):12880–12890, 2019.

[174] Rohit Prasanna, Aryeh Gold-Parker, Tomas Leijtens, Bert Conings, Aslihan Babayigit, Hans-Gerd Boyen, Michael F Toney, and Michael D McGehee. Band gap tuning via lattice contraction and octahedral tilting in perovskite materials for photovoltaics. *Journal of the American Chemical Society*, 139(32):11117–11124, 2017.

[175] Sonja Krach, Nicolás Forero-Correa, Raisa-Ioana Biega, Sebastian E Reyes-Lillo, and Linn Leppert. Emergence of Rashba-/Dresselhaus effects in Ruddlesden–Popper halide perovskites with octahedral rotations. *Journal of physics: Condensed matter*, 35(17):174001, 2023.

[176] Diana Y Qiu, Felipe H Da Jornada, and Steven G Louie. Optical spectrum of MoS_2: many-body effects and diversity of exciton states. *Physical Review Letters*, 111(21):216805, 2013.

[177] Ashish Arora, Matthias Drüppel, Robert Schmidt, Thorsten Deilmann, Robert Schneider, Maciej R Molas, Philipp Marauhn, Steffen Michaelis de Vasconcellos,

Marek Potemski, Michael Rohlfing, et al. Interlayer excitons in a bulk van der Waals semiconductor. *Nature communications*, 8(1):639, 2017.

[178] Elyse Barré, Ouri Karni, Erfu Liu, Aidan L. O'Beirne, Xueqi Chen, Henrique B. Ribeiro, Leo Yu, Bumho Kim, Kenji Watanabe, and Takashi Taniguchi. Optical absorption of interlayer excitons in transition-metal dichalcogenide heterostructures. *Science*, 376(6591):406–410, 2022.

[179] Yuko Takeoka, Miyuki Fukasawa, Takashi Matsui, Kentaro Kikuchi, Masahiro Rikukawa, and Kohei Sanui. Intercalated formation of two-dimensional and multi-layered perovskites in organic thin films. *Chemical Communications*, 0(3):378–380, 2005.

[180] Raja Chakraborty, Goutam Paul, and Amlan J Pal. Quantum confinement and dielectric deconfinement in quasi-two-dimensional perovskites: Their roles in light-emitting diodes. *Physical Review Applied*, 17(5):054045, 2022.

[181] Wenbin Li, Siraj Sidhik, Boubacar Traore, Reza Asadpour, Jin Hou, Hao Zhang, Austin Fehr, Joseph Essman, Yafei Wang, Justin M. Hoffman, Ioannis Spanopoulos, Jared J. Crochet, Esther Tsai, Joseph Strzalka, Claudine Katan, Muhammad A. Alam, Mercouri G. Kanatzidis, Jacky Even, Jean-Christophe Blancon, and Aditya D. Mohite. Light-activated interlayer contraction in two-dimensional perovskites for high-efficiency solar cells. *Nature Nanotechnology*, 17(1):45–52, 2022.

[182] Xiyue Dong, Mingqian Chen, Rui Wang, Qin Ling, Ziyang Hu, Hang Liu, Yufei Xin, Yang Yang, Jian Wang, and Yongsheng Liu. Quantum Confinement Breaking: Orbital Coupling in 2D Ruddlesden-Popper Perovskites Enables Efficient Solar Cells. *Advanced Energy Materials*, page 2301006, 2023.

[183] L. V. Butov, A. Zrenner, G. Abstreiter, G. Böhm, and G. Weimann. Condensation of Indirect Excitons in Coupled AlAs/GaAs Quantum Wells. *Physical Review*

Letters, 73(2):304–307, 1994.

[184] Simon Ovesen, Samuel Brem, Christopher Linderälv, Mikael Kuisma, Tobias Korn, Paul Erhart, Malte Selig, and Ermin Malic. Interlayer exciton dynamics in van der Waals heterostructures. *Communications Physics*, 2(1):1–8, 2019.

[185] Weijie Li, Zach Hadjri, Jin Zhang, Luka M Devenica, Song Liu, James Hone, Kenji Watanabe, Takashi Taniguchi, Angel Rubio, and Ajit Srivastava. Quadrupolar excitons in a tunnel-coupled van der Waals heterotrilayer. *arXiv preprint arXiv:2208.05490*, 2022.

[186] Catherine M. Mauck, Arthur France-Lanord, Alexander C. Hernandez Oendra, Nabeel S. Dahod, Jeffrey C. Grossman, and William A. Tisdale. Inorganic Cage Motion Dominates Excited-State Dynamics in 2D-Layered Perovskites $(C_xH_{2x+1}NH_3)_2PbI_4$ (x = 4-9). *J. Phys. Chem. C*, 123(45):27904–27916, 2019.

[187] Sivan Refaely-Abramson, Diana Y. Qiu, Steven G. Louie, and Jeffrey B. Neaton. Defect-Induced Modification of Low-Lying Excitons and Valley Selectivity in Monolayer Transition Metal Dichalcogenides. *Physical Review Letters*, 121(16):167402, 2018.

[188] M Bokdam, T Sander, A Stroppa, S Picozzi, D D Sarma, C Franchini, and G Kresse. Role of Polar Phonons into the Photo-Excited State of Metal Halide Perovskites. *Sci. Rep.*, 6(28618), 2016.

[189] Paolo Umari, Edoardo Mosconi, and Filippo De Angelis. Infrared Dielectric Screening Determines the Low Exciton Binding Energy of Metal-Halide Perovskites. *J. Phys. Chem. Lett.*, 9(3):620–627, 2018.

[190] Yeongsu Cho and Timothy C. Berkelbach. Optical Properties of Layered Hybrid Organic–Inorganic Halide Perovskites: A Tight-Binding GW-BSE Study. *The Journal of Physical Chemistry Letters*, 10(20):6189–6196, 2019.

[191] Laurent Pedesseau, Daniel Sapori, Boubacar Traore, Roberto Robles, Hong-Hua Fang, Maria Antonietta Loi, Hsinhan Tsai, Wanyi Nie, Jean-Christophe Blancon, Amanda Neukirch, Sergei Tretiak, Aditya D. Mohite, Claudine Katan, Jacky Even, and Mikaël Kepenekian. Advances and Promises of Layered Halide Hybrid Perovskite Semiconductors. *ACS Nano*, 10(11):9776–9786, 2016.

[192] Mauro Del Ben, Felipe H. Jornada, Andrew Canning, Nathan Wichmann, Karthik Raman, Ruchira Sasanka, Chao Yang, Steven G. Louie, and Jack Deslippe. Large-scale GW calculations on pre-exascale HPC systems. *Computer Physics Communications*, 235:187–195, 2019.

[193] Xiaotong Li, Justin M. Hoffman, and Mercouri G. Kanatzidis. The 2D Halide Perovskite Rulebook: How the Spacer Influences Everything from the Structure to Optoelectronic Device Efficiency. *Chemical Reviews*, 121(4):2230–2291, 2021.

[194] Constantinos C. Stoumpos, Chan Myae Myae Soe, Hsinhan Tsai, Wanyi Nie, Jean-Christophe Blancon, Duyen H. Cao, Fangze Liu, Boubacar Traoré, Claudine Katan, Jacky Even, Aditya D. Mohite, and Mercouri G. Kanatzidis. High Members of the 2D Ruddlesden-Popper Halide Perovskites: Synthesis, Optical Properties, and Solar Cells of $(CH_3(CH_2)_3NH_3)_2(CH_3NH_3)_4Pb_5I_{16}$. *Chem*, 2(3):427–440, 2017.

[195] Jack McArthur, Marina R. Filip, and Diana Y. Qiu. Minimal Molecular Building Blocks for Screening in Quasi-Two-Dimensional Organic-Inorganic Lead Halide Perovskites. *Nano Lett.*, 23(9):3796–3802, 2023.

[196] D. Kirk Lewis and Sahar Sharifzadeh. Defect-induced exciton localization in bulk gallium nitride from many-body perturbation theory. *Physical Review Materials*, 3(11):114601, 2019.

[197] Angelica Simbula, Luyan Wu, Federico Pitzalis, Riccardo Pau, Stefano Lai, Fang Liu, Selene Matta, Daniela Marongiu, Francesco Quochi, Michele Saba, et al.

Exciton dissociation in 2D layered metal-halide perovskites. *Nature communications*, 14(1):4125, 2023.

[198] Lingmei Kong, Xiaoyu Zhang, Yunguo Li, Haoran Wang, Yuanzhi Jiang, Sheng Wang, Mengqing You, Chengxi Zhang, Ting Zhang, Stephen V Kershaw, et al. Smoothing the energy transfer pathway in quasi-2D perovskite films using methanesulfonate leads to highly efficient light-emitting devices. *Nature communications*, 12(1):1246, 2021.

[199] Lingping Kong, Gang Liu, Jue Gong, Lingling Mao, Mengting Chen, Qingyang Hu, Xujie Lü, Wenge Yang, Mercouri G. Kanatzidis, and Ho-kwang Mao. Highly tunable properties in pressure-treated two-dimensional Dion–Jacobson perovskites. *Proceedings of the National Academy of Sciences*, 117(28):16121–16126, 2020.

[200] Tingting Yin, Hejin Yan, Ibrahim Abdelwahab, Yulia Lekina, Xujie Lü, Wenge Yang, Handong Sun, Kai Leng, Yongqing Cai, Ze Xiang Shen, and Kian Ping Loh. Pressure driven rotational isomerism in 2D hybrid perovskites. *Nature Communications*, 14(1):411, 2023.

[201] Daniel B. Straus and Cherie R. Kagan. Electrons, excitons, and phonons in two-dimensional hybrid perovskites: Connecting structural, optical, and electronic properties. *The Journal of Physical Chemistry Letters*, 9(6):1434–1447, 2018.

[202] Antonios M. Alvertis, Jonah B. Haber, Edgar A. Engel, Sahar Sharifzadeh, and Jeffrey B. Neaton. Phonon-induced localization of excitons in molecular crystals from first principles. *Phys. Rev. Lett.*, 130(8):086401, 2023.

[203] Bayrammurad Saparov and David B Mitzi. Organic–inorganic perovskites: structural versatility for functional materials design. *Chemical reviews*, 116(7):4558–4596, 2016.

[204] Eric G Tulsky and Jeffrey R Long. Dimensional reduction: a practical formalism for manipulating solid structures. *Chemistry of materials*, 13(4):1149–1166, 2001.

[205] Enzheng Shi, Biao Yuan, Stephen B Shiring, Yao Gao, Akriti, Yunfan Guo, Cong Su, Minliang Lai, Peidong Yang, Jing Kong, et al. Two-dimensional halide perovskite lateral epitaxial heterostructures. *Nature*, 580(7805):614–620, 2020.

[206] M Lumbreras, J Protas, S Jebbari, GJ Dirksen, and J Schoonman. Structure and ionic conductivity of mixed lead halides $\mathrm{PbCl}_{2x}\mathrm{Br}_{2(1-x)}$. ii. *Solid State Ionics*, 20(4):295–304, 1986.

[207] Machteld E Kamminga, Hong-Hua Fang, Marina R Filip, Feliciano Giustino, Jacob Baas, Graeme R Blake, Maria Antonietta Loi, and Thomas TM Palstra. Confinement effects in low-dimensional lead iodide perovskite hybrids. *Chemistry of materials*, 28(13):4554–4562, 2016.

[208] Yinan Chen and Marina R Filip. Tunable interlayer delocalization of excitons in layered organic–inorganic halide perovskites. *The Journal of Physical Chemistry Letters*, 14(47):10634–10641, 2023.

[209] Vesna Eric, Xinmeng Li, Lolita Dsouza, Annemarie Huijser, Alfred R Holzwarth, Francesco Buda, GJ Agur Sevink, Huub JM de Groot, and Thomas LC Jansen. Observation of dark states in two-dimensional electronic spectra of chlorosomes. *The Journal of Physical Chemistry B*, 128(15):3575–3584, 2024.

[210] Marco Ferretti, Ruud Hendrikx, Elisabet Romero, June Southall, Richard J Cogdell, Vladimir I Novoderezhkin, Gregory D Scholes, and Rienk Van Grondelle. Dark states in the light-harvesting complex 2 revealed by two-dimensional electronic spectroscopy. *Scientific reports*, 6(1):20834, 2016.

[211] Jinlin Yin, Huimin Yang, and Honghan Fei. Robust, cationic lead halide layered materials with efficient broadband white-light emission. *Chemistry of Materials*,

31(11):3909–3916, 2019.

[212] Mikaël Kepenekian, Roberto Robles, Claudine Katan, Daniel Sapori, Laurent Pedesseau, and Jacky Even. Rashba and Dresselhaus effects in hybrid organic–inorganic perovskites: from basics to devices. *ACS nano*, 9(12):11557–11567, 2015.

[213] Ethan J Crace, Alexander C Su, and Hemamala I Karunadasa. Reliably obtaining white light from layered halide perovskites at room temperature. *Chemical Science*, 13(34):9973–9979, 2022.

[214] Thorsten Deilmann and Kristian Sommer Thygesen. Quadrupolar and dipolar excitons in symmetric trilayer heterostructures: Insights from first principles theory. *2D Materials*, 2024.

[215] Leo Yu, Kateryna Pistunova, Jenny Hu, Kenji Watanabe, Takashi Taniguchi, and Tony F Heinz. Observation of quadrupolar and dipolar excitons in a semiconductor heterotrilayer. *Nature materials*, 22(12):1485–1491, 2023.

[216] Andre K Geim and Irina V Grigorieva. van der Waals heterostructures. *Nature*, 499(7459):419–425, 2013.

[217] Peiqi Wang, Chuancheng Jia, Yu Huang, and Xiangfeng Duan. van der Waals heterostructures by design: from 1D and 2D to 3D. *Matter*, 4(2):552–581, 2021.

[218] Andres Castellanos-Gomez, Xiangfeng Duan, Zhe Fei, Humberto Rodriguez Gutierrez, Yuan Huang, Xinyu Huang, Jorge Quereda, Qi Qian, Eli Sutter, and Peter Sutter. van der Waals heterostructures. *Nature Reviews Methods Primers*, 2(1):58, 2022.

[219] KS Novoselov, Artem Mishchenko, Alexandra Carvalho, and AH Castro Neto. 2D materials and van der Waals heterostructures. *Science*, 353(6298):aac9439, 2016.

[220] Nathan P Wilson, Wang Yao, Jie Shan, and Xiaodong Xu. Excitons and emergent quantum phenomena in stacked 2D semiconductors. *Nature*, 599(7885):383–392, 2021.

[221] Ouri Karni, Elyse Barré, Sze Cheung Lau, Roland Gillen, Eric Yue Ma, Bumho Kim, Kenji Watanabe, Takashi Taniguchi, Janina Maultzsch, Katayun Barmak, et al. Infrared interlayer exciton emission in MoS_2/WSe_2 heterostructures. *Physical Review Letters*, 123(24):247402, 2019.

[222] Xiaoyang Zhu, Nicholas R Monahan, Zizhou Gong, Haiming Zhu, Kristopher W Williams, and Cory A Nelson. Charge transfer excitons at van der Waals interfaces. *Journal of the American Chemical Society*, 137(26):8313–8320, 2015.

[223] Kaihui Liu, Liming Zhang, Ting Cao, Chenhao Jin, Diana Qiu, Qin Zhou, Alex Zettl, Peidong Yang, Steve G Louie, and Feng Wang. Evolution of interlayer coupling in twisted molybdenum disulfide bilayers. *Nature communications*, 5(1):4966, 2014.

[224] M Shah, LM Schneider, and A Rahimi-Iman. Observation of intralayer and interlayer excitons in monolayered WSe_2/WS_2 heterostructure. *Semiconductors*, 53:2140–2146, 2019.

[225] Mohammed Adel Aly, Manan Shah, Lorenz Maximilian Schneider, Kyungnam Kang, Martin Koch, Eui-Hyeok Yang, and Arash Rahimi-Iman. Radiative pattern of intralayer and interlayer excitons in two-dimensional WS_2/WSe_2 heterostructure. *Scientific Reports*, 12(1):6939, 2022.

Acknowledgement

The past four years have marked a period of tremendous growth for me, both academically and personally.

I would like to first express my gratitude to my supervisor, Prof. Marina Filip, who has made the DPhil research journey the most inspiring and rewarding experience of my life. I thank her for the four years of dedication and support. Under her guidance, I have become a more mature scientist and developed the mindset and skills to ask questions and solve problems, from which I will benefit for life. She is a very good role model, both as an independent and a collaborative researcher. She has always encouraged me to meet and engage more with collaborators and colleagues, to present my research at conferences, poster sessions, academic visits and group meetings. She has provided so many collaboration and presentation opportunities, through which my confidence, knowledge and skills have gradually grown. I thank her for being a very patient and inspiring mentor. She is very knowledgeable, experienced and passionate in this field. Our daily discussions were always filled with creative, intellectual sparks. Most importantly, I have to thank her for nurturing my enthusiasm in my research projects, as I believe passion is one of the keys to success in science, and in any field in life. I am truly grateful for the four-year fulfilling DPhil experience under her supervision.

I would like to acknowledge my collaborators, Prof. Linn Leppert and Dr. Raisa-Ioana Biega from the University of Twente, Prof. Joanne Etheridge and Dr. Weilun Li from the University of Monash, Prof. Laura Herz, Prof. Michael Johnston, Prof. Henry Snaith, Dr. Silvia Motti, Dr. Chelsea Xia, Dr. Harry Sansom, Qimu Yuan and Joshua Lilly in the Department. Their valuable insights, expertise, and collaborative spirits have significantly enriched my research experience here in Oxford. The work presented in Chapters 5 and 6 stems from the collaboration with experimental colleagues at Stanford. I would like to acknowledge Dr. Arundhati Deshmukh, Caravaggio Caniglia and

Prof. Hemamala Karunadasa for their proactive involvement, insightful discussions, and invaluable experimental contributions, which made this project very intriguing. I would like to thank Prof. Sahar Sharifzadeh from Boston University, who initially proposed the exciton correlation function, for her insightful discussions and her kind offer to benchmark our results. I also have to thank Prof. Yuan Ping from the University of Wisconsin, Madison, who introduced me to the field and inspired me to pursue my career as a researcher. I also would like to thank my friends and colleagues at Yale, Prof. Diana Qiu, Bowen Hou, Xian Xu, Xingzhi Sun, Zhiyuan, Xiaowei Ou and Aofeng Bai, who offered a warm welcome, generous support and insightful discussions that greatly enriched my visit to Yale. A huge thanks to all my amazing office mates for enriching my day-to-day experience, Tom, Santanu, Debalina, Austyn, Kiara and Chris. Though we shared a small office, we created a lot of fun experiences together. Thanks to all for making our group such a vibrant environment to work in.

A very special thanks goes to Yifan, whose support has been my constant source of strength. Thank you for sharing this Oxford journey with me (with our cat Domi), for your constant encouragement, and for making every day brighter. The memories we've created together here will always be cherished.

最后，也是最重要的，我想向我亲爱的父亲陈军，母亲黄赛枝表达我最深的感激。你们给予我无条件的爱与支持，是我人生路上取得一切成就的根基。感谢你们对我价值观、人生观、世界观的培养，感谢你们让我成为一个积极向上、热爱生活的人。更重要的是，我由衷地感谢你们一路以来对我的理解，尊重我的想法，支持我的决定并尽可能给我提供最好的条件，不管是当初选择去科大学物理，还是到后来的出国留学。尽管这四年中我们因距离而聚少离多，但不管我在哪里，我都知道你们始终如一在默默支持着我，我也会始终如一的爱你们。